Titre: Title:	Seismic velocities, anisotropy and elastic properties of crystalline rocks and implications for interpretation of seismic data
Auteur: Author:	Shengsi Sun
Date:	2011
Type:	Mémoire ou thèse / Dissertation or Thesis
Référence: Citation:	Sun, S. (2011). Seismic velocities, anisotropy and elastic properties of crystalline rocks and implications for interpretation of seismic data [Thèse de doctorat, École Polytechnique de Montréal]. PolyPublie. https://publications.polymtl.ca/725/

URL de PolyPublie: PolyPublie URL:	https://publications.polymtl.ca/725/
Directeurs de recherche: Advisors:	Shaocheng Ji
Programme: Program:	Génie minéral

UNIVERSITÉ DE MONTRÉAL

SEISMIC VELOCITIES, ANISOTROPY AND ELASTIC PROPERTIES OF CRYSTALLINE ROCKS AND IMPLICATIONS FOR INTERPRETATION OF SEISMIC DATA

SHENGSI SUN
DÉPARTEMENT DES GÉNIES CIVIL, GÉOLOGIQUE ET DES MINES
ÉCOLE POLYTECHNIQUE DE MONTRÉAL

THÈSE PRÉSENTÉE EN VUE DE L'OBTENTION
DU DIPLÔME DE PHILOSOPHIAE DOCTOR (Ph.D.)
(GÉNIE MINÉRAL)
DÉCEMBRE 2011

UNIVERSITÉ DE MONTRÉAL

ÉCOLE POLYTECHNIQUE DE MONTRÉAL

Cette thèse intitulée:

SEISMIC VELOCITIES, ANISOTROPY AND ELASTIC PROPERTIES OF CRYSTALLINE ROCKS AND IMPLICATIONS FOR INTERPRETATION OF SEISMIC DATA

présentée par : SUN Shengsi

en vue de l'obtention du diplôme de : Philosophiae Doctor

a été dûment acceptée par le jury d'examen constitué de :

M. CHOUTEAU Michel, Ph.D., président

M. JI Shaocheng, Ph.D., membre et directeur de recherche

M. MARTIGNOLE Jacques, Ph.D., membre

M. MARESCHAL Jean-Claude, Ph.D., membre

To my father *Heping Sun* 孙和平, my mother *Hong Liu* 刘虹,

and my husband *Kai Liu* 刘凯

ACKNOWLEDGEMENTS

I would like to express my great gratitude to my supervisor Prof. Shaocheng Ji for his guidance, encouragement, and help during my Ph.D. study. Furthermore, without his financial support, I could not come to Canada to complete my thesis. His enthusiasm, insights, diligence, persistence and hard work at science inspired me to continue my research career.

I would like to thank Dr. Matthew Salisbury for his support and kindness during the seismic velocity measurements and Mr. Robert Iuliucci for his technical assistance in the GSC/Dalhousie High Pressure Laboratory. I also express my appreciation to Prof. Jacques Martignole for his financial support, discussion and suggestions, and to Prof. Denis Marcotte for his contribution to the statistic analysis of the experimental data.

I am grateful to Prof. Michel Chouteau, Mrs. Manon Latour, Mrs. Carole Giguère, Mrs. Manon Leduc, and Mr. Yvéric Rousseau for their support and smile. I acknowledge École Polytechnique de Montréal for the exemption of my foreign student tuition fees. I thank the Natural Sciences and Engineering Council of Canada and the Chinese Academy of Geological Sciences for research grants to Prof. Shaocheng Ji.

I also would like to thank Prof. Dong Jia (Nanjing University, China) for encouraging me to study in Canada and Prof. Zhiqin Xu (Chinese Academy of Geological Sciences) for providing the Chinese Continental Scientific Drilling (CCSD) core samples.

Many thanks to all my friends in Canada and in China for sharing wonderful time together.

Finally, and most of all, I would like to thank my family for their unconditional love, support and trust.

RÉSUMÉ

La connaissance des propriétés sismiques et élastiques des roches cristallines polyphasées à haute pression et haute température est nécessaire pour interpréter les données sismiques (profils sismiques réflexion et réfraction, fonctions télésismiques, tomographie) en termes de lithologie, de minéralogie et d'état physique ainsi que pour établir des modèles lithologiques et structuraux de la lithosphère. La présente étude vise à mieux comprendre comment les propriétés sismiques et élastiques (vitesses sismiques en compression et en cisaillement (V_p et V_s), anisotropie, paramètres élastiques) en fonction de la pression de confinement varient avec la composition minéralogique et chimique, la microstructure, l'orientation préférentielle des réseaux cristallins ('lattice preferred orientation': LPO), et la géométrie et l'état des microfissures.

Cette thèse, se compose de six chapitres. Le Chapitre 1 aborde les propriétés sismiques des roches, en se concentrant sur les concepts d'élasticité et des règles mélange, et en donnant un aperçu sur des statistiques relatives aux données sismiques pour divers types lithologiques et pour des minéraux cardinaux, et ce, en relation avec les séismes dans la croûte continentale et la partie supérieure du manteau.

Le Chapitre 2 traite des propriétés sismiques et élastiques mesurées à des pressions hydrostatiques allant jusqu'à 800 MPa pour 12 échantillons représentatifs du complexe du Longmen Shan, siège du grand séisme de Wenchuan en 2008. La plupart des échantillons montrent peu d'anisotropie V_p ou V_s à des pressions supérieures à la pression de fermeture des microfissures (P_c = 200-300 MPa). La variation de l'anisotropie en fonction de la pression fournit des indications importantes sur l'orientation préférentielle des microfissures dans le régime non-linéaire poroélastique en dessous de P_c. Les profils rhéologiques et géothermiques indiquent que la profondeur au foyer (~19 km) correspond à la base de la schizosphere, niveau en dessous duquel le complexe du Longmen Shan passe d'un comportement fragile à un comportement ductile. L'analyse révèle que la croûte du Longmen Shan se compose de 4 couches depuis la surface jusqu'au Moho, soit: Couche 1: V_p <4,88 km/s (0-3 km d'épaisseur, roches sédimentaires type calcaire, grès, conglomérat, mudstone); Couche 2: V_p = 5,95 à 6,25 km/s (25-28 km d'épaisseur, roches felsiques); Couche 3: V_p= 6,55 km/s (10 km d'épaisseur, roches felsiques 67,5% et 32,5% mafiques) et Couche 4: V_p= 6,90 km/s (8 km d'épaisseur, roches felsiques 20,0%

et mafiques, 80,0%). La moyenne de 1,71 pour V_p/V_s ou le rapport de Poisson de 0,24 calculé pour l'ensemble de la croûte est cohérent avec les résultats mesurés à l'aide de techniques de récepteur télésismique. Cette étude offre également des informations nécessaires pour les simulations à large bande de mouvements du sol dans l'évaluation et la prévision régionale des risques sismiques. Par ailleurs, cette étude qui donne une magnitude de moment de 7,9 à 8,0, d'après les variations de pendage et de profondeur de la rupture cosismique fourni la première évaluation de la magnitude du séisme de Wenchuan.

Le Chapitre 3, cœur de la thèse, est une étude détaillée des propriétés sismiques (vitesses des ondes P et S, hystérésis, anisotropie et biréfringence des ondes de cisaillement) sur une suite d'échantillons du projet chinois de forage scientifique continental ('Chinese Continental Scientific Drilling': CCSD) dont le trou principal pénètre jusqu'à 5158m dans le terrane métamorphique à ultra-haute pression (UHP) de Sulu. Les vitesses sismiques des échantillons profonds sont plus sensibles à la pression dans le régime non linéaire de basse pression (<200-300 MPa) et moins sensibles dans le régime de linéaire haute pression (>200-300 MPa), que les échantillons de la surface. La comparaison suggère que les données à haute pression obtenues sur des échantillons profonds sont plus fiables pour l'extrapolation à la croûte profonde que les données obtenues à partir d'analogues de surface qui ont été soumis à une longue histoire d'altération des fissures intergranulaires et transgranulaires. L'augmentation significative de la sensibilité à la pression des vitesses sismiques pour les échantillons de forage dans le régime non-linéaire indique que les microfissures sont dépourvues de minéraux secondaires, et sont donc susceptibles de se fermer complètement dans les conditions de pression hydrostatique appliquées en laboratoire. Les données vitesse-pression fournissent des indices importants sur l'orientation préférentielle des microfissures, responsable de l'anisotropie des vitesse des ondes P et de la biréfringence des ondes de cisaillement dans les roches fissurées alors que l'effet de la compression sur les rapports V_p/V_s est négligeable pour les roches compactées sans fissures. Les vitesses sismiques d'un agrégat cristallin isotrope (sans orientation préférentielle des minéraux) et sans fissures, calculées à partir des constantes élastiques à pression ordinaire pour un monocristal en utilisant des moyennes de Voigt sont en accord avec les données de laboratoire à ~ 200 MPa. En comparant l'image par sismique réflexion à proximité du forage avec celle en incidence normale calculée à partir des vitesses mesurées en laboratoire on peut en déduire que les réflexions sismiques proviennent de roches mafiques (éclogite et éclogite rétrograde) ou d'unités ultramafiques dans les roches principalement felsiques.

Le Chapitre 4 est consacré à la caractérisation des constantes de Lamé pour les types courants de roches cristallines de la croûte terrestre et du manteau supérieur et de leurs variations en fonction de la pression, de la température et de la composition minéralogique. L'analyse est basée sur l'équivalent isotrope de données élastique de 475 roches naturelles citées dans la littérature. Le paramètre de Lamé (λ) et le module de cisaillement (μ) sont les plus importantes des propriétés élastiques des roches. En l'absence de fusion partielle, de réaction métamorphique, de déshydratation ou de transformation de phase, le λ d'une roche cristalline en fonction de P et T peut être décrit par $\lambda=a+(d\lambda/dP)P-c\exp(-kP)-(d\lambda/dT)T$, où a est la valeur λ projetée à la pression nulle si les microfissures étaient absentes; dλ/dP est la dérivée de la pression en régime élastique linéaire; c est la baisse initiale de λ provoquée par la présence de microfissures en extrapolant à la pression nulle ; k est la constante d'affaiblissement de la baisse de λ dans le régime poro-élastique non-linéaire; et dλ/dT est la dérivée de la température. λ augmente avec l'augmentation de la pression de façon non-linéaire à basse pression (<~300 MPa) et de façon linéaire à haute pression (>~300 MPa). Dans le régime des hautes pressions, λ diminue de façon quasi-linéaire avec la température et augmente avec dλ/dT dans la gamme de $1\text{-}10\times10^{-3}$ GPa/ºC. En approchant de la température de transition α-β du quartz, le quartzite affiche les valeurs λ négatives. Dans les diagrammes λ-ρ (densité) et μ-λ les principaux types lithologiques peuvent être clairement distingués. Les roches ultramafiques montrent une diminution systématique de μ et λ avec l'augmentation du degré de serpentinisation. Les éclogites, les roches mafiques (gabbro, diabase, granulites et gneiss mafiques) et les roches felsiques (granite, diorite, de gneiss felsique, de gneiss intermédiaires et des métasédiments) sont caractérisés par des valeurs de μ et λ respectivement élevées, modérées et basses. Pour le pyroxène et l'olivine, λ et ρ, augmentent avec l'augmentation de Fe/Mg alors que μ diminue. Dans la série des plagioclases, λ et μ augmentent avec l'augmentation de la teneur en anorthite. L'augmentation du contenu en grenat, sillimanite, rutile, zircon, ilménite et spinelle se traduit par une augmentation des valeurs λ et μ dans la roche correspondante. Ces résultats fournissent des contraintes améliorées sur la discrimination de la composition des roches de la croûte et du manteau supérieur en termes de λ et μ.

Le Chapitre 5 présente un aperçu sur les derniers développements concernant les modes de la biréfringence des ondes de cisaillement mesurées à partir des zones de subduction océanique et sur les modèles mécaniques (flux de coin 2D, 3D flux parallèles aux induits par leur migration, LPO de l'olivine et serpentinisation). Les zones de subduction sont le siège d'importants processus géologiques (transition de phase, déshydratation, fusion partielle, volcanisme et activité sismique). L'anisotropie sismique dans diverses parties des systèmes de subduction (par exemple plaque chevauchante, biseau de manteau, dalle de subduction, manteau sous la dalle) peut être révélée par l'analyse des trajets des ondes sismiques. Les LPO de l'olivine formés par les systèmes de glissement (010)[100], (010)[001], (100)[001], {0kl}[100], (001)[100] et {110}[001] sont désignés A, B, C, D, E et F, respectivement. Les systèmes A, D, et E peuvent correspondre à des directions de polarisation rapide (ϕ) parallèle à l'écoulement du manteau alors que φ résultant de B est perpendiculaire à l'écoulement du manteau. La LPO de type C correspond également à un flux parallèle au flux ϕ manteau, mais le temps de retard (δt) qui en résulte est beaucoup plus petit que dans le cas du type A. Les fabriques de type F ne causent pas de biréfringence des ondes de cisaillement dans la direction normale au plan de flux du manteau. Dans les biseaux de manteau et dans la lithosphère plongeante du manteau, le minéral hydraté le plus important est l'antigorite, qui se caractérise par une faible résistance, de faibles vitesses sismiques, et une haute anisotropie élastique. Par conséquent, les roches abondamment serpentinisées des biseaux mantelliques ont généralement une forte anisotropie sismique et un fort déphasage. Dans les cas où la serpentinisation dépasse ~10-20%, la LPO de la serpentine contrôle l'anisotropie sismique des roches du manteau déformé. Comme le déphasage dans les biseaux mantelliques dépend à la fois du degré de serpentinisation et du pendage de la dalle, les systèmes de subduction très serpentinisés et fortement inclinés sont plus susceptibles de produire un ϕ parallèle aux tranchées.

Enfin, le Chapitre 6 expose brièvement les principales conclusions et les travaux futurs sur la mesure des propriétés sismiques des éclogites rétrogrades et des péridotites serpentinisées du plateau tibétain.

ABSTRACT

The knowledge of seismic and elastic properties of polyphase crystalline rocks under high pressure and temperature conditions is fundamental in interpreting in-situ seismic data (e.g., reflections, refractions, received functions, and tomography). These data may be understood in terms of lithology, mineralogy, and physical state and as such they allow establishing lithospheric structure and composition models of continents. The present study aims to better understand how the seismic and elastic properties [e.g., compressional- and shear-wave velocities (V_p and V_s), anisotropy, and elastic parameters] under confining pressure are affected by modal and chemical compositions, microstructures, lattice preferred orientations (LPO) of rocks and by the geometry and state of microcracks.

This thesis consists of six chapters. Chapter 1 addresses the framework of rock seismic property studies, focusing on the concepts of elasticity and mixture rules, and providing an overview on results of statistical analysis on previous laboratory-measured seismic data of different lithologies and rock-forming minerals, and on the seismic anisotropy of the continental crust and upper mantle.

Chapter 2 deals with seismic and elastic properties measured at hydrostatic pressures up to 800 MPa for 12 representative samples from the Longmen Shan complex in which the great 2008 Wenchuan earthquake took place. These allowed understanding how coseismic ruptures nucleated and propagated. Most of the samples show little V_p or V_s anisotropy at pressures above the closure-pressure of microcrack (P_c=200-300 MPa), the variation of anisotropy with pressure thus provides important hints for the preferred orientation of microcracks in the nonlinear poroelastic regime below P_c. Geothermal and rheological profiles indicate that the focal depth (~19 km) corresponds to the base of the schizosphere, below which the Longmen Shan complex switches from brittle to ductile behaviour. Investigation reveals that the crust of the Longmen Shan range consists of 4 layers from the surface to the Moho: Layer 1: V_p<4.88 km/s (0-3 km thick, sedimentary rocks such as limestone, sandstone, conglomerate, and mudstone); Layer 2: V_p=5.95-6.25 km/s (25-28 km thick, felsic rocks); Layer 3: V_p=6.55 km/s (10 km thick, 67.5% felsic and 32.5% mafic rocks); and Layer 4: V_p=6.90 km/s (8 km thick, 20.0% felsic and 80.0% mafic rocks). The average V_p/V_s ratio of 1.71 or Poisson's ratio of 0.24

calculated for the whole crust is consistent with the results measured using teleseismic receiver function techniques. This study also offers necessary information for broadband simulations of strong ground motions in the assessment and forecast of earthquake hazards in the region. Furthermore, the study, which yields a moment magnitude of 7.9-8.0 given the variation in the dip of the coseismic ruptures and the uncertainty in the depth to which the coseismic rupture may propagate downwards below the depth of the mainshock hypocenter, presents the first accurate quantification of the 2008 Wenchuan earthquake's size.

Chapter 3 is the strength of this thesis, which provides a detailed study of seismic properties (P- and S-wave velocities, hysteresis, anisotropy and shear wave splitting) on a unique suite of deep borehole core samples from the Chinese Continental Scientific Drilling (CCSD) project. The CCSD penetrated 5158 m into the Sulu ultrahigh-pressure (UHP) metamorphic terrane in China. Seismic velocities of the deep core samples are more sensitive to pressure in the low pressure (<200-300 MPa) nonlinear regime, and less sensitive to pressure in the high pressure (>200-300 MPa) linear regime, respectively, than samples from the surface. The comparison suggests that the high pressure data from the core samples are much more reliable for extrapolation to deeper crust than the data from surface analogues that have been subjected to long histories of weathering and alteration along intergranular and transgranular cracks. The significant increases in the pressure sensitivity of seismic velocities for the core samples in the nonlinear regime indicate that drilling-induced and stress-relief microcracks with small aspect ratios are fresh and clean without secondary mineral in-fillings, and are thus easily closed under applied hydrostatic pressure conditions of the laboratory. The data also show that the velocity-pressure data can successfully provide important hints about the preferred orientation of microcracks that causes P-wave velocity anisotropy and shear wave splitting in cracked rocks, and that the effect of compression on the V_p/V_s ratios is negligible for crack-free compacted rocks. The seismic velocities of equivalent isotropic (fabric-free) and crack-free crystalline aggregates calculated from room pressure single crystal elastic constants using the Voigt average are in agreement with laboratory data at ~200 MPa. Comparison of the seismic reflection image from the vicinity of the borehole with the normal-incidence reflection coefficient profile computed from the laboratory-measured velocities and densities infers that the seismic reflections originate from mafic (eclogite and retrograde eclogite) or ultramafic units within dominantly felsic rocks.

Chapter 4 is devoted to the characterization of Lamé constants for common types of crystalline rocks in the Earth's crust and upper mantle and their variations with pressure (P), temperature (T) and mineralogical composition. The analysis was based on the equivalent isotropic elastic data of 475 natural rocks, reported in the literature. Lamé parameter (λ) and shear modulus (μ) are the most important, intrinsic, elastic properties of rocks. When no partial melting, metamorphic reaction, dehydration or phase transformation occurs, λ of a crystalline rock as a function of P and T can be described by $\lambda=a+(d\lambda/dP)P-c\exp(-kP)-(d\lambda/dT)T$, where a is the projected λ value at zero pressure if microcracks were fully closed; dλ/dP is the pressure derivative in the linear elastic regime; c is the initial λ drop caused by the presence of microcracks at zero pressure; k is a decay constant of the λ drop in the nonlinear poro-elastic regime; and dλ/dT is the temperature derivative. λ increases nonlinearly and linearly with increasing pressure at low (<~300 MPa) and high (>~300 MPa) pressures, respectively. In the regime of high pressures, λ decreases quasi-linearly with increasing temperature with dλ/dT values in the range of $1\text{-}10\times10^{-3}$ GPa/ºC. Approaching the α-β quartz transition temperature, quartzite displays negative λ values. In the λ-ρ (density) and μ-λ plots, the main categories of lithology can be clearly distinguished. The ultramafic rocks display systematic decreases in both μ and λ with increasing the degree of serpentinization. Eclogites, mafic rocks (gabbro, diabase, mafic granulite, and mafic gneiss) and felsic rocks (granite, diorite, felsic gneiss, intermediate gneiss and metasediments) are characterized by high, moderate and low μ and λ values, respectively. For pyroxene and olivine, both λ and ρ increase but μ decreases with increasing Fe/Mg ratios. In the plagioclase series, both λ and μ increases with increasing anorthite content. Increases in the content of garnet, sillimanite, rutile, zircon, ilmenite and spinel result systematically in an increase in rock's λ and μ values. The present results provide improved constraints on the discrimination of composition for crustal and upper mantle rocks in terms of λ and μ.

Chapter 5 presents a state of the art overview on shear wave splitting patterns measured from global oceanic subduction zones, and on mechanism models (2D corner flow, 3D trench-parallel flow induced by trench migration, olivine LPOs and serpentinization). Subduction zones are critical regions where significant geological processes (e.g., phase transition, dehydration, partial melting, volcanism, and seismic activity) take place. Seismic anisotropy formed by different parts of subduction system (i.e., overriding plate, mantle wedge, subducting slab, and subslab mantle) can be distinguished by analyzing seismic wave raypaths. Olivine LPOs formed by (010)[100], (010)[001], (100)[001], {0kl}[100], (001)[100] and {110}[001] slip systems are identified as A, B, C, D, E and F-type fabrics, respectively. The A, D, and E-type fabrics cause fast polarization directions (ϕ) parallel to the mantle flow while ϕ formed by B-type fabric is perpendicular to the mantle flow. Olivine C-type LPO also results in a ϕ parallel to the mantle flow, but the resultant delay time (δt) is much smaller than A-type. F-type fabric results in almost no splitting in the direction normal to the mantle flow plane. In mantle wedge and subducting lithosphere mantle, the most important hydrous mineral is antigorite, which is characterized by extremely low flow strength, low seismic velocities, and high elastic anisotropy. Accordingly, the extensively serpentinized mantle wedge rocks usually have relative high seismic anisotropy and shear wave splitting. If more than ~10-20% serpentinization occurs, serpentine LPO would control the seismic anisotropy of the deformed mantle rocks. As shear wave splitting in mantle wedge depends on both the degree of serpentinization and the slab dip, highly serpentinized and steeply dipped subduction systems are more likely to produce a trench-parallel ϕ.

Finally, Chapter 6 briefly outlines the main conclusions and the future work on measured seismic properties of retrograde eclogites and serpentinized peridotites from the Tibet Plateau (China).

TABLE OF CONTENTS

LIST OF TABLES

LIST OF FIGURES

LIST OF INITIALS AND ABBREVIATIONS

Symbol	**Notation**
P	Pressure
UHP	Ultrahigh pressure
P-wave	Compressional wave
S-wave	Shear wave
CCSD	Chinese Continental Scientific Drilling
ρ	Density in g/cm^3
λ	Lamé parameter
μ	Shear modulus
E	Young’s modulus
K	Bulk modulus
υ	Poisson's ratio
$\boldsymbol{C}$	Stiffness tensor
$\boldsymbol{S}$	Compliance tensor
T	Temperature
V_p	Compressional wave velocity
V_s	Shear wave velocity
V_{s1}	Fast shear wave velocity in shear wave splitting
V_{s2}	Slow shear wave velocity in shear wave splitting
ϕ	Fast polarization direction in shear wave splitting
δt	Delay time in shear wave splitting
X	Direction parallel to the stretching lineation
Y	Direction perpendicular to the lineation and in the foliation
Z	Direction normal to the foliation
Λ	Direction of wave propagation and polarization
A	Seismic velocity anisotropy
H	Seismic velocity hysteresis
LPO	Lattice-preferred orientation

CHAPTER 1 INTRODUCTION

1.1 Objective and organization of the thesis

The major efforts over the last three decades for the acquisition of continental seismic data, and the recent advances in data analysis and interpretation have led to the development of robust models for the formation and tectonic evolution of the continents. The interpretation of seismic data in terms of lithology and chemical composition in the crust and upper mantle has been made essentially by comparison of in-situ seismic velocities with laboratory-measured properties of rock samples. The research objective of this Ph.D. thesis is to better understand how the seismic compressional- and shear-wave velocities (V_p and V_s), hysteresis, anisotropy, and elastic moduli of crystalline rocks in the Earth's crust and upper mantle are affected by their modal and chemical compositions, microstructures (e.g., foliation and lineation), lattice preferred orientations (LPO) of anisotropic minerals, and the geometry and state of microcracks at various confining pressures.

The devastating 2008 Wenchuan earthquake occurred in the Longmen Shan region, the transition zone between the Tibetan Plateau and the Sichuan Basin, representing the largest active tectonic event reported to date in Sichuan (China). In Chapter 2, seismic and elastic properties of 12 representative samples from the Longmen Shan complex are experimentally calibrated up to 800 MPa in order to provide necessary constraints on the regional seismic velocity models used for the tectonic interpretation of seismic data and broadband simulations of strong ground motions in the assessment and forecast of earthquake hazards and on the seismic moment magnitude of the 2008 Wenchuan Earthquake. This study, which yields a moment magnitude of 7.9-8.0 given the variation in the dip of the coseismic ruptures and the uncertainty in the depth to which the coseismic rupture may propagate downwards below the depth of the mainshock hypocenter, presents the first accurate quantification of the 2008 Wenchuan earthquake's size in terms of the fault geometry and coseismic displacement.

Most of the laboratory measurements of seismic velocities and anisotropy have been performed on rock samples collected from surface exposures in North America, Western Europe and Japan. A basic question to be answered remains: can the seismic properties of surface-derived samples be reliably extrapolated to the Earth's interior if these samples have been long exposed to weathering and have experienced alteration along microcracks and grain boundaries? Thus, it is of the utmost importance to quantify the seismic properties of unaltered rock samples from greater depths. The Chinese Continental Scientific Drilling (CCSD) project, which drilled to a depth of 5158 meters into the ultrahigh pressure (UHP) metamorphic terrane in the Sulu region of central eastern China, provides a complete suite of unaltered, rare UHP metamorphic rock samples for measurements of seismic properties. In Chapter 3, the V_p-pressure behaviors of deep core samples from the CCSD borehole are compared with their surface equivalents. The comparison suggests that the high pressure data from the core samples are much more reliable for extrapolation to deeper crust than the data from surface analogues that have been subjected to long histories of weathering and alteration along intergranular and transgranular cracks. Furthermore, Chapter 3 presents new results on P- and S-wave velocities, hysteresis, V_p anisotropy and shear wave splitting as a function of confining pressure up to 800 MPa for a suite of 22 samples collected from the CCSD main hole. The results of this study provide insight into the origin of hysteresis, anisotropy and shear wave splitting and the reflectivity of the UHP metamorphic rocks from the Sulu orogenic belt and perhaps other HP/UHP metamorphic terranes throughout the world. One of the main focuses of the investigation is to elucidate the role of microcrack preferred orientations on seismic anisotropy and shear wave splitting.

The elastic properties of a homogeneous isotropic rock can be uniquely described using two independent moduli termed Lamé parameter (λ) and shear modulus (μ), introduced and named after the 18th century French mathematician and engineer Gabriel Lamé (1795-1870). Only λ and μ appear in the tensor form of Hooke's law, but not Young's modulus (E), bulk modulus (K), or Poisson's ratio (υ). It is thus clear that λ and μ are the most important intrinsic and invariant elastic moduli required to describe stress in terms of strain for materials or rocks. However, most scientists are familiar with the physical significance of μ, E, K, and υ, but not that of λ, probably because the physical significance of λ is less straightforward. Actually, λ, which relates stresses and strains in perpendicular directions, is closely related to the incompressibility and contains a high proportion of information about the resistance to a change in volume caused by a change in pressure. Chapter 4 of this thesis deals with the pressure- and temperature-dependences of Lamé parameters for common categories of crystalline rocks from the Earth's crust and upper mantle, and explores the potential implications of Lamé parameter as a discriminant of composition for common rock types in the Earth's crust and upper mantle.

Subduction zones are critically important regions where significant geological processes (e.g., phase transition, dehydration, partial melting, volcanism, and seismic activity) take place. Since the 80s of the 20th century, shear wave splitting has been one of the powerful tools for investigating oceanic subduction zones. Seismic anisotropy originated from different parts of subduction system (i.e., the overriding plate, the mantle wedge, the subducting slab, and the subslab mantle) can be distinguished through the analysis of seismic wave raypaths. Chapter 5 provides a state-of-art overview on shear wave splitting patterns obtained from global oceanic subduction zones, and on the origins of shear-wave splitting (e.g., 2D corner flow, 3D trench-parallel flow induced by trench migration, olivine LPOs and serpentinization).

Finally, Chapter 6 presents a succinct summary of the main conclusions and discusses the further work needed to perform.

In order to facilitate the reading of this thesis, an introduction to the basic principles of elasticity (Section 1.2), a statistical analysis of previous laboratory-measured seismic data (Section 1.3), and an overview on the seismic anisotropy of the continental crust and upper mantle (Section 1.4) are provided below.

1.2 Elasticity

1.2.1 Theory of elasticity

Many materials such as crystalline rocks can be approximately considered perfectly linear elastic without appreciable error when the deformations are small, as is the case for seismic waves except near a seismic source. The theory of elasticity deals with the relations between the stress (σ_{ij}) and the resulting strain (ε_{ij}) on a body, where i and j may take the values 1, 2, or 3, parallel to the coordinate axes x_1, x_2, x_3, respectively, the first suffix denotes the direction of the stress component and the second the direction of the outward normal to the plane upon which it acts (Nye, 1957, Figure 1.1). Stresses of σ_{11}, σ_{22} and σ_{33} are normal stresses, whereas the remaining six stress components which have different suffices are shear stresses (e.g., σ_{12}, σ_{23}, and σ_{32}).

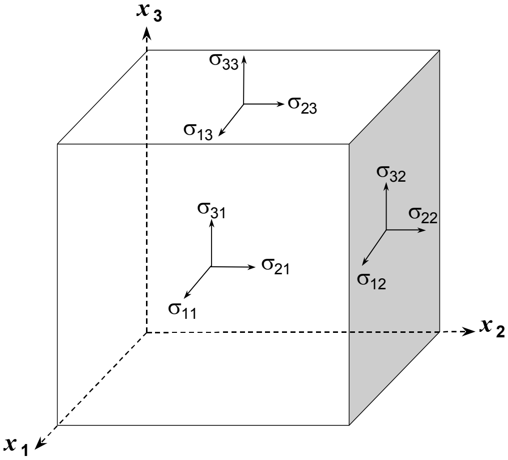

Figure 1.1 Stress components acting on the faces of a unit cube.

The relation between stress and strain was first identified by Robert Hooke, a 17th century British physicist. A perfect elastic body deforms as linear elasticity, which is stated by Hooke's law:

$$\sigma_{ij} = C_{ijkl}\varepsilon_{kl} \tag{1.1}$$

or

$$\varepsilon_{ij} = S_{ijkl}\sigma_{kl} \tag{1.2}$$

where C_{ijkl} and S_{ijkl} are the elastic stiffness and compliance, respectively, and i, j, k, l =1, 2, or 3. Because the conditions for zero rotation of the body are $\sigma_{12}=\sigma_{21}$, $\sigma_{13}=\sigma_{31}$ and $\sigma_{23}=\sigma_{32}$, σ_{ij} contains only 6 independent components and the stiffness C_{ijkl} can be expressed by a 6×6 tensor. C_{ijkl} is usually written using two indices as C_{qr} when new indices are defined as 11→1, 22→2, 33→3, 23→4, 13→5, 12→6. Thus $C_{1111}=\mathrm{C}_{11}$, $C_{1213}=C_{65}$, etc.

$$C_{qr} = \begin{pmatrix} C_{11} & C_{12} & C_{13} & C_{14} & C_{15} & C_{16} \\ C_{21} & C_{22} & C_{23} & C_{24} & C_{25} & C_{26} \\ C_{31} & C_{32} & C_{33} & C_{34} & C_{35} & C_{36} \\ C_{41} & C_{42} & C_{43} & C_{44} & C_{45} & C_{46} \\ C_{51} & C_{52} & C_{53} & C_{54} & C_{55} & C_{56} \\ C_{61} & C_{62} & C_{63} & C_{64} & C_{65} & C_{66} \end{pmatrix} \tag{1.3}$$

The components of compliance S_{ijkl} can be specified in a similar way to the stiffness. The compatibility between C_{qr} and S_{qr} requires

$$C_{qr} \bullet S_{q_r} = I \tag{1.4}$$

where I is the unit tensor.

Due to the reciprocal relations $C_{qr}=C_{rq}$ imposed by thermodynamic requirements, the stiffnesses C_{qr} can be further simplified into 21 independent elastic coefficients, which are used to describe the elastic behavior of a material belonging to the triclinic crystal system (e.g., plagioclase). The existence of symmetry will reduce the number of independent elastic constants to 13 for monoclinic (e.g., hornblende, clinopyroxene, coesite and muscovite), 9 for orthorhombic (e.g., sillimanite, olivine and orthopyroxene), 7 or 6 for trigonal (e.g., dolomite, α-quartz, and calcite) or tetragonal (e.g., rutile and zircon), 5 for hexagonal (e.g., graphite and nepheline), and 3 for cubic crystal systems (e.g., garnets, spinel, magnetite, halite, pyrite, and sphalerite). For isotropic material, its elastic behavior can be completely described by two independent elastic constants (Table1.1).

Table 1.1 The stiffness C_{qr} for isotropic, cubic, hexagonal, and orthorhombic systems.

Symmetry	C_{qr}	**Symmetry**	C_{qr}
Isotropic	$\begin{pmatrix} C_{11} & C_{12} & C_{12} & 0 & 0 & 0 \\ C_{12} & C_{11} & C_{12} & 0 & 0 & 0 \\ C_{12} & C_{12} & C_{11} & 0 & 0 & 0 \\ 0 & 0 & 0 & (C_{11}-C_{12})/2 & 0 & 0 \\ 0 & 0 & 0 & 0 & (C_{11}-C_{12})/2 & 0 \\ 0 & 0 & 0 & 0 & 0 & (C_{11}-C_{12})/2 \end{pmatrix}$	Hexagonal	$\begin{pmatrix} C_{11} & C_{12} & C_{13} & 0 & 0 & 0 \\ C_{12} & C_{11} & C_{13} & 0 & 0 & 0 \\ C_{13} & C_{13} & C_{33} & 0 & 0 & 0 \\ 0 & 0 & 0 & C_{44} & 0 & 0 \\ 0 & 0 & 0 & 0 & C_{44} & 0 \\ & 0 & 0 & 0 & 0 & (C_{11}-C_{12})/2 \end{pmatrix}$
Cubic	$\begin{pmatrix} C_{11} & C_{12} & C_{12} & 0 & 0 & 0 \\ C_{12} & C_{11} & C_{12} & 0 & 0 & 0 \\ C_{12} & C_{12} & C_{11} & 0 & 0 & 0 \\ 0 & 0 & 0 & C_{44} & 0 & 0 \\ 0 & 0 & 0 & 0 & C_{44} & 0 \\ 0 & 0 & 0 & 0 & 0 & C_{44} \end{pmatrix}$	Orthorhombic	$\begin{pmatrix} C_{11} & C_{12} & C_{13} & 0 & 0 & 0 \\ C_{12} & C_{22} & C_{23} & 0 & 0 & 0 \\ C_{13} & C_{23} & C_{33} & 0 & 0 & 0 \\ 0 & 0 & 0 & C_{44} & 0 & 0 \\ 0 & 0 & 0 & 0 & C_{55} & 0 \\ 0 & 0 & 0 & 0 & 0 & C_{66} \end{pmatrix}$

For a statistically isotropic (e.g., fabric-free polycrystalline rocks and amorphous glasses), linearly elastic solid, only two of the following elastic constants are required to characterize the seismic and elastic properties: the Young's (E), shear (μ) and bulk (K) moduli, Lamé parameter (λ) and Poisson's ratio (υ). Once two independent constants are known, other constants can be calculated according to the well-known equations in elastic mechanics. The magnitudes of the elastic constants reflect crystal interatomic bonding, grain boundary strength, and microstructural characteristics (e.g., microcracks, porosity, phase connectivity and continuity) of rocks during uniaxial extension/compression, simple shear and hydrostatic compression.

Young's modulus (E) is defined as the ratio of compressional stress to the resultant longitudinal strain for a small cylinder under compression at both ends:

$$E = \frac{\sigma_{11}}{\varepsilon_{11}} \tag{1.5}$$

Bulk modulus (K) is defined as:

$$K = -V\frac{\partial P}{\partial V} \tag{1.6}$$

where P is pressure, V is volume, and ∂P/∂V denotes the partial derivative of pressure with respect to volume.

Poisson's ratio (υ) was defined by a French mathematician Simeon Poisson in 1829 as the negative of the ratio of transverse strain (ε_{jj}) to the axial strain (ε_{ii}) when an isotropic elastic solid is subjected to uniaxial stress (σ_{ii}) only (Gercek, 2007).

$$\upsilon = -\frac{\varepsilon_{jj}}{\varepsilon_{ii}} \tag{1.7}$$

For an isotropic material at a given temperature and a given pressure, Poisson's ratio is a constant that does not depend on the choice of *i* and *j*, and lies between -1 and 0.5. Liquids have no resistance to shear but are incompressible and hence υ=0.5. Materials with υ<0 are called auxetic materials (e.g., foams) because there is an increase in volume when compressed (Lakes, 1987). A negative value of Poisson's ratio implies that a cylinder undergoing compression along its axis would contract simultaneously in all directions, which has been observed for certain directions in single crystals (Svetlov et al., 1988). The values of Poisson's ratio vary from 0.05

for very hard, rigid rocks to about 0.45 for soft, poorly consolidated materials. For most rocks, Poisson's ratio is about 0.22-0.30.

The elastic constants of an isotropic rock are usually determined through acoustic measurements of compressional (P) and shear (S) wave velocities (V_p and V_s) using the pulse transmission technique (Birch, 1960; Christensen, 1974; Ji et al., 1993; Ji and Salisbury, 1993), along with the density (ρ), because they are the most common geophysical parameters measurable.

$$K = \rho\left(V_p^{\,2} - \frac{4}{3}V_s^{\,2}\right) \qquad (1.8)$$

$$E = \frac{\rho V_s^{\,2}\left(3V_p^{\,2} - 4V_s^{\,2}\right)}{V_p^{\,2} - V_s^{\,2}} \qquad (1.9)$$

$$\upsilon = \frac{0.5(V_p/V_s)^2 - 1}{(V_p/V_s)^2 - 1} \qquad (1.10)$$

1.2.2 Lamé constants

The elastic properties of an isotropic material or rock can be described by two independent moduli termed lambda (λ) and mu (μ), introduced and named after the 18th century French mathematician and engineer Gabriel Lamé (1795-1870). In 1828, Lamé formulated the modern version of Hooke's law relating stress (σ_{ij}) to strain (ε_{ij}) in its general tensor form, thereby creating the basis for the materials sciences and rock mechanics:

$$\sigma_{ij} = \delta_{ij}\lambda\Delta + 2\mu\varepsilon_{ij} \qquad (1.11)$$

where the volume strain $\Delta=\varepsilon_{11}+\varepsilon_{22}+\varepsilon_{33}$, δ_{ij} is the Kronecker delta, $\delta_{ij}=1$ when $i=j$, and $\delta_{ij}=0$ when $i\neq j$; λ and μ are the first and second Lamé constants, respectively. Hereafter Lamé parameter (λ) is used in place of the first Lamé constant as it varies with pressure and temperature. The second Lamé constant μ is identical to the shear modulus or rigidity, which reflects the resistance to a simple shear strain that produces a shape change without changing total volume. Shear modulus μ is defined as:

$$\mu = \frac{\sigma_{12}}{2\varepsilon_{12}} \tag{1.12}$$

λ relates stresses and strains in perpendicular directions (Jaeger, 1969). The physical meaning of λ can be clearly illustrated in a special case of uniaxial strain where $\varepsilon_1 \neq 0$, and $\varepsilon_2=\varepsilon_3=0$ (i.e., no displacement occurs perpendicular to the x-axis): $\lambda=\sigma_2/\varepsilon_1=\sigma_3/\varepsilon_1$. Interestingly and most notably, only λ and μ appear in Hooke's law, but not Young's modulus (E), the bulk modulus (K), or Poisson's ratio (υ). This indicates that λ and μ are the most intrinsic elastic coefficients to express stress in terms of strain.

For an isotropic medium, Eq. (1.11) can be written in matrix-vector form that is composed of 6 rows and 6 columns:

$$\begin{bmatrix} \sigma_{11} \\ \sigma_{22} \\ \sigma_{33} \\ \sigma_{12} \\ \sigma_{13} \\ \sigma_{23} \end{bmatrix} = \begin{bmatrix} \lambda+2\mu & \lambda & \lambda & 0 & 0 & 0 \\ \lambda & \lambda+2\mu & \lambda & 0 & 0 & 0 \\ \lambda & \lambda & \lambda+2\mu & 0 & 0 & 0 \\ 0 & 0 & 0 & 2\mu & 0 & 0 \\ 0 & 0 & 0 & 0 & 2\mu & 0 \\ 0 & 0 & 0 & 0 & 0 & 2\mu \end{bmatrix} \begin{bmatrix} \varepsilon_{11} \\ \varepsilon_{22} \\ \varepsilon_{33} \\ \varepsilon_{12} \\ \varepsilon_{13} \\ \varepsilon_{23} \end{bmatrix} \tag{1.13}$$

Thus,

$$\sigma_{11}+\sigma_{22}+\sigma_{33} = (3\lambda+2\mu)(\varepsilon_{11}+\varepsilon_{22}+\varepsilon_{33}) \tag{1.14}$$

as

$$\varepsilon_{11}+\varepsilon_{22}+\varepsilon_{33} = -\frac{\Delta V}{V} \tag{1.15}$$

$$\sigma_{11}+\sigma_{22}+\sigma_{33} = 3P \tag{1.16}$$

According to Eq. (1.6), bulk modulus K equals

$$K = -V\frac{\partial P}{\partial V} = -P\frac{V}{\Delta V} = \lambda + \frac{2}{3}\mu \tag{1.17}$$

Therefore, Goodway (2001) believes that λ is closely related to material's incompressibility and contains a higher proportion of information about the resistance to a change in volume caused by a change in pressure ($\lambda=K-2\mu/3$). λ is negative if $K<2\mu/3$ as $K>0$ and $\mu>0$.

The Lamé parameter λ and shear modulus μ for isotropic elasticity can be easily determined from the measured seismic data:

$$\lambda = \rho(V_p^2 - 2V_s^2) \tag{1.18}$$

$$\mu = \rho V_s^2 \tag{1.19}$$

The merits of using λ and μ has been highlighted in the exploration of oil or gas reservoirs (Goodway et al., 1997; Gray and Andersen, 2000; Goodway, 2001; Dufour et al., 2002; Gray, 2003; Li et al., 2003). As shown in Table 1.2, distinguishing gas sand from shale is difficult or impossible using common P-wave methods as the V_p contrast between these two rocks is only 1.4%. However, the λ and λ/μ contrasts between these two rocks are as high as 70% and 110%, respectively. The conventional measurements from V_p/V_s of 26.8% or υ of 45.2% are also far less sensitive. The reason for the above fact is that V_p depends on both λ and μ, the effect of decreasing λ as a consequence of the gas porosity is almost completely offset by an increase in μ in going from capping shale to gas sand (Goodway, 2001). The discrimination between porous and tight sand is also significantly improved by using λ and μ values with respect to V_p/V_s of 2.0% or υ of 3.8% (Table 1.2).

Table 1.2 Merits of using Lamé constants rather than V_p and V_s data (Data from Goodway, 2001)

Lithology	**V_p (km/s)**	**V_s (km/s)**	**ρ (g/cm^3)**	**V_p/V_s**	**υ**	**E (GPa)**	**K (GPa)**	**μ (GPa)**	**λ (GPa)**	**λ/μ**
Shale	2.898	1.29	2.425	2.25	0.38	11.137	15.468	4.035	12.3	3.1
Gas sand	2.857	1.666	2.275	1.71	0.24	15.659	10.038	6.314	5.9	0.9
Contrast (%)	1.4	25.4	6.4	26.8	45.2	33.8	42.6	44	70.3	110.0
Porous sand	4.098	2.342	2.35	1.75	0.26	32.481	22.556	12.889	13.685	1.062
Tight sand	4.684	2.623	2.55	1.79	0.27	44.565	32.293	17.545	20.859	1.189
Contrast (%)	13.3	11.3	8.2	2.0	3.8	31.4	35.5	30.6	41.5	11.3

For reservoir sedimentary rocks that are generally porous, Goodway et al. (1997) and Gray and Andersen (2000) used a crossplot of μρ versus λρ (Fig. 1.2) in place of a μ-λ diagram. According to these authors, different types of lithology tend to separate along orthogonal boundaries in such a μρ-λρ crossplot: (1) coals have the lowest values of both λρ and μρ. (2) Carbonates have high values of both λρ and μρ. (3) Gas-filled sandstones have low λρ values but high μρ values. A combination of λρ and μρ values has been used for quick determination of reservoir lithology and gas content (e.g., Li et al., 2003).

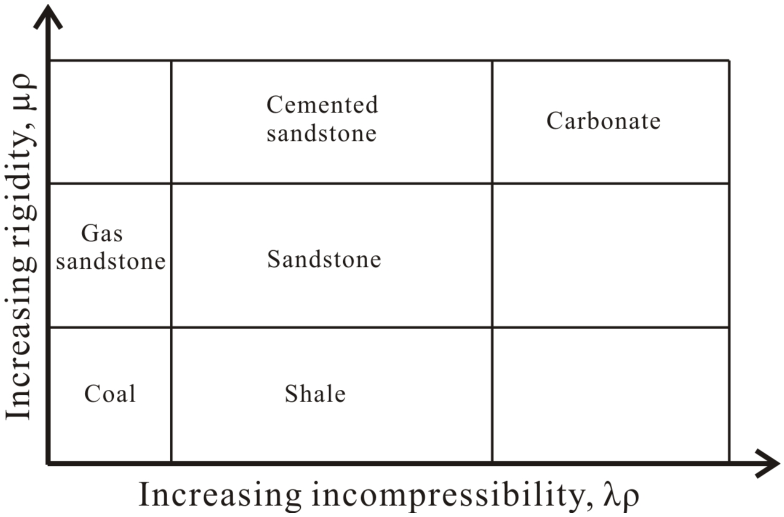

Figure 1.2 The crossplot of μρ versus λρ for gas field sedimentary rocks. Modified from Gray and Andensen (2000). Note that different types of lithologies are separated along orthogonal boundaries in the crossplot.

1.2.3 Mixture rules

Elastic moduli, flow strength, density, magnetic susceptibility, electrical conductivity, thermal conductivity and heat generation are some important physical properties of rocks in the Earth's crust and upper mantle. These physical properties of polyphase rocks depend on the relative abundance of each constituent minerals and of their related physical properties, thus, are generally calculated from laboratory-measured physical properties of constituent minerals and appropriate rules of mixture. A rule of mixture or a mixing law describes the variation of a given physical property of polymineralic composite as a function of their end-member properties and volume fractions. The success of such a commonly practiced scientific approach depends not only on accurate information about the physical properties of the proposed minerals but also on the relevance of the mixture rule used. The application of different rules of mixture yields different results. It is thus especially important to understand the physical meaning of each existing rule of mixture. In the following, I will list only some rules of mixture which are commonly used for statistically isotropic composite materials or rocks.

(1) Voigt average

Voigt (1928) proposed an averaging relation over all possible lattice orientations expressing the stress in a single crystal in terms of the given strain. Voigt average is actually an arithmetic mean, that is,

$$M_c = \sum_{i=1}^{N} \left(f_i M_i \right) \tag{1.20}$$

where M is a given physical property (e.g., elastic modulus, electrical conductivity, and thermal conductivity), the subscript c stands for the composite which consists of N phases in total, f_i is the volume fraction of the ith phase.

$$\sum_{i=1}^{N} f_i = 1 \tag{1.21}$$

Voigt average yields a linear variation of M_c with any volume fraction f_i. For the elasticity (e.g., Young's modulus, shear modulus, and bulk modulus), Eq. (1.20) suggests that the overall stress in the composite is equal to the arithmetic weight average of the stresses in the constituent phases and the weight factors are the volume fractions of the phases, but the strain is uniform in the composite (Fig. 1.3a).

The density of a composite rock consisting of N components always obeys the mixing law given by Eq. (1.20):

$$\rho_c = \sum_{i=1}^{N} \left(f_i \rho_i \right) \tag{1.22}$$

(2) Reuss average

As opposed to Voigt's isostrain model, Reuss (1929) proposed an averaging relation expressing the strain in terms of the given stress in an aggregate of crystals. Reuss's theory is a harmonic mean, yields

$$\frac{1}{M_c} = \sum_{i=1}^{N} \frac{f_i}{M_i} \tag{1.23}$$

Eq. (1.23) yields a non-linear variation of M_c with any volume fraction f_i. For the elasticity of materials and rocks, Eq. (1.23) means that the overall strain is equal to the arithmetic weight average of the strains in the phases and the stress is uniform (Fig. 1.3b).

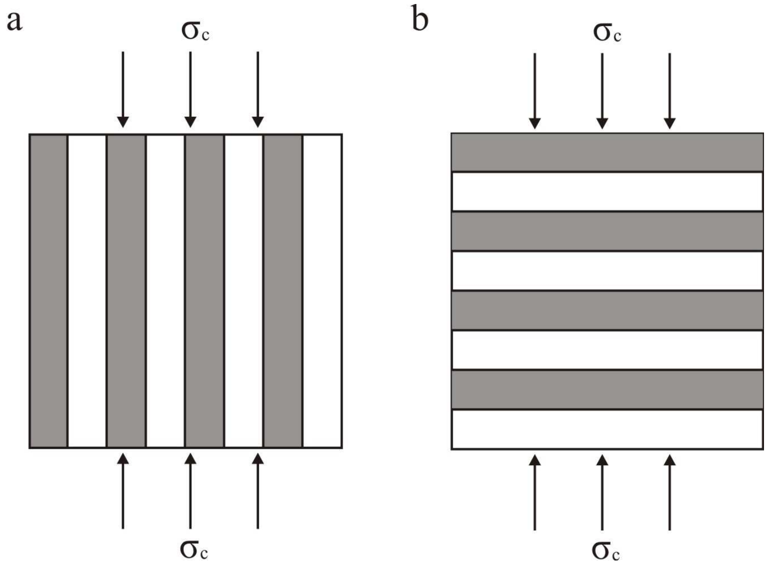

Figure 1.3 Models of two-phase composites: (a) homogeneous strain and (b) homogeneous stress.

(3) Voigt-Reuss-Hill average

Since Voigt and Reuss averages only form, respectively, the upper and lower bounds for effective properties and bracket the permissible range in which the effective properties must lie, they are not useful for calculating effective elastic properties of rocks. Hill (1952) proved mathematically that the measured moduli of an aggregate of crystals invariably lie between the Voigt and Reuss values and suggested an empirical averaging relation, which is called Voigt-Reuss-Hill or VRH average. VRH average yields an arithmetic mean of the Voigt and Reuss bounds, that is

$$M_{VRH} = \frac{1}{2}\left(M_{Voigt} + M_{\mathrm{Re}uss}\right) \tag{1.24}$$

Voigt-Reuss-Hill average have been widely used as an approximation of the overall elastic or seismic properties of polymineralic aggregates in the interpretation of worldwide seismic data (e.g., Preliminary reference Earth model, Dziewonski and Anderson, 1981; Zhao and Anderson, 1994). However, the VRH average has no clear physical significance and does not give compatible elastic stiffness (C_{ij}) or compliance (S_{ij}) tensors (Matthies and Humbert, 1993; Mainprice and Humbert, 1994; Ji and Xia, 2002). Moreover, the VRH average failed in the test by comparing with the experimental data in both the regimes of strong-phase-supported structure and weak-phase-supported structure (Ji et al., 2004).

(4) Geometric average

The geometric average yields

$$M_c = \prod_{i=1}^{N} M_i^{f_i} \tag{1.25}$$

Geometric average yields a result very close to the much more complicated iterative self-consistent micromechanical model in the predication of the bulk elastic properties for composite materials (Matthies and Humbert, 1993; Mainprice and Humbert, 1994). However, the geometrical average becomes physically meaningless when one of the constituent phases has a null property (for example, pores have zero shear strength). In this case, the overall property of the composite materials or rocks given by the geometrical average will always vanish for any finite volume fraction of the constituent that has a null property (Ji, 2004).

(5) Generalized mixture rule (GMR)

Ji et al. (2004) and Ji (2004) put the Voigt average, Reuss average and geometric average into a unified model called the generalized mean:

$$M_c^{\ J} = \sum_{i=1}^{N} \left(V_i M_i^{\ J} \right) \tag{1.26}$$

where J is a scaling, fractal parameter, which is mainly controlled by the shape and distribution (continuity and connectivity) of the phases. The case J=1 yields the arithmetic average or Voigt average. The case J=-1 yields the Reuss average. Variations of the composite properties with the volume fraction are nonlinear for all J values other than J=1. The GMR yields the geometric average as $J \rightarrow 0$.

For more specific mixing models for physical properties of rocks, the reader is referred to a comprehensive review by Berryman (1995), Schon (1996) and Ji (2008). A comparison of seismic velocities calculated using 4 mixture rules (i.e., Voigt, Reuss, VRH and geometric averages) with the laboratory-measured values will be presented in Chapter 3.

1.3 Seismic velocities

1.3.1 Seismic velocities of crystalline rocks

Whereas the upper crust is accessible to geological sampling and mapping, the deeper portions of the crust and the upper mantle are relatively inaccessible. Much of our understanding about the chemical composition, physical state, structure and evolution of the deep crust and upper mantle has been derived from various seismic refraction and reflection measurements and from other methods. Successful interpretation of these seismic data in terms of radial and lateral variations of chemical composition, mineralogy, temperature and pressure requires statistical information on seismic properties of rocks under the conditions that characterize the Earth's interior. In addition, elastic properties of rocks have significant practical applications in mining industry and geotechnical engineering (e.g., construction of buildings, dams, tunnels, bridges and nuclear plants and waste storage). The past 5 decades have seen an explosion in the amount of data on seismic velocities and anisotropy of rocks from around the world. It is thus of great importance to statistically analyze seismic data on main rock categories.

Natural rocks may be elastically anisotropic due to the presence of compositional layering, lattice preferred orientations and shape preferred orientations (i.e., foliation and lineation) of rock-forming minerals, and alignment of microcracks. The arithmetic mean of V_p and V_s values measured from various directions from each sample give values very close to those of true isotropic rocks, even in highly anisotropic rocks (Christensen and Ramananantoandro, 1971; Ji et al., 2003; Wang and Ji, 2009). In this section, the mean V_p and V_s values for each rock sample will be used to explore the relationships between lithologies and seismic velocities.

Previous authors (e.g., Pickett, 1963; Castagna et al., 1985, 1993; Mavko et al., 2009) reported that the relationship between V_p and V_s for sedimentary rocks (e.g., sandstone, limestone, dolomite, shale, and mudstone), which are generally porous, can be described by a linear correlation. Brocher (2005a, 2008) plotted thousands of V_p and V_s data for a wide variety of lithologies (from unconsolidated sediments to very low porosity igneous rocks, and from non-welded volcanic tuffs to highly compact metamorphic rocks) all together on a single figure to draw a nonlinear fitting curve by eye. His empirical curve is described by

$$V_p = 0.9409 + 2.0947V_s - 0.8206V_s{}^2 + 0.2683V_s{}^3 - 0.0251V_s{}^4 \qquad (1.27)$$

or

$$V_s = 0.7858 - 1.2344V_p + 0.7949V_p{}^2 - 0.1238V_p{}^3 + 0.0064V_p{}^4 \qquad (1.28)$$

Equations (1.27) and (1.28) are valid for V_s between 0.3373 km/s and 5.0 km/s and V_p between 1.5 and 8.5 km/s, respectively. Equation (1.28) indicates that V_s=0.3373 km/s when V_p=1.5 km/s (in fresh water, P-wave travels at about 1.5 km/s at 25 °C). Theoretically speaking, V_s should be zero in the liquid. The V_p and V_s data used for Brocher's regression fit, obtained from various methods (wireline borehole logs, vertical seismic profiles, laboratory or field measurements on hand samples at various effective confining pressures, in-situ estimates from seismic tomography studies, and regional velocity models) and are of different qualities, are extremely scattered. Furthermore, in Brocher's (2005a, 2008) compilation, most of the velocity measurements were made on samples from California, USA.

Figure 1.4 provides V_p-density, V_s-density, V_p-V_s and V_s-V_p plots for dry igneous and metamorphic rocks (i.e., amphibolite, anorthosite, basalt, diorite, eclogite, felsic gneiss, gabbro-diabase, granite, intermediate gneiss, limestone, mafic gneiss, and peridotite) at a hydrostatic pressure of 600 MPa for 442 samples. As shown in Figs. 1.4a-b, the velocities of both P- and S-wave at 600 MPa illustrate a clear trend of linear increase with density (ρ), but the increase for V_p is much more pronounced than that for V_s. The equations of regression lines for P- and S-wave velocities are: $V_p=2.219\rho+0.343$ ($R^2=0.79$) and $V_s=1.305\rho$ ($R^2=0.70$), where V_p and V_s are in km/s, and ρ in g/cm^3. These relations are valid when ρ ranges from 2.6 to 3.8 g/cm^3. The slope of the velocity-density trend for V_p is remarkably higher than that for V_s. The serpentinized peridotite, which has reduced density (2.4-2.8 g/cm^3), displays significantly lower

V_p and V_s values than the trend lines. Table 1.3 lists the average ρ, V_p and V_s for 12 lithologies in Fig. 1.4. Among the 12 lithologies, eclogite shows the highest average ρ, V_p and V_s values, while these values of granite, felsic gneiss, and limestone are relative low.

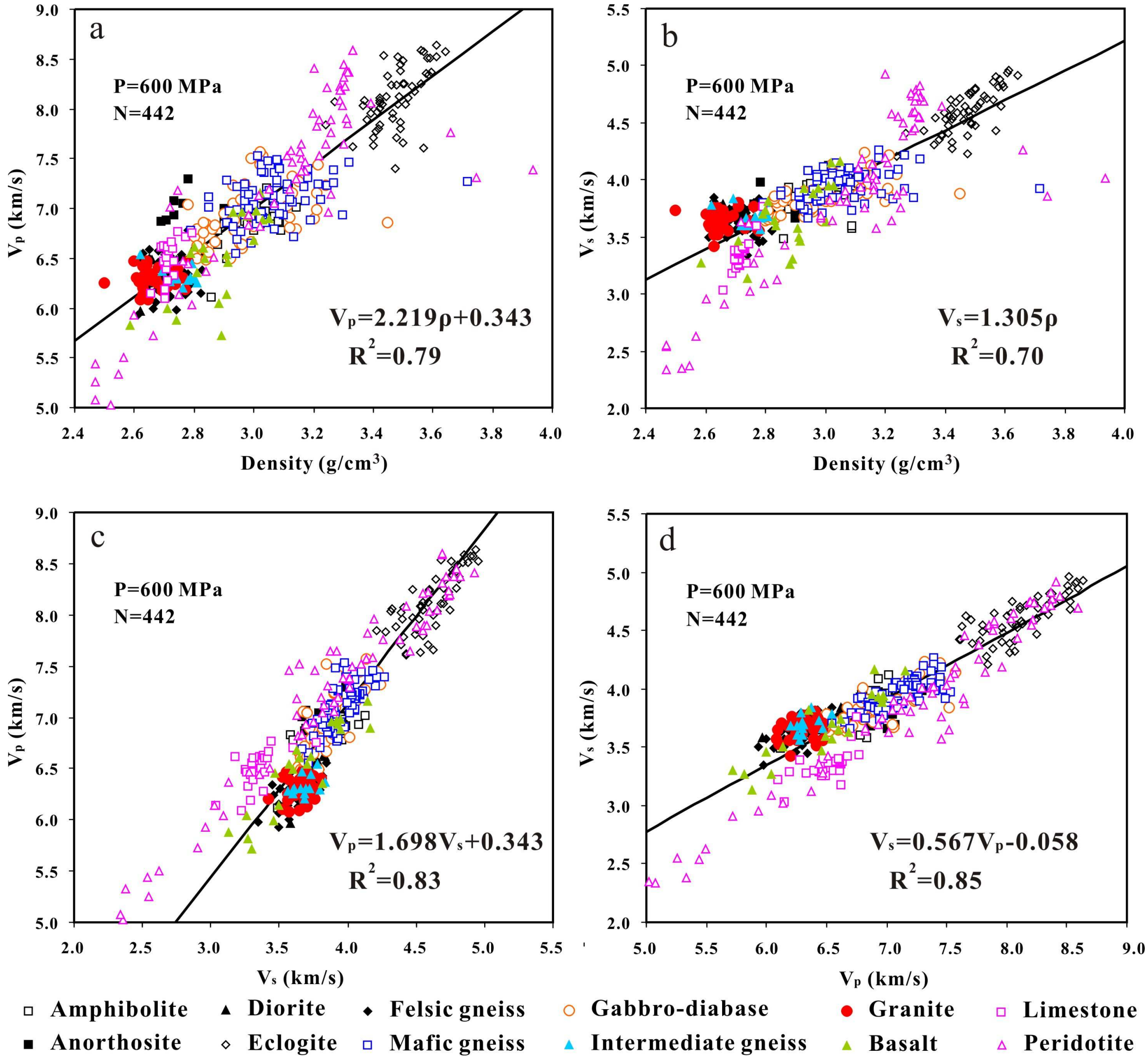

Figure 1.4 V_p-density, V_s-density, V_p-V_s, and V_s-V_p plots for 12 types of rocks at a hydrostatic pressure of 600 MPa for 442 samples.

Figures 1.4c-d show that the high-pressure V_p and V_s data of dry igneous and metamorphic rocks for 442 samples can be best fitted by the linear correlations: V_p=1.698V_s+0.343 (R^2=0.83) in the V_s range between 3.0 and 5.0 km/s, and V_s=0.567V_p-0.058 (R^2=0.85) in the V_p range between 5.4 and 8.8 km/s. However, these relations are significantly different from the linear regressions to V_s-V_p and V_p-V_s data of each of the 12 lithologies (i.e., amphibolite, anorthosite, basalt, diorite, eclogite, felsic gneiss, gabbro-diabase, granite, intermediate gneiss, limestone, mafic gneiss, and peridotite).

Table 1.3 Average density, V_p and V_s, and parameters of the V_s-V_p linear relations for 12 common lithologies. N-number of measurements.

Lithology	**N**	**Density**	**V_p**	**V_s**	**$V_s=aV_p+b$**		
		g/cm^3	**km/s**	**km/s**	**a**	**b**	**R**
Granite	31	2.66	6.29	3.65	0.172	2.575	0.22
Felsic gneiss	67	2.7	6.32	3.65	0.346	1.462	0.59
Limestone	26	2.72	6.50	3.35	0.482	0.217	0.65
Diorite	9	2.76	6.48	3.74	0.337	1.555	0.82
Intermediate gneiss	14	2.76	6.33	3.69	0.366	1.371	0.42
Anorthosite	8	2.78	7.00	3.74	0.632	-0.678	0.85
Basalt	21	2.89	6.51	3.67	0.622	-0.382	0.92
Gabbro-diabase	47	2.98	6.92	3.84	0.401	1.068	0.77
Amphibolite	29	3.01	6.87	3.89	0.501	0.451	0.72
Mafic gneiss	70	3.06	7.11	3.95	0.426	0.924	0.75
Peridotite	65	3.1	7.29	3.92	0.728	-1.380	0.98
Eclogite	55	3.47	8.11	4.6	0.496	0.580	0.79

Figure 1.5a shows the V_s-V_p plots for 65 peridotites with various degrees of serpentinization, measured at a hydrostatic confining pressure of 600 MPa. The least-squares linear fit gives $V_s=0.728V_p-1.380$ (R=0.98) and $V_p=1.310V_s+2.149$ (R=0.98). These relations are valid when V_p ranges from 4.8 to 8.8 km/s and V_s ranges from 2.2 to 5.0 km/s. The trends of velocity variation from high to low values reflect essentially a progressive increase in serpentine content.

Figure 1.5b shows the V_s-V_p variations for 55 eclogite samples at 600 MPa. The linear fitting yield: $V_s=0.496V_p+0.580$ (R=0.79) in the V_p range between 7.3 and 8.7 km/s, and $V_p=1.257V_s+2.327$ (R=0.79) in the V_s range between 4.2 and 5.0 km/s. When only V_p data exist, these V_s-V_p relations seem to give a reasonable estimate for the average V_s values.

The linear regressions to V_s-V_p (Fig. 1.5c) and V_p-V_s data of 70 mafic gneisses give: $V_s=0.426V_p+0.924$ (R=0.75) in the V_p range from 6.5 to 7.6 km/s and $V_p=1.325V_s+1.872$

(R=0.75) in the V_s range from 3.6 to 4.3 km/, respectively. Although the linear correlation is clear, the data are somewhat scattered about the trend line. This is not surprising in view of the highly variable composition and microstructure of the gneisses deformed and metamorphosed under various conditions. Some points in Fig. 1.5c deviated markedly from the regression lines, probably implying that these samples were inaccurately classified in term of lithology.

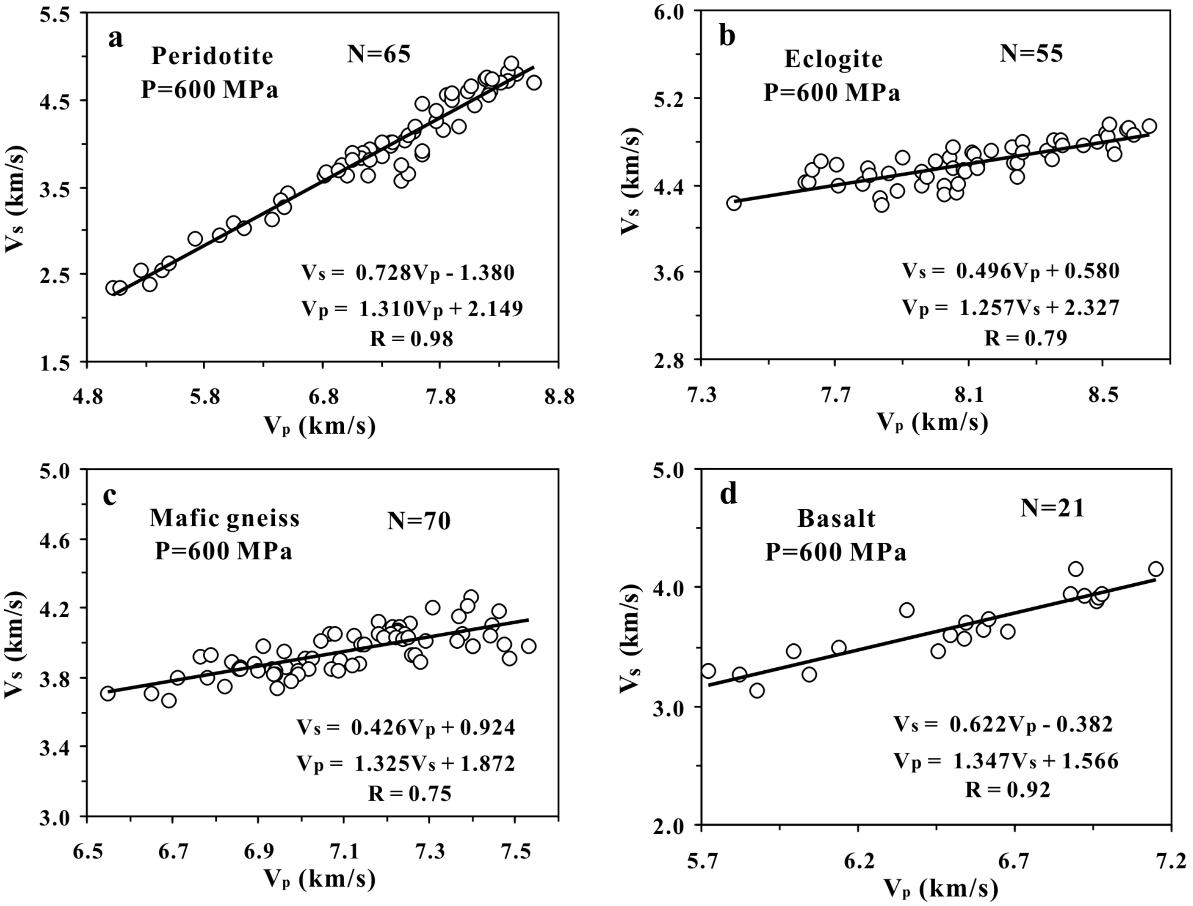

Figure 1.5 V_s-V_p plots for peridotite (a), eclogite (b), mafic gneiss (c) and basalt (d) samples at 600 MPa. The experimental data are fitted using linear correlation.

Figure 1.5d plots 21 sets of seismic velocity data for basalts at a hydrostatic confining pressure of 600 MPa. The least-squares linear fitting yields V_s=0.622V_p-0.382 (R=0.92) and V_p=1.347V_s+1.566 (R=0.92). The scattering of data around the trend line reflects mainly the variations in both porosity and pore geometry of the basalts. It is worthy to note that the small pores with larger aspect-ratios (width/length) may remain at pressures as high as 600 MPa.

The linear relation between V_s and V_p is defined by $V_s=aV_p+b$, where a and b are two parameters to describe the slope and intercept, respectively. The statistically fitting results for the relation $V_s=aV_p+b$ for 12 different lithologies are summarized in Table 1.3. It is surprising to see that in the b-a diagram (Fig. 1.6) felsic rocks (i.e., granite, diorite, felsic gneiss and intermediate gneiss), mafic rocks (i.e., amphibolite, gabbro-diabase, eclogite, and mafic gneiss) and ultramafic rocks (i.e., peridotite) are characterized by low a and high b, moderate a and b, and high a and low b values, respectively. The exact reason for the above evolution remains unclear and is an interesting theme for further study.

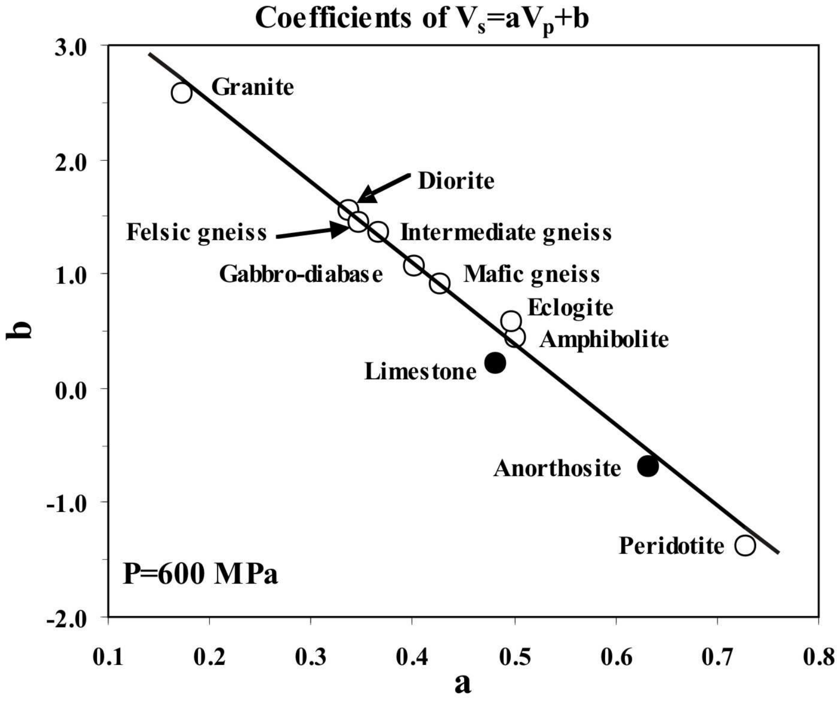

Figure 1.6 b-a plots for the relation $V_s=aV_p+b$ of 12 lithologies.

The ultrahigh pressure (UHP) metamorphism is thought to bridge the gap between upper mantle and crustal processes and the UHP rocks can provide vital constraints on the chemical and physical properties of the materials associated with subduction and continental collision. In the following, I will summarize the results on the seismic velocities of 115 crystalline rocks collected from the Dabie-Sulu UHP metamorphic terrane, which is part of a deep orogenic root produced by collision between the North China Craton and the Yangtze Block during the Triassic (Xu et al., 2009b). These 115 samples represent typical lithologies in the UHP metamorphic terrane: felsic orthogneiss, paragneiss, amphibolite, eclogites with various extents of retrogression, and garnet-bearing ultramafic rocks such as dunite, harzburgite and lherzolite (Fig. 1.7 and 1.8). The garnet peridotites were fragments of the mantle wedge overlying the subduction zone and may provide new constraints on variations in elastic properties due to slab/mantle interactions, metasomatism, and tectonic processes associated with convergent plate boundaries.

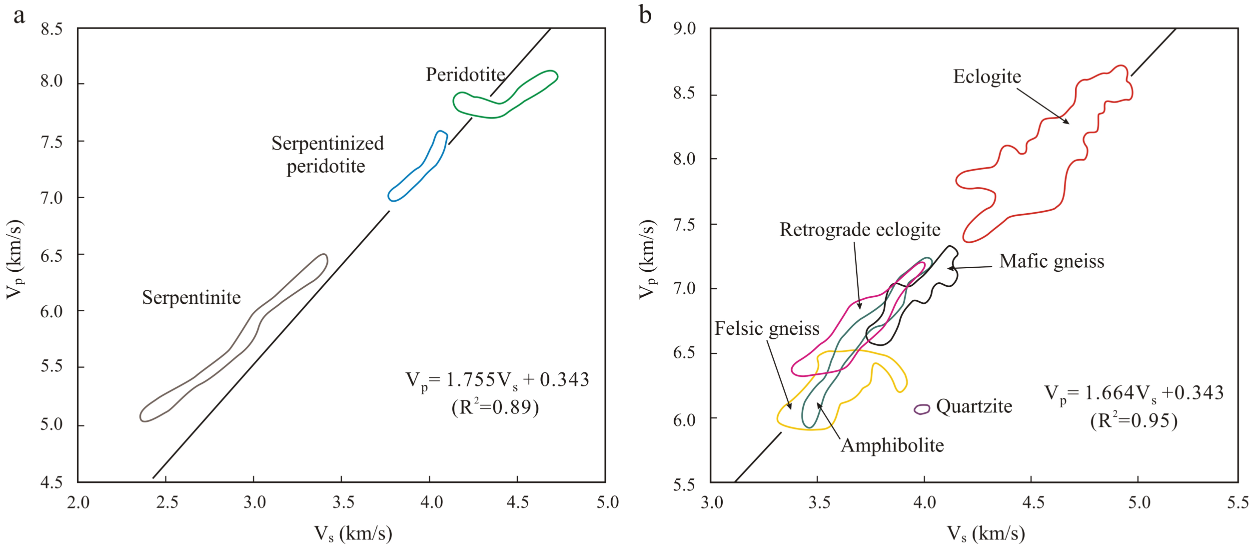

Figure 1.7 V_p-V_s plots for the ultramafic series (a) and the acid-intermediate-mafic series (b) from the Dabie-Sulu UHP metamorphic terrane at a hydrostatic pressure of 600 MPa and room temperature. 115 samples.

Figure 1.7 shows fields of different types of rocks within the V_p-V_s plots for 115 UHP metamorphic rocks from the Dabie-Sulu orogenic belt at a hydrostatic confining pressure of 600 MPa (Kern et al., 1999, 2002; Wang et al., 2005a, b; Ji et al., 2007a, 2009). Two groups of rocks can be distinguished: the ultramafic series (Fig. 1.7a) and the acid-intermediate-mafic (AIM) series (Fig. 1.7b). The ultramafic series includes peridotites, serpentinites and partially serpenitized peridotites. The AIM series includes felsic orthogneisses, paragneisses, amphibolites, metagabbros-mafic gneisses, eclogites and retrograde eclogites. The least-squares linear fit gives: V_p=1.755V_s+0.343 (R^2=0.89) for the ultramafic series (14 samples), and V_p=1.664V_s+0.343 (R^2=0.95) for the AIM series (101 samples).

Figure 1.8 summarizes the variations of V_p and V_s as a function of density for the 115 UHP metamorphic rocks from the Dabie-Sulu region at a hydrostatic confining pressure of 600 MPa under which the effect of microcracks is eliminated. Fresh peridotites, serpentinites and partially serpentinized peridotites occupy distinct fields, and display a trend of linearly increasing V_p (V_p=2.173ρ+0.343, R^2=0.82) and V_s (V_s=1.235ρ, R^2=0.74) with ρ, where V_p and V_s are in km/s, and ρ in g/cm^3 (Fig. 1.8a). This suggests that V_p, V_s and ρ all decrease progressively with increasing serpentine content for ultramafic rocks. For mafic rocks, fresh eclogites display significantly higher values of V_p, V_s and ρ than mafic gneisses, metagabbros, amphibolites and retrograde eclogites (Fig. 1.8b). The large variations in V_p, V_s and ρ for eclogites are attributed to varying volume fractions of rock-forming minerals such as garnet, omphacite, rutile and magnetite. Retrograde eclogites are almost indistinguishable from amphibolites and mafic gneisses. Felsic gneisses, including granitic orthogneisses and paragneisses, have lower V_p, V_s and ρ values than the mafic rocks (Fig. 1.8b). A quartzite displays an extremely low V_p value. For the acid-intermediate-mafic (AIM) series (Fig. 1.8b), both V_p and V_s illustrate a linear increase with density: V_p=2.188ρ+0.343 (R^2=0.86) and V_s=1.314ρ (R^2=0.83). Quartz-rich felsic gneisses and quartzites lie outside the general trend line because quartz has a significantly higher V_s value with respect to its density.

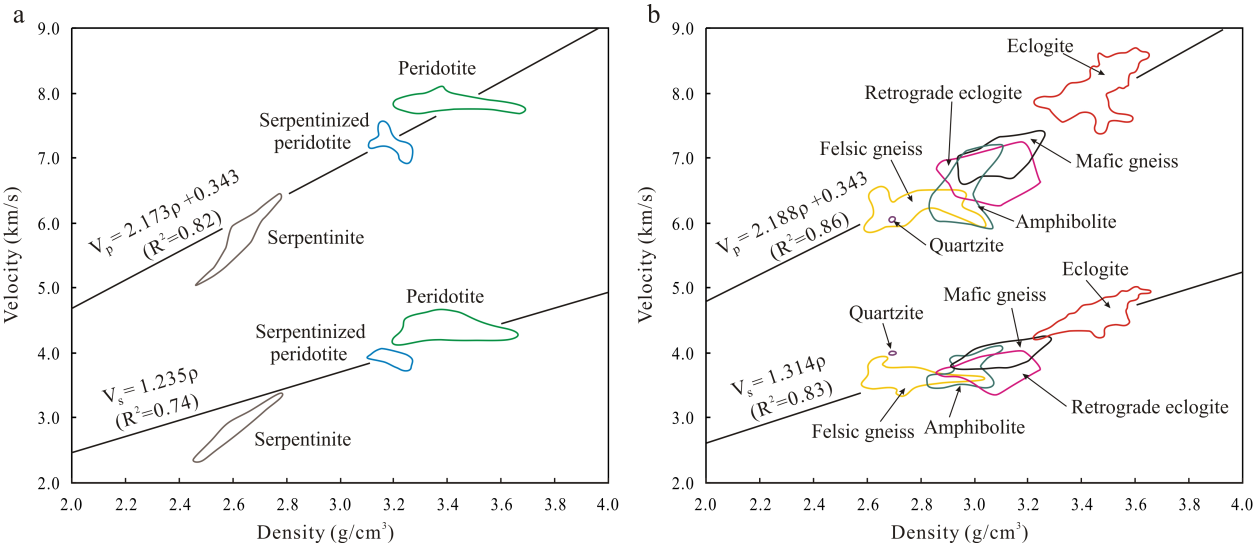

Figure 1.8 V_p and V_s as a function of density for the ultramafic series (a) and the acid-intermediate-mafic series (b) from the Dabie-Sulu UHP metamorphic terrane at a confining pressure of 600 MPa and room temperature. 115 samples.

1.3.2 Seismic velocities of rock-forming minerals

The seismic velocities of a polymineralic composite rock depend on the volume fractions and the elastic properties of its constituent minerals. Table 1.4 lists densities, P- and S-wave velocities for 40 monomineralic aggregates of common rock-forming minerals. The values of V_p and V_s for each mineral except of lizardite, chlorite and antigorite were calculated from the elastic constants compiled by Bass (1995) using the VRH mean. The V_p and V_s data for the monomineralic aggregates of lizardite and chlorite were taken from Ji et al. (2009) and Christensen (2004). The V_p and V_s data for monomineralic aggregates of antigorite were taken from Bezacier et al. (2010). Figures 1.9a and b illustrate V_p-ρ and V_s-ρ plots for monomineralic aggregates of common rock-forming minerals listed in Table 1.4, respectively.

Table 1.4 Densities, P- and S-wave velocities for 40 monomineralic aggregates of common rock-forming minerals[a]

Mineral	Density (g/cm^3)	V_p (km/s)	V_s (km/s)	Mineral	Density (g/cm^3)	V_p (km/s)	V_s (km/s)
Lizardite	2.52	5.03	2.50	Pyrope	3.58	9.08	5.07
Antigorite	2.62	6.76	3.83	Spessartine	4.19	8.41	4.72
Nepheline	2.57	5.91	3.46	Almandine	4.19	8.55	4.81
Orthoclase	2.54	5.57	3.07	Grossular	3.60	9.33	5.50
Albite	2.62	6.02	3.30	Andradite	3.84	8.52	4.84
Anorthite	2.76	7.06	3.80	Uvarovite	3.84	8.61	4.84
Quartz	2.64	6.09	4.12	Enstatite	3.20	8.08	4.87
Calcite	2.71	6.57	3.42	Diopside	3.29	7.84	4.51
Muscovite	2.84	6.08	3.52	Diallage	3.30	7.11	4.31
Dolomite	2.86	7.38	4.00	Augite	3.32	7.23	4.22
Coesite	2.91	8.20	4.60	Bronzite	3.35	7.80	4.74
Lawsonite	3.09	7.93	4.10	Epidote	3.40	7.43	4.24
Hornblende	3.12	6.80	3.71	Aegirine	3.50	7.37	4.10
Chlorite	3.16	5.99	3.18	Hedenbergite	3.66	7.42	4.08
Forsterite	3.22	8.59	5.04	Ferrosilite	4.00	6.52	3.60
Fayalite	4.38	6.83	3.41	Spinel	3.58	9.76	5.50
Sillimanite	3.24	9.50	5.31	Ilmenite	3.80	10.11	5.90
Omphacite	3.33	8.43	4.88	Rutile	4.24	9.24	5.16
Jadeite	3.33	8.77	5.05	Zircon	4.65	8.95	4.82
Zoisite	3.34	8.16	4.67	Magnetite	5.21	7.37	4.19

[a] The values of V_p and V_s for each mineral except of lizardite, chlorite and antigorite were calculated from the elastic constants compiled by Bass (1995) using the VRH mean.The V_p and V_s data for monomineralic aggregates of lizardite and chlorite were taken from Ji et al. (2009) and Christensen (2004). The V_p and V_s data for monomineralic aggregates of antigorite were taken from Bezacier et al. (2010).

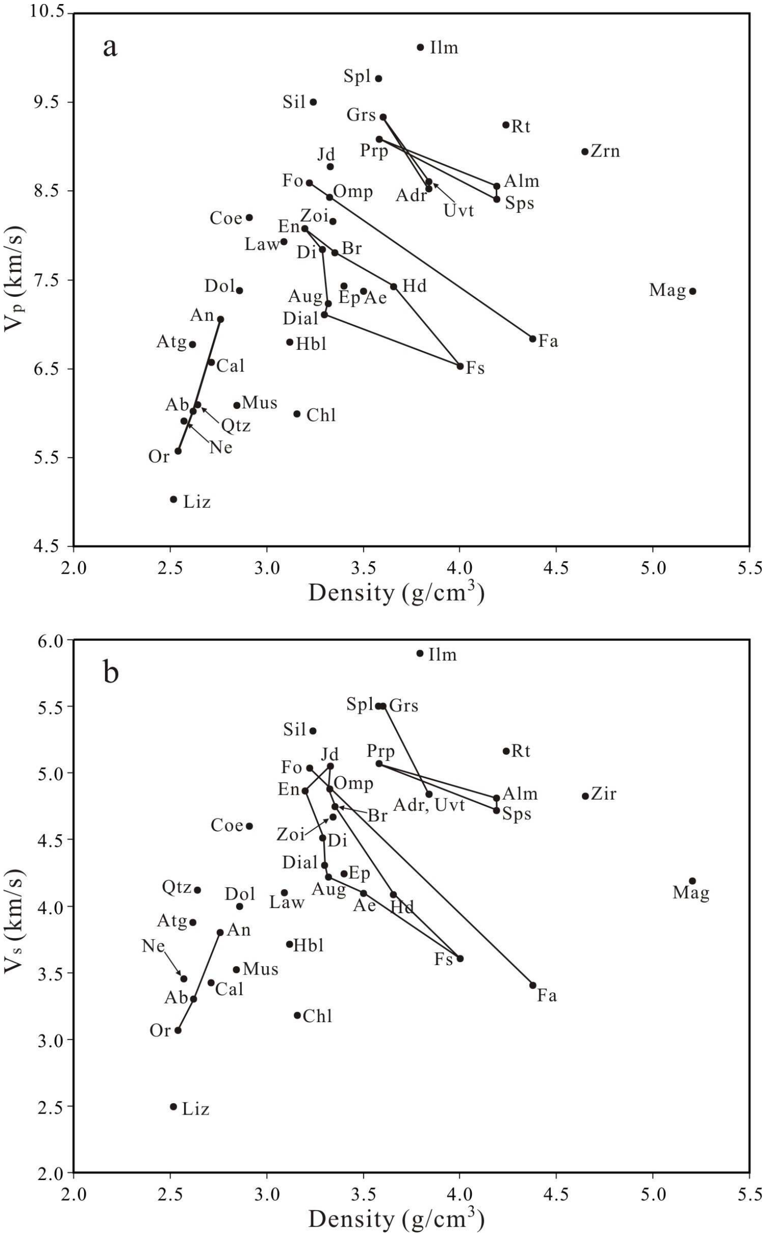

Figure 1.9 V_P-ρ (a) and V_S-ρ (b) plots for main rock-forming minerals list in Table 1.4. Solid lines connect minerals belonging to same group (e.g., garnets, olivine, pyroxenes, and feldspars). Ab: albite; Adr: andradite; Ae: aegirine; Alm: almandine; An: anorthite; Atg: antigorite; Aug: augite; Br: bronzite; Cal: calcite; Chl: chlorite; Coe: coesite; Cpx: clinopyroxene; Di: diopside; Dial: diallage; Dol: dolomite; En: enstatite; Ep: epidote; Fa: fayalite; Fo: forsterite; Fs: ferrosilite; Grs: grossular; Hbl: hornblende; Hd: hedenbergite; Ilm: ilmenite; Jd: jadeite; Law: lawsonite; Liz: lizardite; Mag: magnetite; Mus: muscovite; Ne: nepheline; Omp: omphacite; Or: orthoclase; Prp: pyrope; Qtz: quartz; Rt: rutile; Sil: sillimanite; Spl: spinel; Sps: spessartine; Uvt: uvarovite; Zoi: zoisite; Zrn: zircon.

Accessory minerals such as spinel, sillimanite, zircon, rutile and ilmenite show extremely high V_p and V_s values with respect to the main rock-forming silicate minerals (Table 1.4, Fig. 1.9). Increasing the content of these minerals in metamorphic rocks will increase the V_p, V_s and ρ values of the bulk rocks.

In the V_p-ρ diagram (Fig. 1.9a), pyroxenes (ferrosilite, augite, diallage, bronzite, enstatite, diopside, hedenbergite and aegirine) form a lozenge-shaped domain while high pressure pyroxenes, omphacite and jadeite, lie outside this domain. Compared with jadeite and omphacite (Figs. 1.9-1.10), diopside, bronzite, hedenbergite, augite and aegirine have relatively lower V_p and V_s values. The role of Fe-Mg substitution in orthopyroxenes can be seen by comparisons between enstatite ($MgSiO_3$) and ferrosilite ($FeSiO_3$): $\rho=3.198$ g/cm^3, $V_p=8.08$ km/s, $V_s=4.87$ km/s, and $V_p/V_s=1.66$ for enstatite whereas $\rho=4.002$ g/cm^3, $V_p=6.52$ km/s, $V_s=3.60$ km/s, and $V_p/V_s=1.81$ for ferrosilite.

In the V_p-ρ and V_s-ρ diagrams (Fig. 1.9), silicate garnets are classified into two groups: noncalcic pyralspite (pyrope-almandine-spessartine) and calcic ugrandite (uvarovite-grossular-andradite). From pyrope to almandine or spessartine, both V_p and V_s decrease, but ρ increases considerably. Thus, a relative high proportion of pyrope results in a low density but high V_p and V_s values of pyralspite. Uvarovite and andradite have almost the same values of V_p, V_s and ρ. Grossular has higher V_p and V_s but a lower ρ. From grossular to uvarovite or andradite, V_p and V_s decrease significantly but ρ increases slightly (Figs. 1.9-1.10).

In the eclogites from the Dabie-Sulu orogenic belt, garnet and omphacite are the main constituent minerals, with rutile and magnetite as accessory minerals. This explains why the eclogites have very high V_p, V_s and ρ values (Figs. 1.7-1.8). The mafic gneiss-eclogite transformation occurs in the subducting continental slab or near the base of thickened continental crust that is forced into the upper mantle during collision. Particularly large masses of eclogite may delaminate from the crust and sink into the mantle. As indicated by Figs. 1.7-1.8, the transition from mafic gneiss to eclogite should result in a significant increase in V_p, V_s and ρ, making it possible to distinguish between eclogite and mafic gneiss.

Hornblende and probably most other amphiboles have significantly lower values of V_p, V_s and ρ than omphacite (Fig. 1.9). Compared with hornblende, muscovite and chlorite show even lower V_p and V_s values. It is reasonable to assume that the V_p and V_s values of other phyllitic minerals such as biotite, phengite and phlogopite are similar to those of muscovite although their seismic properties are not available. Hence the retrograde eclogites, which contain large contents of amphibole and phyllitic minerals, are significantly lower in V_p, V_s and ρ than fresh eclogites (Figs. 1.7-1.8). In the Dabie-Sulu terrane, the retrograde eclogites are distributed within the ductile shear zones that were active during the late stages of crustal exhumation. These retrograde shear zones should be characterized by low V_p, V_s and ρ values.

For olivines [$(Fe, Mg)_2SiO_4$], both V_p and V_s increase with increasing Mg_2SiO_4 (forsterite) content whereas ρ increases with increasing Fe_2SiO_4 (fayalite) content. The role of Fe-Mg substitution in olivine is remarkable: ρ=3.222 g/cm^3, V_p=8.59 km/s, V_s=5.04 km/s, and V_p/V_s=1.71 for forsterite whereas ρ=4.377 g/cm^3, V_p=6.83 km/s, V_s=3.41 km/s, and V_p/V_s=2.01 for fayalite. Increasing Mg# leads to a significant increase in V_p and V_s and a significant decrease in ρ. Upper mantle olivine with a typical forsterite content of Fo100 to Fo90 shows almost the same V_p, V_s and ρ values as omphacite (Fig. 1.9). A peridotite, which is a mixture of olivine, orthopyroxene and clinopyroxene, should lie somewhere among these three end-members, with the exact position depending on the volume fraction of these constituent minerals and also on the amount of accessory minerals such as spinel, garnet, magnetite and ilmenite.

It is noteworthy that quartz is characterized by extremely low values of both V_p (6.09 km/s) and ρ (2.65 g/cm^3) but a moderate value of V_s (4.12 km/s). It is characterized by relatively low V_p and high V_s value with respect to its density (Fig. 1.9). Quartzites should have significantly lower V_p or ρV_p values than calcite marbles. Dolomite marbles have higher V_p, V_s and ρ values than calcite marbles.

Feldspars form a ternary system of three end-members: $KAlSi_3O_8$ (orthoclase), $NaAlSi_3O_8$ (albite) and $CaAl_2Si_2O_8$ (anorthite). For the plagioclase series, V_p, V_s and ρ all increase nearly linearly with increasing anorthite content (Fig. 1.9). There is a nearly linear relationship between V_p and ρ, and V_s and ρ for plagioclase feldspars. The alkali feldspars have lower V_p and V_s values than plagioclase feldspars.

In the V_s-ρ diagram, quartz has an extremely higher V_s value than either alkali or plagioclase feldspars. Thus, this characteristic may be used to discriminate quartz- from feldspar-dominant domains in the continental crust. Figure 1.9 illustrates clearly why the felsic orthogneisses and paragneisses, whose main constituent minerals are alkali feldspar, plagioclase and quartz with pyroxene, amphibole and mica as minor minerals, display low V_p, V_s and ρ values (Table 1.3, Figs. 1.4, 1.9-1.10). This figure also explains why quartz-rich felsic rocks and quartzites are characterized by significantly higher V_s values than V_p values. The mafic gneisses or metagabbros, in which pyroxene, mafic plagioclase, and garnet are the principal constituents, have moderate V_p, V_s and ρ values lying between end-members values (Table 1.3, Figs. 1.4, 1.9-1.10). The amphibolites, which contain varying contents of amphibole, plagioclase, garnet, mica and quartz, display a relatively large range of variations in V_p and V_s (Figs. 1.4, 1.9-1.10).

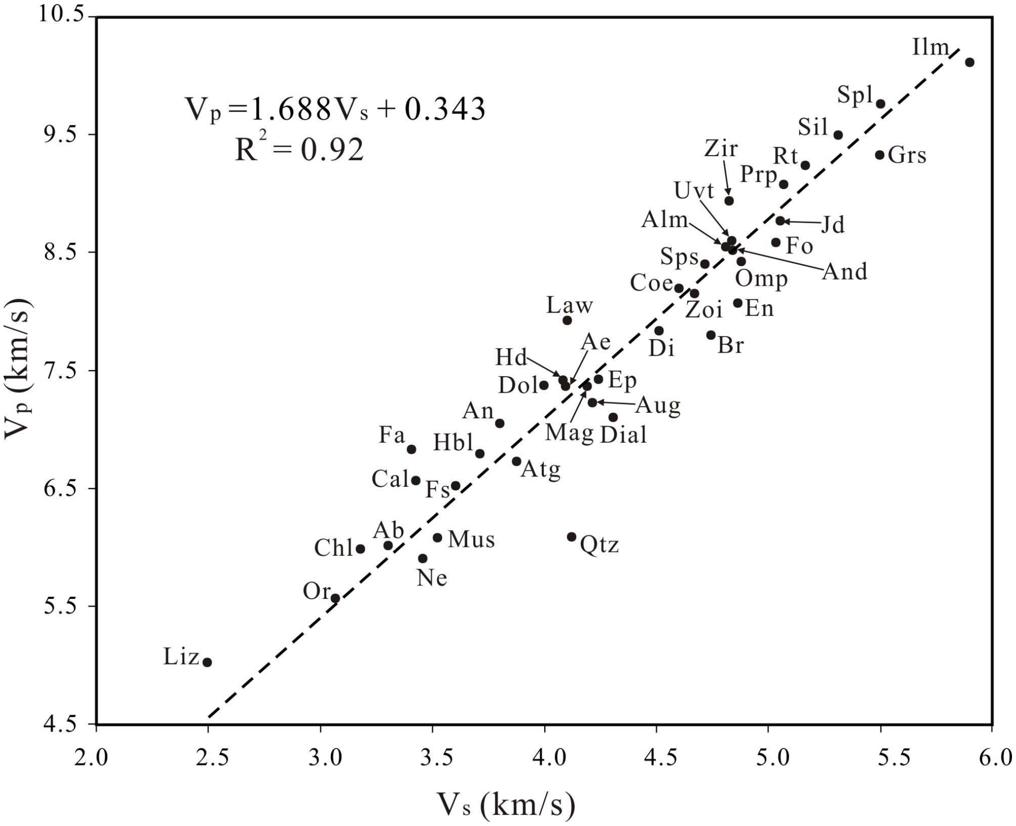

Figure 1.10 The V_p-V_s plot for main rock-forming minerals. Mineral abbreviations and data references are given in Fig. 1.9.

As shown in Figure 1.10, V_p illustrates a nearly linear increase with V_s for 40 monomineralic aggregates. The best fitting of the data gives: V_p=1.688V_s+0.343 (R^2=0.92). Quartz has clearly lowest V_p/V_s (~1.48) or Poisson's ratio (~0.08) compared with other minerals.

Thus V_p/V_s and Poisson's ratio are used to distinguish quartz-rich rocks from calcite-rich rocks in the sedimentary basins or from feldspar-rich rocks in crystalline basements.

Serpentines are phyllosilicates formed from hydration of ultramafic mantle rocks and distributed mainly along the water-infiltrated faults or shear zones. There are three major forms of serpentine: lizardite, chrysotile, and antigorite. Antigorite is the only serpentine mineral can be stable at temperatures >350 °C, while lizardite and chrysotile are stable below 300 °C (Evans, 2004). Serpentines have low V_p, V_s and ρ values (Fig. 1.9), and high V_p/V_s and Poisson's ratio (Fig. 1.10). As shown in Figs. 1.9-1.10, lizardite has the lowest V_p (~5.03 km/s), V_s (~2.50 km/s) and ρ (~2.52 g/cm^3) values, and the highest V_p/V_s (~2.02) and Poisson's ratio (~0.34). Therefore, ultramafic rocks serpentinized with low temperature lizardite and/or chrysotile are characterized by reduced seismic velocities and anomalously high Poisson's ratio (Figs. 1.7-1.8). This feature provides an excellent opportunity for the Earth scientists to investigate the subduction zones and fault zones within an oceanic lithosphere.

1.4 Seismic anisotropy

1.4.1 Propagation and polarization anisotropy

Seismic anisotropy is revealed as velocity variations both as a function of propagation and polarization direction of seismic waves. Propagation anisotropy (also called azimuthal anisotropy) reflects the differences in compressional wave (or surface wave) velocity as a function of propagation direction. The first confirmed observations of propagation anisotropy were measurements of azimuthal velocity variations of Pn phase (P wave that propagates just below the Moho) in oceanic basins recognized by Hess in 1964. P-waves are sensitive to a wide variety of phenomena, however, identifiable observations of P-wave velocity anisotropy require accurate measurements of travel times over a wide range of directions in a uniform homogeneous rock mass (Crampin and Peacock, 2005). At present, researchers studying propagation anisotropy usually exploit azimuthal variations in the seismic velocity of Pn phase (e.g., Barazangi and Ni, 1982; Shearer and Orcutt, 1986; Liang and Song, 2006) and of long-period surface waves (e.g., Smith and Dahlen, 1973; Tanimoto and Anderson, 1985; Montagner and Tanimoto, 1991).

As propagation anisotropy is measured by comparing seismic waves travelling different paths, there is always a tradeoff with laterally varying isotropic structures that also produce path-dependent velocity variations. For polarization anisotropy, which describes the differences in seismic velocity as a function of polarization direction, this tradeoff is much weaker in the case of surface waves and is non-existent in the case of shear wave splitting (Silver, 1996). The early evidence of polarization anisotropy was a discrepancy between dispersion of Rayleigh waves (hybrid compressional and vertically polarized shear) and Love waves (horizontally polarized shear) reported by Anderson in 1961. This is the basis for allowing the upper 220 km of the mantle in the Preliminary reference Earth model to be transversely isotropic (hexagonal symmetry anisotropic) with a vertical symmetry axis (Dziewonski and Anderson, 1981; Anderson and Dziewonski, 1982). The observations of quasi-Love waves (Love waves that have converted from Rayleigh waves) were used to map locations of lateral gradients in anisotropy at 100-300 km depth (Park and Yu, 1993; Yu and Park, 1994). At present, shear wave birefringence, or splitting, is the most popular and powerful tool for investigating polarization anisotropy, and has been used to study anisotropy throughout the Earth's crust and upper mantle (e.g., Vinnik et al., 1992; Silver, 1996; Long and Silver, 2009).

A compressional (P) wave and a shear (S) wave propagate in an isotropic, homogeneous medium, with the particle displacement directions of P and S wave, respectively, parallel and perpendicular to the propagation direction. In a weakly anisotropic medium (as in the Earth's crust and upper mantle), there are three body waves, a quasi-P wave and two quasi-S waves. In general, the particle displacement directions of quasi-P and quasi-S wave are still nearly parallel and perpendicular to the propagation direction, respectively. The two shear waves have orthogonal polarization directions and propagate at different velocities; this phenomenon is known as shear wave splitting, or birefringence. For a homogeneous elastic anisotropic medium of density ρ, the velocities and displacement directions of seismic waves are given by the eigenvalues and eigenvectors of the polarization matrix V defined by the Christoffel equation (Backus, 1965),

$$\rho V_{il} \equiv C_{ijkl} \hat{p}_j \hat{p}_k \tag{1.29}$$

where C_{ijkl} is the elasticity tensor for the medium and $\hat{p}$ is the unity vector in the propagation direction. The two basic shear wave splitting parameters obtained from seismic data are the fast polarization direction (ϕ) and the delay time between the fast and slow shear waves (δt). δt is proportional to effective path length L according to the approximate expression for small anisotropy (Silver, 1996),

$$\delta t = L\delta\hat{\beta} / \beta_0 \qquad (1.30)$$

where β_0 is the isotropically averaged shear wave velocity, $\delta\hat{\beta}$ is the dimensionless intrinsic anisotropy, which is a function of $\hat{p}$.

Nur and Simons (1969a) and Christensen (1971) were among the first to observe experimentally acoustoelastic birefringence in naturally deformed rocks. Crampin (1981) termed this phenomenon S-wave splitting. In-situ observations of LPO-induced S-wave splitting in the Earth did not begin until the pioneer work of Ando et al. (1983) using digital three-component seismograph stations. Due to the fact that steep incidence of S-waves is a pre-requisite for the observation of S-wave splitting, the S-waves emitted directly from earthquake focuses can be used only for studying crack-induced seismic anisotropy in the brittle upper crust (e.g., Crampin et al., 1984; Crampin and Booth, 1985; Tanimoto and Anderson, 1984; Kaneshima et al., 1988; Savage et al., 1990; Shih and Meyer, 1990) and in upper mantle wedges above Wadati-Benioff zones (Ando et al., 1983; Fukao, 1984; Shih et al., 1991). In order to be able to study LPO-induced seismic anisotropy beneath the continents, Vinnik et al. (1984) measured S-wave splitting in SKS teleseismic phases. Since then, there has been considerable progress made in the measurement of shear wave splitting in the Earth's crust and upper mantle (Silver and Chan, 1988, 1991; Savage, 1999; Makeyeva et al., 1992; Savage and Silver, 1993; Vinnik et al., 1992, 1994; Silver and Kaneshima, 1993; Ji and Salisbury, 1993; Ji et al., 1994, 1996; Saruwatari et al., 2001; McNamara, 1994; Sol et al., 2007). Although shear wave splitting technique affords excellent lateral resolution, it has little vertical resolution to contribute to the question depth location of the anisotropy. An overview of shear wave splitting patterns measured from global oceanic subduction zones will be presented in Chapter 5.

1.4.2 Seismic anisotropy of different lithologies

In laboratory study, one P-wave velocity (V_p) and two shear wave velocities (V_{s1} and V_{s2}, $V_{s1}>V_{s2}$) are usually measured from each of the three orthogonal directions in a rock sample. For the rocks in which both foliation and lineation are developed, these directions are parallel to the X, Y and Z axes of the tectonic framework (X-parallel to the stretching lineation, Y-perpendicular to the lineation and parallel to the foliation, and Z-normal to the foliation) or the strain ellipsoid (Fig. 1.11). If the sample is foliated but not lineated (deformed by flattening strain), both X- and Y-directions are arbitrarily aligned in the foliation plane. For samples that displayed neither foliation nor lineation (e.g., undeformed isotropic igneous rocks), all three directions are aligned in an arbitrary direction or only one direction is taken because such rocks are generally isotropic.

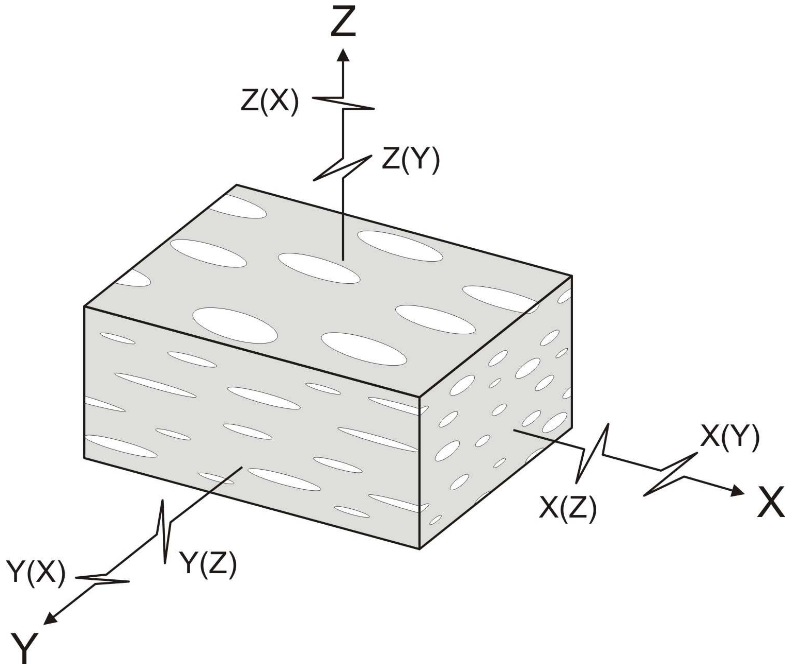

Figure 1.11 Relative orientations between rock structural framework (X-Y-Z) and seismic wave propagation and polarization directions. X is parallel to stretching lineation, Y is normal to lineation in the foliation plane, and Z is normal to foliation plane.

The average elastic properties of an anisotropic rock, which are equivalent to the properties of their isotropic counterparts, can be computed from the mean V_p and mean V_s values derived from the Equations (1.31) and (1.32).

$$\overline{V}_p = [V_p(X) + V_p(Y) + V_p(Z)]/3 \qquad (1.31)$$

$$\overline{V}_s = [V_s(XY) + V_s(XZ) + V_s(YX) + V_s(YZ) + V_s(ZX) + V_s(ZY)]/6 \qquad (1.32)$$

In Eq. (1.31), $V_p(X)$, $V_p(Y)$ and $V_p(Z)$ are, respectively, the P-wave velocities along the propagation directions X, Y and Z. In Eq. (1.36), $V_s(XY)$, $V_s(XZ)$, $V_s(YX)$, $V_s(YZ)$, $V_s(ZX)$, and $V_s(ZY)$ are the S-wave velocities with the first letter in the brackets to refer to the propagation direction and the second letter to the polarization direction. The mean V_p and V_s values calculated from Eqs. (1.31)-(1.32) give values very close to those of true isotropic rocks, even in highly anisotropic rocks (Christensen and Ramananantoandro, 1971; Ji et al., 2003; Wang and Ji, 2009).

V_p anisotropy (A_p) is defined by Birch (1961) as:

$$A_p = (V_{p,\max} - V_{p,\min}) / \overline{V}_p \times 100\% \qquad (1.33)$$

where $V_{p,\max}$ and $V_{p,\min}$ are, respectively, the maximum and minimum values of the P-wave velocities measured in a given sample along different propagation directions. Thus, A_p depends only on the maximum and minimum velocity values and does not carry any information about their orientations.

For each bulk sample, the V_s anisotropy (A_s) is defined as

$$A_s = (V_{s,\max} - V_{s,\min}) / \overline{V}_s \times 100\% \qquad (1.34)$$

where $V_{s,\max}$ and $V_{s,\min}$ are the maximum and minimum V_s values measured in a given sample along different propagation and polarization directions, respectively.

For a given propagation direction Λ, shear wave splitting (ΔV_s) is defined as the difference in velocity between fast and slow split S-waves propagating in the same direction Λ:

$$\Delta V_s = V_{s1} - V_{s2} \qquad (1.35)$$

The percentage shear wave splitting (S_Λ) is referred to the normalized difference between the fast and the slow S-wave velocities for a given propagation direction Λ:

$$S_{\Lambda} = \frac{(V_{s1} - V_{s2})}{(V_{s1} + V_{s2})/2} \times 100\% \qquad (1.36)$$

Thus, S_X, S_Y, and S_Z are directional parameters, while A_s calculated from Eq. (1.34) does not carry any information about orientation.

Ji et al. (2002) summarized the available data on seismic velocities and anisotropies in rock samples, which were collected mainly from North America, Western Europe, Japan and the ocean basins. Figures 1.12a and b show, respectively, the distributions of V_p and V_s anisotropy at 600 MPa and 25 ºC for 1438 and 467 rock samples, in which ~ 45% of the studied samples have A_p and A_s values less than 3%, and ~70% of those have anisotropy values no more than 6%. The mean V_p and V_s anisotropy are 5.29% and 5.73%, respectively.

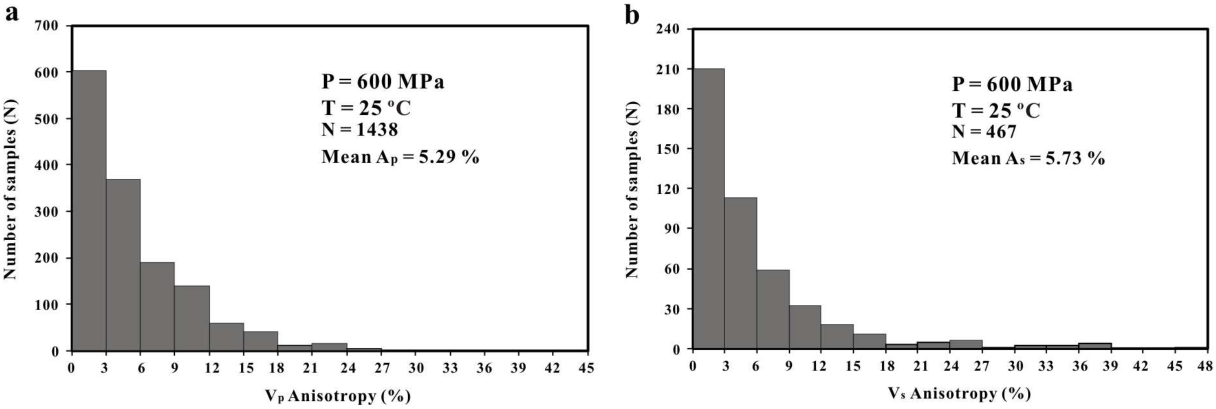

Figure 1.12 Histograms showing the distributions of V_p (a) and V_s (b) anisotropy of rocks at 600 MPa. N – number of measurements. (After Ji et al., 2002)

Figure 1.13 illustrates the mean V_p anisotropy ($\overline{A_p}$) values for 31 common lithologies. The igneous rocks are, to a first approximation, isotropic ($\overline{A_p}$ ≈2.5-3.5%), whereas many of the metamorphic rocks show significant anisotropy. Anisotropy is a particularly important parameter in the low-grade pelitic rocks, for example, the mean V_p anisotropy of slate and phyllite are up to 10.36% and 11.89%, respectively. The medium-grade metamorphic rocks, such as gneiss ($\overline{A_p}$ ≈4.5-5.5%) and amphibolite ($\overline{A_p}$ =9.15%) have higher anisotropy than that of high-grade metamorphic rocks. The mean V_p anisotropy of high grade granulite and eclogite facies rock are relatively low, only about 2-3%. Thus seismic anisotropy is likely to be a more significant property of upper and middle crustal regions than the lower crust. For mantle rocks, 82 peridotites and 18 pyroxenites have $\overline{A_p}$ of 5.92% and 3.61%, respectively. The causes of seismic anisotropy of the crust and upper mantle will be discussed in Section 1.4.3 and 1.4.4, respectively. Seismic anisotropy in many rocks can dominate the effect of compositional variation on wave velocity. This makes the prediction of rock type from seismic velocity more complex.

Figures 1.14 plot V_p anisotropy versus V_s anisotropy at confining pressure of 50, 100, 200 and 600 MPa. The literature data were taken from Handbook of Seismic Properties of Minerals, Rocks and Ores (Ji et al., 2002) and laboratory data were from references (Wang et al., 2005a, b; Wang et al., 2009). These figures are used to show the effects of confining pressure. A linear relation is used to best-fit the correlations: $A_p=0.875A_s$ ($R^2=0.51$) at 50 MPa (Fig. 1.14a); $A_p=0.774A_s$ ($R^2=0.57$) at 100 MPa (Fig. 1.14b); $A_p=0.757A_s$ ($R^2=0.70$) at 200 MPa (Fig. 1.14c); and $A_p=0.737A_s$ ($R^2=0.72$) at 600 MPa (Fig. 1.14d). It is suggested that A_p values are lower than A_s values for most of the rock samples. The ratio of A_p/A_s and the goodness of fit (R^2) significantly decrease and increase with pressure from 50 MPa to 600 MPa, respectively. The mean values of A_p and A_s are 9.2 %, 8.7% at 50 MPa; 8.2% and 11.0% at 100 MPa; 8.9 % and 10.5% at 200 MPa, 8.2 % and 10.0% at 600 MPa, respectively. These data indicate clearly that anisotropy is a general property for natural rocks.

It is worthy to note that seismic anisotropy at low pressures (<~300MPa) is mainly caused by the interaction between the alignment of microcracks and the lattice preferred orientations (LPO) of minerals. In the high pressure regime (>~300 MPa), the rock samples become crack-free, compacted aggregates, thus the seismic anisotropy is mainly induced by the LPO of constituent minerals and compositional layering. For a certain category of lithology, the seismic anisotropy values may vary significantly. For example, A_p values of amphibolites are in the range of 2.8-16.3% at 600 MPa (Fig. 1.14d). The variations in seismic anisotropy at high pressures reflect the variations in strength of LPOs of rock-forming minerals (e.g., amphibole and plagioclase in the case of amphibolite) and the orientation of compositional layering.

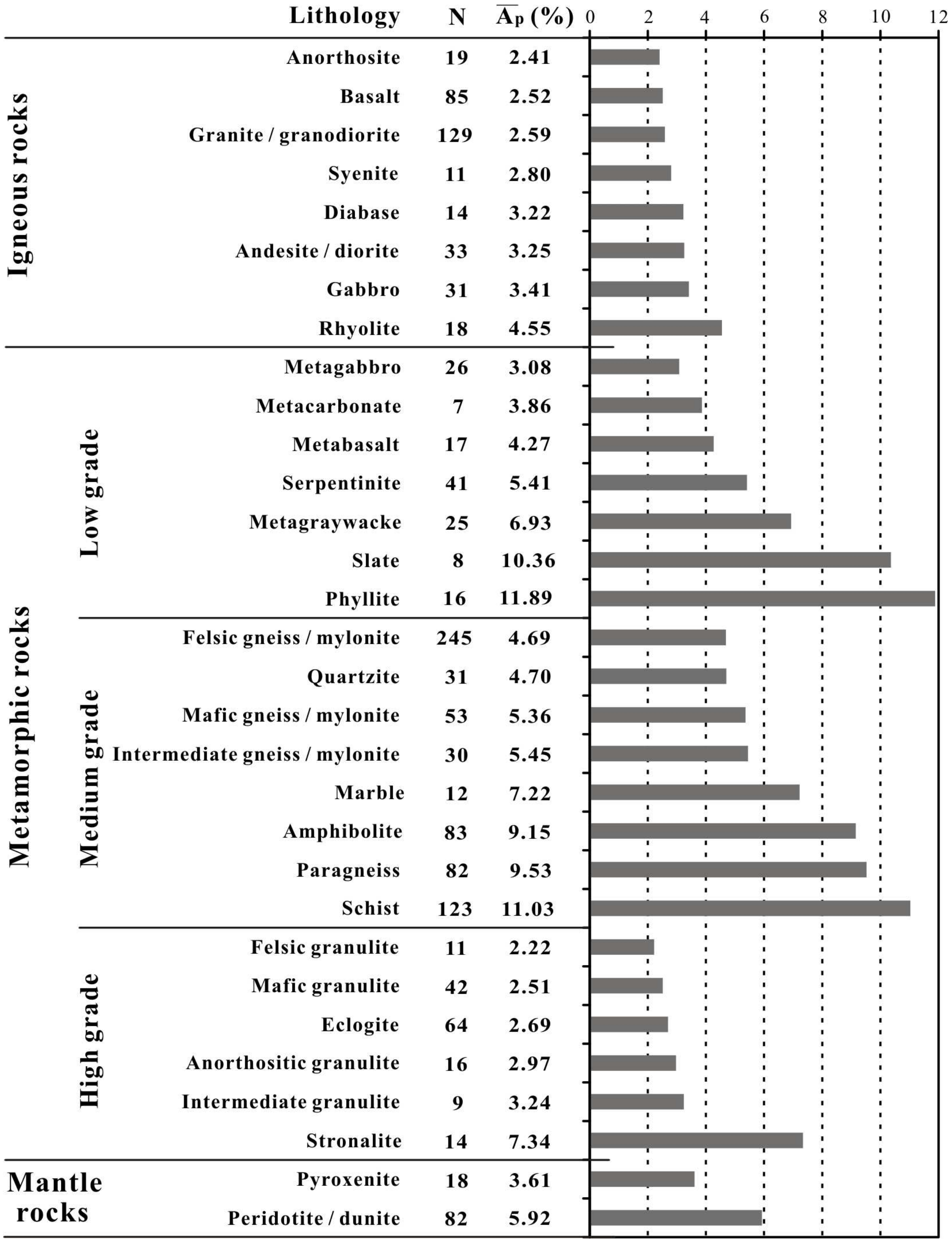

		Lithology	N	$\overline{A}_p$ (%)
Igneous rocks		Anorthosite	19	2.41
		Basalt	85	2.52
		Granite / granodiorite	129	2.59
		Syenite	11	2.80
		Diabase	14	3.22
		Andesite / diorite	33	3.25
		Gabbro	31	3.41
		Rhyolite	18	4.55
Metamorphic rocks	Low grade	Metagabbro	26	3.08
		Metacarbonate	7	3.86
		Metabasalt	17	4.27
		Serpentinite	41	5.41
		Metagraywacke	25	6.93
		Slate	8	10.36
		Phyllite	16	11.89
	Medium grade	Felsic gneiss / mylonite	245	4.69
		Quartzite	31	4.70
		Mafic gneiss / mylonite	53	5.36
		Intermediate gneiss / mylonite	30	5.45
		Marble	12	7.22
		Amphibolite	83	9.15
		Paragneiss	82	9.53
		Schist	123	11.03
	High grade	Felsic granulite	11	2.22
		Mafic granulite	42	2.51
		Eclogite	64	2.69
		Anorthositic granulite	16	2.97
		Intermediate granulite	9	3.24
		Stronalite	14	7.34
Mantle rocks		Pyroxenite	18	3.61
		Peridotite / dunite	82	5.92

Figure 1.13 Mean anisotropy of V_p for igneous, metamorphic and mantle rocks at 600 MPa and room temperature. The numbers of measurements (N) are also indicated. (Data from Ji et al., 2002)

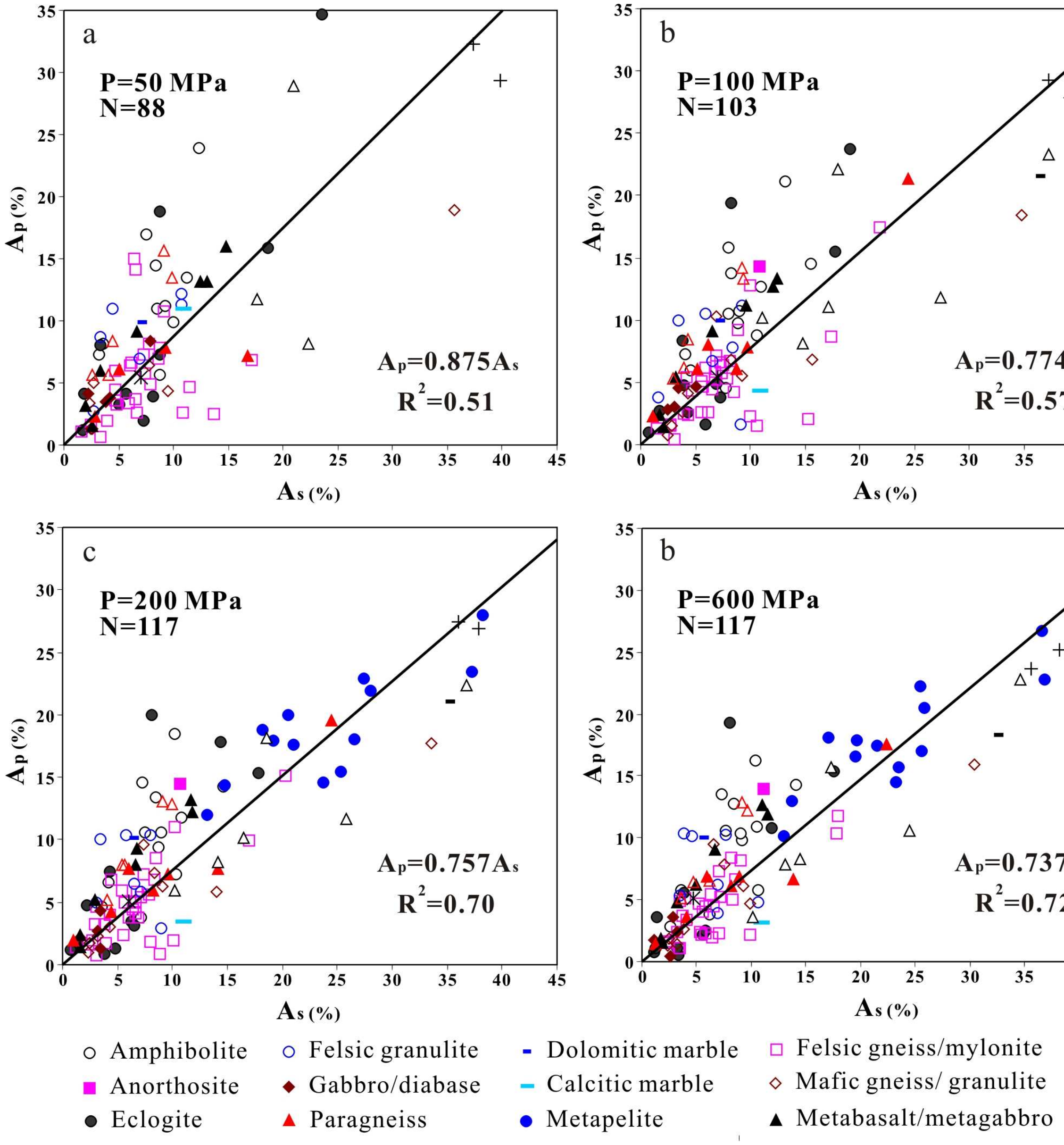

Figure 1.14 V_p anisotropy (A_p) versus V_s anisotropy (A_s) at 50 MPa (a), 100 MPa (b), 200 MPa (c), and 600 MPa (d).

1.4.3 Seismic anisotropy of the continental crust

The origin of seismic anisotropy on Earth is non-unique. A range of phenomena may cause rocks seismic anisotropy, such as lattice preferred orientations (LPO) and shape preferred orientation (SPO) of rock-forming minerals, small-scale compositional layering, and aligned microcracks of various dimensions, either open or filled with fluid or melt.

The uppermost part of the crust is constituted by sedimentary rocks, which usually developed layered structures named bedding. Layered rocks can be considered as transversely isotropic media. Within a single layer of massive rocks such as sandstones, seismic velocities vary slightly with directions. However, the rocks are interlayered with other lithological units (e.g., sandstone with mudstone or limestone), such composite media exhibit substantial anisotropy with faster velocities parallel to bedding and slower velocities perpendicular to bedding or shear wave splitting (Fig. 1.15). The layering of sedimentary rocks has been recognized as a source of seismic anisotropy since the early 1950s (e.g., Riznichenko, 1949; Postma, 1955; Crampin, 1970). Seismic anisotropy may range up to 30% and is particularly pronounced for P-wave velocities from about 2.0 to 4.2 km/s (Gebrande, 1982).

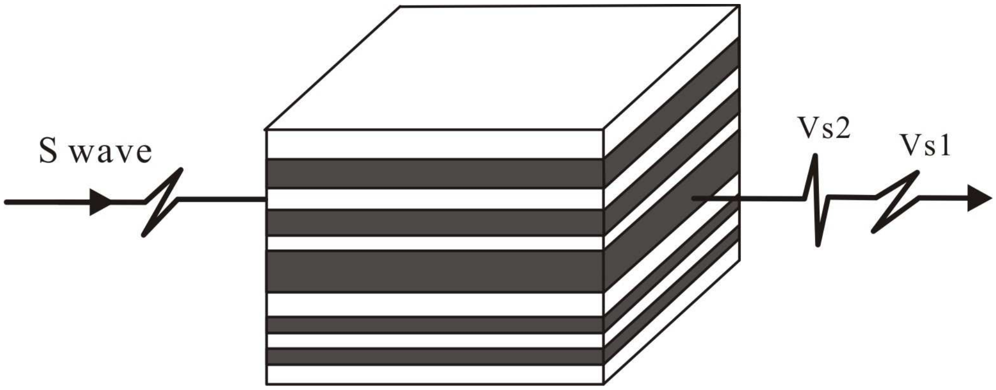

Figure 1.15 Shear wave splitting in layered rocks, with the faster polarized wave (V_{s1}) parallel to bedding and the slower polarized wave (V_{s2}) perpendicular to bedding.

In crystalline and sedimentary rocks of the upper crust, the preferred orientations of microcracks, and particularly stress-induced fluid-saturated microcracks, present an important contribution to the observed seismic anisotropy. To a first approximation, such an anisotropic medium can be considered as a transverse isotropy with a symmetry axis normal to the microcrack plane which is perpendicular to the minimum principal stress. Typical mutually-parallel vertical crack orientations (Fig. 1.16) are generally found below the critical depth (typically between 500 m and 1000 m), where the increasing vertical stress (σ_V) becomes greater than the minimum horizontal stress (σ_h), so that the minimum stress is horizontal (Crampin and Peacock, 2008). For propagation within 30º of the vertical, the faster shear waves (V_{s1}) are polarized parallel to the strike of the cracks and the direction of maximum horizontal stress (σ_H), and the slower shear waves (V_{s2}) are polarized perpendicular to the microcrack plane and parallel to the direction of σ_h. Such vertically aligned crack-induced anisotropy is limited only to the brittle portion of the crust, say, the uppermost 10 to 15 km with the maximum of fractured anisotropy rock located less than 3-5 km of the uppermost crust (Kaneshima and Ando, 1988; Kaneshima, 1990). This critical depth of crack-induced anisotropy corresponds to the depth of the brittle-ductile transition and decreases with increasing regional geothermal gradient.

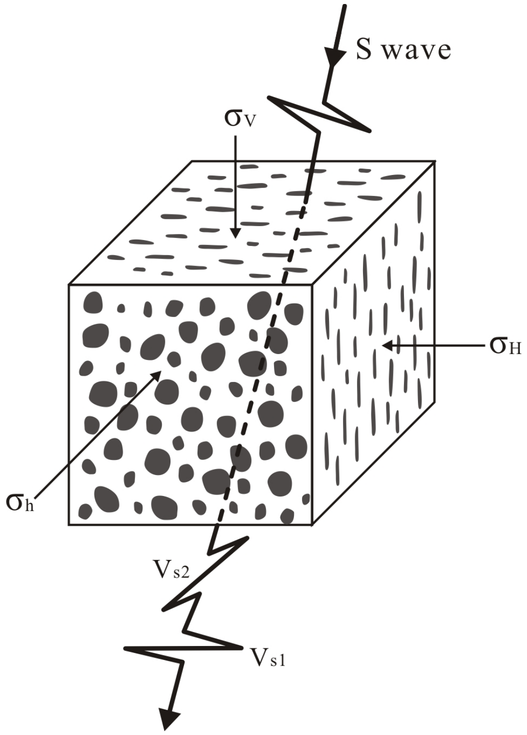

Figure 1.16 Schematic illustration of shear-wave splitting through distributions of stress-aligned parallel vertical microcracks aligned normal to the direction of minimum horizontal stress (σ_h).

As variations in shear wave splitting are the most sensitive diagnostic indicators of stress-induced changes to microcrack geometry, it is possible to estimate the times and magnitudes of impending larger earthquakes by analyzing shear wave splitting. Characteristic temporal variations of shear wave delay time (δt) are now seen before earthquakes worldwide (Crampin and Peacock, 2008 and references therein). When there is sufficient seismicity before the impending earthquake to provide effective shear wave splitting data, the normalized delay time display an initial increase, followed by an abrupt precursory decrease immediately before the larger earthquake (Fig. 1.17). Typically, the initial increases in delay time are interpreted as stress-accumulation, and the following abrupt decreases are interpreted as stress relaxation due to cracks coalescing onto the eventual fault break. Both the logarithm of the duration of the increases and decreases are proportional to the magnitude of the impending earthquake (Gao and Crampin, 2004; Crampin and Peacock, 2008). There has been one successful real-time stress-forecast of time, magnitude and fault break of an M=5 earthquake in southwest Iceland, when the increase in delay time was recognized early enough before the earthquake had occurred (Fig. 1.17b; Crampin et al., 1999). In addition, variations in shear-wave splitting caused by changes to microcrack geometry have also been observed before volcanic eruptions (Bianco et al., 2006; Miller and Savage, 2001; Gerst and Savage, 2004), and in hydrocarbon reservoirs following fluid-injection (Angerer et al., 2002) and possible variations with ocean tides (Teanby et al., 2004).

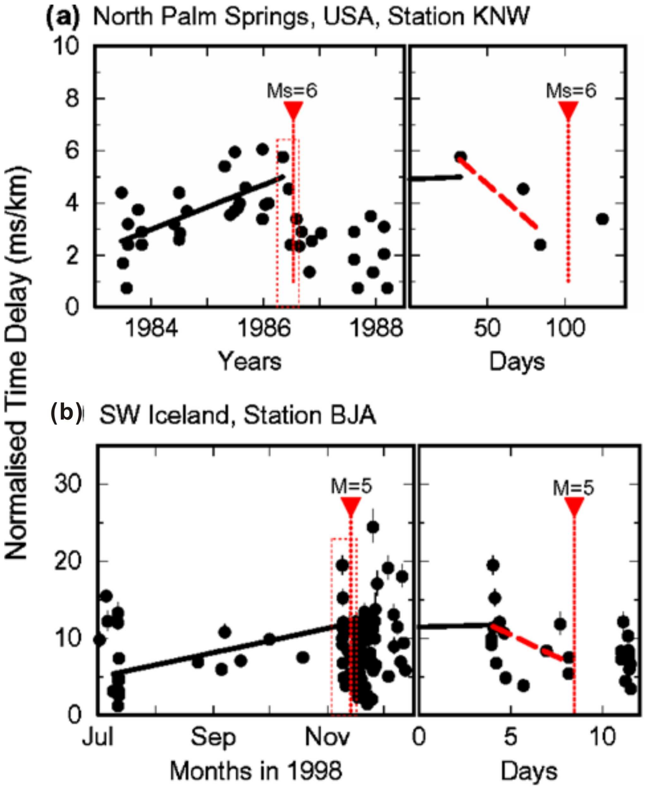

Figure 1.17 Temporal variations in normalized shear wave delay time (ms/km) observed before earthquakes (after Crampin and Peacock, 2008). Left-hand-side: delay time with a least-squares line showing general increase before the earthquake. Right-hand-side: enlarged time scale for dotted box in left-hand-side, with dashed line showing precursory decrease in delay times before the earthquake. (a) Ms 6 North Palm Springs Earthquake (Peacock et al., 1988). (b) M 5 earthquake in SW Iceland (Crampin et al., 1999). This earthquake was stress-forecast.

In the lower crust, most aligned microcracks are closed due to high pressure, thus seismic anisotropy is caused mainly by mineral LPOs and metamorphic/structural layering (Ji et al., 1993; Ji and Salisbury, 1993). The lower crust may include metasedimentary and metavolcanic rocks, layered mafic complexes, gneisses, magmatic layers and ultramafic bodies. The presence of isoclinal folds, boudinage structures and mylonitic shear zones in the deep cross sections attests to the dominance of ductile deformation mechanisms in the lower crust. These structures, coupled with igneous and metamorphic processes, formed during post-collisional extension, result in a horizontally layered deep crust from centimeter to kilometer scales (Fountain, 1987). Such a layering in combination with a lattice preferred orientation of minerals in metamorphic rocks produces appreciable seismic anisotropy within the lower continental crust.

The lower crust consists of amphibolite-granulite facies metamorphic rocks, in which mica, amphibole, feldspar, clinopyroxene and orthopyroxene are dominant minerals (Fig. 1.18). The LPOs of amphibole and mica are considered to control seismic anisotropy in the middle-to-lower crust (Ji et al., 1993; Ji and Salisbury, 1993; Barruol and Mainprice 1993; Takanashi et al. 2001; Cholach et al. 2005).

Amphibole (e.g., hornblende) has a large V_p anisotropy (23.8 %), with the maximum velocity (~7.9 km/s) along the [001] direction and the minimum velocity (~6.0 km/s) close to the [100] direction (Fig. 1.18). The maximum shear wave splitting (ΔV_s=1.1 km) occurs in the (100) plane. Seismic anisotropy of amphibolites is essentially controlled by amphibole LPO that is generally simple, consistent, and strong (e.g., Ji et al., 1993; Tatham et al., 2008): the [001] directions have a strong concentration parallel to the stretching lineation, the (100) planes are parallel to foliation, and [010] directions are parallel to Y direction. This LPO pattern result in a prominent anisotropy (up to ~10%) with an orthorhombic symmetry: $V_p(X)>V_p(Y)>V_p(Z)$ (Ji et al. 1993; Barruol and Kern 1996; Takanashi et al. 2001; Kitamura, 2006). The maximum ΔV_s is observed for propagation in the foliation plane and almost no shear wave splitting is observed normal to foliation (Wang et al., 2009). In most deformed amphibolites, both A_p and ΔV_s increase progressively with increasing hornblende content, reflecting the impact of the strong hornblende LPO (Tatham et al., 2008).

Hornblende $(Ca,Na)_{2-3}(Mg,Fe,Al)_5(Al,Si)_8O_{22}(OH)_2$

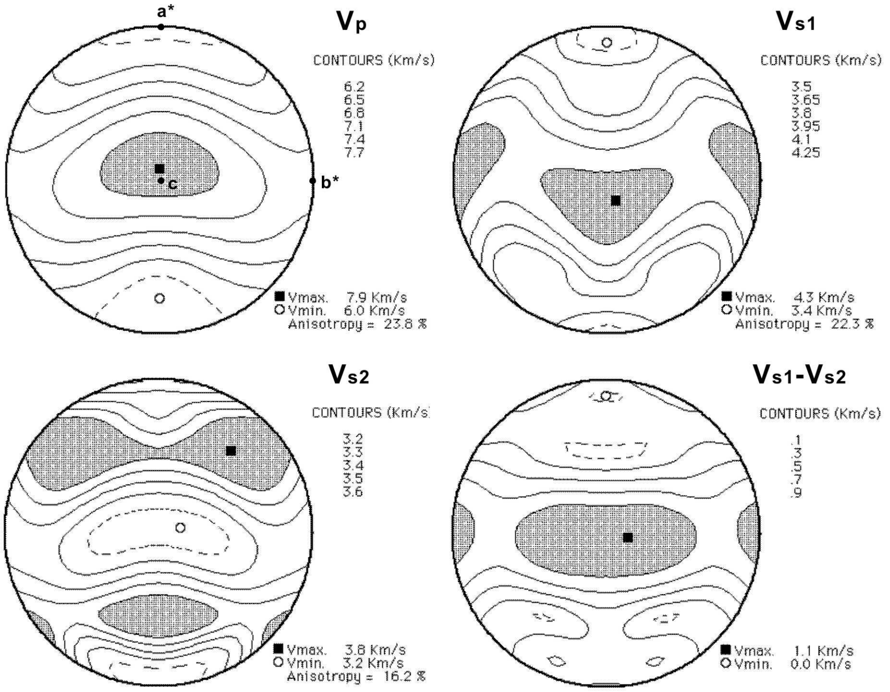

Muscovite $KAl_3Si_3O_{10}(OH)_2$

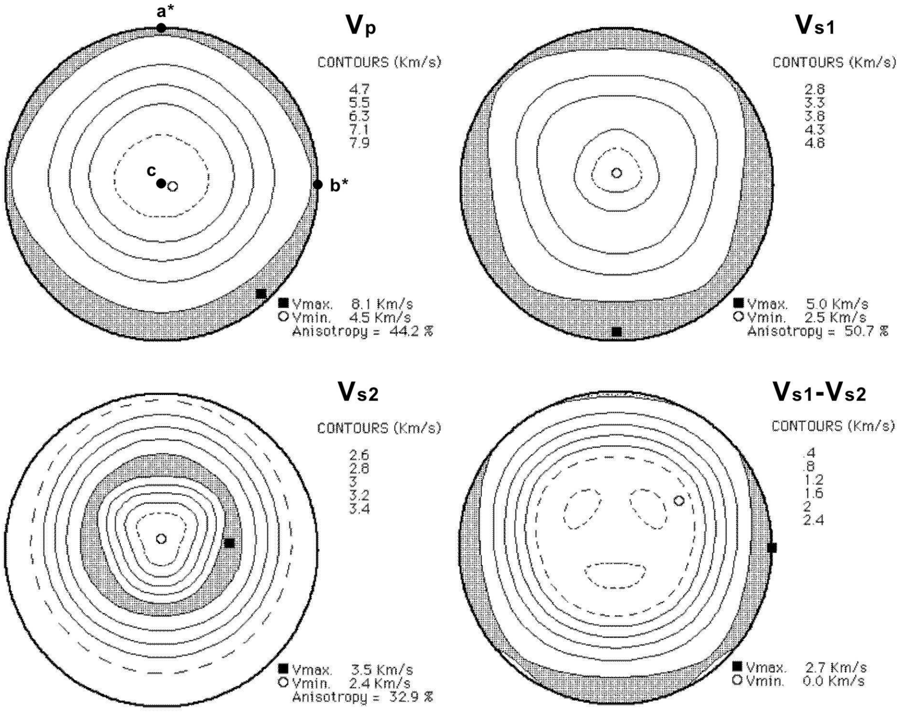

Plagioclase An53

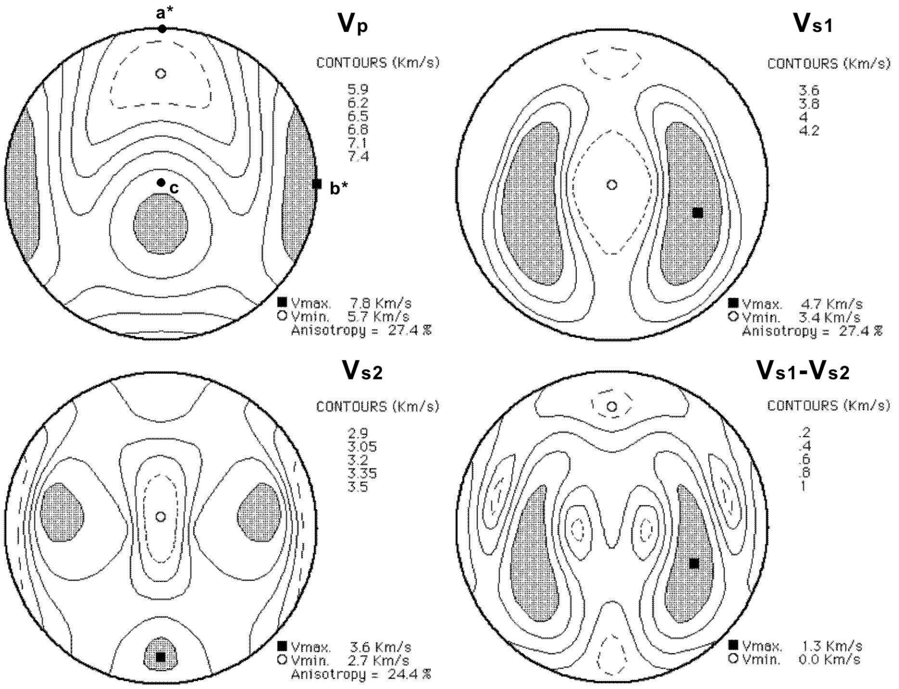

Quartz SiO_2

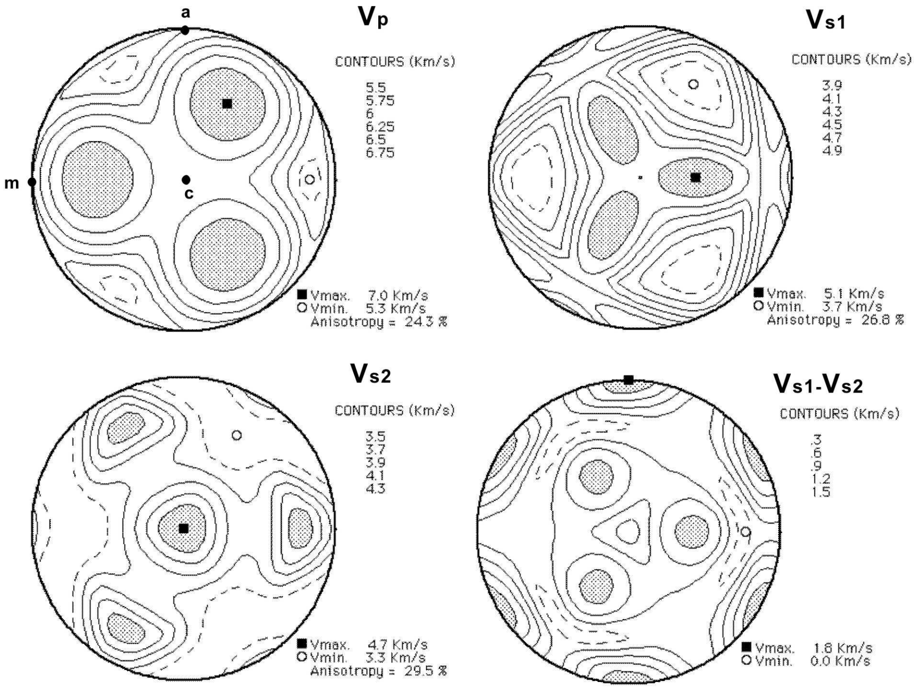

Olivine Fo93Fa7

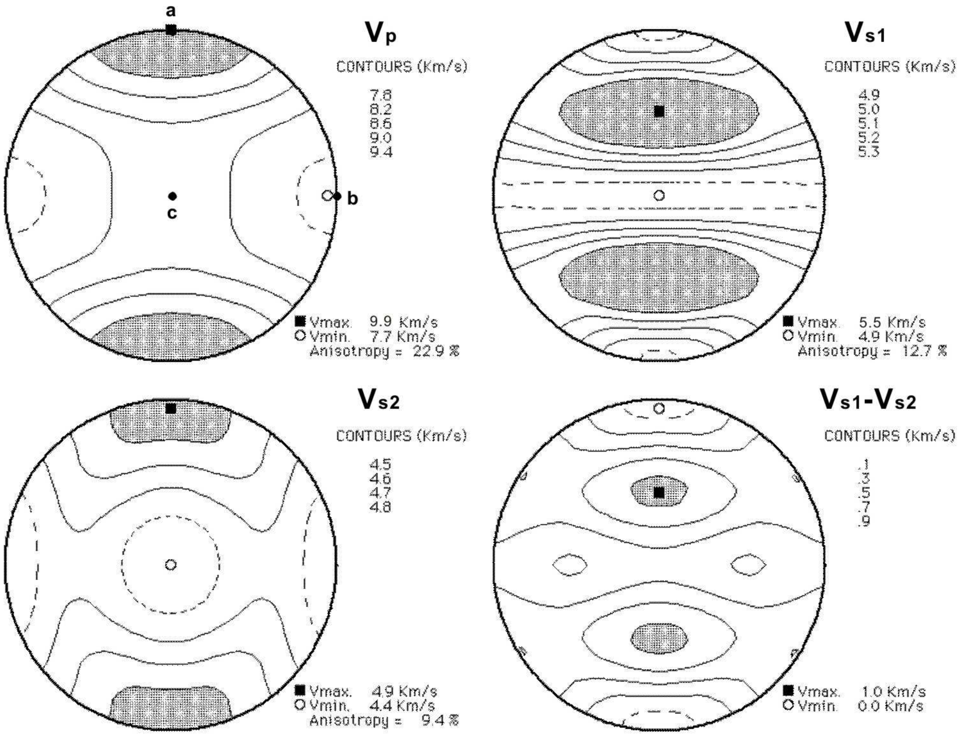

Enstatite $MgSiO_3$

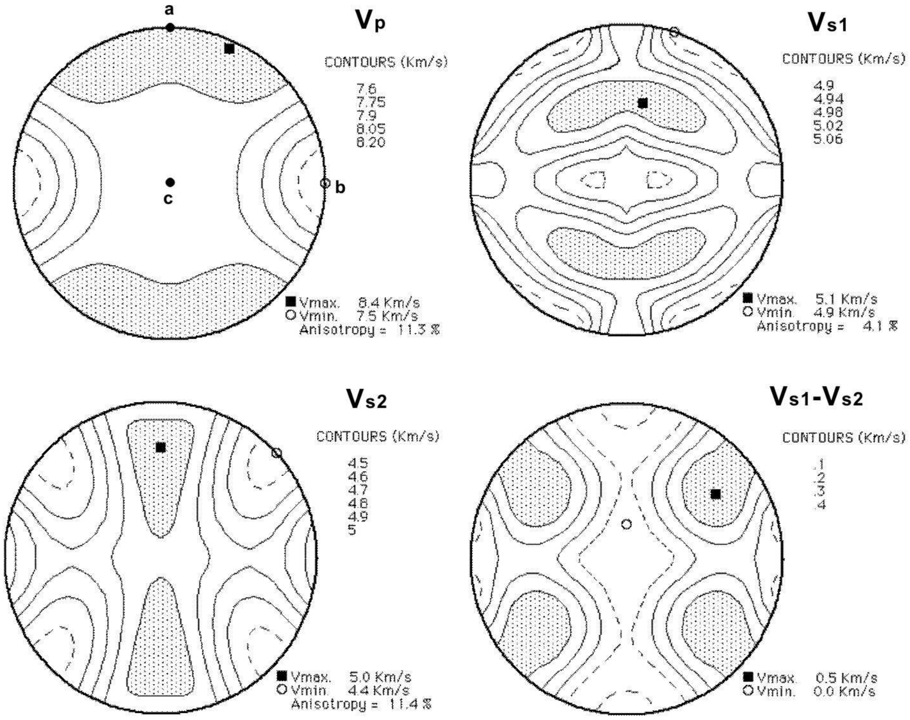

Diopside $CaMgSi_2O_6$

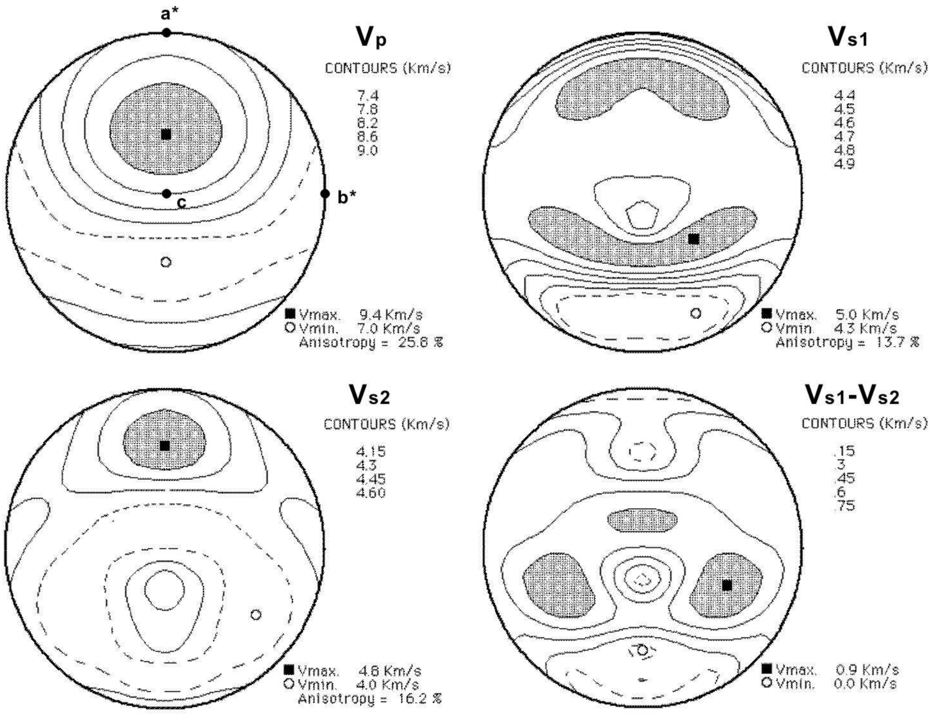

Figure 1.18 P- and S-wave properties of 7 main minerals in the continental lower crust and upper mantle. The P-wave phase velocities (V_p, up-left), the fast S-wave velocities (V_{s1}, up-right), the slow S-wave velocities (V_{s2}, low-left), and the S-wave birefringence or shear-wave splitting (V_{s1}-V_{s2}, low-right) are shown in equal area stereographic projection with respect to the crystallographic orientations of a, b, c, a* and b*, where a* and b* are the directions normal to (100) and (010) planes, respectively. The maximum velocity (in km/s) is marked by a solid square and the minimum by an open circle. The anisotropy is in percent. Notice that the contour intervals are not the same for every diagram. Shaded areas correspond to directions of high P- or S-wave velocities. After Ji et al. (2002).

Mica has an extremely large V_p anisotropy (44.2% for muscovite and 64.2% for biotite), with the minimum P-wave velocity along the [001] direction (Fig. 1.18, Ji et al., 2002; Kitamura, 2006). In the (001) plane, mica is almost seismically isotropic. In schists or phyllites, mica (biotite and/or muscovite) develop strong LPOs with (001) parallel to the foliation. This LPO pattern produce a prominent anisotropy (mostly ~10-12%, Fig. 1.13) with a transversely isotropic pattern: $V_p(X) \approx V_p(Y) > V_p(Z)$ (Ji et al., 1993; Kern and Wenk, 1990). The maximum ΔV_s is generally observed for propagation in the foliation plane and little or no shear wave splitting is observed normal to foliation. Thus, mica will enhance the magnitude of seismic anisotropy which originates in the LPO of amphibole.

Plagioclase (e.g., An53, triclinic symmetry) has a high V_p anisotropy (up to 30%), with the maximum P-wave velocity in the direction normal to the (010) plane and the minimum 26-30º from the [100] direction. The shear wave splitting behavior is more complex, with two maxima inclined to the c-axis, although there is some variation in all of these values with Ca content (e.g. Lloyd and Kendall, 2005). A number of measurements on naturally and experimentally deformed plagioclase revealed a dominant (010)[001] or (010)[100] slip system (Ji and Mainprice, 1988; Ji et al., 2004, 2005). In plagioclase-dominated metamorphic rocks such as anorthositic mylonites, plagioclase generally develop strong LPO with (010) plane parallel to the foliation and [001] parallel to the lineation. As a result, anisotropic pattern is characterized by $V_p(Z)>V_p(X)>V_p(Y)$ (Ji and Mainprice, 1988; Ji et al., 1993). Therefore, plagioclase has a negative contribution to the seismic anisotropy formed by LPO of amphibole and mica in the amphibolites.

Pyroxene-bearing mafic or felsic granulites and deformed tonalite, granodiorite and granite generally display very low anisotropy (commonly <3-4%, Fig. 1.13, Ji et al., 1993; Burke and Fountain, 1990; Kern, 1990). This is due to the fact that the contribution of plagioclase and clinopyroxene/orthopyroxene cancel one another to produce low anisotropy. Similarly, the contribution of plagioclase and quartz cancel also one another to produce low anisotropy.

1.4.4 Seismic anisotropy of the upper mantle

Table 1.5 lists the mineralogical modal compositions of the upper mantle above the transition zone (~400 km depth). The models of pyrolite (Ringwood, 1975) and piclogite (Anderson, 1989) are two end-members for the composition of the upper mantle. The compositions estimated from the mantle xenoliths brought by basaltic eruption to the Earth's surface (Ji et al., 1994; Saruwatari et al., 2001) and from peridotite samples dredged at six oceanic ridges (Dick, 1987) are also given in this table. The seismic anisotropy of upper mantle is mainly controlled by LPOs of three anisotropic minerals: olivine, orthopyroxene (enstatite or bronzite) and clinopyroxene (diopside). Cubic garnet and spinel are weakly anisotropic and hence has little contribution to observed seismic anisotropy.

Table 1.5 Modal composition of the upper mantle above the transition zone

Sample source	Modal Composition (vol. %)							Reference
	Olivine	Orthopyroxene	Clinopyroxene	Garnet	Spinel	Plagioclase	Phlogopite	
Pyrolite model	61.0	15.0	10.0	14.0				Ringwood (1975)
Piclogite model	40.0	10.0	37.0	13.0				Duffy and Anderson (1989)
Spinel Lherzolite	66.7	23.7	7.9		1.7			Maaloe and Aoki (1977)
Garnet Lherzolite	62.6	30.0	2.0	5.0			0.4	Maaloe and Aoki (1977)
Southern Canadian Cordillera	60.9	24.8	11.8		2.5			Ji et al. (1994)
Northern Canadian Cordillera	54.3	27.9	14.9		2.9			Saruwatari et al. (2001)
Oceanic ridges	74.8	20.6	3.6		0.5	0.5		Dick (1987)

A certain number of accurate determinations of the elastic constants of olivine are now available which all agree that olivine has a V_p anisotropy of up to 25%, with the maximum velocity (~9.9 km/s) along the [100] direction, the intermediate velocity (~8.4 km/s) along the [001] direction, and the minimum velocity (~7.7 km/s) along the [010] direction (Fig.1.18, Webb, 1989; Isaak, 1992; Mainprice et al., 2000; Ji et al., 2002). The maximum shear wave splitting (~1.0 km/s) occurs in the [101] direction, while little or no splitting occurs in the [100] direction. Olivine displays a large variation of fabric patterns. The most common olivine LPO (Type A) found in natural and experimental samples is characterized by [100], [010] and [001] parallel to the X, Z and Y directions, respectively (Fig. 1.19).

The elastic properties of orthopyroxene (enstatite or bronzite) with a magnesium number (Mg/Mg+Fe) near the typical upper mantle value of 0.9 have been extensively studied (e.g., Duffy and Vaughan, 1989; Webb and Jackson, 1993; Chai et al., 1997). The V_p anisotropy varies between 11.3% (enstatite; Ji et al., 2002) and 15.1% (bronzite; Frisillo and Barsch, 1972). The maximum P-wave velocity (~8.4 km/s) is parallel to [100] and the minimum (~7.5 km/s) is parallel to [010]. The maximum (~0.5 km/s) and minimum shear wave splitting occur in the directions of [110] and [100], respectively (Fig. 1.18). Some of the variation in the elastic constants and anisotropy may result from composition and structure in the orthopyroxenes (Duffy and Vaughan, 1989). The most common orthopyroxene fabric is characterized by [100], [010] and [001] parallel to Z, Y and X directions, respectively (Fig. 1.19).

The elastic constants of clinopyroxene (diopside) of mantle composition have also been determined at ambient conditions (e.g., Levien et al., 1979; Collins and Brown 1998). The V_p anisotropy varies from 25.8% (Ji et al., 2002) to 29.5% (Levien et al., 1979), with the maximum velocity (~9.4 km/s) close to the [101] direction and the minimum velocity (~7.0 km/s) close to the [001] direction. The maximum shear wave splitting (~0.9 km/s) occurs close to the [-111] direction, and the minimum splitting occurs close to the [100] direction (Fig. 1.18). A typical diopside LPO is characterized by [100] close to Y, [010] close to Z, and [001] close X (Fig. 1.19, Barruol and Mainprice, 1993; Xu et al., 2009a).

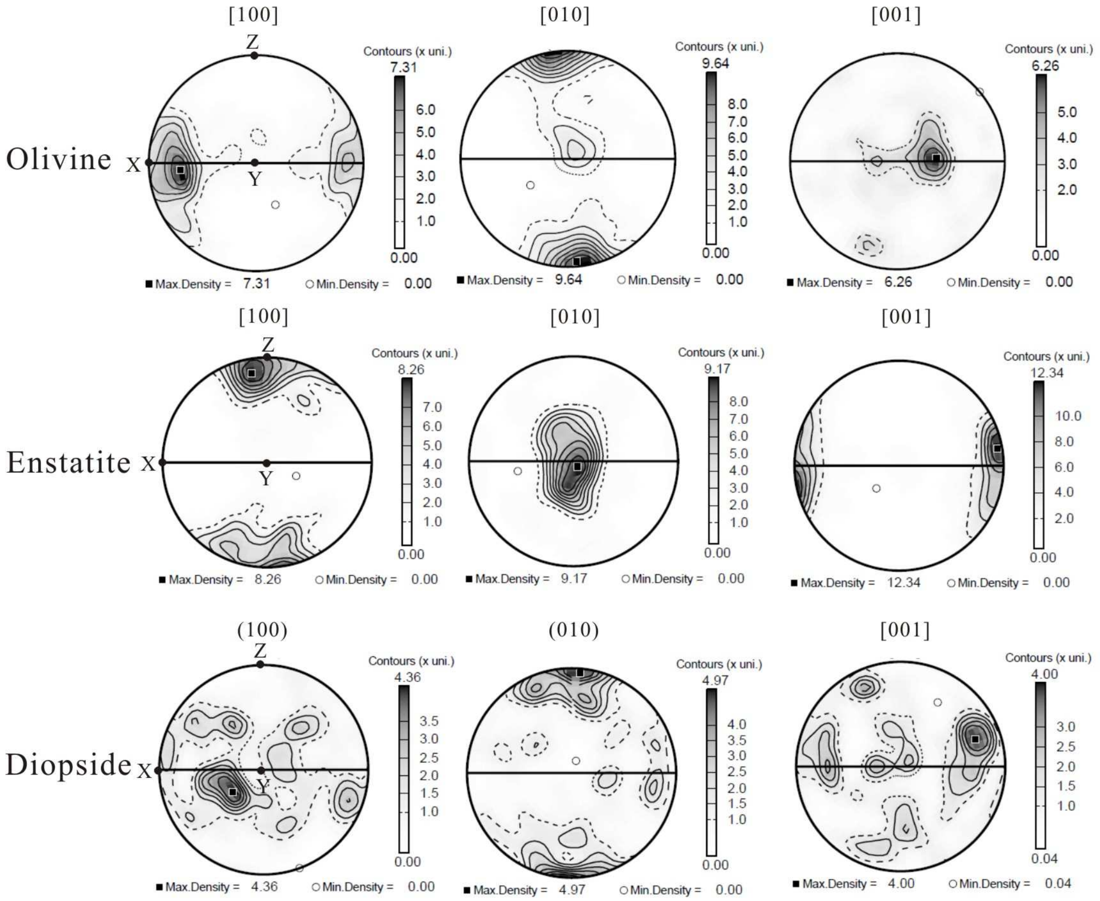

Figure 1.19 Typical pole figures showing LPO of olivine, enstatite and diopside. Olivine and enstatite pole figures for [100], [010] and [001]. Diopside pole figures for (100), (010) and [001]. Contours in multiples of a uniform distribution. After Mainprice et al. (2000).

The seismic anisotropy of upper mantle rocks is a result of the interaction of olivine, orthopyroxene and clinopyroxene. According to the LPO patterns given in Fig. 1.19, Mainprice et al. (2000) calculated the seismic anisotropy produced by LPO of olivine, orthopyroxene (enstatite) and clinopyroxene (diopside). The maximum P-wave velocities of olivine, orthopyroxene and clinopyroxene are parallel to X, in the XZ plane, and parallel to Y, respectively (Fig. 1.20). Destructive interference occurs between these minerals and hence V_p anisotropy should be vary as a function of composition content in olivine, orthopyroxene and clinopyroxene. Olivine is volumetrically the most important mineral of the Earth's upper mantle, therefore, P-wave anisotropy of upper mantle rocks largely depends on olivine LPO pattern.

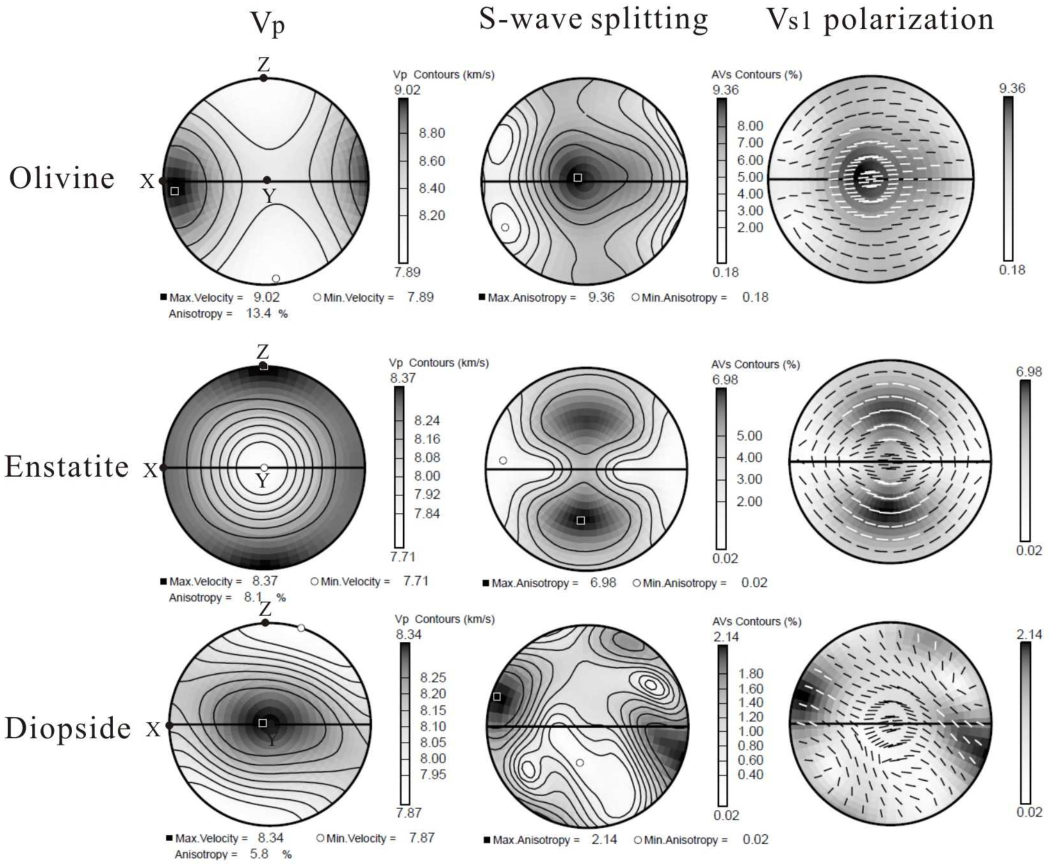

Figure 1.20 Seismic anisotropy induced by LPO of olivine, enstatite and diopside. Corresponding LPO patterns are given in Figure 1.19. Contours for V_p in km/s, S-wave splitting in % and trace of the V_{s1} polarization plane. (After Mainprice et al., 2000)

Typical olivine and orthopyroxene LPOs result in similar shear wave splitting patterns, with the maximum splitting in the YZ plane, the minimum splitting close to the lineation (X), and the fast shear wave (V_{s1}) polarized approximately parallel to the foliation (XY plane). A typical clinopyroxene LPO on the other hand produces destructive interference as the maximum shear wave splitting is close to X and the minimum splitting is in the YZ plane. The V_{s1} polarization is a more complex pattern than either olivine or orthopyroxene, being oblique to the foliation by 30° or more. Consequently, shear wave splitting will be fairly constant for differing proportions of olivine and orthopyroxene, however changing the fraction of clinopyroxene will vary the shear wave splitting.

Samples of the Earth's upper mantle which one can find from the Earth's surface are mainly in the form of ultramafic massifs, xenoliths in basaltic or kimberlitic volcanics and as inclusions in diamonds. The South Africa kimberlite nodules constitute one of the most extensively studied and numerically important collections of subcontinental mantle samples. Chemical analyses indicate the garnet lherzolite and harzburgite peridotite nodules from kimberlite pipes in the Kaapvaal craton originated at depths 120-200 km (Boyd and Nixon, 1973; Boyd and Gurney, 1986). Based on the measurements of the olivine and pyroxene LPO and the single crystal elastic constants, Mainprice and Silver (1993) and Ben-Ismail et al. (2001) calculated the seismic anisotropy of Kaapvaal upper mantle nodules, giving a mean V_p anisotropy value of 3% and a mean maximum shear wave splitting of ~3-4%.

The Canadian Cordillera is another one of the most productive regions of mantle xenoliths in the world. Abundant ultramafic xenoliths occur within the calc-alkaline and alkaline basalts that have been erupted in the pull-aparts within the strike-slip fault zones since the early Cenozoic (Clowes et al., 1992). The mantle xenoliths from Canadian Cordillera are dominated by spinel lherzolite that evidently represents the upper mantle lithology (Peslier, 1999). Ji et al. (1994) and Saruwatari et al. (2001) measured the seismic anisotropy of mantle xenoliths from Canadian Cordillera. Their results suggest that the average values of V_p anisotropy and maximum shear wave splitting of the studied samples are ~ 7% and ~5%, respectively (Fig. 1.21).

The ultramafic xenoliths from Canadian Cordillera (Ji et al., 1994; Saruwatari et al., 2001), and those from South Africa (Mainprice and Silver, 1993; Ben-Ismail et al., 2001), may be representative of the subcontinental mantle underneath active orogenic regions and stable cratonic regions, respectively. Although the seismic anisotropy of the upper mantle is slightly higher in active orogenic regions than in stable cratonic regions, the seismic patterns of the xenoliths from these two regions are very similar. The V_p distribution is generally related to the olivine fabric pattern (Fig. 1.20) and is characterized by the maximum, intermediate, and minimum P-wave velocity parallels to X, Y and Z direction, respectively (Fig. 1.21). Two shear wave splitting patterns are observed: (1) a complete or partial girdle occurs along the YZ-plane, in which two point maxima are symmetrically distributed with respect to the foliation (XY) plane (sample KL3 in Fig. 1.21) (2) a point maximum occurs nearly parallel to the Y-direction (sample JLL9 in Fig. 1.21). Theses distributions of shear wave splitting display different and more complicated patterns than that of olivine, which is a result of the interaction of olivine, orthopyroxene and clinopyroxene.

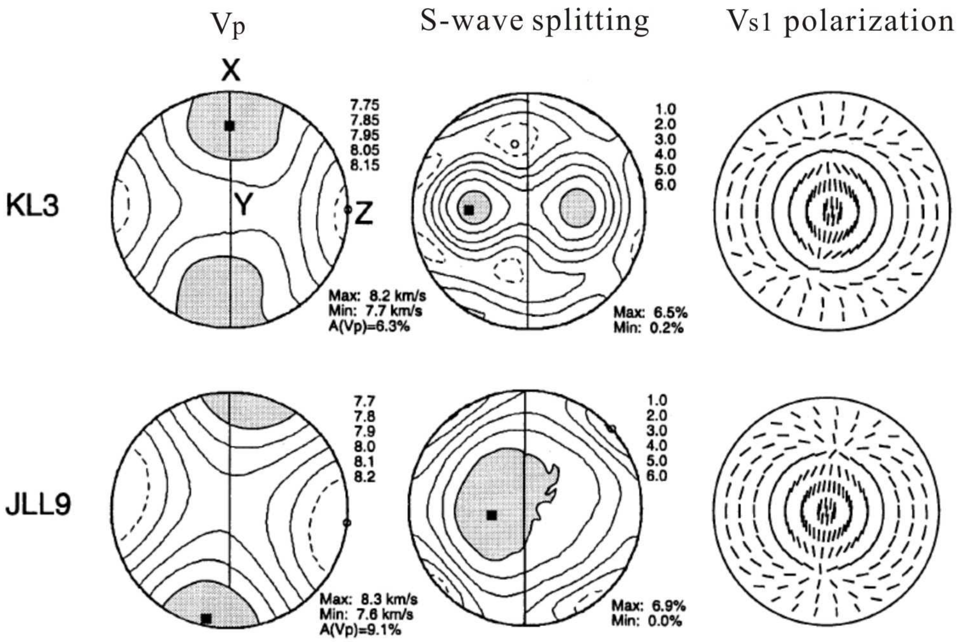

Figure 1.21 P wave velocities (V_p), S-wave splitting and fast S-wave (Vs_1) polarization direction for two mantle xenolith samples collected from Canadian Cordillera. Contours for V_p in km/s, S-wave splitting in %. (After Saruwatari et al., 2001)

CHAPTER 2 SEISMIC PROPERTIES OF THE LONGMEN SHAN COMPLEX: IMPLICATIONS FOR THE MOMENT MAGNITUDE OF THE GREAT 2008 WENCHUAN EARTHQUAKE IN CHINA

2.1 Abstract

The Wenchuan earthquake (12 May 2008) is the largest active tectonic event reported to date in Sichuan (China). Seismic and elastic properties have been experimentally calibrated up to 800 MPa for 12 representative samples from the Longmen Shan complex in which this great earthquake took place and its coseismic ruptures nucleated and propagated. Most of the samples show little V_p or V_s anisotropy at pressures above the microcrack-closure pressure (P_c=200-300 MPa), and so the variation of anisotropy with pressure provides important hints for the preferred orientation of microcracks in the nonlinear poroelastic regime below P_c. Geothermal and rheological profiles indicate that the focal depth (~19 km) corresponds to the base of the schizosphere, below which the Longmen Shan complex switches from the brittle to ductile behaviour. The investigation reveals that the crust of the Longmen Shan range consists of 4 layers from the surface to the Moho: Layer 1: V_p<4.88 km/s (0-3 km thick, sedimentary rocks such as limestone, sandstone, conglomerate, and mudstone); Layer 2: V_p=5.95-6.25 km/s (25-28 km thick, felsic rocks); Layer 3: V_p=6.55 km/s (10 km thick, 67.5% felsic and 32.5% mafic rocks); and Layer 4: V_p=6.90 km/s (8 km thick, 20.0% felsic and 80.0% mafic rocks). The average V_p/V_s ratio of 1.71 or Poisson's ratio of 0.24 calculated for the whole crust is consistent with the results measured using teleseismic receiver function techniques. This study also offers necessary information for broadband simulations of strong ground motions in the assessment and forecast of earthquake hazards in the region. Furthermore, the study, which yields a moment magnitude of 7.9-8.0 given the variation in the dip of the coseismic ruptures and the uncertainty in the depth to which the coseismic rupture may propagate downwards below the depth of the

mainshock hypocenter, presents the first accurate quantification of the 2008 Wenchuan earthquake's size.

2.2 Introduction

The devastating Wenchuan earthquake occurred at 14:28 LT on 12 May 2008 in the Longmen Shan region of China, the transition zone between the Tibetan Plateau and the Sichuan Basin (Fig. 2.1). A moment magnitude (M_w) of 7.9 and a surface-wave magnitude (M_s) of 8.0 were obtained from the inversion of moment-release functions (USGS, 2008) and the seismographic data (CENC, 2008), respectively. A government report published on 11 September 2008 stated that 69,226 people were confirmed dead, 374,643 injured and 17,923 missing. More than 7.7891 million homes collapsed and 24.59 million were damaged. The earthquake induced strong ground movements that caused a tremendous amount of hazards including avalanches, landslides, mud flows, soil liquefaction, and large barrier lakes.

The Longmen Shan range strikes NE-SW for a distance of ~500 km (e.g., Jia et al., 2006; Xu et al., 2008), and lies between the Songpan-Ganzi terrane (a Triassic orogenic belt) and the Sichuan Mesozoic-Cenozoic foreland basin on the Yangtze block. Located on the eastern side of the Tibetan Plateau, the Longmen Shan range rises 6 km above the Sichuan basin, exhibiting the greatest topographic relief (over 5 km) and the steepest mountain fronts on earth. The uplift mechanism for the Longmen Shan range is still controversial, two end-member models have been proposed: (1) crustal thickening through large amounts of slip along thrust faults rooted in the lithosphere (e.g., Tapponnier et al., 2001; Xu et al., 2008; Hubbard and Shaw, 2009), and (2) channel flow or extrusion of middle-to-lower crustal materials with extremely low-viscosity (probably partially molten) outwards from the Tibetan Plateau, which inflates the crust north and east of the Himalayas since about 4 Ma (e.g., Royden et al., 1997; Clark and Royden, 2000; Burchfiel et al., 2008).

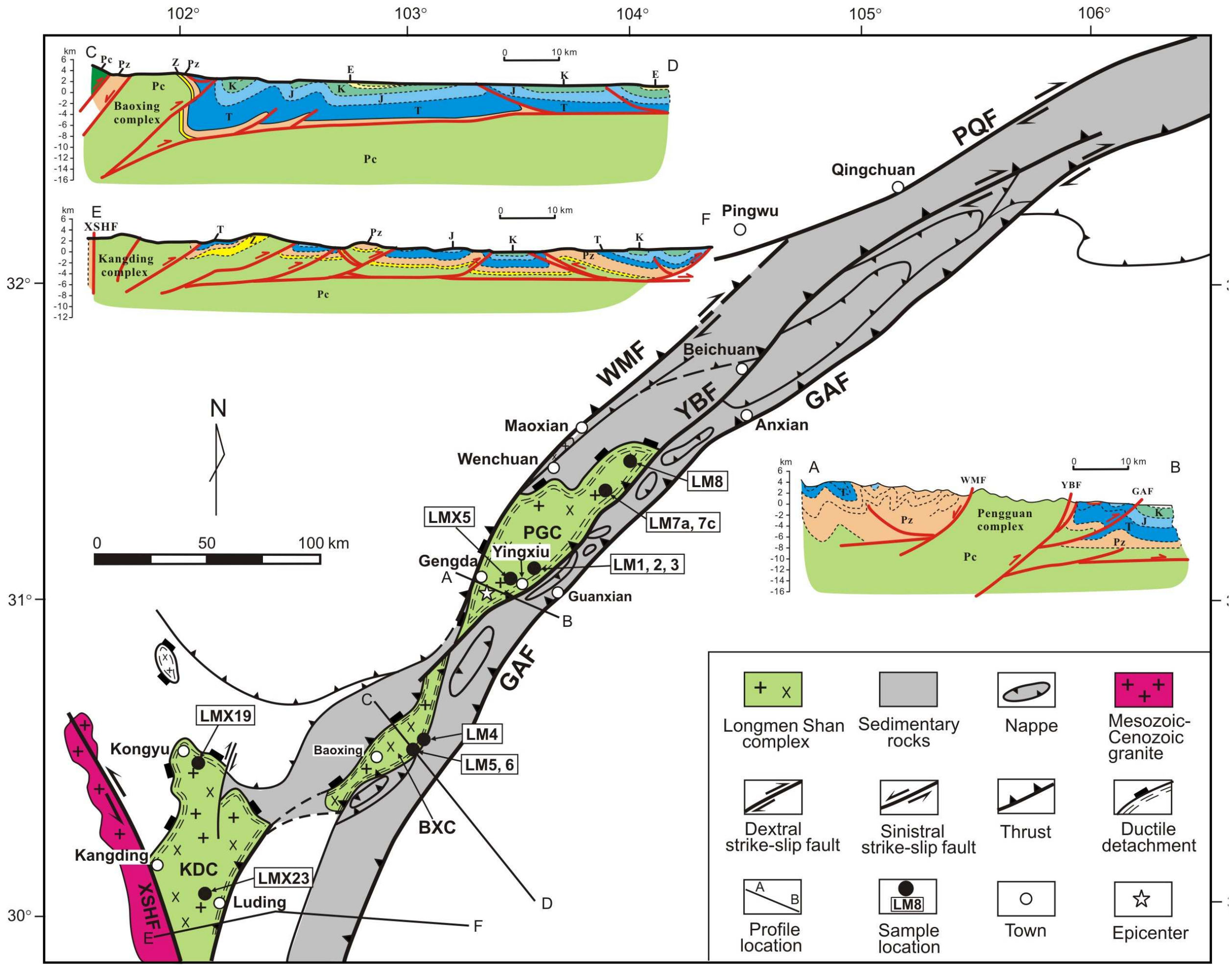

Figure 2.1 Tectonic map and cross sections of the Longmen Shan range and adjacent areas. WMF: Wenchuan-Maoxian fault; YBF: Yingxiu-Beichuan fault; GAF: Guanxian-Anxian fault; PQF: Pingwu-Qingchuan fault; XSHF: Xianshuihe fault. PGC: Pengguan complex; BXC: Baoxing complex; KDC: Kangding complex. The cross sections from Burchfiel et al. (2008), Jia et al. (2006, 2010), and Xu et al. (2008).

Three main thrust faults have been recognized along the Longmen Shan range from west to east: the Wenchuan-Maoxian fault, the Yingxiu-Beichuan fault and the Guanxian-Anxian fault. The Wenchuan-Maoxian fault (WMF) defines the northwest boundary of the Longmen Shan thrust belt, and has been considered a normal ductile shear zone (Xu et al., 1992, 2008), a thrust (Chen and Wilson, 1995) and a Triassic transpressional fault (Wang et al., 2001). The 2008 Wenchuan mainshock resulted in a main coseismic thrusting or transpressional rupture along the Yingxiu-Beichuan fault (YBF in Fig. 2.1) over a length of ~240 km, and a secondary rupture over a length of ~72 km along the Guanxian-Anxian fault (GAF in Fig. 2.1), representing the largest active tectonic event reported to date in Sichuan (China). These two faults merge at a depth of ~8 km with a major fault plane which is moderately dipping (28°-38°) to NW between Yingxiu and Beichuan and steeply dipping (58°) between Beichuan and Qingchuan. These southwestern and northeastern segments are characterized by dominantly thrusting and strike-slip components of coseismic displacement, respectively. The average coseismic slip is ~2-3 m, with a maximum vertical displacement of ~6.5 m measured at North Beichuan Town, and a maximum horizontal displacement of ~4.9 m measured at Pingtong Town (Xu et al., 2008; Li et al., 2008; Dong et al., 2008; Ji et al., 2008; Xu et al., 2009; Liu-Zeng et al., 2009; Lin et al., 2009, 2010; Li et al.. 2010).

The Longmen Shan range is mainly composed of Precambrian (700-800 Ma) magmatic and metamorphic rocks at depth, with small amounts of Neoproterozoic volcanic rocks and Sinian to early-middle Triassic marine sedimentary rocks (i.e., limestone, conglomerate, sandstone, mudstone and shale) near the surface (Xu et al., 2008; Burchfiel et al., 2008; Hubbard and Shaw, 2009). The Precambrian magmatic and metamorphic rocks, which are probably reactivated basement materials of the Yangtze block, are equivalent, from north to south, to the Pengguan complex, the Baoxing complex and the Kangding complex (Fig. 2.1). The complexes, hereafter called the Longmen Shan complex, consist of predominantly felsic rocks such as granite, granodiorite, diorite, monzonite and grabbroic diorite (Fig. 2.2), and their deformed counterparts (i.e., mylonites and gneiss), intruded by mafic veins with ages of 757-805 Ma (Xu et al., 2008). The metamorphic peak temperature for the Longmen Shan complex was estimated to be 530-590 °C, suggesting an exhumation of ~25 km since the Triassic (Robert et al., 2010). The epicenter of the 2008 Wenchuan mainshock (31.021ºN, 103.367ºE) indicates that the great earthquake nucleated in the Pengguan complex. Using the aftershock data, Pei et al. (2010) derived a three-dimensional velocity structure showing relatively high V_p and V_s but low V_p/V_s for the Longmen Shan complex with respect to its surrounding rocks in the crust above the depths of 20-25 km.

In this chapter, seismic properties and anisotropy as a function of confining pressure up to 800 MPa for 12 representative samples collected from the Longmen Shan complex were investigated in order to provide necessary constraints on the regional seismic velocity models used for the tectonic interpretation of seismic data (Zhao et al., 1997; Wang et al., 2003; Yang et al., 2004; Pei et al., 2010; Wang, Zhu et al., 2010; Xu and Song, 2010) and broadband simulations of strong ground motions in the assessment and forecast of earthquake hazards (Brocher, 2005b; Koketsu et al., 2005; Aagaard, 2006) and on the seismic moment magnitude of the 2008 Wenchuan Earthquake (Wang et al., 2008; Lu et al., 2010; Wang, Liu et al., 2010).

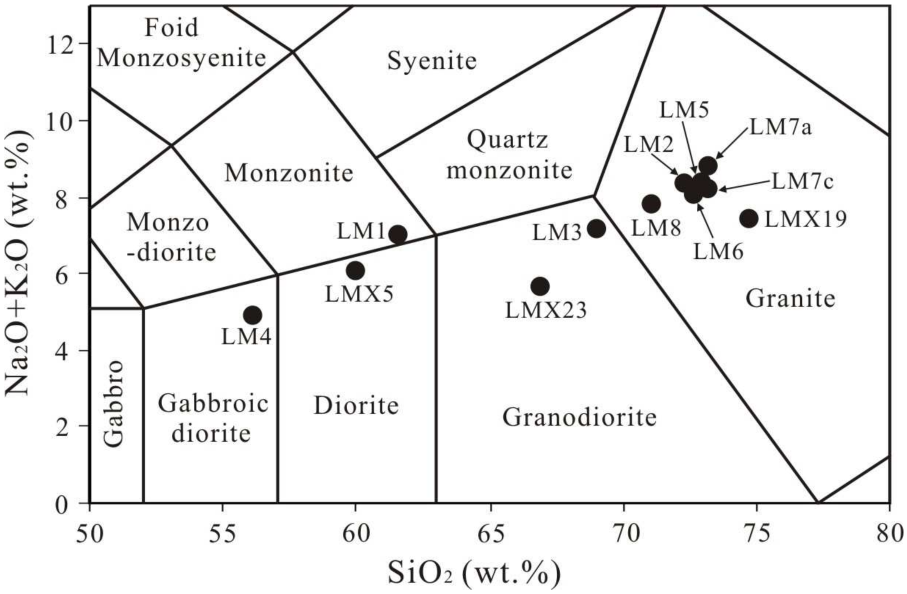

Figure 2.2 A total alkali–silica (TAS) classification diagram (Middlemost, 1994) for rock samples from the Longmen Shan complex.

2.3 Samples

Twelve samples collected from the Longmen Shan complex were used in this study (Fig. 2.1), representing typical lithologies of the basement of the Longmen Shan range: a gabbroic diorite, a monzonitic mylonite, a meta-andesite, two granodiorites and seven fine- or coarse-grained granites. Table 2.1 gives the lithology, density and modal composition for each of these samples. The samples selected for velocity measurements are dry, highly compact rocks with porosities less than 0.1-0.2%. The modal compositions were determined by point counting on thin sections cut perpendicular to the foliation and parallel to the lineation. The densities were determined using the immersion method with an accuracy of ±0.005 g/cm^3 at room conditions. Bulk density data for this suite of samples show a continuous reduction from diorite ($\overline{\rho}$=2.79 g/cm^3), through granodiorite ($\overline{\rho}$=2.71 g/cm^3), to granite ($\overline{\rho}$=2.63 g/cm^3).

Table 2.1 Description of the studied samples from the Longmen Shan complex, China

Sample	Lithology	Density (g/cm^3)	Modal composition[a] (vol. %)
LM1	Folded, sheared, monzonitic mylonite	2.72	Pl 60.0, Hbl 12.0, Srp 9.0, Kfs 6.8, Qtz 6.0, Di 3.0, Ms 1.0, Mag 1.0, Spn 1.0, Zrn 0.2
LM2	Fine-grained granite	2.62	Pl 50.0, Qtz 26.4, Kfs 16.0, Srp 4.0, Ms 3.0, Mag 0.6
LM3	Moderate-grained granodiorite	2.65	Pl 49.0, Qtz 25.0, Kfs 13.0, Srp 5.0, Chl 4.0, Bt 3.0, Mag 1.0
LM4	Gabbroic diorite	2.84	Pl 45.0, Hbl 12.0, Di 12.0, Qtz 8.0, Kfs 7.0, Srp 6.0, Ep 5.0, Chl 3.0, Mag 1.0, Spn 1.0
LM5	Coarse-grained granite	2.63	Pl 42.0, Qtz 28.0, Kfs 19.5, Ms 4.0,Chl 2.0, Srp 2.0, Bt 1.0, Grt 1.0, Mag 0.5
LM6	Coarse-grained granite	2.64	Pl 45.0, Qtz 29.0, Kfs 19.0, Ms 3.0, Chl 2.0, Srp 1.0, Mag 0.5, Grt 0.5
LM7a	Granite	2.62	Pl 50.0, Qtz 26.0, Kfs 20.0, Chl 2.0, Ms 1.0, Srp 1.0
LM7c	Granite	2.62	Pl 49.0, Qtz 28.0, Kfs 19.0, Ms 2.0, Chl 1.0, Srp 1.0
LM8	Granite	2.63	Pl 63.0, Qtz 23.0, Kfs 8.0, Srp 4.0, Ms 1.0, Chl 1.0
LMX5	Meta-andesite	2.81	Pl 47.0, Hbl 30.0, Qtz 13.0, Chl 5.0, Srp 2.0, Bt 2.0, Ep 1.0
LMX19	Granite	2.66	Pl 46.0, Qtz 30.0, Kfs 12.0, Srp 4.0, Hbl 4.0, Ep 2.0, Bt 1.0, Chl 1.0
LMX23	Hbl-Cpx granodiorite	2.77	Pl 36.0, Qtz 20.0, Srp 10.0, Di 10.0, Hbl 8.0, Kfs 7.0, Ms 4.0, Bt 2.0, Chl 2.0, Grt 1.0

[a] Abbreviations: Bt: biotite; Chl: chlorite; Di, diopside; Ep: epidote; Grt: garnet; Hbl: hornblende; Kfs: K-feldspar; Mag: magnetite; Ms: muscovite; Pl: plagioclase; Qtz: quartz; Spn: sphene; Srp: serpentine; Zrn: zircon

Table 2.2 lists the major element compositions for the samples used for this study. The compositions were determined by X-ray fluorescence (XRF) in ALS Laboratory in Guangzhou (China). The samples exhibit a slight compositional variability, which is illustrated by the total alkali-silica (TAS) diagram (Fig. 2.2). The data from this study together with other data sets on samples from the Pengguan complex (Yan et al., 2008; Zhang et al., 2008) display positive and quasi-linear correlations of the total alkali content (Na_2O+K_2O) but negative correlations of Al_2O_3, MgO, CaO, and FeO^T (total iron) contents with the SiO_2 content (Fig. 2.3). In addition, CaO content increases with increasing MgO content (Fig. 2.3f).

Table 2.2 Chemical composition (wt.%) of each sample from the Longmen Shan complex, China.

Sample	Lithology	SiO_2	TiO_2	Al_2O_3	Fe_2O_3	FeO	MnO	MgO	CaO	Na_2O	K_2O	P_2O_5	SrO	BaO	LOI	Total
LM1	Folded, sheared, monzonitic mylonite	61.59	0.74	17.14	0.25	1.14	0.03	3.94	6.81	6.03	0.91	0.11	0.04	0.02	1.19	99.94
LM2	Fine-grained granite	72.29	0.03	15.63	0.09	0.32	0.01	0.47	1.28	5.39	2.95	0.02	0.04	0.21	0.90	99.63
LM3	Moderate-grained granodiorite	69.00	0.18	16.32	0.65	1.39	0.04	0.85	2.22	5.02	2.11	0.07	0.06	0.05	2.06	100.02
LM4	Gabbroic diorite	56.11	0.57	18.97	4.02	2.52	0.20	2.38	6.85	3.61	1.32	0.33	0.08	0.05	2.53	99.54
LM5	Coarse-grained granite	73.00	0.08	15.57	0.31	0.50	0.17	0.34	0.87	5.02	3.33	0.06	0.03	0.11	0.71	100.10
LM6	Coarse-grained granite	72.71	0.08	15.49	0.32	0.57	0.13	0.36	1.08	4.84	3.23	0.06	0.04	0.13	0.94	99.98
LM7a	Granite	73.18	0.03	14.91	0.04	0.51	0.02	0.16	0.91	5.37	3.44	0.01	0.05	0.22	0.77	99.62
LM7c	Granite	73.13	0.04	15.11	0.26	0.44	0.02	0.15	1.40	5.03	3.21	0.02	0.06	0.24	0.80	99.91
LM8	Granite	71.09	0.16	15.90	0.63	0.76	0.03	0.46	1.76	6.51	1.30	0.06	0.05	0.04	1.16	99.91
LMX5	Meta-andesite	60.00	1.10	15.70	3.65	4.60	0.13	2.04	4.85	3.85	2.28	0.31	0.05	0.09	1.14	99.79
LMX19	Granite	74.75	0.18	13.61	1.11	0.76	0.04	0.26	1.08	5.36	2.08	0.04	0.02	0.09	0.61	99.99
LMX23	Hbl-Cpx granodiorite	66.90	0.29	16.61	1.47	1.38	0.06	1.03	3.96	3.71	1.95	0.14	0.05	0.06	1.82	99.43

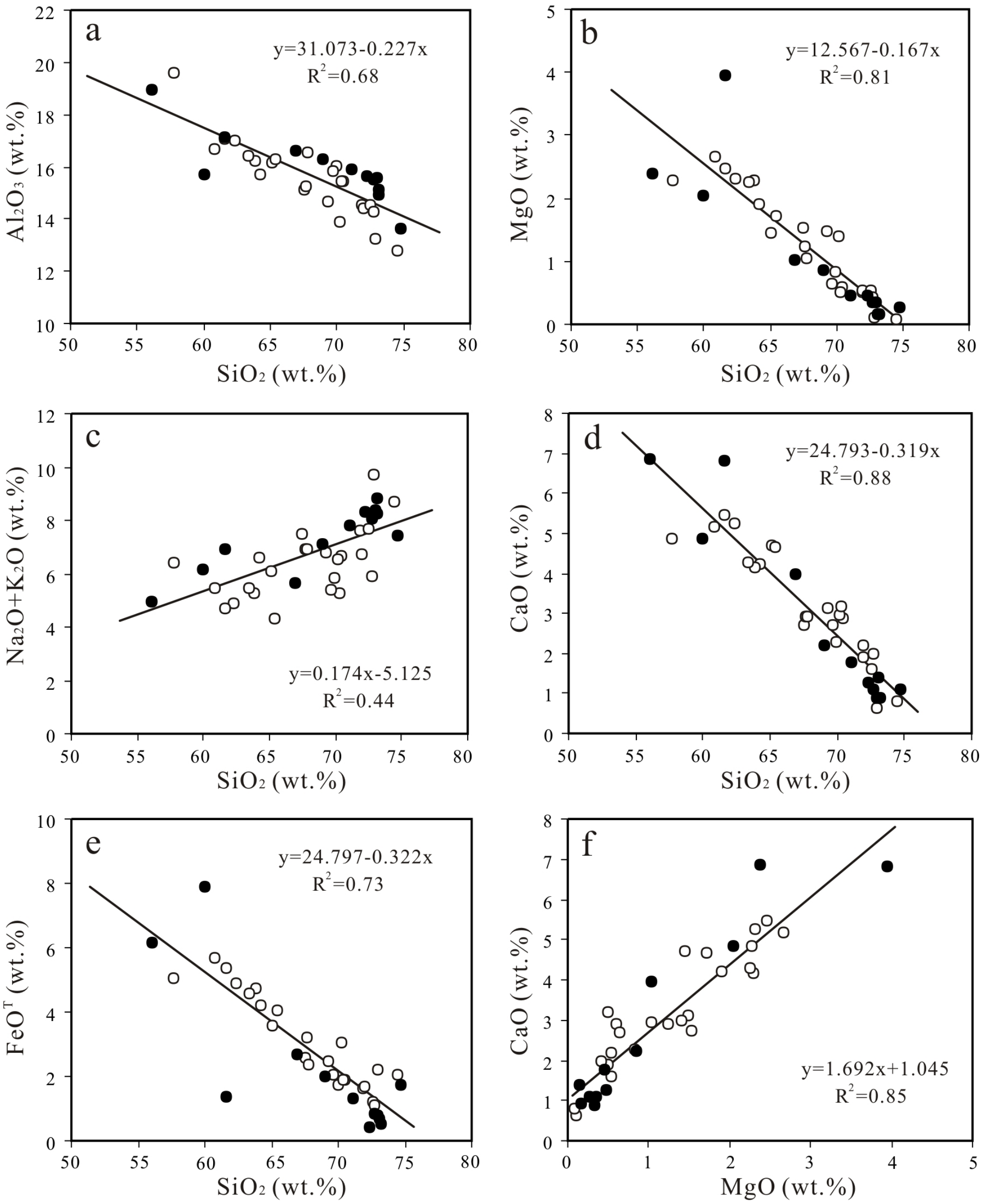

Figure 2.3 Relationships between major oxides (wt.%) for the Longmen Shan complex. (a) Al_2O_3 vs. SiO_2, (b) MgO vs. SiO_2, (c) Na_2O+K_2O vs. SiO_2, (d) CaO vs. SiO_2, (e) FeO^T (total iron) vs. SiO_2, (f) CaO vs. MgO. Solid dots: this study; open dots: data from Yan et al. (2008) and Zhang et al. (2008).

2.4 Experimental details

Measurements of P- and S-wave velocities (V_p and V_s) and their directional dependence (P-wave anisotropy and shear wave splitting) were performed at hydrostatic pressure ranging

10-800 MPa using the pulse transmission technique (Birch, 1960; Wepfer and Christensen, 1991; Kern, 1990). For sufficiently large samples which display clearly defined foliation and lineation (e.g., LM2, LM4, LM5 and LM6), three cylindrical minicores (2.54 cm in diameter by 3-5 cm in length) were cut in orthogonal directions with the X direction parallel to the stretching lineation (minicore X), the Y direction perpendicular to lineation and parallel to foliation (minicore Y), and the Z direction normal to foliation (minicore Z), respectively. However, if the sample displays neither foliation nor lineation (i.e., isotropic rock) or is insufficiently large, cylindrical minicores were usually cut in one reference direction (e.g., minicore Y for sample LM1) or in arbitrary directions (e.g., minicores A and B for sample LM3). Each minicore was trimmed to ensure possession of two polished plan-parallel end faces.

The high-pressure experiments were carried out at the GSC/Dalhousie High Pressure Laboratory in Halifax, Nova Scotia (Ji et al., 1993, 1997a, 2007a; Wang et al., 2005a, b; Wang and Ji, 2009). The apparatus is a seven ton, double-walled steel vessel with a 40 cm long by 10 cm diameter working chamber, which can operate to a pressure of up to 1.4 GPa. The pressure medium consists of light hydraulic oil pumped into the working chamber by means of a two-stage intensifier. Waves were generated and received by lead zirconate titanate transducers with a 1 MHz resonance frequency. To prevent the pressure medium from invading the sample during the pressure run, the minicores were sheathed in impermeable thin copper foil and the entire sample/transducer/electrode assembly was enclosed in neoprene tubing. Once the sample assembly was sealed in the pressure vessel and the pressure was raised, a high voltage spike from a pulse generator excited the sending transducer and the time of flight to the receiving transducer was measured using a digital oscilloscope.

Errors in velocity measurement mainly arise from the following two sources: (1) Errors in measuring minicore length and travel time. Core lengths are accurate to 0.005 cm and travel time to 2.5 nanoseconds. (2) Changes in minicore length at elevated confining pressure. No corrections were made for this effect in the present study because it is significant only at extremely high pressures. The absolute error associated with the pulse transmission technique is generally regarded to be 0.5% for V_p and 1% for V_s (Christensen, 1985; Ji et al., 1993; Ji and Salisbury, 1993; Kern et al., 1999, 2002).

2.5 Results and discussion

2.5.1 Velocity hysteresis and velocity-pressure relationships

In order to characterize the seismic hysteresis, velocity measurements of each cylindrical sample were performed both during pressurization and then depressurization for each run. Typical P- and S-wave velocities measured during a cycle of pressurization and subsequent depressurization are shown in Figs. 2.4 and 2.5, respectively, for fine-grained granite (LM2), gabbroic diorite (LM4), and coarse-grained granites (LM5 and LM6). Three V_p measurements (along the X, Y, and Z directions) and six V_s measurements (with geometric configurations XY, XZ, YX, YZ, ZX and ZY, where the first letter refers to the propagation direction and the second to the polarization direction) were performed for each sample with three orthogonal minicores.

Due to the presence of seismic velocity hysteresis (Birch, 1960; Gardner et al., 1965; Ji et al., 2007a), the depressurization curve consistently lies on or above the pressurization curve in the pressure range of 10-800 MPa (Figs. 2.4-2.5). The magnitude of the hysteresis (H in km/s) is defined as the velocity difference between depressurization and pressurization at each given pressure. $H \approx 0$ in the perfectly linear-elastic regime (i.e., nonporous or crack-free material) while $H > 0$ in the nonlinear poro-elastic regime (porous or microcrack-bearing material). It is found that the progressive decrease in H with increasing pressure can be well described by the following equation:

$$H(P) = H_0 \exp(-mP) \qquad (2.1)$$

where H_0 is the velocity hysteresis at $P=0$, and m is a positive number called the decay constant (MPa^{-1}). Equation (2.1) possesses the same form of the equation that is commonly used to describe natural phenomena such as radioactive decay, heat diffusion, and vibration attenuation because they decrease at a rate proportional to their values.

H_0 and m values for P-wave velocities are given in Table 2.3. Goodness-of-fit coefficients (R^2), which are statistical indicators of how well the measured data fit the empirical relation, are consistently higher than 0.95. For the samples from the Longmen Shan complex, H_0 varies from 0.245 km/s to 1.044 km/s with an average value of 0.521 km/s whereas m varies in the range from 0.72×10^{-2} MPa^{-1} to 1.82×10^{-2} MPa^{-1} with a mean value of 1.23×10^{-2} MPa^{-1}. Seismic hysteresis, which has been systematically observed in porous or microcrack-bearing materials (Birch, 1960; Gardner et al., 1965; Holcomb, 1981; Guyer and Johnson, 1999), is caused by three main possible mechanisms: irreversible closure of microcracks or the effect of so-called crack lips adhesion, irreversible compaction of pore spaces, and improvement of contact conditions (Burke and Fountain, 1990; Burlini and Kunze, 2000; Ji et al., 1993, 2007a). However, the details of the physical mechanisms and potential implications for earthquake forecasting have not been made clear.

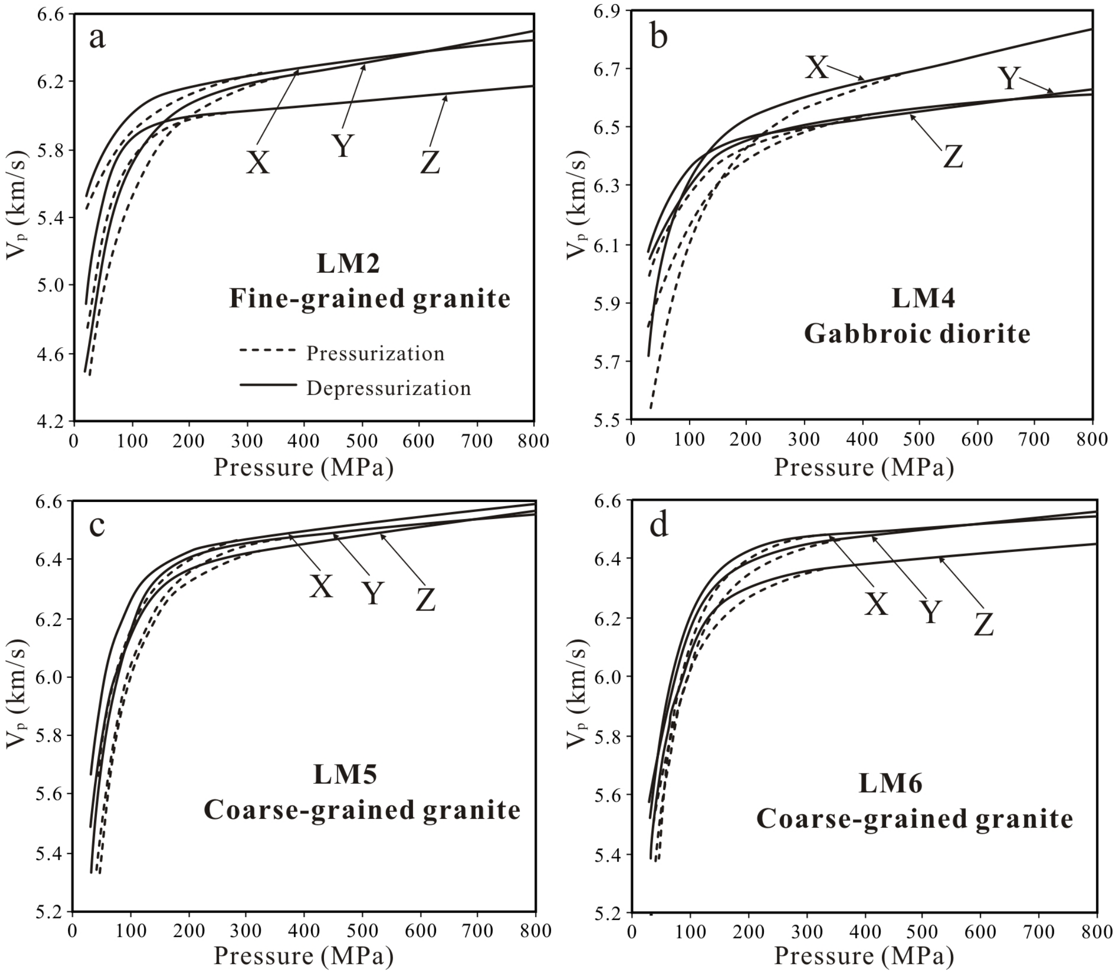

Figure 2.4 P-wave velocities (V_p) versus pressure in three orthogonal directions through samples LM2 (a), LM4 (b), LM5 (c) and LM6 (d).

S-wave velocity hysteresis (Fig. 2.5) was not analyzed according to Eq. (2.1) because S-wave velocities were measured after each sample had been pressurized and subsequently depressurized for the determination of P-wave velocities and their hysteresis. The first pressurization-depressurization cycle in the laboratory should modify both the number and aspect-ratio spectra of microcracks within each minicore sample. Previous experiments on the variation of seismic hysteresis during successive pressurization-depressurization cycles showed that the hysteresis loop did not stabilize after one or two pressurization-depressurization cycles or reached an equilibrium value for an imposed confining pressure (Ji et al., 2007a). Thus, both the velocities and the hysteresis are sensitive to the state of microcracks in the sample below the critical pressure for closing microcracks.

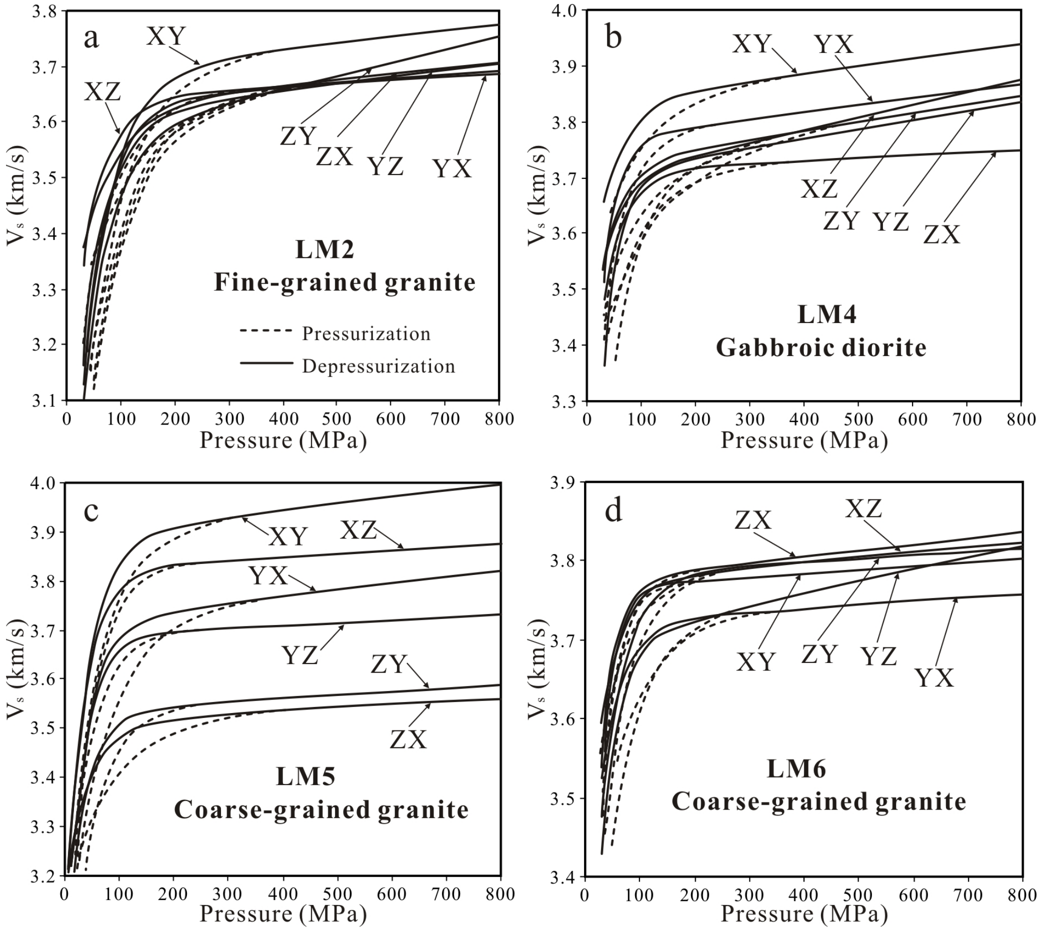

Figure 2.5 S-wave velocities (V_S) versus propagation and polarization directions in samples LM2 (a), LM4 (b), LM5 (c) and LM6 (d) as a function of pressure. The first letter signifies the propagation direction and the second letter the polarization direction.

In the following, only the velocity values measured during depressurization will be analyzed because they correspond to the more stable microstructural state (e.g., Burke and Fountain, 1990; Ji et al., 2007a). For all the samples studied, both P- and S-wave velocity curves display a rapid, non-linear increase with pressure at low pressures (generally <200-300 MPa) and then increase slowly in velocity at high pressures (Figs. 2.4-2.5). The transition from the non-linear regime to the linear regime is caused by the closure of microcracks in samples with increasing hydrostatic pressure (Birch, 1960; Christensen, 1965; Ji et al., 1993; Kern et al, 2001).

Both P- and S-wave velocities as a function of confining pressure were fitted by the following equation (e.g., Zimmerman et al., 1986; Greenfield and Graham, 1996; Ji et al., 2007a):

$$V(P) = V_0 + DP - B_0 \exp(-kP) \qquad (2.2)$$

where V_0 is the reference velocity representing the intrinsic velocity of the non-porous or crack-free compacted rock at zero pressure, which is determined by extrapolating the linear velocity-pressure relationship obtained at high pressures to zero pressure; D is the intrinsic pressure derivative of velocity in the linear elastic regime; B_0, which is the ambient velocity drop caused by the presence of pores/microcracks at zero pressure, determines the maximum magnitude of the velocity increases due to the closure of pores and microcracks; and k, which is the decay constant of the velocity drop, controls the shape of the nonlinear segment of the velocity-pressure curve (Fig. 2.6; Ji et al., 2007a).

Parameters V_0, D, B_0 and k determined for the P- and S-wave velocities of each minicore sample during depressurization, using a least square regression method, are given in Tables 2.3 and 2.4, respectively. As indicated by the goodness-of-fit coefficients (mostly $R^2 \geq 0.95$), the velocity-pressure curves for P- and S-waves can be well fitted by Eq. (2.2).

When the pressure is higher than a critical value (P_c), the rock sample can be regarded as a nearly crack-free aggregate and the seismic velocities increase almost linearly with increasing pressure. The critical pressure to fully close the microcracks and pores in the rock depends on the k value. If $\exp(-kP) \leq 1\%$, the $B_0\exp(-kP)$ value becomes very small. Thus, P_c can be estimated from the equation below:

$$P_c = -\frac{\ln 0.01}{k} \approx \frac{4.605}{k} \tag{2.3}$$

As shown in Table 2.3, P_c values determined for the P-wave velocities of the samples from the Longmen Shan complex during depressurization vary from 132 to 370 MPa with an average value of 234 MPa, which corresponds to a depth of ~9 km. The discrepancy in P_c between sample and sample reflects the microcrack geometry, as a sample containing more spherical pores has a high P_c value than the same sample but containing flatter cracks (Walsh, 1965; Sneddon and Lowengrub, 1969; Ji et al., 2007a).

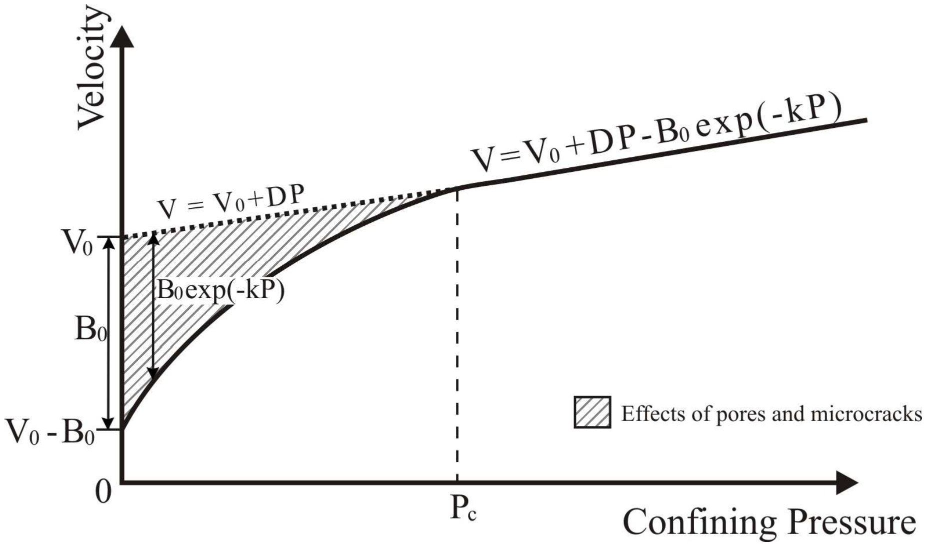

Figure 2.6 Physical significance of the parameters in Equation (2.2). Each parameter is defined in the text. Effects of microcracks/pores on the velocity occur in the shadowed area.

2.5.2 Seismic properties of equivalently isotropic rocks

Natural rocks can be elastically anisotropic due to the presence of compositional layering (e.g., Postma, 1955; Crampin, 1970), lattice preferred orientation (LPO), shape preferred orientation (i.e., foliation and lineation) of rock-forming minerals (e.g., Ji et al., 1993; Ji and Salisbury, 1993; Meissner et al., 2006) and alignment of intragranular and intergranular microcracks (e.g., Crampin and Peacock, 2008). However, the arithmetic means of the V_p and V_s values measured from various directions from each sample, which can also be well fitted by Eq. (2.2) (Tables 2.3 and 2.4), give values very close to those of true isotropic rocks, even in highly anisotropic rocks (Christensen and Ramananantoandro, 1971; Ji et al., 2003; Wang and Ji, 2009).

Table 2.3 Parameters of V_p hysteresis and V_p-pressure curves measured during depressurization for samples from the Longmen Shan complex, China.

Sample	Lithology	Λ*	Density	V_0	D	B_0	k	R^2	P_c	H_0	m
			(g/cm^3)	(km/s)	(10^{-4} km/s/MPa)	(km/s)	(10^{-2} MPa^{-1})		MPa	(km/s)	(10^{-2} MPa^{-1})
LM1	Folded, sheared, monzonitic mylonite	Y	2.73	6.124	6.408	1.846	2.099	0.99	219.4	0.336	1.28
		Y	2.71	6.204	5.001	2.358	2.422	0.99	190.1	0.364	1.30
		Mean	2.72	6.164	5.705	2.102	2.260	0.99	203.7	0.350	1.29
LM2	Fine-grained granite	X	2.62	6.118	4.073	0.868	1.768	0.99	260.5	0.281	0.85
		Y	2.62	6.002	6.191	2.209	1.806	0.99	255.0	0.422	0.88
		Z	2.62	5.938	2.892	1.917	2.957	0.99	155.7	0.603	1.60
		Mean	2.62	6.019	4.385	1.665	2.177	0.99	211.5	0.435	1.11
LM3	Moderate-grained granodiorite	A	2.64	5.815	2.772	0.611	1.692	0.99	272.1	0.299	0.72
		B	2.66	6.432	0.449	1.790	1.433	0.99	321.3	0.398	0.78
		Mean	2.65	6.123	1.610	1.200	1.563	0.99	294.7	0.348	0.75
LM4	Gabbroic diorite	X	2.86	6.461	4.684	1.373	1.957	0.99	235.3	0.639	0.97
		Y	2.83	6.433	2.463	0.667	1.882	0.99	244.7	0.245	0.99
		Z	2.83	6.468	1.849	0.616	1.244	0.99	370.1	0.277	0.72
		Mean	2.84	6.454	2.999	0.885	1.694	0.99	271.8	0.387	0.89
LM5	Coarse-grained granite	X	2.63	6.399	2.371	1.422	2.165	0.99	212.7	0.441	1.42
		Y	2.63	6.401	1.960	1.996	2.063	0.97	223.2	0.595	1.26
		Z	2.63	6.335	2.900	1.520	1.909	0.99	241.3	0.670	1.56
		Mean	2.63	6.379	2.410	1.646	2.045	0.98	225.1	0.568	1.41
LM6	Coarse-grained granite	X	2.64	6.441	1.296	1.642	1.867	0.99	246.6	0.640	1.67
		Y	2.64	6.399	1.961	1.417	1.731	0.99	266.0	0.391	1.08
		Z	2.64	6.300	1.913	1.715	1.997	0.99	230.6	0.388	1.28
		Mean	2.64	6.380	1.723	1.591	1.865	0.99	246.9	0.473	1.34
LM7a	Granite	A	2.62	6.238	1.709	2.369	2.772	0.99	166.1	0.648	1.64
LM7c	Granite	A	2.63	6.286	1.244	1.944	2.244	0.99	205.2	1.044	1.82
		X	2.62	6.293	2.261	1.360	2.005	1.00	229.7	0.574	1.03
		Mean	2.62	6.289	1.753	1.652	2.124	1.00	216.8	0.809	1.43
LM8	Granite	A	2.64	6.166	1.959	1.776	2.288	1.00	201.2	0.618	1.42
		B	2.62	6.094	2.094	1.839	3.482	0.98	132.3	1.016	1.69
		Mean	2.63	6.130	2.026	1.807	2.885	0.99	159.6	0.817	1.56
LMX5	Meta-andesite	A	2.81	6.231	3.271	1.465	1.782	0.99	258.4	0.525	0.96
LMX19	Granite	A	2.66	5.994	6.207	1.828	1.807	1.00	254.9	0.679	1.16
LMX23	Hbl-Cpx granodiorite	A	2.77	6.552	0.811	1.290	2.140	0.98	215.2	0.415	1.31

* Direction of wave propagation

Table 2.4 Parameters of V_S-pressure curves measured during depressurization for samples from the Longmen Shan complex, China

Sample	**Lithology**	**Λ***	**Density** (g/cm^3)	**V_0** (km/s)	**D** (10^{-4} km/s/MPa)	**B_0** (km/s)	**k** (10^{-2} MPa^{-1})	**R^2**
LM1	Folded, sheared, monzonitic mylonite	YX	2.73	3.665	1.593	0.609	1.967	0.98
		YZ	2.73	3.462	3.650	0.671	1.571	1.00
		YX	2.71	3.636	2.526	0.745	2.811	0.99
		YZ	2.71	3.560	2.423	0.638	1.503	1.00
		Mean	2.72	3.581	2.548	0.666	1.963	0.99
LM2	Fine-grained granite	XY	2.62	3.682	1.161	1.004	1.792	1.00
		XZ	2.62	3.637	0.677	0.568	2.133	0.99
		YX	2.62	3.634	0.660	1.030	2.171	0.95
		YZ	2.62	3.602	1.317	0.864	2.143	0.99
		ZX	2.62	3.625	1.021	0.398	1.471	0.99
		ZY	2.62	3.560	2.436	0.904	2.069	0.98
		Mean	2.62	3.623	1.212	0.794	1.963	0.98
LM3	Moderate-grained granodiorite	A	2.64	3.425	1.228	0.684	2.790	0.99
		B	2.66	3.910	0.572	0.664	2.396	0.98
		Mean	2.65	3.667	0.900	0.674	2.593	0.99
LM4	Gabbroic diorite	XY	2.86	3.830	1.378	0.340	2.156	1.00
		XZ	2.86	3.692	2.302	0.385	2.915	1.00
		YX	2.83	3.766	1.252	0.788	3.640	1.00
		YZ	2.83	3.703	1.677	0.931	3.138	0.99
		ZX	2.83	3.711	0.471	0.490	2.472	1.00
		ZY	2.83	3.719	1.592	0.367	2.441	0.99
		Mean	2.84	3.737	1.445	0.550	2.793	0.99
LM5	Coarse-grained granite	XY	2.63	3.885	1.398	0.832	2.547	0.99
		XZ	2.63	3.820	0.704	0.727	2.725	0.99
		YX	2.63	3.710	1.390	0.716	2.808	1.00
		YZ	2.63	3.685	0.586	0.724	3.081	0.98
		ZX	2.63	3.509	0.652	0.360	2.313	0.99
		ZY	2.63	3.534	0.678	0.566	2.830	0.98
		Mean	2.63	3.691	0.901	0.654	2.717	0.99
LM6	Coarse-grained granite	XY	2.64	3.770	0.839	0.747	3.831	1.00
		XZ	2.64	3.779	0.459	0.606	2.289	0.98
		YX	2.64	3.720	0.469	0.415	2.476	0.98
		YZ	2.64	3.697	1.515	0.730	3.153	0.99
		ZX	2.64	3.763	0.505	0.909	4.140	0.97
		ZY	2.64	3.772	0.612	0.395	2.618	1.00
		Mean	2.64	3.750	0.733	0.634	3.084	0.99
LM7a	Granite	A	2.62	3.665	0.572	0.607	2.915	0.99
LM7c	Granite	A	2.63	3.722	0.555	0.780	2.142	0.96
		B	2.63	3.592	0.603	0.723	2.601	1.00
		XY	2.62	3.695	0.811	0.885	3.026	0.98
		XZ	2.62	3.582	0.487	0.367	2.473	0.99
		Mean	2.62	3.648	0.614	0.689	2.561	0.98
LM8	Granite	A	2.64	3.621	1.676	0.780	2.334	1.00
		B	2.62	3.523	1.220	0.640	2.257	0.99
		Mean	2.63	3.572	1.448	0.710	2.295	0.99
LMX5	Meta-andesite	A	2.81	3.604	2.454	0.448	1.682	0.98
LMX19	Granite	A	2.66	3.658	4.772	0.877	1.743	0.99
LMX23	Hbl-Cpx granodiorite	A	2.77	3.825	0.844	0.718	2.199	1.00

* Directions of S-wave propagation and polarization

Figure 2.7 illustrates the variations in mean V_p and V_s as functions of density (a-b) and SiO_2 content (c-d) for felsic rocks (i.e., granite, granodiorite, and diorite and quartzofeldspathic gneisss) from the Longmen Shan complex (solid dots) and the other regions (open dots) compiled in Handbook of Seismic Properties of Minerals, Rocks and Ores (Ji et al., 2002) at a hydrostatic confining pressure of 600 MPa. At such a high pressure, the effect of microcracks is eliminated and the velocities correspond to the intrinsic properties controlled only by the modal composition and LPO of the rocks. In the range of density (2.55-2.90 g/cm^3) and SiO_2 content (50-80 wt.%), the V_p and V_s vary between 6.0-6.8 km/s and 3.4-4.0 km/s, respectively, but display little correlation with either density or SiO_2 content. This reflects the fact that K-feldspar, Na-plagioclase and quartz, which are abundant rocking-forming minerals of felsic rocks, have small differences in either seismic velocities or density: ρ=2.65 g/cm^3, V_p=6.06 km/s and V_s=4.09 km/s for quartz, ρ=2.55-2.63 g/cm^3, V_p=5.91 km/s and V_s=3.25 km/s for perthite, ρ=2.63 g/cm^3, V_p=6.07 km/s and V_s=3.40 km/s for An9 (Christensen, 1989).

2.5.3 Microcrack-related seismic anisotropy

Above the critical pressure (P_c), the rocks are considered as non-porous or crack-free compacted aggregates, the seismic anisotropy are mainly related to the intrinsic properties, such as LPOs of highly anisotropic minerals (e.g., amphibole, mica, and feldspar) and compositional layering. Below P_c (~200-300 MPa), seismic anisotropy is caused by constructive or destructive interference of the effects resulting from oriented microcracks and LPOs of anisotropic minerals (Kern and Wenk, 1990; Ji and Salisbury, 1993; Kern et al., 2001). The samples from the Longmen Shan complex show little V_p or V_s anisotropy at high pressures (Fig. 2.8), therefore, only the anisotropy behavior at low pressures will be discussed below, which are mainly caused by preferred orientations of microcracks.

It is well known that velocities of P-waves propagating across aligned cracks are much lower than those parallel to the cracks. With increasing pressure, microcracks with smaller aspect-ratios will close first and subsequently those with larger aspect-ratios. The variation in velocities and their directional dependence with increasing pressure can thus offer information about the preferred orientation of microcracks within the rocks. At pressures below P_c, the progressive closure of Z-normal (foliation-parallel) microcracks cause gradual increases in $V_p(Z)$

but little influence on $V_p(X)$ or $V_p(Y)$. Accordingly, the closing of Z-normal microcracks with increasing pressure would cause a rapid decrease in $V_p(X)-V_p(Z)$ and $V_p(Y)-V_p(Z)$, while the influence on $V_p(X)-V_p(Y)$ is almost negligible. The Y-normal microcracks occur along grain boundaries and commonly very flat with small ratios of aperture to length, are easily closed below ~100 MPa. The closing of Y-normal microcracks would result in a rapid decrease in $V_p(X)-V_p(Y)$, a rapid increase in $V_p(Y)-V_p(Z)$, and almost no change in $V_p(X)-V_p(Z)$. The X-normal microcracks are generally intragranular cracks (Ji et al., 1997b, 2003). Compared with Z-normal and Y-normal microcracks, the X-normal cracks are more difficult to be closed. With increasing pressure, the closing of X-normal microcracks would produce a rapid increase in $V_p(X)-V_p(Y)$ and $V_p(X)-V_p(Z)$ and a negligible effect on $V_p(Y)-V_p(Z)$.

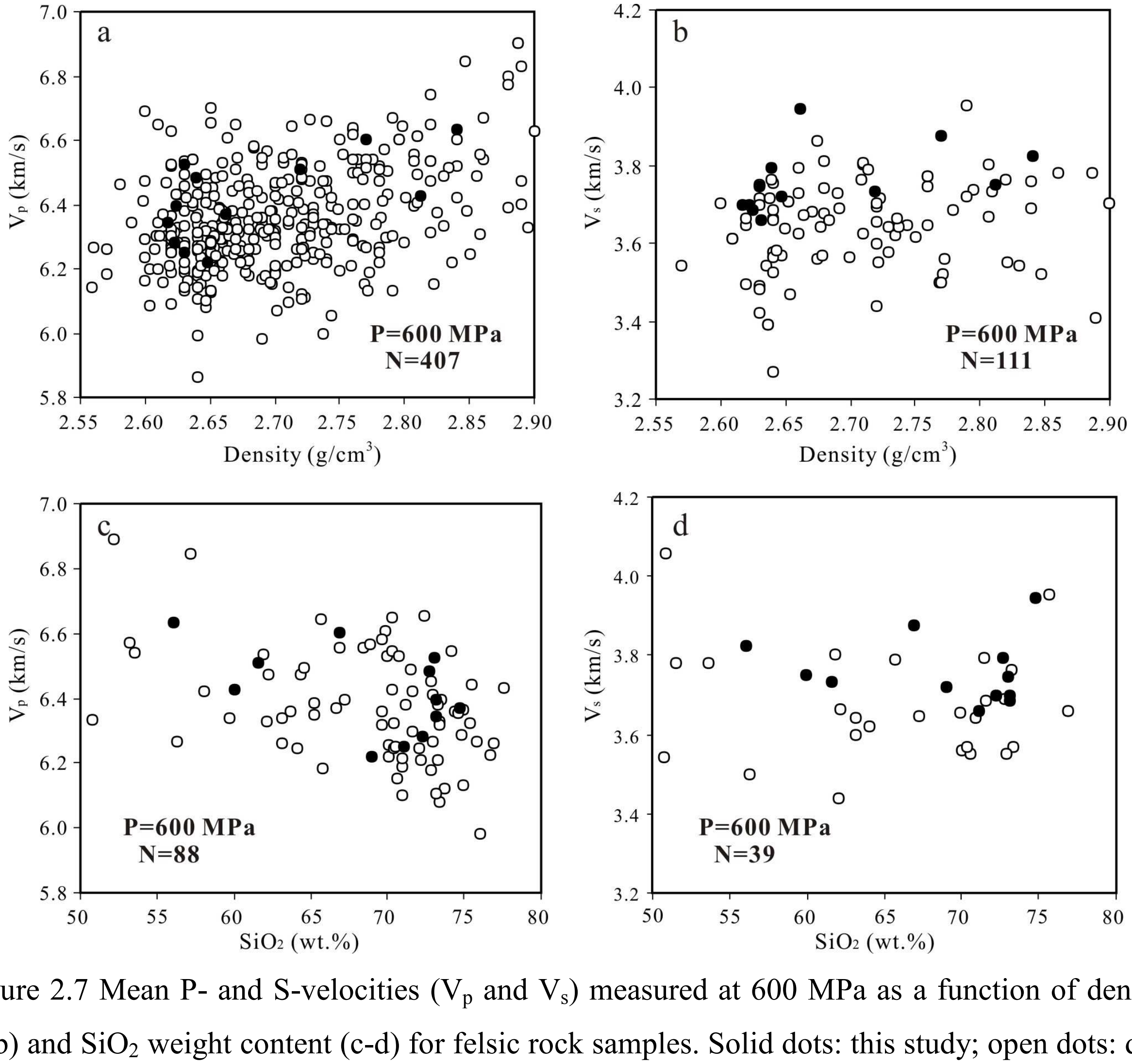

Figure 2.7 Mean P- and S-velocities (V_p and V_s) measured at 600 MPa as a function of density (a-b) and SiO_2 weight content (c-d) for felsic rock samples. Solid dots: this study; open dots: data compiled from Handbook of Seismic Properties of Minerals, Rocks and Ores (Ji et al., 2002).

Figure 2.8 shows some examples how the variations of values $V_p(X)$-$V_p(Y)$, $V_p(X)$-$V_p(Z)$ and $V_p(Y)$-$V_p(Z)$ with pressure provide some hints for the preferred orientation of microcracks in the low pressure regime. In fine-grained granite LM2 (Fig. 2.8a), the decrease of $V_p(X)$-$V_p(Y)$ and the increase of $V_p(Y)$-$V_p(Z)$ at pressures <~200 MPa suggest that the Y-normal microcracks are dominant over those perpendicular to the X-direction and particularly the Z-normal microcracks. For gabbroic diorite sample LM4 (Fig. 2.8b), the rapid increase in $V_p(X)$-$V_p(Z)$ and $V_p(X)$-$V_p(Y)$ and the little change in $V_p(Y)$-$V_p(Z)$ below ~200 MPa reveal the dominance of microcracks perpendicular to the lineation (X). In coarse-grained granite LM5 (Figs. 2.8c), the P-wave anisotropy is characterized by a decrease in $V_p(X)$-$V_p(Y)$, an increase in $V_p(Y)$-$V_p(Z)$ and almost unchanged $V_p(X)$-$V_p(Z)$. These characteristics can be easily explained by the predominance of Y-normal microcracks in this sample. In coarse-grained granite LM6 (Fig. 2.8d), both $V_p(Y)$-$V_p(Z)$ and $V_p(X)$-$V_p(Z)$ display a gradual decrease while $V_p(X)$-$V_p(Y)$ increases progressively with increasing pressure. Such a trend indicates the presence of both Z- and X-normal microcracks but the first are dominant over the latter.

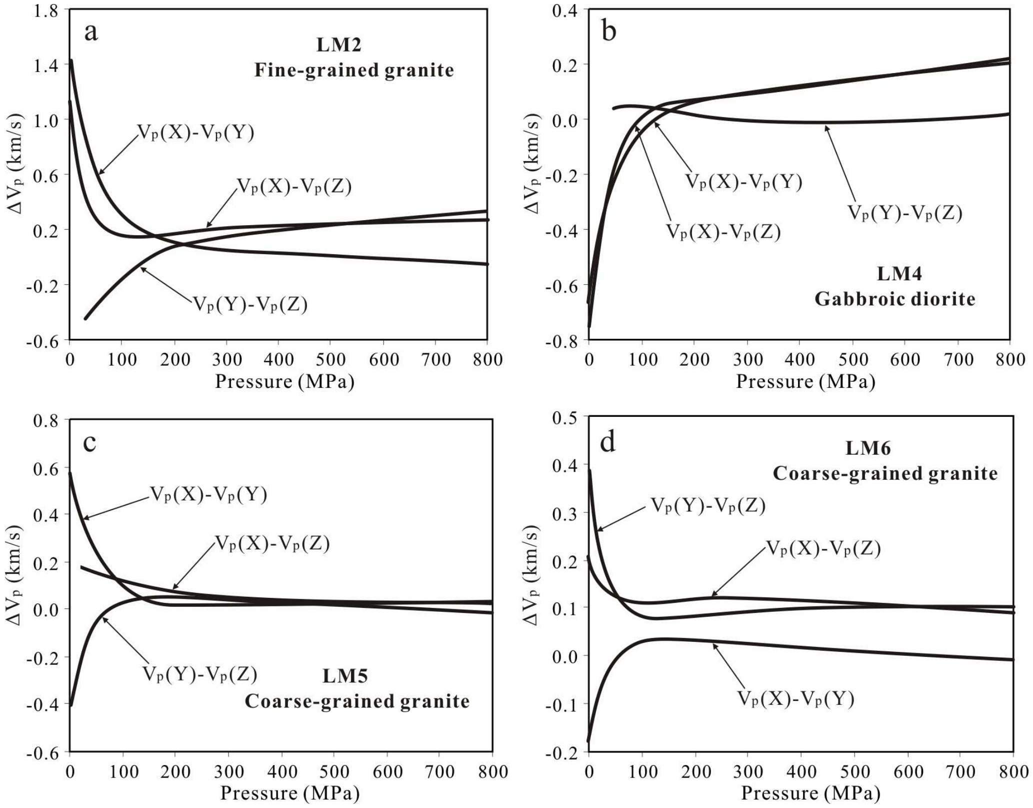

Figure 2.8 Differences in P-wave velocity (ΔV_p km/s) between different propagating directions as a function of pressure for samples LM2 (a), LM4 (b), LM5 (c) and LM6 (d).

2.5.4 Velocity model for the Longmen Shan complex

The laboratory data can be extrapolated to the in-situ P-T conditions according to the following equation:

$$V(z) = V_0 + DP(z) - B_0 \exp[-kP(z)] + (dV/dT)[T(z) - 20] \tag{2.4}$$

where z is the depth, dV/dT is the temperature derivative of velocity and P is the lithostatic pressure, equal to ρgz, where ρ is the average density of the overlying rocks from surface to depth z, and g is the acceleration of gravity. The density of the crust was assumed to be 2.685 g/cm^3, which is the average density of our rock samples from the Longmen Shan complex.

The temperature-depth profile of the Longmen Shan range is given in Fig. 2.9a with a surface heat flow value of 59.7 mW/m^2 (Hu et al., 2001; Xu et al., 2011; Zhong, Dalai, personal communication). The geothermal structure yields a reasonably depth of the brittle-ductile transition at ~19 km (342 °C, Fig. 2.9a), which corresponds to the focal depth of the 2008 Wenchuan mainshock (19.0 km, USGS, 2008; 18.8 km, Chen et al., 2009). This also coincides with the fact that most of the aftershocks are located above this depth (Zhu et al., 2008; Jia et al., 2010). At a typical strain-rate ($\dot{\varepsilon}$) of 10^{-13}/s for the eastern margin of the Tibet Plateau, quartz deforms in the brittle and ductile regimes below and above 342 °C, respectively (Scholz, 1990; Tullis, 1990). In the brittle deformation regime, the frictional strength (σ) of the rocks increases linearly with depth according to $\sigma = \mu_f \rho gz$, where μ_f is the friction coefficient and equal to 0.75 (Byerlee, 1978). In the ductile deformation regime, however, the flow strength of rocks deformed by dislocation creep is controlled by

$$\sigma = \left(\frac{\dot{\varepsilon}}{A}\right)^{1/n} \exp\left(\frac{Q}{nRT}\right) \tag{2.5}$$

where A is a constant, n is the stress exponent, Q is the activation energy, R is the gas constant (8.314 J/K/mol), and T is the temperature in Kelvin. For granite or felsic rock, A=2.0×10^{-6} MPa^{-n}/s, n=3.3 and Q=187 KJ/mol (Hansen and Carter, 1982). As illustrated in Fig. 2.10a, the 2008 Wenchuan mainshock nucleated at the depth of 19 km where highest shear stresses and highest strain energy capably occur and so large earthquakes are most likely initiated. The upper crust above 19 km is the seismogenic layer in the Longmen Shan region.

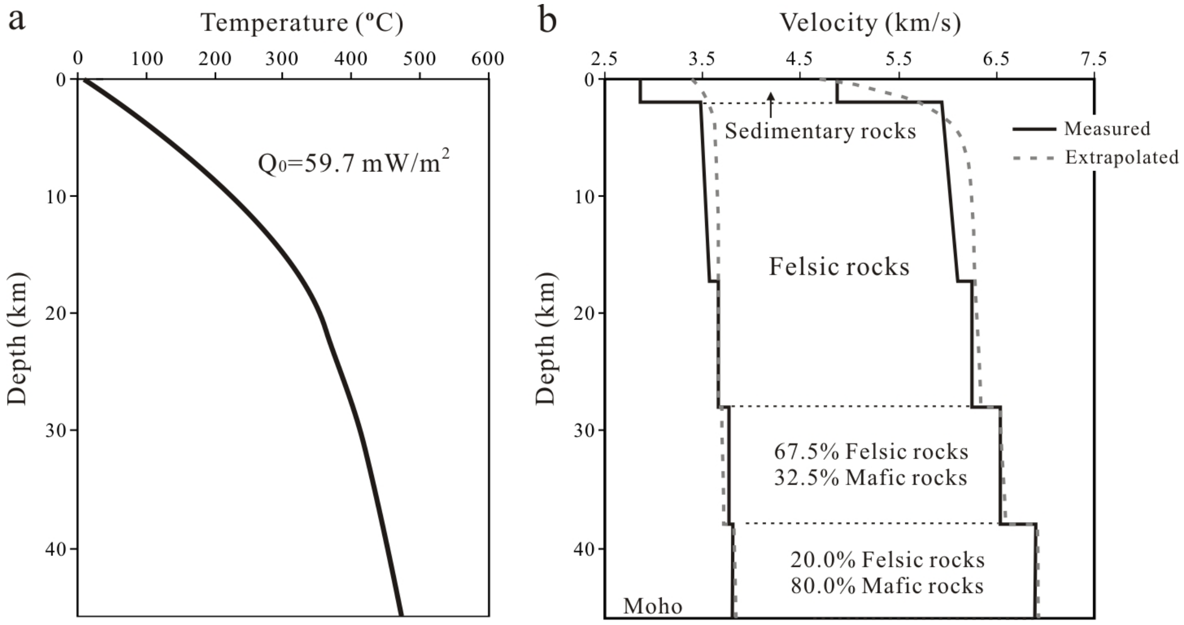

Figure 2.9 Temperature (a) and velocity (b) profiles for the Longmen Shan range. See the text for the comparison between the calculated (dashed line) and in-situ (solid line) P- and S-wave velocities at each depth.

The parameters of Eq. (2.4) for sedimentary rock, felsic rock, and mafic rock (i.e., gabbro-metagabbro-mafic gneiss) are listed in Table 2.5. Figures 2.10b-f illustrate calculated V_p, V_s, K (bulk modulus), E (Young's modulus) and μ (shear modulus) with depth up to 28 km for typical rocks from the Longmen Shan complex. In the uppermost crust (<10 km), the rapid increase of velocities or elastic moduli with depth reflects the closure of microcracks with increasing pressure while the effect of temperature is minor. Below this depth, the contribution of pressure to seismic velocities or elastic moduli is partially offset by the increase of temperature. All the rocks studied consistently display gently increasing velocities or elastic moduli with depth. At the focal depth of the Wenchuan mainshock (19 km), $\overline{V}_p$=6.29 km/s (6.11-6.51 km/s), $\overline{V}_s$=3.68 km/s (3.60-3.77 km/s), $\overline{K}$=57.8 GPa (52.0-63.0 GPa), $\overline{E}$= 90.1 GPa (86.2-95.1 GPa), and $\overline{\mu}$=36.3 GPa (34.8-38.1 GPa). The integral average μ value derived from Fig. 2.10f for the Longmen Shan complex will be used, in next section, to estimate the seismic moment magnitude of the 2008 Wenchuan mainshock. Because the strongest ground motions are generated mainly by shear- and surface-wave arrivals, the V_s data with depth (Fig. 2.10c) are important parameters for assessing and forecasting earthquake hazards for the whole Longmen Shan region and particularly the segment between Yingxiu and Kangding, capable of producing an M_w 7.7 earthquake in the next 50 years (Ji, 2009; Wang, Liu et al., 2010).

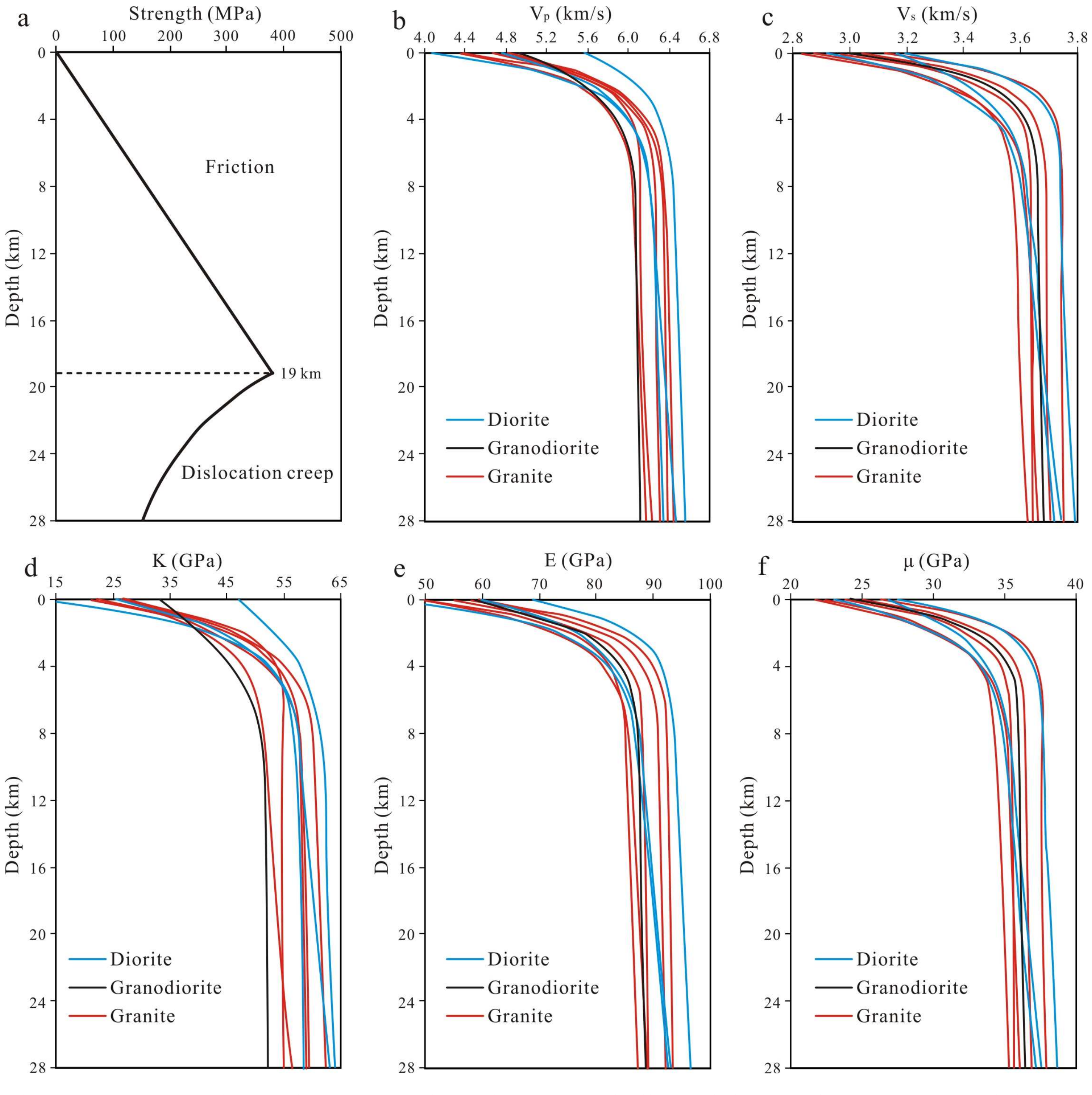

Figure 2.10 Strength envelope (a), and V_p (b), V_s (c), bulk modulus K (d), Young's modulus E (e), and shear modulus μ (f) as a function of depth for the upper crust (down to 28 km) represented by the rock samples from the Longmen Shan complex.

The crustal thickness in the region of the Longmen Shan range is ~46 km (Wang et al., 2007; Xu and Song, 2010), and the highest temperature in the crust is less than 500 °C (Fig. 2.9a) which is significantly lower than the melting point of dry or wet felsic rocks. Using multi-equilibrium calculations on white mica and chlorite, de Sigoyer et al. (2008) determined that T=350 °C at P=900-1000 MPa for the conditions of vein formation in the Pengguan complex. Their results yield an average geothermal gradient of ~10 °C/km, which is even lower than that given in Fig. 2.9a. Therefore, channel flow (Royden et al., 1997; Clark and Royden, 2000; Burchfiel et al., 2008), which requires partial melting and an extremely low viscosity of the rocks, is unlikely to occur beneath the Longmen Shan range.

Table 2.5 Average parameters of velocity-P and velocity-T relations for each lithologic category.

Category		**Density** (g/cm^3)	V_0 **(km/s)**	**D** $(10^{-4}$ **km/s/MPa)**	B_0 **(km/s)**	**k** $(10^{-2}\ MPa^{-1})$	**dV/dT** $(-10^{-4}\ km\ s^{-1}\ {}^{o}C^{-1})$
Cabonatic sandstone*	V_p	2.670	5.615	4.009	0.583	1.732	9.333
Felsic rocks**	V_p	2.685	6.241	2.876	1.557	2.044	2.990
Felsic rocks**	V_s	2.685	3.653	1.362	0.647	2.406	1.352
Gabbro/Metagabbro*	V_p	3.020	6.949	2.417	0.723	2.453	4.110

* Compiled from Handbook of Seismic Properties of Minerals, Rocks and Ores (Ji et al., 2002); ** this study

Previous seismic investigations (Zhao et al., 1997; Wang et al., 2003, 2007; Yang et al., 2004) reveal that the crust of the Longmen Shan range consists of 4 layers from the surface to the Moho: Layer 1: V_P<4.88 km/s (0-3 km thick); Layer 2: V_P=5.95-6.25 km/s (25-28 km thick); Layer 3: V_P=6.55 km/s (10 km thick); and Layer 4: V_P=6.90 km/s (8 km thick). Layer 1 represents the sedimentary rocks which are absent at the outcrops of the Longmen Shan complex. Layer 2 corresponds to felsic rocks of the Longmen Shan complex. The V_p and V_s values calculated from Eq. (2.4) display good agreements with the measured velocities (Wang et al., 2007) between 17-28 km, but are slightly higher than the in-situ measured values at depths shallower than 17 km. Above this depth, the rocks are deformed in the brittle regime and thus fractured in various scales and probably saturated with water, and thus display an obvious discrepancy in either P- or S-wave velocity with the dry samples under the laboratory conditions. Moreover, seismic properties measured in the field represent much larger volumes than those samples measured in the laboratory (Jahns et al., 1994; Huenges et al., 1997). This is so-called “scaling problems”. Larger volumes display certainly higher heterogeneity in either lithology or structure. In addition, not all of the rocks presented at the outcrops are satisfactory for laboratory high-pressure measurements and those selected are free of visible fractures and may thus not be representative of all of the rocks at depth.

Layers 3 and 4 cannot consist of monotonous lithology of either felsic or mafic rock because their velocities lie clearly between these two end-members. The Voigt-Reuss-Hill average (Hill, 1965) suggests that Layers 3 and 4 be mixtures composed of 67.5% felsic and 32.5% mafic components, and 20.0% felsic and 80.0% mafic rocks, respectively. These compositional models satisfy in-situ seismic data for these layers (Fig. 2.9b). The V_p and V_s models inferred from our experimental data (Fig. 2.9b) yield an average V_p/V_s ratio of 1.71 or Poisson's ratio of 0.24 for the whole crust beneath the Longmen Shan range, which is consistent with the data measured using teleseismic receiver function techniques (Ji et al., 2009; Wang et al., 2010). All the data indicate the dominance of felsic composition in the Longmen Shan crust.

2.6 Seismic moment magnitude of the great Wenchuan earthquake

The 2008 Wenchuan earthquake provided a rare opportunity for accurate quantification of seismic moment (M_0) in terms of the fault geometry and coseismic displacement. While magnitude is a convenient way of measuring earthquake size from seismographic data, M_0 is a more physically meaningful measurement of earthquake size (Ji, 2008; Koketsu et al., 2009; Zhang et al., 2009; Nakamura et al., 2010).

The seismic moment of the Wenchuan earthquake is computed from the following equation:

$$M_0 = \int_0^{Z_f} \mu_i s_i d_i \qquad (2.6)$$

where Z_f is the depth to which the fault can propagate dynamically, μ is the shear modulus of fault rocks, and *s* and *d* are the area and average displacement of each fault at a given depth. The subscript *i*=1 for the Yingxiu-Beichuan fault, and *i*=2 for the Guanxian-Anxian fault, respectively. The Yingxiu-Beichuan fault developed fully in the Longmen Shan complex with an integral averaging shear modulus of 35.0 GPa while the Guanxian-Anxian fault cuts through the Longmen Shan complex and the sedimentary rocks (limestone, sandstone, mudstone and shale) below and above a depth of ~4 km. The shear modulus is taken as 26.1 GPa for the upper portion of the Guanxian-Anxian fault, which is obtained from averaging of 90 measurements for sedimentary rocks (Fig. 2.11).

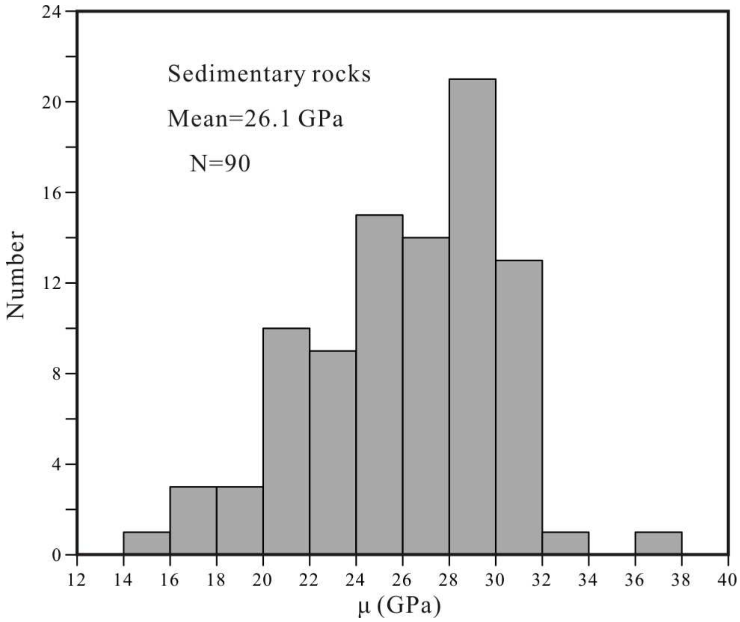

Figure 2.11 Histogram showing the distribution of shear moduli (μ) for 90 sedimentary rocks (i.e., limestone, sandstone and conglomerate). Data compiled from Handbook of Seismic Properties of Minerals, Rocks and Ores (Ji et al., 2002).

Figures 2.12a-b illustrate the histograms of coseismic displacements produced by the Wenchuan earthquake along the Yingxiu-Beichuan and Guanxian-Anxian faults. The data were compiled from Xu et al. (2008), Li et al. (2008), Dong et al. (2008), Ji et al. (2008), Xu et al. (2009), Liu-Zeng et al. (2009). Lin et al. (2009, 2010), Li et al. (2010). The coseismic slips along the Yingxiu-Beichuan fault vary in the range 1-7 m with a mean value of 2.75 m. The coseismic displacements along the Guanxian-Anxian fault, however, are relatively smaller, and vary in the range of 0.5-4.5 m with an average value of 1.30 m.

Field investigations reveal that the total lengths of coseismic ruptures along the Yingxiu-Beichuan and Guanxian-Anxian faults are 240 km and 72 km, respectively (Xu et al., 2008; Li et al., 2008; Dong et al., 2008; Ji et al., 2008; Xu et al., 2009; Liu-Zeng et al., 2009; Lin et al., 2009, 2010; Li et al., 2010).

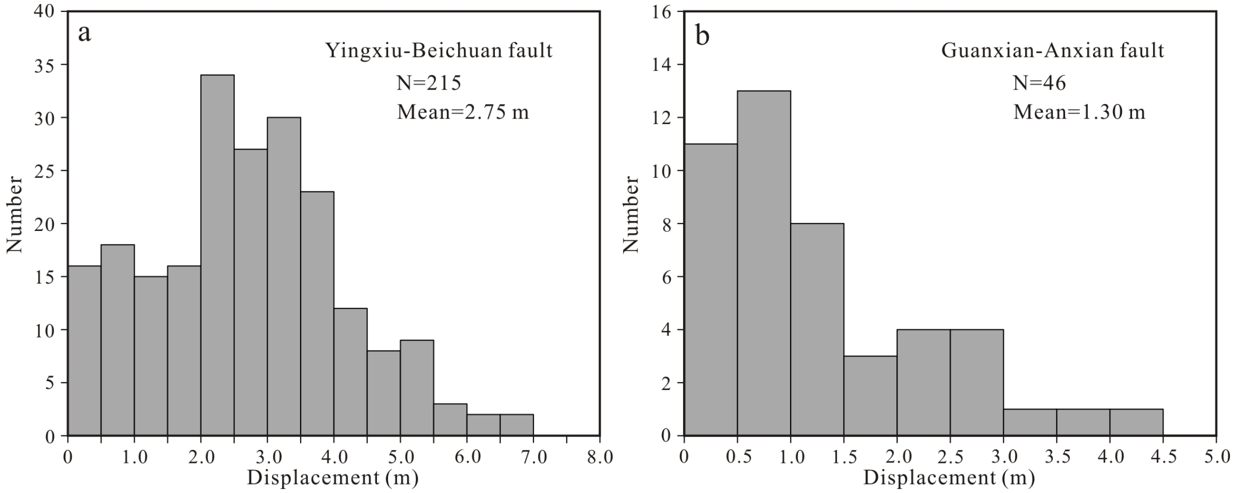

Figure 2.12 Histograms illustrating coseismic displacements produced by the 12 May 2008 Wenchuan mainshock along the Yingxiu-Beichuan fault (a) and the Guanxian-Anxian fault (b). Data compiled from Xu et al. (2008), Li et al. (2008), Dong et al. (2008), Ji et al. (2008), Xu et al. (2009), Liu-Zeng et al. (2009), Lin et al. (2009, 2010), Li et al. (2010).

The geometrical information of the coseismic ruptures is schematically illustrated in Fig. 2.13. To a first approximation, the fault planes are assumed to be rectangular. The areas of the coseismic ruptures (*s*) in the Yingxiu-Beichuan and Guanxian-Anxian fault zones, which are separated by a horizontal distance (*W*) of 12 km on the surface and join together at the depth of 8 km, are given by:

$$s_1 = L_1 \times (Z_0 + \Delta Z) / \sin\theta \tag{2.7}$$

$$s_2 = L_2 \times [z^2 + (z\cot\theta + W)^2]^{0.5} \tag{2.8}$$

where L_1 and L_2 are the lengths of coseismic ruptures along the Yingxiu-Beichuan and Guanxian-Anxian faults and equal to 240 km and 72 km, respectively; Z_0 is the focal depth which is taken as 19 km (USGS, 2008); ΔZ is the depth to which the coseismic rupture propagated downwards below the focal depth until dynamic rupture ceases at certain final perimeter (Das, 1982; Tse and Rice, 1986); z is the depth at which these two faults join together; θ is the dip of the Yingxiu-Beichuan fault, which was estimated from the three dimensional distribution of aftershocks to be 28-38° for the southwestern segment between Yingxiu and Beichuan, and 58° for the northeastern portion between Beichuan and Qingchuan. The focal mechanism results yielded *θ*=33º (Harvard University, 2008) and 32º (Wang et al., 2008) at the depth of mainshock hypocenter. As shown by Eqs. (2.7)-(2.8), the downdip width of the coseismic rupture increases with decreasing *θ* and increasing ΔZ. The bottom of the rupture zone of the mainshock is limited by $Z_0+\Delta Z$. The region between the depth of mainshock hypocenter (Z_0) and $Z_0+\Delta Z$ is of alternating behavior with coseismic dynamic slip and interseismic semibrittle flow. Geological evidence that has been found from the Wenchuan Fault Scientific Drilling (WFSD) core samples and surface outcrops for such an exhumed transitional zone includes greenschist-facies mylonites interlaced with pseudotachylytes and breccias.

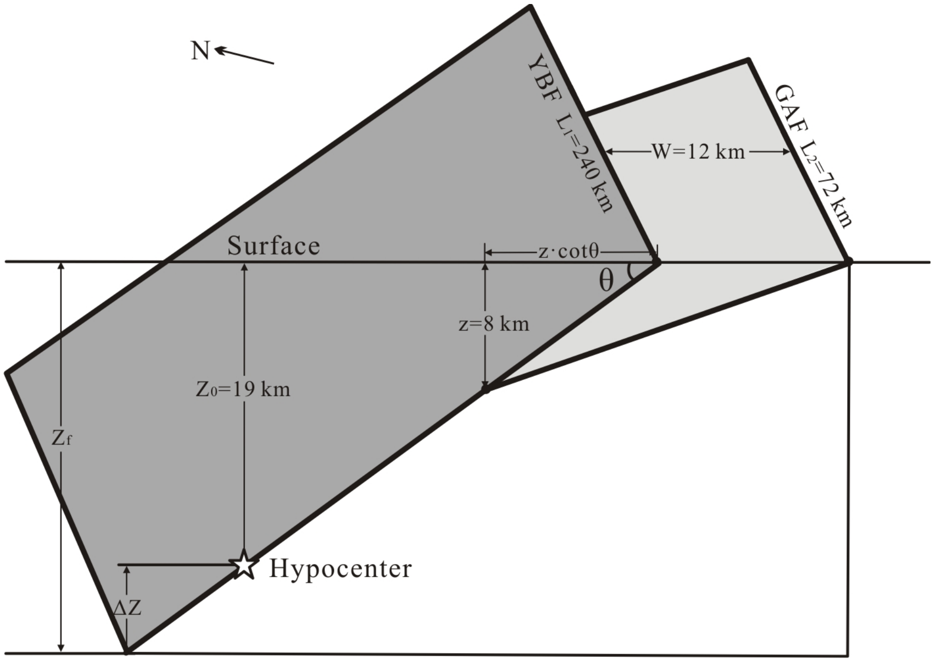

Figure 2.13 Geometrical information of the coseismic ruptures produced by the 12 May 2008 Wenchuan mainshock in the Longmen Shan crust. YBF: Yingxiu-Beichuan fault; GAF: Guanxian-Anxian fault. Other letters are defined in the text.

The moment magnitude (M_w), which has important advantages over other magnitude scales because it does not saturate for large earthquakes, is calculated from the following equation:

$$M_w = \frac{2}{3}\log_{10} M_0 - 6.03 \qquad (2.9)$$

where M_0 is in N·m. Figure 2.14 shows M_w as functions of ΔZ and *θ* (the dip of the southwestern segment of the Yingxiu-Beichuan fault). If ΔZ=0, M_w=7.93 when θ=28°, while

M_w=7.87 when θ=38°. If ΔZ=3 km, however, M_w=7.96 when θ=28°, whereas M_w=7.91 when θ=38°. The results agree with the estimates of Zhang et al. (2009, $M_0=0.94\times10^{21}$ N·m, M_w=7.95), Koketsu et al. (2009, $M_0=1.00\times10^{21}$ N·m, M_w=7.97), Wang et al. (2008, $M_0=1.04\times10^{21}$ N·m, M_w=7.98), Ji (2008, $M_0=1.15\times10^{21}$ N·m, M_w=8.01), and Nakamura et al. (2010, $M_0=1.20\times10^{21}$ N·m, M_w=8.02) based on joint inversions of teleseismic and strong motion data. Hence, this study, which yields a moment magnitude of 7.9-8.0 given the variation in the dip of the coseismic ruptures and the uncertainty in the depth to which the coseismic rupture may propagate downwards below the depth of the mainshock hypocenter, presents the first accurate quantification of the 2008 Wenchuan earthquake's size.

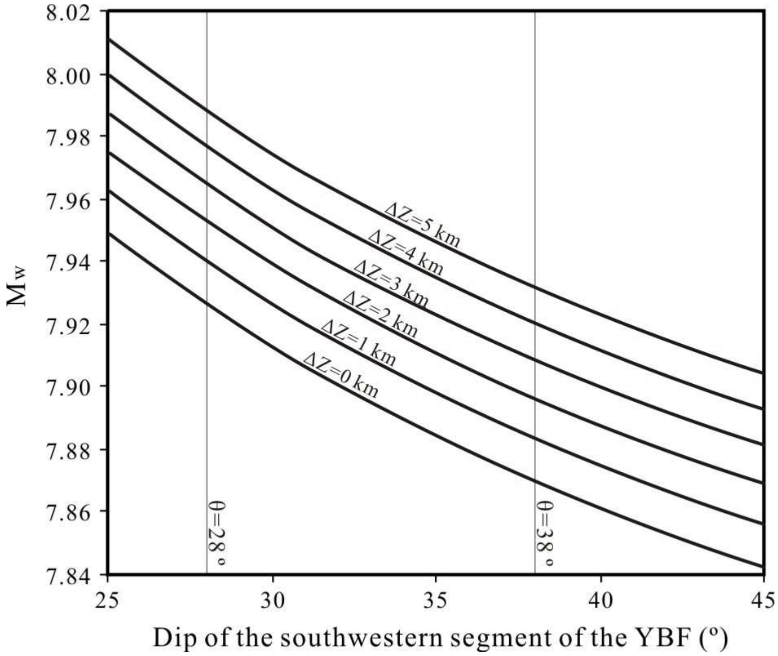

Figure 2.14 The seismic moment magnitude (M_w) as a function of the dip (θ) of the southwestern segment of the Yingxiu-Beichuan fault (YBF) and the depth to which the coseismic rupture may propagate downwards below the depth of the mainshock hypocenter (ΔZ). The dip of the northeastern segment of the Yingxiu-Beichuan fault is fixed to 58°.

2.7 Conclusions

Both P- and S-wave velocities (V_p and V_s) have been measured, at hydrostatic confining pressure up to 800 MPa, for 12 representative samples from the Longmen Shan complex in which the 12 May 2008 Wenchuan earthquake took place and its coseismic ruptures nucleated and propagated. The felsic rock samples show little V_p or V_s anisotropy at pressures above the microcrack-closure pressure (P_c=200-300 MPa), and thus the variation of anisotropy with pressure can be used to constrain the preferred orientation of microcracks in the nonlinear poroelastic regime below P_c. The calculated geothermal and rheological profiles indicate that the depth of the mainshock hypocenter (~19 km) corresponds to the base of the schizosphere, below which the Longmen Shan complex switches from the brittle to ductile behaviour. The comparison of experimental data with in-situ previous seismic data reveals that the crust of the Longmen Shan range consists of 4 layers from the surface to the Moho: Layer 1: V_p<4.88 km/s (0-3 km thick, sedimentary rocks such as limestone, sandstone, conglomerate, and mudstone); Layer 2: V_p=5.95-6.25 km/s (25-28 km thick, felsic rocks equivalent to the Longmen Shan complex); Layer 3: V_p=6.55 km/s (10 km thick, 67.5% felsic and 32.5% mafic rocks); and Layer 4: V_p=6.90 km/s (8 km thick, 20.0% felsic and 80.0% mafic rocks). The average V_p/V_s ratio of 1.71 or Poisson's ratio of 0.24 calculated for the whole crust is consistent with the results measured using teleseismic receiver function techniques. Considering the crustal structure, surface heat flow (59.7 mW/m^2), and thickness of the schizosphere, the highest temperature in the crust above the Moho at 46 km is less than ~500 °C which is significantly lower than the melting point of dry or wet felsic rocks. Therefore, channel flow, which requires partial melting and an extremely low viscosity of the rocks, is unlikely to occur beneath the Longmen Shan range. The average seismic velocities and elastic moduli as a function of depth offer prerequisite information for broadband simulations of strong ground motions in the assessment and forecast of earthquake hazards in the region. Furthermore, this study, which yields a moment magnitude of 7.9-8.0 given the variation in the dip of the coseismic ruptures and the uncertainty in the depth to which the coseismic rupture may propagate downwards below the focal depth of the mainshock, presents the first accurate quantification of the 2008 Wenchuan earthquake's size.

CHAPTER 3 SEISMIC VELOCITIES AND ANISOTROPY OF CORE SAMPLES FROM THE CHINESE CONTINENTAL SCIENTIFIC DRILLING (CCSD) BOREHOLE IN THE SULU UHP TERRANE, EASTERN CHINA

3.1 Abstract

A detailed study of seismic properties (P- and S-wave velocities, hysteresis, anisotropy and shear wave splitting) has been carried out on a unique suite of deep borehole core samples from the Chinese Continental Scientific Drilling (CCSD) project, which penetrated 5158 m into the Sulu ultrahigh-pressure (UHP) metamorphic terrane (China). Seismic velocities of the deep core samples are respectively, more and less sensitive to pressure in the low pressure (<200-300 MPa) nonlinear and high pressure (>200-300 MPa) linear regimes, than samples from the surface. The comparison suggests that the high pressure data from the core samples are much more reliable for extrapolation to deeper crust than the data from surface analogues that have been subjected to long histories of weathering and alteration along intergranular and transgranular cracks. The significant increases in the pressure sensitivity of seismic velocities for the core samples in the nonlinear regime indicate that drilling-induced and stress-relief microcracks with small aspect ratios are fresh and clean without secondary mineral in-fillings, and are thus easy to close completely under the applied hydrostatic pressure conditions of the laboratory. The data also elucidate that the velocity-pressure data can successfully provide important hints about the preferred orientation of microcracks that causes P-wave velocity anisotropy and shear wave splitting in cracked rocks, and that the effect of compression on the V_p/V_s ratios is negligible for crack-free compacted rocks. The seismic velocities of equivalent isotropic (fabric-free) and crack-free crystalline aggregates calculated from room pressure single crystal elastic constants using the Voigt average are in agreement with the laboratory data at ~200 MPa. Comparison of the seismic reflection image from the vicinity of the borehole with the normal-incidence reflection coefficient profile computed from the laboratory-measured velocities and densities infers that the seismic reflections originate from mafic (eclogite and retrograde eclogite) or ultramafic units within dominantly felsic rocks.

3.2 Introduction

The interpretation of seismic data in terms of mineralogical and chemical compositions and physical state (e.g., partial melting) in the crust and upper mantle is usually made by comparison of in-situ seismic velocities with laboratory-measured properties of rock samples. A large number of laboratory measurements of seismic velocities and anisotropy have been performed on rock samples collected mainly from surface exposures in North America, Western Europe and Japan (Christensen, 1989; Ji et al., 2002). However, a basic question remains to be answered: Can the seismic properties of samples from surface exposures be reliably extrapolated to the Earth's interior if these samples have been long exposed to weathering and have experienced alteration along microcracks and grain boundaries? To answer this question it is critical to determine the seismic properties of unaltered rock samples from greater depths. Scientific drilling is probably the unique tool to provide such rock samples (Berckhemer et al., 1997; Kern et al., 2001). The Chinese Continental Scientific Drilling (CCSD) project, which drilled to a depth of 5158 meters into the ultrahigh pressure (UHP) metamorphic terrane in the Sulu region of central eastern China (Fig. 3.1), provides a complete suite of unaltered, rare UHP metamorphic rock samples for measurements of seismic properties (i.e., velocities, hysteresis, anisotropy and shear wave splitting) and densities and for petrographic and chemical analyses.

The finding of the Qinling-Dabie-Sulu UHP metamorphic terrane has been considered as one of the most important discoveries in solid Earth sciences during the last 30 years (e.g., Liou et al., 1998, 2000; Xu et al., 2009b). In this large (>1000 km long) unusual terrane, eclogite contains both diamond and coesite, and orthogneiss, paragneiss, quartzite and marble contain coesite, suggesting that supracrustal materials were subducted to depths greater than 100 km. A large number of investigations on petrologic, mineralogical, geochemical and geochronological properties of the UHP rocks during the last three decades have provided important constraints on the tectonic processes and metamorphic reactions that took place during the deep subduction and subsequent rapid exhumation of continental crustal materials that gave rise to the terrane (see Ji and Xu, 2009 and the references herein).

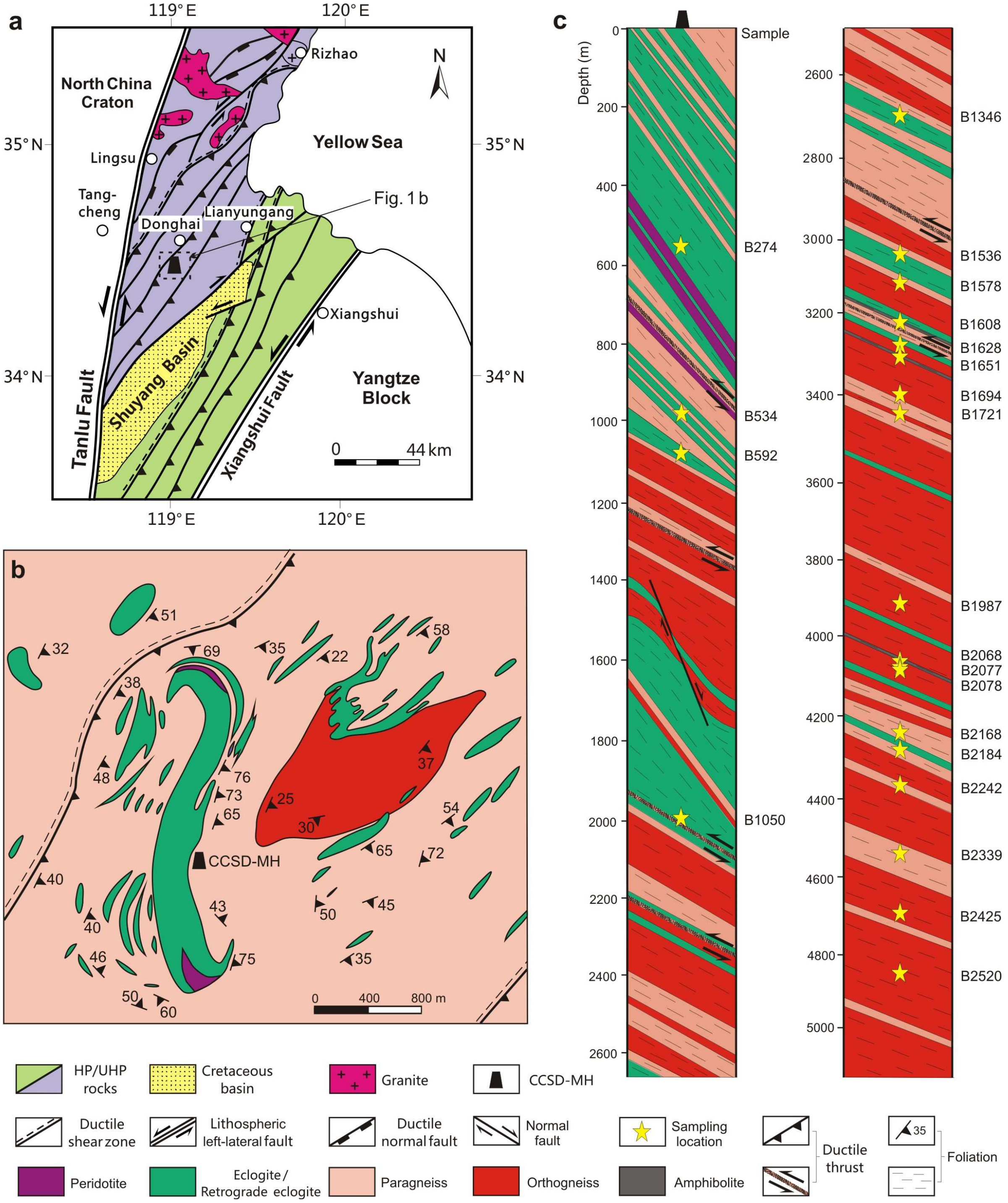

Figure 3.1 Map showing the Sulu UHP metamorphic terrane (a), the location of the CCSD main hole (MH) (b), and the lithological profile revealed by the CCSD main hole (c). Stars indicate sample locations.

The CCSD main borehole (34.40° N, 118.67° E), which is located in Maobei village, about 12 km southwest of Donghai town in Jiangsu Province (Fig. 3.1), was spudded in June 2001, and reached its target depth of 5158 m in April 2005. The borehole, which was continuously cored with an average core recovery of 85%, is the deepest borehole into hard rocks such as eclogite, felsic gneiss, quartzite and garnet peridotite (Ji and Xu, 2009; Xu et al., 2009b), although it is shallower than the German 9101 m KTB hole (Berckhemer et al., 1997; Emmermann and Lauterjung, 1997) and the Russian 12000 m Kola hole (Kozlovsky, 1987; Kern et al., 2001; Ivankina et al., 2005). The Kola superdeep borehole penetrates ~7 km of Proterozoic sequences (i.e., mafic and intermediate metavolcanics, and metasedimentary rocks) and ~5 km of Archean basement (i.e., amphibolites and migmatitic gneisses). Metamorphic grade varies from greenschist facies above 4.5 km, through epidote-amphibolite facies between 4.5-6.0 km, to amphibolites facies below 6.0 km. The rocks penetrated by the KTB borehole are mainly paragneisses and metabasites (amphibolites, metagabbros and subordinate ultramafics) metamorphosed at amphibolites facies. The crustal geology and lithology of the CCSD hole differ fundamentally from those sampled by the Kola and KTB boreholes. The major scientific objectives of the CCSD were: (1) to reconstruct the composition and structure of the root zone of the convergent boundary between the North China Craton and the Yangtze Block, (2) to determine the formation and exhumation mechanisms of the Sulu UHP metamorphic terrane, and (3) to calibrate the laboratory and in-situ seismic properties (i.e., P- and S-velocities, anisotropy and shear wave splitting) of the UHP rocks that are probably representative of the materials within the deep root zone of modern convergent orogenic belts.

This chapter presents new results on P- and S-wave velocities, hysteresis, anisotropy and shear wave splitting as a function of confining pressure up to 800 MPa for a unique suite of 22 samples collected from the CCSD main hole. The results of this study provide insight into the origin of hysteresis, anisotropy and shear wave splitting and the reflectivity of the UHP metamorphic rocks from the Sulu orogenic belt and perhaps other HP/UHP metamorphic terranes throughout the world. One of the main focuses of the investigation is to elucidate the role of microcrack preferred orientations on seismic anisotropy and shear wave splitting and the differences in seismic properties between surface-derived and deep borehole core samples.

3.3 Samples

The CCSD drill core consists mainly of orthogneiss, paragneiss and eclogite or retrogressed eclogite, with lesser amounts of amphibolite and ultramafic rock, and minor mica schist, mica-quartz schist, kyanite quartzite, granite and mylonite (Xu et al., 2009b). Coesite inclusions are common in zircon from various rocks throughout the borehole and in surface outcrops, suggesting that all of the materials in the area were subducted to depths >100 km (Liu et al., 2007). The UHP peak metamorphic event (P>2.8 GPa, T=650-900 ˚C) took place at 240-220 Ma, and the UHP rocks were later overprinted by amphibolite-facies retrograde metamorphism at 220-210 Ma (Liu et al., 2004; Xu et al., 2009b). The structural profile (Fig. 3.1c), revealed by the CCSD main borehole, is characterized by 4 units: (1) Unit A comprises the upper 1113.14 m of the drilled section and consists of eclogite and ultramafic rocks in the upper 735.76 m and paragneiss intercalated with retrograded eclogite and ultramafic rocks in the lower 377.38 m (Fig. 3.1c). In this unit, the foliation changes progressively from steeply eastward-dipping in the upper portion (0-735.76 m) to gently SE- or ESE-dipping below 735.76 m. (2) Unit B has a total thickness of 925.2 m and consists of granitic gneisses intercalated with thin layers of paragneiss in the upper part (1113.14-1596.22 m) and phengite eclogite in the lower part (1596.22-2038.34 m). (3) Unit C (2038.34-3225.00 m) is composed of paragneiss intercalated with thin layers of granitic gneiss and eclogite. (4) Unit D (3225.00-5158.00 m) consists of granitic gneiss intercalated with thin layers of paragneiss and eclogite.

Twenty-two samples collected from the CCSD drill core at different depths of recovery (552.0 to 4864.2 m) were examined in this study. These samples represent typical lithologies from the 5158-m-deep crustal section penetrated by the CCSD main hole: one eclogite, five retrograde eclogites, three amphibolites, nine orthogneisses and four paragneisses (Fig. 3.1c). Table 3.1 gives the recovery depth, lithology, density, and modal composition for each of these samples. The samples selected for velocity measurements are dry, compact rocks with porosities less than 0.1-0.2%. The modal compositions were determined by point counting on thin sections cut perpendicular to the foliation and parallel to the lineation. The densities were determined using the immersion method with an accuracy of ±0.005 g/cm^3 at room conditions. Bulk density data for this suite of samples show a continuous reduction from eclogite ($\overline{\rho}$=3.66 g/cm^3), through retrograde eclogite ($\bar{\rho}$=3.08 g/cm^3) and amphibolite ($\bar{\rho}$=2.95 g/cm^3), to paragneiss ($\bar{\rho}$=2.66 g/cm^3) and orthogneiss ($\bar{\rho}$=2.64 g/cm^3).

Table 3.1 Description of study samples from the CCSD main hole

Sample	**Depth (m)**	**Lithology**	**Density (g/cm^3)**	**Modal composition[a] (vol. %)**	**Ref.[b]**
B274	552.0	Rt eclogite	3.66	Grt 56.0, Omp 36.5, Rt 5.0, Hbl 1.5, Ab 0.5, Qtz 0.5	1
B534	972.5	Retrograde Qtz eclogite	3.17	Grt 34.0, Qtz 15.5, Hbl 15.5, Zo 15.0, Ab 11.0, Phn 8.0, Mag 0.5, Rt 0.5	1
B592	1073.4	Retrograde eclogite	3.21	Hbl 46.0, Grt 25.0, Ep 9.0, Phn 7.0, Qtz 5.0, Omp 4.0, Zo 3.0, Rt 1.0	1
B1050	1994.2	Retrograde eclogite	2.94	Amp 71.0, Mus 13.0, Di 6.0, Zo 4.0, Chl 2.0, Tlc 2.0 Qtz 1.0, Mag 0.5, Rt 0.5	1
B1346	2688.2	Retrograde eclogite	3.00	Hbl 35.0, Ab 30.0, Grt 20.0, Phn 7.3, Ep 6.0, Qtz 1.0, Rt 0.5, Cal 0.2	1
B1536	3019.6	Retrograde eclogite	3.08	Grt 26.0, Hbl 23.5, Ab 23.5, Qtz 12.0, Amp 9.0, Phn 5.0, Rt 1.0	2
B1578	3092.0	Bt-Ms-Pl-Kfs orthogneiss	2.65	Pl 40.0, Kfs 25.0, Qtz 25.0, Ms 4.0, Bt 3.0, Grt 1.0, Opq 2.0	2
B1608	3212.0	Grt-Bt-Pl amphibolite	2.99	Pl 42.0, Amp 40.0, Grt 4.0, Bt 8.0, Qtz 4.0, Chl 2.0	2
B1628	3254.5	Hbl-Mag felsic orthogneiss	2.65	Pl 38.5, Qtz 35.5, Kfs 15.5, Amp 7.0, Grt 1.5, Opq 2.0	2
B1651	3297.2	Amphibolite	3.00	Amp 48.0, Chl 13.0, Grt 3.0, Cpx 15.0, Pl 12.0, Qtz 5.0, Ep 2.0, Opq 2.0	2
B1694	3393.9	Felsic orthogneiss	2.63	Kfs 42.0, Pl 30.0, Qtz 21.0, Cpx 4.0, Amp1.5, Opq 1.0, Rt 0.5	2
B1721	3441.5	Grt-Zo-Bt-Ep dioritic gneiss	2.73	Pl 52.5, Qtz 14.5, Ep 10.0, Kfs 7.0, Bt 6.0, Zo 5.0, Grt 3.0, Di 2.0	1
B1987	3926.7	Mus-Hbl granodioritic gneiss	2.62	Pl 34.0, Qtz 34.0, Kfs 26.0, Hbl 3.0, Mus 1.3, Mag 1.0, Grt 0.5, Zrn 0.2	1
B2068	4072.8	Bt-Pl amphibolite	2.85	Pl 39.0, Amp 39.0, Bt 12.0, Qtz 7.0, Chl 3.0	2
B2077	4087.4	Bt granodioritic gneiss	2.61	Pl 36.0, Qtz 35.0, Kfs 26.0, Bt 2.5, Mag 0.5	1
B2078	4088.9	Felsic orthogneiss	2.63	Kfs 35.0, Pl 31.0, Qtz 25.0, Bt 4.0, Amp 4.0, Opq 1.0	2
B2168	4249.1	Bt-Hbl-Pl-Kfs paragneiss	2.65	Pl 39.0, Qtz 30.0, Kfs 20.0, Amp 6.0, Bt 4.0, Opq 1.0	2
B2184	4276.3	Bt-Hbl-Pl-Kfs paragneiss	2.66	Pl. 40.0, Qtz 40.0, Kfs 15.0, Bt 4.0, Opq 1.0	2
B2242	4385.7	Hbl-Bt-Pl-Kfs paragneiss	2.66	Pl 38.0, Kfs 18.0, Qtz 35.0, Amp 7.5, Opq 1.5	2
B2339	4561.7	Hbl-Pl-Kfs paragneiss	2.65	Pl 42.0, Qtz 25.0, Kfs 21.0, Amp 8.0, Grt. 3.0, Mag 1.0	2
B2425	4711.0	Bt-Grt granodioritic gneiss	2.62	Pl 35.5, Qtz 35.0, Kfs 26.0, Bt 1.6, Grt 1.5, Mag 0.4	1
B2520	4864.2	Bt-Hbl granodioritic gneiss	2.62	Qtz 37.0, Pl 32.5, Kfs 26.5, Hbl 2.0, Bt 1.5, Mag 0.5	1

[a] Abbreviations: Ab: albite; Amp: amphibole; Bt: biotite; Cal: calcite; Chl: chlorite; Cpx: clinopyroxene; Di, diopside; Ep: epidote; Grt: garnet; Hbl: hornblende; Kfs: K-feldspar; Mag: magnetite; Ms: muscovite; Omp:omphacite; Opx: orthopyroxene; Phn: phengite; Pl: plagioclase; Qtz: quartz; Rt: rutile; Tlc: talc; Zo: zoisite, Zrn: zircon

[b] 1: this study; 2: Ji et al. (2007a) and Wang and Ji (2009)

Table 3.2 lists the major element compositions for the 22 CCSD core samples used in this study. The compositions were determined by X-ray fluorescence (XRF) in the Guangzhou Institute of Geochemistry (China). The SiO_2 weight percent of samples is 43% for the eclogite, 47-53% for the retrograde eclogites, 46-48% for amphibolite, 64-78% for orthogneiss, and 74-75% for paragneiss. As shown in Fig. 3.2, the borehole core and surface samples display similar chemical trends: increases in Na_2O+K_2O and decreases in CaO, MgO, and FeO+Fe_2O_3 with increasing SiO_2, although the data for the surface samples are more scattered. Furthermore, for each lithologic type, the CCSD core samples and their surface analogues have similar grain sizes, fabrics, and mineral assemblages. P-wave velocities and Poisson's ratio data for 12 of the 22 core samples were given in Ji et al. (2007a) and Wang and Ji (2009), respectively. These core samples collectively provided an excellent opportunity for characterizing the effects of microcracks on the seismic properties of the rocks because the microcracks were newly generated by stress relaxation processes following retrieval of the cores from their in-situ surroundings.

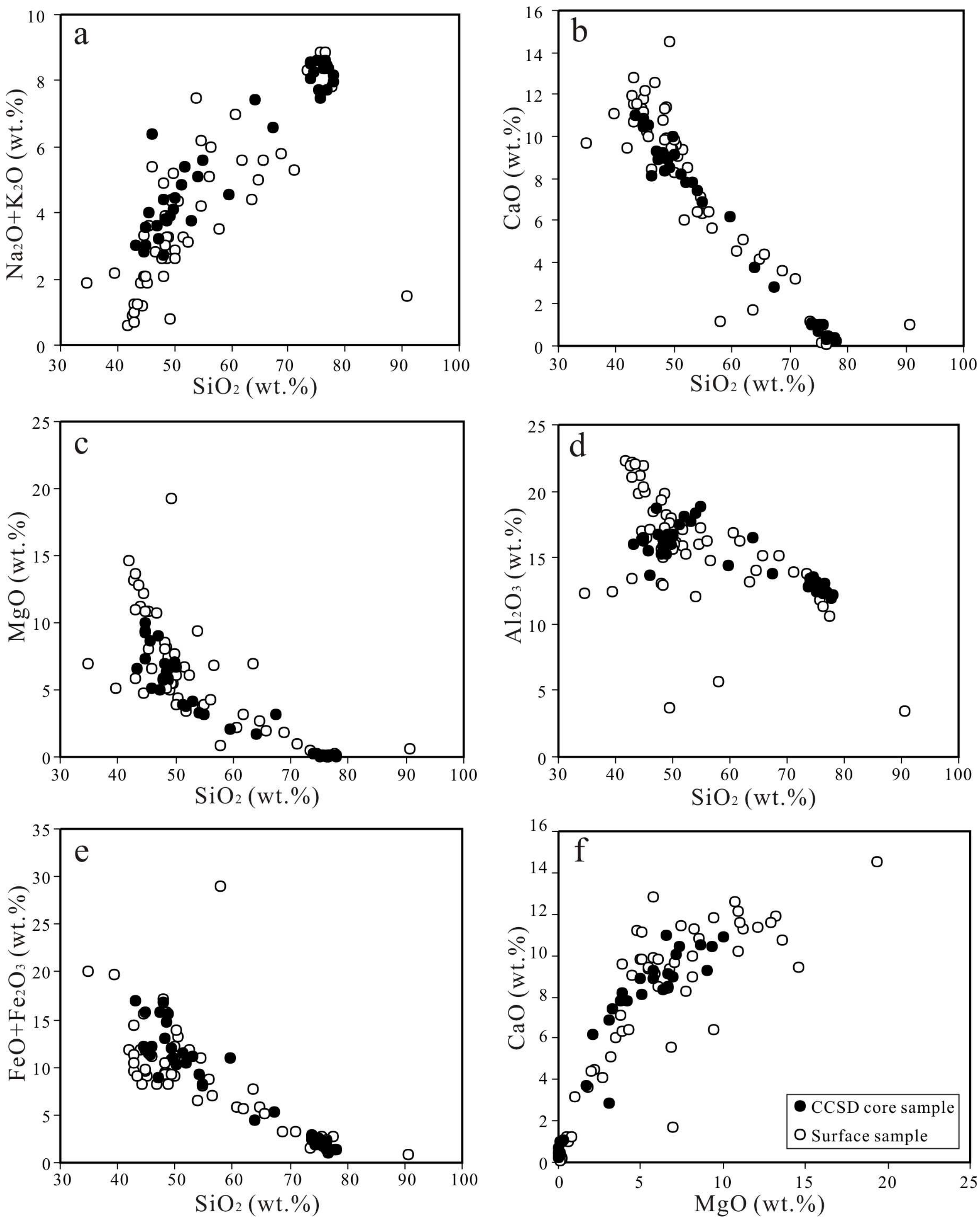

Figure 3.2 Variations of wt.% Na_2O+K_2O (a), CaO (b), MgO (c), Al_2O_3 (d) and $FeO+Fe_2O_3$ (e) versus SiO_2, and CaO as function of MgO (f) for the CCSD deep borehole core samples (solid dots) and their surface equivalents (open dots).

Table 3.2 Chemical composition (wt.%) of UHP samples from Sulu, China

Sample	Lithology	SiO_2	TiO_2	Al_2O_3	Fe_2O_3	FeO	MnO	MgO	CaO	Na_2O	K_2O	P_2O_5	LOI	Total
B274	Rt eclogite	43.22	3.23	16.07	4.00	13.00	0.27	6.56	11.00	3.00	0.02	0.24	-0.75	99.86
B534	Retrograde Qtz eclogite	53.05	1.35	17.75	2.87	8.34	0.18	4.19	7.79	2.50	1.27	0.38	0.21	99.88
B592	Retrograde eclogite	49.22	1.51	16.79	4.66	7.31	0.19	6.69	8.53	2.96	0.96	0.43	0.37	99.62
B1050	Retrograde eclogite	47.00	0.62	18.69	2.42	6.44	0.14	9.03	9.29	2.53	1.06	0.13	2.56	99.91
B1346	Retrograde eclogite	50.13	1.14	16.74	2.71	7.59	0.17	6.68	9.14	3.46	1.02	0.41	0.63	99.82
B1536	Retrograde eclogite	49.71	0.95	16.00	4.54	6.38	0.15	7.09	10.03	3.22	0.89	0.20	0.60	99.76
B1578	Bt-Ms-Pl-Kfs orthogneiss	76.69	0.19	13.07	0.13	0.91	0.03	0.10	0.43	3.01	4.70	0.01	0.64	99.92
B1608	Grt-Bt-Pl amphibolite	48.15	1.42	16.36	7.22	5.75	0.18	6.93	8.98	2.94	1.48	0.24	0.75	100.38
B1628	Hbl-Mag felsic orthogneiss	76.27	0.20	12.30	1.59	0.62	0.06	0.01	0.28	3.97	4.41	0.01	0.14	99.87
B1651	Amphibolite	45.62	1.20	15.47	4.91	6.49	0.15	8.64	10.53	2.34	1.69	0.25	2.87	100.15
B1694	Felsic orthogneiss	76.41	0.20	12.31	1.11	0.45	0.03	0.02	0.46	3.87	4.75	0.00	0.55	100.17
B1721	Grt-Zo-Bt-Ep dioritic gneiss	64.00	0.67	16.53	1.86	2.66	0.09	1.73	3.71	4.71	2.71	0.29	0.84	99.80
B1987	Mus-Hbl granodioritic gneiss	76.32	0.04	12.26	0.55	0.88	0.02	0.09	0.37	3.81	4.64	0.01	0.60	99.59
B2068	Bt-Pl amphibolite	45.95	1.40	13.68	4.12	8.02	0.16	5.09	8.12	3.67	2.74	0.43	6.86	100.24
B2077	Bt granodioritic gneiss	76.75	0.04	12.45	0.55	0.63	0.01	0.07	0.39	4.01	4.48	0.01	0.48	99.87
B2078	Felsic orthogneiss	76.51	0.09	12.45	0.60	0.93	0.02	0.00	0.44	3.86	4.53	0.00	0.35	99.79
B2168	Bt-Hbl-Pl-Kfs paragneiss	73.88	0.25	13.40	0.95	1.46	0.03	0.21	0.98	3.54	4.95	0.03	0.31	100.00
B2184	Bt-Hbl-Pl-Kfs paragneiss	73.84	0.29	12.75	1.46	1.41	0.04	0.26	1.10	3.49	4.57	0.04	0.47	99.71
B2242	Hbl-Bt-Pl-Kfs paragneiss	75.00	0.22	12.46	1.10	1.40	0.05	0.05	0.72	3.65	4.94	0.02	0.46	100.06
B2339	Hbl-Pl-Kfs paragneiss	73.86	0.28	13.09	1.22	1.52	0.04	0.20	1.00	3.93	4.61	0.03	0.39	100.18
B2425	Bt-Grt granodioritic gneiss	77.00	0.04	12.27	0.54	0.88	0.02	0.07	0.42	3.97	4.42	0.01	0.39	100.03
B2520	Bt-Hbl granodioritic gneiss	77.80	0.05	11.91	0.47	0.89	0.02	0.07	0.38	3.68	4.51	0.01	0.26	100.05

3.4 Experimental Details

All the original, 10 cm-diameter CCSD core samples examined display clearly defined foliation planes which are inclined steeply to moderately to the core axis (Fig. 3.1c). Because only half of the core material can be sampled after splitting, it is not always possible to cut three cylindrical minicores, each 2.54 cm in diameter by 3-5 cm in length, in orthogonal directions with the X direction parallel to the stretching lineation (minicore X), the Y direction perpendicular to lineation and parallel to foliation (minicore Y), and the Z direction normal to foliation (minicore Z), as required to measure anisotropy. In the samples where the above conditions could not be met, cylindrical minicores were oriented at other angles with respect to the foliation and lineation although the minicores are still orthogonal to each other. A detailed description of the orientation of each minicore is given in Table 3.3.

Measurements of P- and S-wave velocities (V_p and V_s) and their directional dependence (P-wave velocity anisotropy and shear wave splitting) were performed at hydrostatic confining pressures ranging from 10 to 800 MPa using the pulse transmission technique (Birch, 1960; Wepfer and Christensen, 1991; Kern, 1990). In order to characterize the seismic hysteresis of the samples, velocity measurements were performed on each cylindrical minicore both during pressurization and then depressurization for each run. Each minicore sample was trimmed to a right cylinder with two polished plan-parallel end faces. The details of high-pressure experiments were described in Section 2.4.

Table 3.3 Orientations of minicore samples from the CCSD main hole

Sample	**Minicore orientation**				
B274	X	Y	Z		
B534	X	Y	Z		
B592	X	Y	Z		
B1050		Y		A (in XZ plane, 50° to X)	
B1346		Y	Z		
B1536	X		Z		
B1578	X		Z		
B1608	X		Z		
B1628		Y	Z		
B1651			Z		
B1694			Z		
B1721	X	Y	Z		
B1987		Y		A (in XZ plane, 50° to X)	B (in XZ plane, 50° to Z)
B2068			Z		
B2077		Y		A (in XZ plane, 30° to X)	B (in XZ plane, 30° to Z)
B2078			Z		
B2168			Z		
B2184	X		Z		
B2242	X				
B2339			Z		
B2425		Y		A (in XZ plane, 30° to Z)	B (in XZ plane, 30° to X)
B2520	X			A (in YZ plane, 30° to Z)	B (in YZ plane, 30° to Y)

3.5 Experimental Results

3.5.1 Velocity-Pressure relationships and seismic hysteresis

Typical P- and S-wave velocities measured during a cycle of pressurization and subsequent depressurization are shown in Figs. 3.3 and 3.4, respectively, for an eclogite (B274), a retrograde eclogite (B592), and two felsic gneisses (B1721 and B2077). Three V_p measurements (e.g., along the X, Y, and Z directions) and six V_s measurements (e.g., with geometric configurations XY, XZ, YX, YZ, ZX and ZY, where the first letter refers to the propagation direction and the second to the polarization direction) were performed for each sample with three orthogonal minicores. For most of the samples, both the pressurization and depressurization curves display a rapid, non-linear increase in velocity with pressure at low pressures (generally <200-300 MPa) and then increase slowly and linearly in velocity at high pressures (Figs. 3.3-3.4). The transition from the non-linear regime to the linear regime is caused by the closure of microcracks in samples with increasing hydrostatic pressure (Birch, 1960; Christensen, 1965; Ji et al., 1993; Kern et al., 2001). Only the nearly linear segment of the velocity-pressure curves at high pressures can be reproduced and reversed in the laboratory while those at low pressures vary slightly from run to run. This suggests that the rocks become crack-free, compacted aggregates in the high pressure linear regime, while in the low pressure non-linear regime, seismic velocities are very sensitive to the state of microcracks (e.g., the ratio of crack aperture to length) within the rocks that possess discrete memories of their past pressure history (Ji et al., 2007a).

In all cases, the depressurization curve consistently lies on or above the pressurization curve, and the pressure derivative (dV/dP) in the high pressure regime is always lower for the depressurization curve than the pressurization curve (Figs. 3.3-3.4). The progressive decrease in the magnitude of hysteresis (*H*) with increasing pressure was analyzed according to the following equation:

$$H = H_0 \exp(-mP) \tag{3.1}$$

where H_0 (in km/s) is the velocity hysteresis at zero pressure, and m (in MPa^{-1}) is a positive number called the decay constant (Table 3.4). Goodness-of-fit coefficients (R^2), which are statistical indicators of how well the measured data fit the empirical relation, are consistently higher than 0.94.

As shown in Fig. 3.5, the hysteresis decreases very rapidly as the confining pressure initially increases. When the pressure is sufficiently large, say above a critical pressure P_c (crack-closing pressure), the hysteresis reaches almost zero. Above P_c, which ranges generally from 150 to 400 MPa, the rock sample can be regarded as a nearly crack-free aggregate and the seismic velocities increase almost linearly with increasing pressure. If P_c is defined as the value at which *H* is sufficient small, say 0.01 km/s, then

$$P_c = \frac{-\ln(0.01/H_0)}{m} \tag{3.2}$$

Taking minicore Z from sample B1651 (amphibolite, Fig. 3.5c) as an example, H_0=0.98 km/s, and m=2.32×10^{-2} MPa^{-1} (Table 3.4), hence P_c=198 MPa. As a rock containing more spherical pores has a higher P_c value than the same rock containing flatter cracks with smaller ratios of crack aperture to length, the m value in Eq. (3.1) is thus a measurable coefficient which can provide a statistical measurement of the geometrical shape or sphericity of pores.

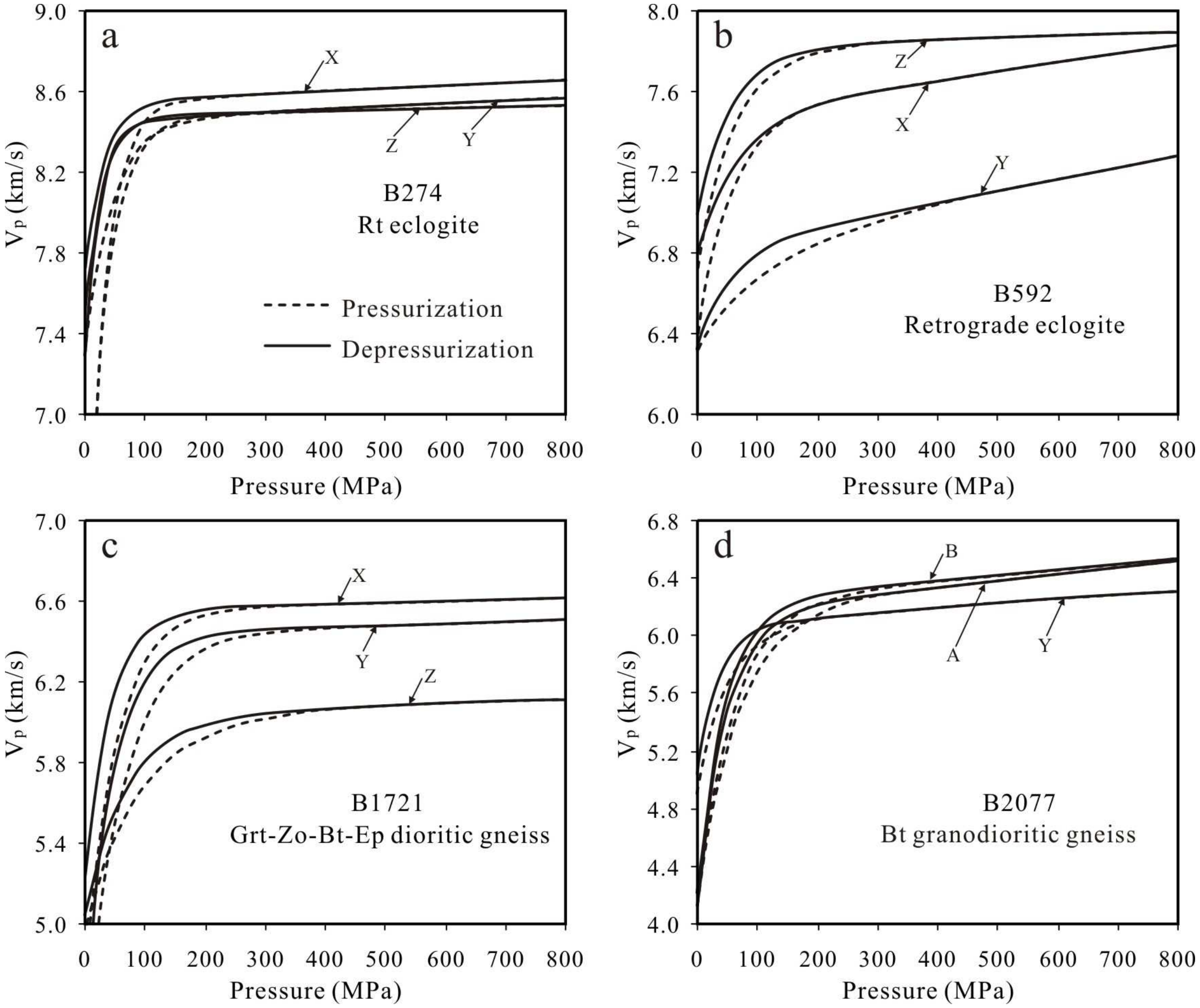

Figure 3.3 P-wave velocity (V_p) versus pressure in three orthogonal directions through samples B274 (a), B592 (b), B1721 (c) and B2077 (d). Information about the orientation of each minicore is given in Table 3.3.

Both P- and S-wave velocities measured during depressurization as a function of confining pressure were fitted to the following equation (Zimmerman et al., 1986; Greenfield and Graham, 1996; Ji et al., 2007a):

$$V(P) = V_0 + DP - B_0 \exp(-kP) \tag{3.3}$$

where V_0 is the intrinsic velocity of the crack-free compacted rock at zero pressure, which is determined from extrapolation of the linear velocity-pressure relationship obtained at high pressures to zero pressure; D is the intrinsic pressure derivative of velocity in the linear elastic regime; B_0 is the maximum velocity increase due to crack closure; k, which is the decay constant of the velocity increase, controls the shape of the nonlinear segment of the velocity-pressure curve.

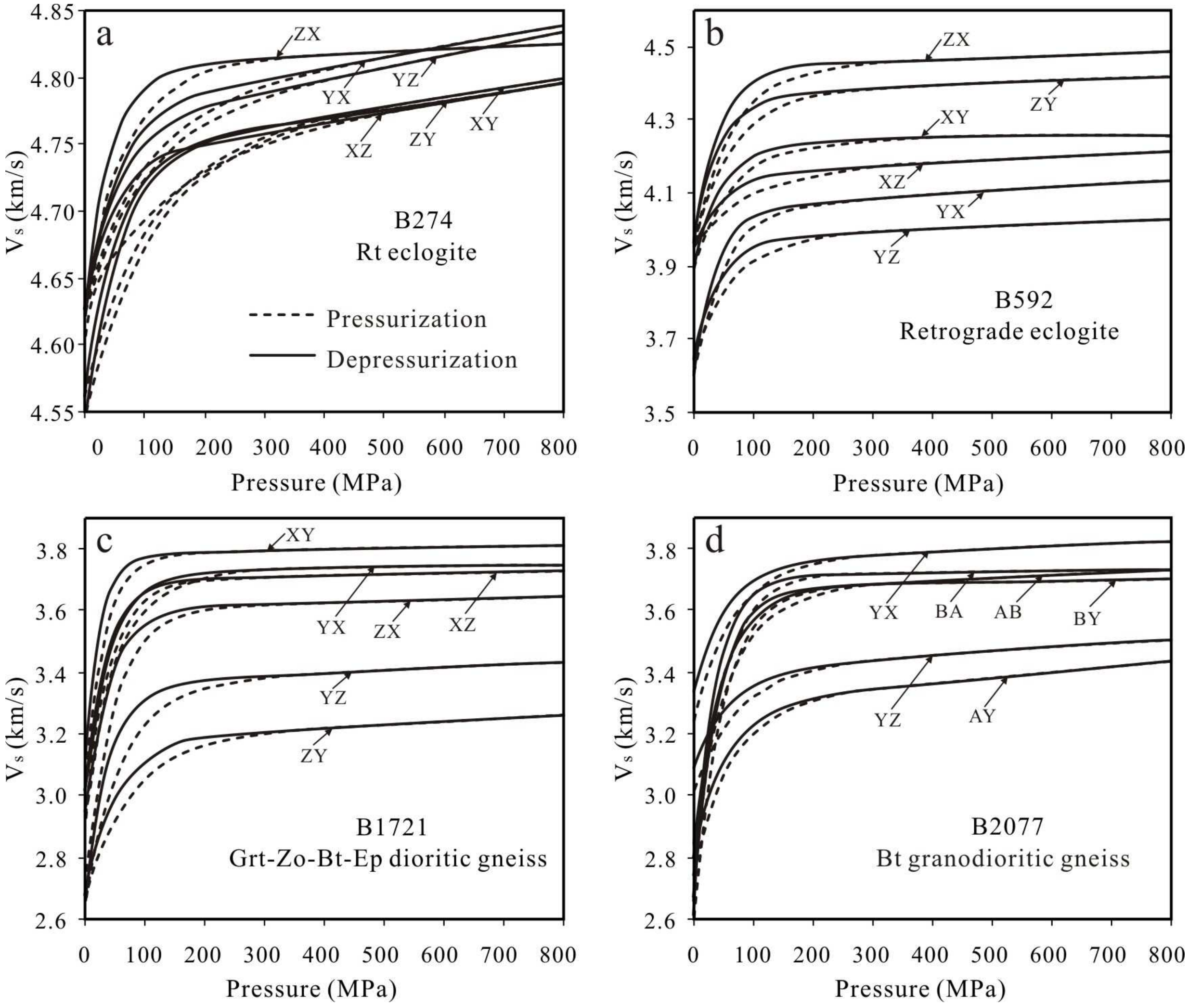

Figure 3.4 S-wave velocity (V_s) versus propagation and polarization directions in samples B274 (a), B592 (b), B1721 (c) and B2077 (d) as a function of pressure. The first letter signifies propagation direction and the second letter the polarization direction. The three minicores are orthogonal and the information about the orientation of each minicore is given in Table 3.3.

In Eq. (3.3), V_0 and D are two parameters which describe the intrinsic seismic properties of the microcrack- or pore-free solid matrix, while B_0 and k are parameters which describe the extrinsic seismic properties related to the porosity and geometrical shape of microcracks (e.g., aspect ratio, spatial arrangement, orientation and size distribution) and thus the deformation processes of the rocks. The physical significance of Eq. (3.3) has been discussed in Ji et al. (2007a).

Parameters V_0, D, B_0 and k determined for the P- and S-wave velocities of each minicore sample during depressurization, using a least square regression method, are given in Tables 3.4 and 3.5, respectively. As indicated by the goodness-of-fit coefficients (mostly $R^2 \geq 0.95$), the pressure-velocity curves for P- and S-waves can be well represented by Eq. (3.3).

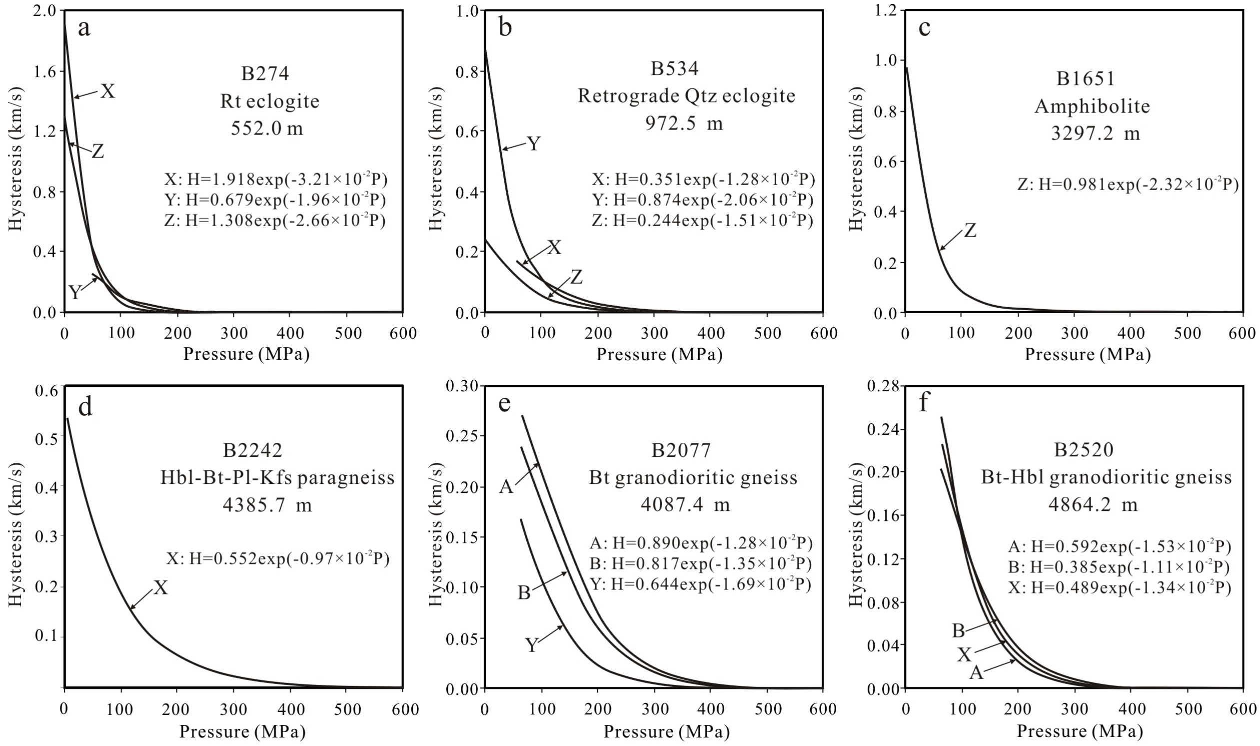

Figure 3.5 P-wave velocity hysteresis (km/s) versus confining pressure (MPa) in each propagating direction through samples B274 (a), B534 (b), B1651 (c), B2242 (d), B2077 (e) and B2520 (f).

Table 3.4 Parameters of V_p-pressure curves measured during depressurization and V_p hysteresis for samples from the CCSD main hole

Sample	Lithology	Depth (m)	Λ*	Density (g/cm^3)	V_0 (km/s)	D (10^{-4} km/s/MPa)	B_0 (km/s)	k (10^{-2} MPa^{-1})	R^2	H_0 (km/s)	m (10^{-2} MPa^{-1})	R^2
B274	Rt eclogite	552.0	X	3.66	8.548	1.383	0.825	3.162	0.99	1.9176	3.21	1.00
			Y	3.65	8.453	1.374	1.144	4.162	1.00	0.6793	1.96	1.00
			Z	3.66	8.471	0.788	0.978	3.548	0.99	1.3079	2.66	1.00
			Mean	3.66	8.491	1.182	0.982	3.624	0.99	1.3016	2.61	1.00
B534	Retrograde Qtz eclogite	972.5	X	3.16	7.344	1.727	1.043	2.486	1.00	0.3509	1.28	0.99
			Y	3.18	7.336	1.716	0.867	2.020	0.99	0.8739	2.06	1.00
			Z	3.15	7.093	3.664	0.781	2.456	0.99	0.2437	1.51	0.99
			Mean	3.17	7.258	2.369	0.897	2.321	0.99	0.4895	1.62	0.99
B592	Retrograde eclogite	1073.4	X	3.15	7.474	4.445	0.677	1.500	0.99	0.3990	2.53	0.99
			Y	3.10	6.819	5.781	0.494	1.810	0.99	0.2946	0.72	0.99
			Z	3.38	7.810	1.089	0.821	1.811	0.99	0.2635	1.35	1.00
			Mean	3.21	7.368	3.772	0.664	1.707	0.99	0.3190	1.53	0.99
B1050	Retrograde eclogite	1994.2	A	2.95	7.055	5.061	0.858	1.741	0.99	0.3634	0.76	0.99
			Y	2.94	6.858	2.777	1.003	2.567	0.99	0.6631	1.34	1.00
			Mean	2.94	6.956	3.919	0.930	2.154	0.99	0.5133	1.05	0.99
B1346	Retrograde eclogite	2688.2	Y	2.95	6.966	1.159	1.124	1.710	0.97	0.2319	0.90	0.99
			Z	3.12	6.937	2.933	0.839	2.572	0.98	0.3335	1.45	0.99
			Mean	3.00	6.957	1.750	1.029	1.998	0.97	0.2658	1.08	0.99
B1536	Retrograde eclogite	3019.6	X	3.11	7.250	1.383	2.302	2.881	1.00	0.7024	1.47	0.96
			Z	3.01	6.924	2.053	2.003	2.820	1.00	0.9198	1.97	0.99
			Mean	3.08	7.141	1.606	2.202	2.861	1.00	0.7749	1.64	0.97
B1578	Bt-Ms-Pl-Kfs orthogneiss	3092.0	X	2.65	6.452	1.855	3.373	2.214	1.00	0.4556	1.24	0.99
			Z	2.65	5.944	1.527	1.885	2.286	1.00	0.9941	2.05	0.99
			Mean	2.65	6.283	1.746	2.877	2.238	1.00	0.6351	1.51	0.99
B1608	Grt-Bt-Pl amphibolite	3212.0	X	3.01	7.259	1.676	1.132	1.798	0.92	0.1797	0.44	0.99
			Z	2.95	6.670	2.108	0.879	1.620	1.00	0.0589	0.47	0.99
			Mean	2.99	7.063	1.820	1.048	1.739	0.95	0.1394	0.45	0.99
B1628	Hbl-Mag felsic orthogneiss	3254.5	Y	2.65	6.375	2.329	2.394	2.654	1.00	0.7980	1.88	0.99
			Z	2.65	6.381	1.516	1.057	1.553	1.00	0.5159	0.94	0.99
			Mean	2.65	6.377	2.058	1.948	2.287	1.00	0.7040	1.57	0.99
B1651	Amphibolite	3297.2	Z	3.00	6.592	1.708	0.691	2.483	0.98	0.9813	2.32	1.00
B1694	Felsic orthogneiss	3393.9	Z	2.63	6.394	1.710	1.500	0.739	0.87	1.0000	1.06	0.51 (?)
B1721	Grt-Zo-Bt-Ep dioritic gneiss	3441.5	X	2.73	6.560	0.774	1.330	2.281	0.99	0.4960	1.30	0.99
			Y	2.72	6.431	1.002	1.800	2.033	0.97	0.5068	1.06	0.99
			Z	2.74	6.020	1.186	0.975	1.446	0.98	0.2857	0.80	0.99
			Mean	2.73	6.337	0.987	1.368	1.920	0.98	0.4295	1.05	0.99
B1987	Mus-Hbl granodioritic gneiss	3926.7	A	2.62	6.290	0.768	2.409	1.913	0.97	0.5267	1.42	1.00
			B	2.62	6.089	4.068	1.591	2.407	0.99	0.8354	1.61	1.00
			Y	2.62	6.283	2.618	2.270	2.364	1.00	1.1032	1.62	1.00
			Mean	2.62	6.221	2.485	2.090	2.228	0.98	0.8218	1.55	1.00
B2068	Bt-Pl amphibolite	4072.8	Z	2.85	6.244	1.313	0.890	2.843	1.00	0.0870	0.98	0.99
B2077	Bt granodioritic gneiss	4087.4	A	2.61	6.151	4.613	2.039	2.130	0.98	0.8900	1.28	1.00
			B	2.62	6.234	3.671	2.023	2.152	0.98	0.8172	1.35	1.00
			Y	2.61	6.066	3.054	1.030	2.836	0.97	0.6442	1.69	1.00
			Mean	2.61	6.150	3.780	1.697	2.372	0.98	0.7838	1.44	1.00
B2078	Felsic orthogneiss	4088.9	Z	2.63	6.315	1.932	3.449	3.012	1.00	0.2155	0.98	0.99
B2168	Bt-Hbl-Pl-Kfs paragneiss	4249.1	Z	2.65	6.129	1.870	2.171	2.522	0.98	0.4572	1.23	0.99
B2184	Bt-Hbl-Pl-Kfs paragneiss	4276.3	X	2.66	5.954	1.739	2.203	2.149	1.00	0.2746	1.67	0.99
			Z	2.66	6.170	1.264	1.782	1.088	0.95	0.2379	0.52	0.97
			Mean	2.66	6.026	1.581	2.062	1.795	0.98	0.2624	1.29	0.98
B2242	Hbl-Bt-Pl-Kfs paragneiss	4385.7	X	2.66	6.357	1.970	1.545	1.592	1.00	0.5521	0.97	0.99
B2339	Hbl-Pl-Kfs paragneiss	4561.7	Z	2.65	6.193	1.779	0.902	1.173	0.95	0.9514	0.95	0.95
B2425	Bt-Grt granodioritic gneiss	4711.0	A	2.62	6.132	2.076	1.262	2.697	0.98	0.6245	1.51	1.00
			B	2.62	6.212	2.835	1.392	2.526	1.00	0.4417	1.29	0.99
			Y	2.62	6.369	1.467	2.247	2.617	1.00	0.9048	1.62	1.00
			Mean	2.62	6.238	2.126	1.634	2.613	0.99	0.6570	1.47	0.99
B2520	Bt-Hbl granodioritic gneiss	4864.2	A	2.62	6.265	2.057	2.407	2.854	0.99	0.5919	1.53	0.99
			B	2.63	6.184	2.261	2.307	2.289	0.99	0.3853	1.11	0.97
			X	2.62	6.282	1.772	2.156	2.586	0.99	0.4893	1.34	0.98
			Mean	2.62	6.244	2.030	2.290	2.576	0.99	0.4888	1.33	0.98

* Direction of wave propagation, other terms defined in text.

Table 3.5 Parameters of V_S-pressure curves measured during depressurization for samples from the CCSD main hole

Sample	Lithology	Depth (m)	Λ*	Density (g/cm^3)	V_0 (km/s)	D (10^{-4} km/s/MPa)	B_0 (km/s)	k (10^{-2} MPa^{-1})	R^2
B274	Rt eclogite	552.0	XY	3.66	4.742	0.713	0.198	1.754	0.99
			XZ	3.66	4.737	0.736	0.117	2.185	1.00
			YX	3.65	4.775	0.799	0.149	1.909	1.00
			YZ	3.65	4.764	0.882	0.138	1.866	1.00
			ZX	3.66	4.807	0.227	0.183	2.304	1.00
			ZY	3.66	4.743	0.663	0.183	1.877	0.99
			Mean	3.66	4.761	0.670	0.161	1.983	0.99
B534	Retrograde Qtz eclogite	972.5	XY	3.16	4.257	1.242	0.212	1.578	0.99
			XZ	3.16	4.028	2.227	0.372	1.679	0.99
			YX	3.18	4.146	1.752	0.242	1.685	0.99
			YZ	3.18	4.127	1.737	0.217	1.554	0.99
			ZX	3.15	4.177	1.328	0.196	2.425	0.99
			ZY	3.15	4.134	0.887	0.346	2.052	0.99
			Mean	3.17	4.145	1.529	0.264	1.829	0.99
B592	Retrograde eclogite	1073.4	XY	3.15	4.233	0.394	0.341	2.255	0.99
			XZ	3.15	4.150	0.837	0.198	1.991	0.99
			YX	3.10	4.049	1.100	0.448	2.736	0.99
			YZ	3.10	3.970	0.739	0.333	2.464	0.99
			ZX	3.38	4.440	0.622	0.490	2.469	0.99
			ZY	3.38	4.361	0.719	0.412	2.549	0.99
			Mean	3.21	4.200	0.735	0.370	2.411	0.99
B1050	Retrograde eclogite	1994.2	AB	2.95	3.896	0.581	0.224	2.315	0.99
			AY	2.95	3.971	1.108	0.137	1.714	1.00
			YX	2.94	3.958	0.666	0.320	2.386	1.00
			YZ	2.94	3.741	0.880	0.282	2.260	0.99
			Mean	2.94	3.892	0.809	0.241	2.169	0.99
B1346	Retrograde eclogite	2688.2	YX	2.95	3.990	0.357	0.581	4.001	0.99
			YZ	2.95	3.715	1.312	0.351	1.974	0.99
			ZX	3.12	3.940	1.303	0.276	3.362	1.00
			ZY	3.12	3.960	1.106	0.247	1.887	1.00
			Mean	3.00	3.885	0.958	0.398	2.866	0.99
B1536	Retrograde eclogite	3019.6	XY	3.11	4.191	0.569	0.857	2.375	1.00
			XZ	3.11	4.100	0.558	0.941	2.550	1.00
			ZX	3.01	4.105	0.585	0.726	2.256	1.00
			ZY	3.01	3.804	0.781	0.921	3.017	0.99
			Mean	3.08	4.082	0.604	0.874	2.520	1.00
B1578	Bt-Ms-Pl-Kfs gneiss	3092.0	XY	2.65	4.005	0.582	0.989	2.413	0.94
			XZ	2.65	3.603	0.325	1.105	1.957	0.96
			ZX	2.65	3.598	1.173	1.120	2.071	0.93
			ZY	2.65	3.561	0.353	1.035	2.181	0.98
			Mean	2.65	3.729	0.557	1.057	2.165	0.95
B1608	Grt-Bt-Pl amphibolite	3212.0	XY	3.01	4.070	0.511	0.545	2.459	1.00
			XZ	3.01	3.825	0.814	0.809	3.661	0.99
			ZX	2.95	3.823	1.083	0.469	3.022	1.00
			ZY	2.95	3.783	0.854	0.450	2.653	0.99
			Mean	2.99	3.899	0.764	0.604	2.986	0.99
B1628	Hbl-Mag felsic gneiss	3254.5	YX	2.65	3.646	0.667	1.038	2.274	0.96
			YZ	2.65	3.615	1.119	1.501	3.820	0.99
			ZX	2.65	3.684	0.409	1.277	2.040	1.00
			ZY	2.65	3.721	1.021	1.037	1.847	0.97
			Mean	2.65	3.654	0.833	1.232	2.679	0.98
B1651	Amphibolite	3297.2	ZX	3.00	3.795	0.668	0.734	3.123	0.95
			ZY	3.00	3.555	0.628	0.503	4.075	0.98
			Mean	3.00	3.675	0.648	0.618	3.599	0.96
B1694	Felsic gneiss	3393.9	ZX	2.63	3.764	0.656	1.001	1.211	0.92
			ZY	2.63	3.630	0.714	1.151	1.703	0.99
			Mean	2.63	3.697	0.685	1.076	1.457	0.96

Table 3.5 (continued)

Sample	**Lithology**	**Depth (m)**	**Λ***	**Density (g/cm^3)**	**V_0 (km/s)**	**D $(10^{-4}$ km/s/MPa)**	**B_0 (km/s)**	**k $(10^{-2}$ MPa$^{-1})$**	**R^2**
B1721	Grt-Zo-Bt-Ep dioritic gneiss	3441.5	XY	2.73	3.783	0.388	0.650	3.925	1.00
			XZ	2.73	3.696	0.456	0.686	2.885	0.99
			YX	2.72	3.724	0.260	0.698	2.353	0.99
			YZ	2.72	3.356	0.983	0.698	2.478	0.99
			ZX	2.74	3.601	0.555	0.679	2.593	1.00
			ZY	2.74	3.181	1.019	0.503	1.863	0.99
			Mean	2.73	3.557	0.610	0.652	2.683	0.99
B1987	Mus-Hbl granodioritic gneiss	3926.7	AB	2.62	3.456	2.332	0.066	1.542	0.99
			AY	2.62	3.650	0.899	1.206	2.659	0.99
			BA	2.62	3.476	1.094	0.294	1.827	0.99
			BY	2.62	3.520	1.996	0.687	3.776	1.00
			YX	2.62	3.677	0.900	1.052	2.692	1.00
			YZ	2.62	3.655	0.279	1.035	2.368	0.98
			Mean	2.62	3.572	1.250	0.723	2.477	0.99
B2068	Bt-Pl amphibolite	4072.8	ZX	2.85	3.544	0.701	0.368	2.895	0.99
B2077	Bt granodioritic gneiss	4087.4	AB	2.61	3.657	0.938	0.819	2.157	1.00
			AY	2.61	3.291	1.760	0.492	1.876	0.99
			BA	2.62	3.706	0.354	1.077	2.970	1.00
			BY	2.62	3.661	0.540	1.056	2.675	0.99
			YX	2.61	3.750	0.933	0.419	1.856	1.00
			YZ	2.61	3.398	1.359	0.310	1.710	1.00
			Mean	2.61	3.577	0.981	0.695	2.207	1.00
B2078	Felsic gneiss	4088.9	ZX	2.63	3.833	1.172	1.118	1.967	0.97
			ZY	2.63	3.654	1.251	1.223	2.743	1.00
			Mean	2.63	3.743	1.212	1.170	2.355	0.98
B2168	Bt-Hbl-Pl-Kfs gneiss	4249.1	ZX	2.65	3.492	0.967	1.173	2.828	1.00
			ZY	2.65	3.293	1.671	0.340	2.285	1.00
			Mean	2.65	3.393	1.319	0.757	2.556	1.00
B2184	Bt-Hbl-Pl-Kfs gneiss	4276.3	XY	2.66	3.773	0.611	0.943	2.448	0.96
			XZ	2.66	3.495	0.968	1.347	3.382	1.00
			ZX	2.66	3.683	0.445	1.372	2.045	1.00
			ZY	2.66	3.525	0.990	1.271	3.298	1.00
			Mean	2.66	3.624	0.765	1.204	2.834	0.98
B2242	Hbl-Bt-Pl-Kfs gneiss	4385.7	XY	2.66	3.733	0.650	1.009	1.076	0.93
			XZ	2.66	3.461	0.809	1.170	1.529	0.95
			Mean	2.66	3.597	0.729	1.089	1.302	0.94
B2339	Hbl-Pl-Kfs gneiss	4561.7	ZX	2.65	3.585	0.928	1.129	2.715	1.00
			ZY	2.65	3.647	0.791	0.909	2.664	0.97
			Mean	2.65	3.616	0.859	1.019	2.689	0.98
B2425	Bt-Grt granodioritic gneiss	4711.0	AB	2.62	3.693	1.145	0.482	1.923	0.99
			AY	2.62	3.365	1.218	0.255	2.321	1.00
			BA	2.62	3.522	1.682	0.289	1.756	0.99
			BY	2.62	3.534	0.965	0.446	2.248	1.00
			YX	2.62	3.528	2.326	0.109	1.869	1.00
			YZ	2.62	3.408	1.631	0.300	1.697	0.99
			Mean	2.62	3.508	1.495	0.314	1.969	0.99
B2520	Bt-Hbl granodioritic gneiss	4864.2	AX	2.62	3.761	0.878	0.815	2.446	0.99
			AB	2.62	3.716	0.795	0.608	2.184	0.99
			BX	2.63	3.747	1.056	1.019	2.283	1.00
			BA	2.63	3.681	0.394	0.935	2.363	0.99
			XY	2.62	3.796	0.430	1.122	2.703	0.97
			XZ	2.62	3.723	0.573	1.112	2.720	1.00
			Mean	2.62	3.737	0.688	0.935	2.450	0.99

* Directions of S-wave propagation and polarization, other terms defined in text.

3.5.2 Velocity-density relationships

Figures 3.6a-b show the relationships between the mean velocities (V_0 and values at 600 MPa) and densities for the samples collected from the CCSD borehole. The dots represent the mean P- and S-wave velocities whereas the vertical lines illustrate the ranges of velocity variation due to seismic anisotropy. The mean velocities (Tables 3.4 and 3.5), which were calculated by arithmetical averaging of all the values measured for the minicores from each sample, can also be well fitted by Eq. (3.3). The densities are those determined at room pressure since the effect of pressure on density is negligible in these high-grade metamorphic rocks with very low porosity (<0.5%).

Each V_0 value shown in Fig. 3.6a, which is the projected reference velocity of each non-porous or crack-free compacted rock at zero pressure, is thus an intrinsic property of each sample. The V_0 values of both P- and S-waves increase with increasing density, but the increase for P-wave velocity is much more pronounced than that for S-wave velocity. Arranged in an order of decreasing mean V_0 values for P- and S-waves, the samples can be grouped as follows: eclogite ($\overline{V_p}$ = 8.49 km/s, $\overline{V_s}$ = 4.76 km/s), retrograde eclogite ($\overline{V_p}$ =7.14 km/s, $\overline{V_s}$ =4.04 km/s), amphibolite ($\overline{V_p}$ = 6.63 km/s, $\overline{V_s}$ =3.71 km/s) and felsic gneiss ($\overline{V_p}$ =6.25 km/s, $\overline{V_s}$ =3.62 km/s). The equations of the best-fit regression lines for V_0 values of P- and S-waves are: $V_p=2.197\rho+0.343$ ($R^2=0.93$) and $V_s=1.308\rho$ ($R^2=0.83$). In dry air at 20 °C, the speed of sound is 0.343 km/s. The slope of the velocity-density trend for V_p is significantly higher than that for V_s. The data cluster at the left ends of the regression lines reflects the similarities of both density and velocities for orthogneiss and paragneiss.

At 600 MPa, both P- and S-wave velocities also vary linearly versus density in the whole range of density between 2.5-3.8 g/cm^3 (Fig. 3.6b): $V_p=2.244\rho+0.343$ ($R^2=0.94$) and $V_s=1.329\rho$ ($R^2=0.84$). Linear relations between density and velocities such as the Nafe-Drake curves are related to compositional differences rather than temperature differences. In contrast, Birch's Law (1961) holds when density is varied by compression for a constant composition (the mean atomic weight), but does not hold either through a structural phase transition or compositional change (Liebemann and Ringwood, 1973; Campbell and Heinz, 1992). The simple linear relation between seismic velocities and density underlines the importance of density changes that are a function of chemical and modal compositions. Such velocity-density relations should work particularly for the interpretation of seismic data from the continental crust where lithology is much more heterogeneous than that in the upper mantle. However, large anisotropy of some samples may give rise to significant scatter in the velocity-density relationships. For example, sample B592 (retrograde eclogite) ranges in V_p between 7.17-7.88 km/s (Fig. 3.6a), and V_s between 4.01-4.48 km/s (Fig. 3.6b). Using the velocity-density relations, these would correspond to density ranges of 3.04-3.36 g/cm^3, and 3.02-3.37 g/cm^3, respectively, which span a range in composition from gabbro to peridotite. Thus care must be taken in interpreting in-situ seismic velocity data in terms of petrology according to the mean velocity-density relations when the ray path geometry with respect to the structural framework (i.e., foliation and lineation) is unknown.

The mean V_p and V_s velocities (V_0 and values at 600 MPa) as a function of density for the samples from the Sulu surface exposures are given in Figs. 3.6c-d. All samples except serpentinites show well-defined linear trends: $V_p=2.100\rho+0.343$ ($R^2=0.80$) and $V_s=1.282\rho$ ($R^2=0.80$) for the reference velocities (V_0), and $V_p=2.172\rho+0.343$ ($R^2=0.84$) and $V_s=1.311\rho$ ($R^2=0.82$) for the velocities at 600 MPa. A comparison between Fig. 3.6a and Fig. 3.6c or between Fig. 3.6b and Fig. 3.6d shows that the CCSD core materials have systematically higher P- and S-wave velocities than the surface-derived samples for any given density. In addition, the surface-derived samples display a much larger scattering of the data around the trend line, reflecting mainly their large variations in the degree of weathering and alteration (Fig. 3.2). This fact points out a potential pitfall of extrapolating laboratory velocity data from surface-derived rocks to estimate deeper crustal compositions. Clearly, the CCSD borehole core samples represent completely fresh samples of the UHP metamorphic rocks in the region.

3.5.3 Correlation between P- and S-wave velocities

Figures 3.7a-b show V_s-V_p plots for the calculated equivalent isotropic rocks from the CCSD borehole. The least-squares linear fit gives $V_p=1.676V_s+0.343$ ($R^2=0.90$) for the V_0 values, and $V_p=1.685V_s+0.343$ ($R^2=0.91$) for the velocities at 600 MPa. These relations are valid when V_p ranges from 5.5 to 8.8 km/s and V_s ranges from 3.0 to 5.0 km/s. When only V_p data exist, the V_s-V_p relations may provide a reasonable estimate for the corresponding V_s value. Interestingly, almost no change between the above two equations implies that the effect of compression on the

V_p/V_s ratios is negligible for non-porous or crack-free compacted rock. However, large ranges in V_p and V_s due to the presence of anisotropy in the rocks may cause significant scatter around the trend lines (Figs. 3.7a-b).

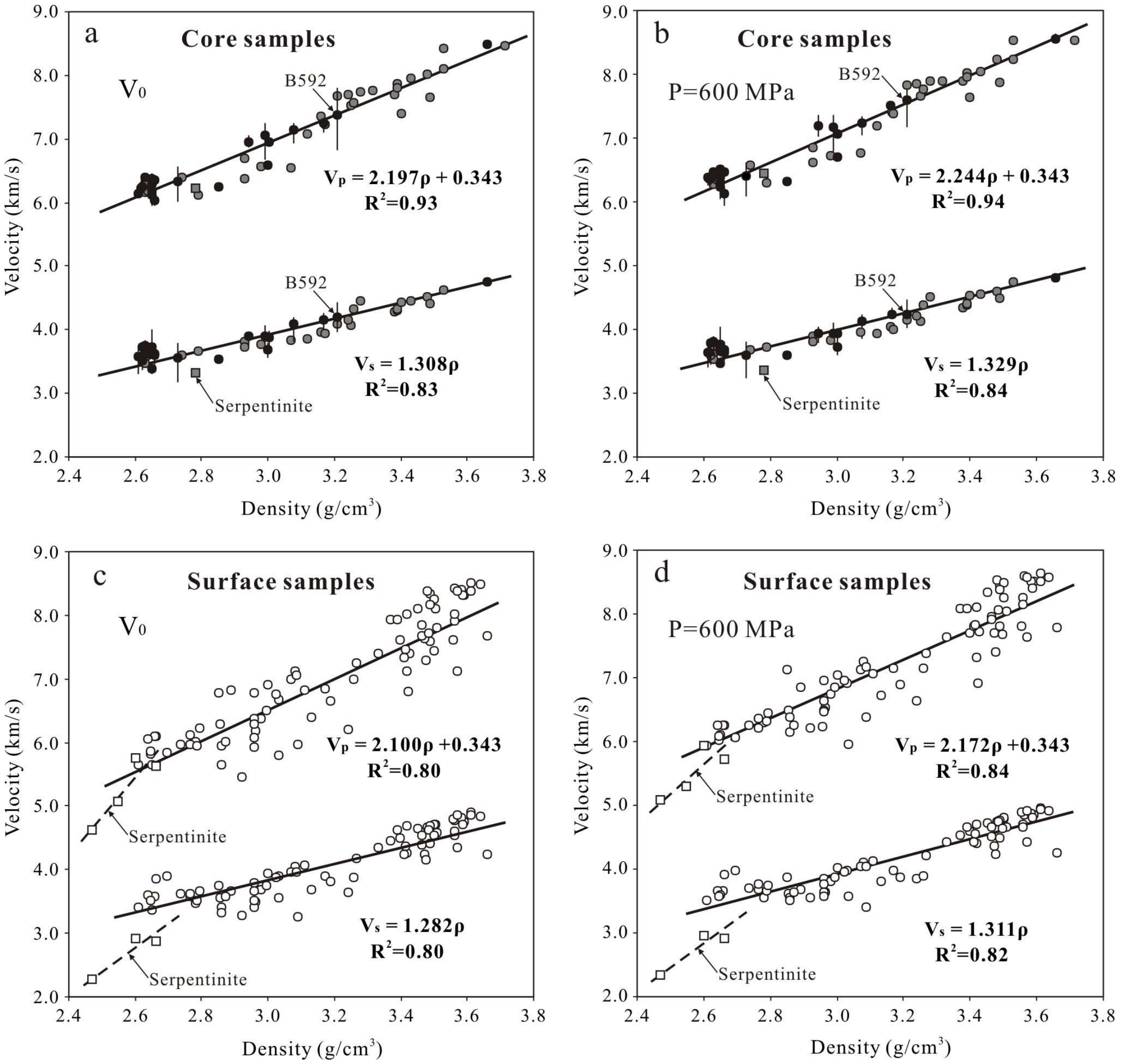

Figure 3.6 Mean P- and S-wave velocities (reference values V_0 and the measured values at 600 MPa) as a function of density for samples collected from the CCSD borehole [a-b, solid dots from this study, and grey dots from Ji et al. (2007a), Kern et al. (2002), Wang and Ji (2009), and Wang et al. (2009)] and from the surface exposures [c-d, data from Wang et al. (2005a, b), Ji et al. (2007a), Wang and Ji (2009) and Kern et al. (1999, 2002)]. Serpentinites (grey or open squares) display different trends from the other categories of rocks. The vertical bars illustrate the ranges of velocity variation due to seismic anisotropy.

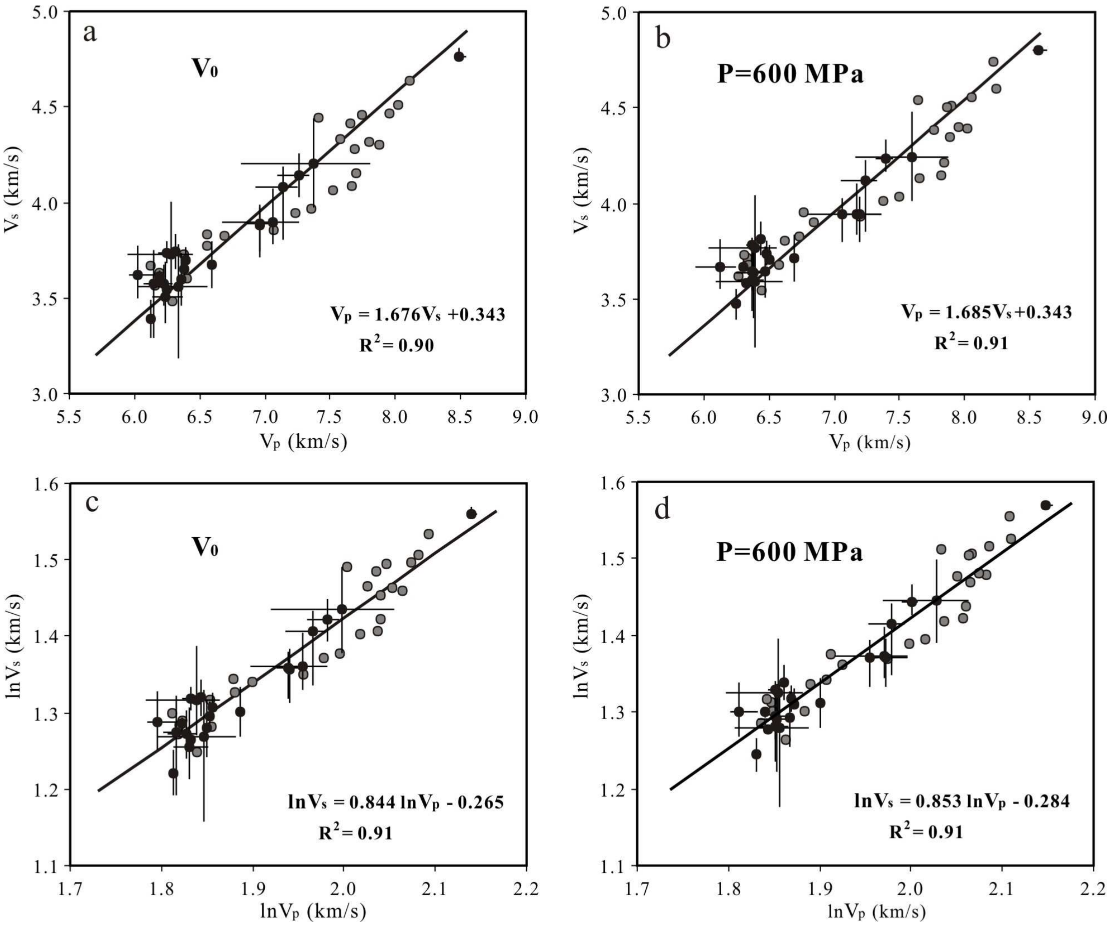

Figure 3.7 V_s-V_p (a-b) and $\ln V_s$-$\ln V_p$ (c-d) plots for the reference velocities V_0 and the measured values at 600 MPa of the samples from the CCSD borehole core material. Solid dots: data from this study; grey dots: data from Ji et al. (2007a), Kern et al. (2002), and Wang and Ji (2009). The experimental data are fitted using linear correlation. Bars illustrate the ranges of velocity variation due to seismic anisotropy.

The $\ln V_s$-$\ln V_p$ plots are illustrated in Figs. 3.7c-d. The least-squares linear fit yields: $\ln V_s=0.844\ln V_p-0.265$ ($R^2=0.91$) for the V_0 values, and $\ln V_s=0.853\ln V_p-0.284$ ($R^2=0.91$) for the velocities at 600 MPa. The slope of the $\ln V_s$-$\ln V_p$ trend corresponds to a scaling factor, $R_{s/p}$.

$$R_{s/p} = \frac{\partial \ln V_s}{\partial \ln V_p} = \frac{\partial V_s / V_s}{\partial V_p / V_p} \qquad (3.4)$$

where $\partial V_s / V_s$ and $\partial V_p / V_p$ are the S- and P-wave velocity anomalies, respectively. $R_{s/p}$ can be estimated from the P-wave travel time delay (∂t_p) and S-wave travel time delay data (∂t_s) at a given depth: $R_{s/p} \approx \left(V_s/V_p\right)\left(\partial t_s/\partial t_p\right)$. It is necessary to determine whether the velocity heterogeneities in the Earth's interior are caused by variations in temperature, chemical composition or phase transformation. The $R_{s/p}$ values obtained here, which are mainly induced by compositional change, should be different from those induced by temperature variation or phase transformation. Thus, $R_{s/p}$, which is a potential diagnostic for the origin of heterogeneities, may provide important constraints on the composition, physical state and structure of the Earth's interior because this factor, derived from seismic inversions, is less ambiguous than the absolute values of the anomalies (Kennett et al., 1998; Karato and Karki, 2001).

3.5.4 Elastic moduli

The average elastic properties of an anisotropic rock, which are equivalent to the properties of their isotropic counterparts, can be computed from the mean V_p, V_s and density values. The bulk modulus (K), Young's modulus (E), Lamé parameter (λ) and shear modulus (μ) for these equivalent isotropic rocks at 600 MPa, under which the effect of microcracks is eliminated, are plotted as a function of density in Fig. 3.8. Among these four moduli, only two are independent. As shown in Fig. 3.8, each of the elastic moduli (in GPa) increases linearly with increasing density (in g/cm^3): $K=87.55\rho-173.56$ ($R^2=0.93$), $E=111.32\rho-209.68$ ($R^2=0.95$), $\lambda=58.78\rho-119.98$ ($R^2=0.87$) and $\mu=43.16\rho-80.36$ ($R^2=0.94$). The fresh eclogite, which consists of garnet, omphacite, rutile and magnetite, displays significantly higher values of elastic moduli and ρ than retrograde eclogite, amphibolite, orthogneiss and paragneiss. Retrograde eclogites show slightly higher elastic moduli and densities than amphibolites. Felsic gneisses, including orthogneiss and paragneiss, display low elastic moduli and low densities, all clustering into an area at the left ends of the regression lines. Orthogneisses are indistinguishable from paragneisses in terms of either seismic velocities or elastic moduli.

3.5.5 P-wave velocity anisotropy

V_p anisotropy (A_p) is defined by Birch (1961) as:

$$A_p = (V_{\max} - V_{\min}) / V_m \times 100\% \qquad (3.5)$$

where V_{max}, V_{min} and V_m are, respectively, the maximum, minimum and mean values of the P-wave velocities measured in a given sample along different propagation directions. It is found that the anisotropy varies strongly with pressure. Three patterns have been distinguished (Fig. 3.9).

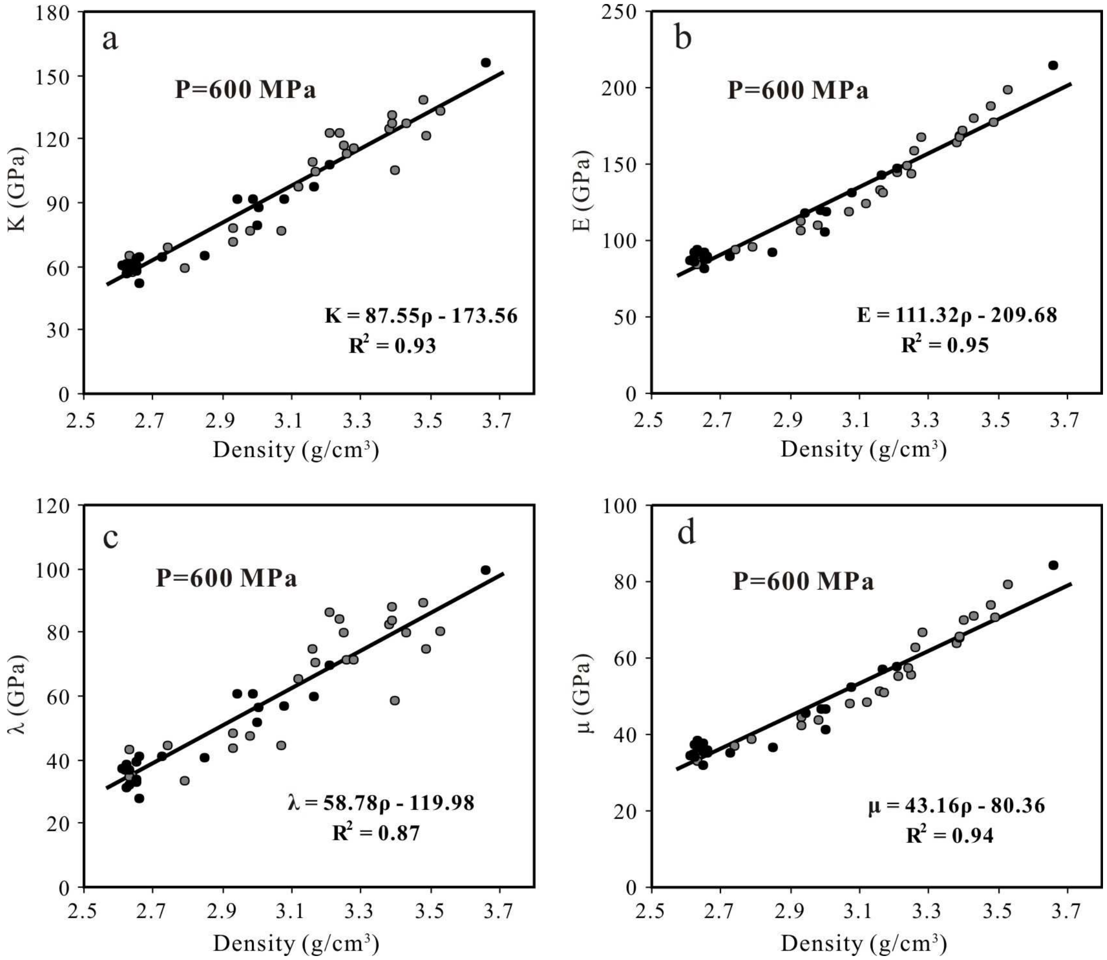

Figure 3.8 Bulk modulus K (a), Young's modulus E (b), Lamé parameter λ (c) and shear modulus μ (d) as a function of density for the samples from the CCSD borehole. Solid dots: data from this study; grey dots: data from Ji et al. (2007a), Kern et al. (2002), and Wang and Ji (2009).

Pattern 1: With increasing pressure, the anisotropy decreases rapidly below ~200 MPa and then slowly decreases or reaches a constant value above this pressure (e.g., sample B2520, Bt-Hbl granodioritic gneiss, Fig. 3.9). This pattern, which has been reported extensively for surface-derived samples (Christensen and Szymanski, 1988; Kern et al., 1999; Burke and Fountain, 1990; Wepfer and Christensen, 1991; Wang et al., 2005a; Ji et al., 1993, 2007a) and borehole core samples (Berckhemer et al., 1997; Ivankina et al., 2005) can be attributed to the closure of the aligned microcracks which reinforce the anisotropy induced by the lattice preferred orientations (LPO) of anisotropic minerals such as plagioclase, amphibole and mica (Ji et al., 1993; Ivankina et al., 2005).

Pattern 2: The anisotropy increases first with increasing pressure in the low-pressure range (< ~150 MPa), and then decreases at higher pressures (e.g., sample B592, retrograde eclogite, Fig. 3.9). This pattern can be attributed to a rapid closure at low pressures of aligned microcracks which oppose the LPO-induced anisotropy (Ji et al., 1993, 2007a).

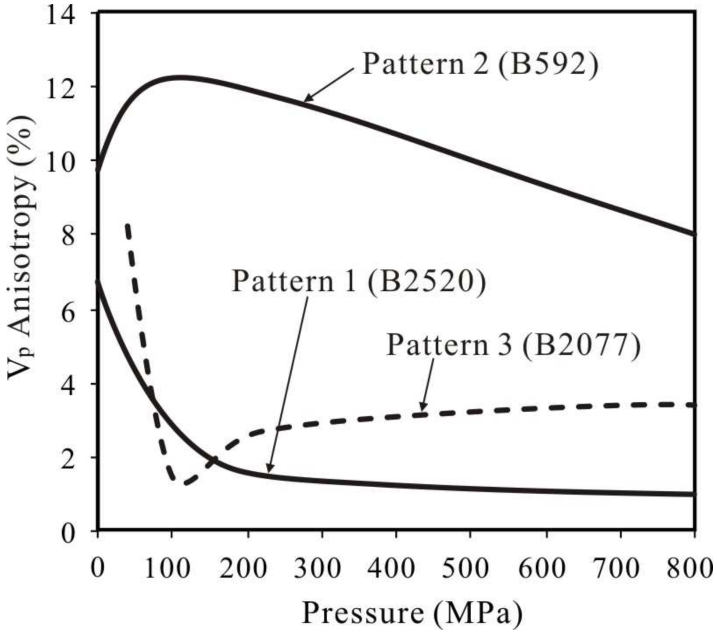

Figure 3.9 P-wave velocity anisotropy defined by Eq. (3.5) as a function of pressure for samples B2520 (Pattern 1), B592 (Pattern 2) and B2077 (Pattern 3). Modal and chemical compositions of each sample are given in Tables 3.1 and 3.2, respectively.

Pattern 3: The anisotropy decreases rapidly with increasing pressure at low pressures (<~100 MPa), then increases at moderate pressures (100-200 MPa) and finally increases slightly at high pressures >~200 MPa (e.g., sample B2077, Bt granodioritic gneiss, Fig. 3.9). This pattern, which was also reported in Ji et al. (1993, 2007a) and Wang et al. (2005a), is caused by a complex interaction between the effects of the closure of orthogonal microcracks, LPO and confining pressure. The reduction in anisotropy at lower pressures and the increase at higher pressures have the same origins as Pattern 1 and Pattern 2, respectively.

3.5.6 Shear wave splitting

For a given propagation direction Λ, shear wave splitting $(\Delta V_s)_\Lambda$ is defined as the difference in velocity between fast and slow split, or polarized, S-waves propagating in the same direction Λ. The splitting is both direction- and pressure-dependent. The variation of shear wave splitting with pressure can be classified into 4 patterns (Fig. 3.10): Pattern 1 (Fig. 3.10a) is characterized by an initial rapid decrease in splitting with increasing pressure in the low pressure regime, and then approaches a quasi-constant value (e.g., X-directions of samples B1536 and B1721) or decreases slightly with increasing pressure until a constant value is reached (e.g., X-direction of sample B534) in the high pressure regime. Pattern 2 (Fig. 3.10b) displays a pattern in which the splitting increases rapidly, then becomes nearly constant (e.g., Z-directions of samples B1651 and B592). Interestingly, shear wave splitting along the X-direction in an eclogite sample (B274) is nearly zero at pressures above ~200 MPa, indicating that the splitting below this pressure is purely due to the orientation of microcracks (Crampin, 1987). Pattern 3 (Fig. 3.10c) is characterized by an initial rapid decrease in splitting at low pressures (<100 MPa), followed first by an increase at moderate pressures (100-300 MPa) and then a quasi-constant value at high pressures (>300-400 MPa). Finally, Pattern 4 shows little variations in splitting with increasing pressure (Fig. 3.10d).

3.6 Discussion

3.6.1 Seismic velocity hysteresis

Seismic velocity hysteresis is well known but poorly understood. Crack-free single crystals and glasses (McSkimin and Andreatch, 1962; Peselnick and Wilson, 1968) do not show any acoustic hysteresis while the hysteresis phenomenon is systematically observed in porous materials such as soils (e.g., Lu, 2005), concretes (e.g., Guyer and Johnson, 1999) and natural sedimentary and crystalline rocks (e.g., Birch, 1960; Gardner et al., 1965; Holcomb, 1981; Burke and Fountain, 1990; Ji et al., 1993, 2007a; Burlini and Kunze, 2000). Seismic velocity hysteresis (Fig. 3.5) may be caused by the following three mechanisms.

(1) Irreversible closure of microcracks or the effect of so-called crack lips adhesion: the microcracks closed during pressurization do not reopen completely during subsequent

depressurization (Birch, 1960; Gardner et al., 1965; Burke and Fountain, 1990). However, the details of the adhesion mechanism have not been made clear.

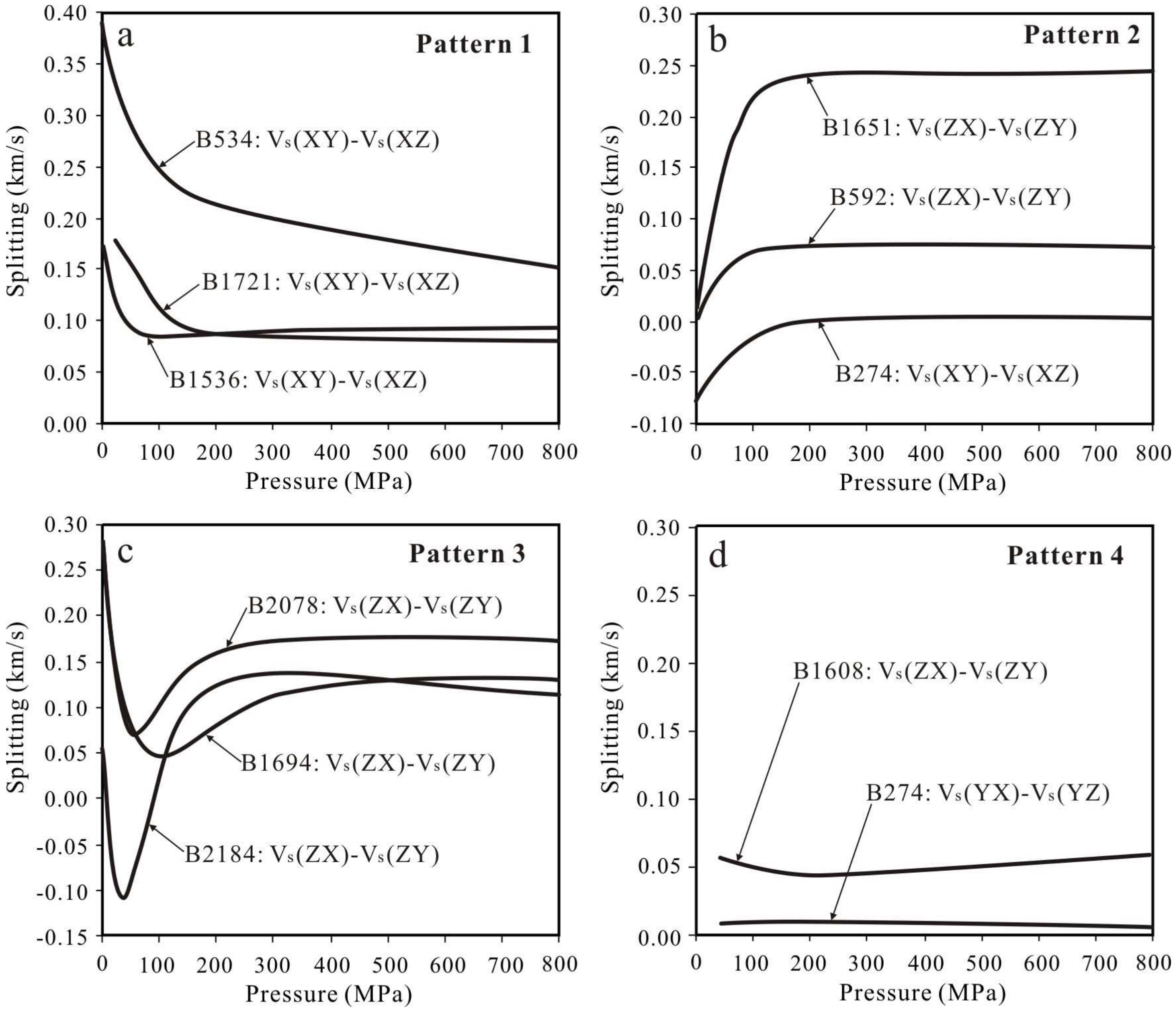

Figure 3.10 Four types of shear wave splitting versus pressure curves observed for samples from the CCSD cores. (a) Pattern 1; (b) Pattern 2; (c) Pattern 3; and (d) Pattern 4. See text for characteristics of each pattern.

(2) Irreversible compaction of pore spaces: the pores collapsed at higher pressures do not recover their original shapes or dimensions when returned to lower pressures. This mechanism occurs more likely in porous sedimentary rocks such as shale (Jones and Wang, 1981), but is almost impossible in high-grade metamorphic rocks that contain very low porosity (≤0.5%) and consist of high strength minerals such as quartz and garnet.

(3) Improvement of contact conditions: the contact conditions can be significantly improved by local ductile cushions of weak, retrograde, alteration or weathering materials (e.g., chlorite, sericite, serpentine, talc, muscovite, illite, kaolinite, smectite, and halloysite) along grain boundaries, interfaces, cleavages and microcracks. The ductile cushion likely prevents crushing of asperities. Previous investigations were done on the seismic hysteresis of rock samples collected from surface outcrops (Birch, 1960; Burke and Fountain, 1990; Ji et al., 1993), in which microcracks and grain boundaries are often altered and filled with alteration materials such as sericite or chlorite. The ductile cushion of these soft minerals should be able to improve grain-to-grain contact conditions during pressurization, but the soft minerals do not recover their original shapes at lower pressures, causing strong seismic velocity hysteresis (Ji et al., 2007a).

However, all the samples studied here were collected from various depths of the CCSD main borehole in which most of the microcracks likely formed during drilling, core retrieval and subsequent stress-relief processes. Our results show that only the nearly-linear segment of the velocity-pressure curves above P_c can be reproduced and reversed in the laboratory while those below P_c vary to a certain degree from run to run. This suggests that seismic velocity hysteresis is indeed very sensitive to the state of microcracks (e.g., the ratio of crack aperture to length) within rocks that possess a discrete memory of their past pressure history. The density and aspect-ratio of stress-relief microcracks depend on many factors such as lithology, mineralogy and microstructure (e.g., grain size, and density of foliation) and their density probably also increases with increasing sampling depth for rocks with the same lithology, mineralogy and microstructure (Meglis et al., 1991). In hard minerals such as garnet and quartz, the newly formed microcracks are fresh and clear without alteration products and thus the ductile cushion mechanism may not be operative. The stress-relief is often direction-dependent in foliated and lineated core samples that are anisotropic in terms of their mechanical properties (Ji et al., 1997b). This explains qualitatively why seismic velocity hysteresis varies with direction in most CCSD samples (Fig. 3.5).

3.6.2 P-wave velocity anisotropy

Crack-free single crystals and glasses do not display discernible B_0 values (Bass, 1995), suggesting that B_0 is indeed an indicator of microcrack density and geometry within rocks (Ji et al., 2007a). The higher B_0 values for the CCSD core samples are caused by the presence of the large number of microcracks formed during polyphase brittle deformation events: microfracturing during exhumation, drilling and stress relaxation after rapid removal of the drill cores. It should be noted that the B_0 value depends on direction. Its value for the P-wave velocity in the X direction is often larger than that in the Z direction, indicating that the intragranular and transgranular microcracks normal to the lineation are more effective in lowering velocity than the grain boundary cracks in the UHP metamorphic rock samples from the CCSD main hole. The opposite has been reported for greenschist- or amphibolite-facies rocks from the KTB drill core (Prasad et al., 1994). These authors reported that $V_p(Z)$ increases more strongly with pressure than either $V_p(X)$ or $V_p(Y)$, which they attributed to microfracturing induced by stress release that is largest in the direction normal to the foliation. The above discrepancy is due to differences in the composition of constituent minerals and the orientation of the structural framework (i.e., foliation and lineation) with respect to the regional tectonic stress field. The higher volume fractions of phyllosilicates such as mica and chlorite favor grain-boundary microfracturing parallel to the foliation (Jahns et al., 1994) while stress-release microfracturing in quartz and garnet are frequently normal to the lineation (Siegesmund et al., 1993; Ji et al., 1997b). The (001) cleavage planes of biotite, muscovite and chlorite, which are preferentially aligned parallel to the foliation, are easily opened (Vollbrecht et al., 1999; Jahns et al., 1994) during stress relaxation because the phyllosilicates are extremely anisotropic in compressibility (Bass, 1995).

Equation (3.5), which was defined by Birch (1961), has been used widely in the quantification of seismic anisotropy in rocks in the full range of pressures. However, this equation is relevant only for the description of LPO-induced seismic anisotropy which does not vary much with pressure, but may be inappropriate for crack-related seismic anisotropy that often varies in a complex manner with increasing pressure. For sample B270 (Figure 3.11a), which is a rutile eclogite collected from a depth of 547.20 m in the CCSD main borehole (Wang et al., 2009), $V_p(Y)>V_p(X)>V_p(Z)$ below 360 MPa while $V_p(X)>V_p(Y)>V_p(Z)$ above this pressure. The use of Eq. (3.5) leads unavoidably to an ambiguity in the relation between the P-wave velocity anisotropy pattern and the preferred orientation of microcracks. Actually, variations of the values of $V_p(X)$-$V_p(Y)$, $V_p(X)$-$V_p(Z)$ and $V_p(Y)$-$V_p(Z)$ with pressure (Fig.3.11) can provide important hints regarding the preferred orientation of microcracks that causes P-wave velocity anisotropy in the low pressure regime. Velocities propagating across aligned cracks are much lower than parallel to them. With increasing pressure, microcracks with smaller aspect-ratios will close first, followed by those with larger aspect ratios. The variations in velocities and their directional dependence with increasing pressure thus offer information about the preferred orientation of microcracks within the rocks. The velocity anisotropy pattern in sample B270 (Fig. 3.11a), for instance, infers that two sets of orthogonal microcracks are aligned equally normal to Z- (Type 1) and X- (Type 2, Fig 3.12) directions. These microcracks are progressively closed with increasing pressure: the progressive closures of Type 1 and Type 2 cracks cause gradual increases in both $V_p(Z)$ and $V_p(X)$ but have little effect on $V_p(Y)$. As a result, $V_p(X)$-$V_p(Y)$, $V_p(Y)$-$V_p(Z)$ and $V_p(X)$-$V_p(Z)$ increase, decrease and remain almost unchanged, respectively, with increasing pressure from 0.1 to 360 MPa (Fig. 3.11a). The anisotropy above 360 MPa is caused by the LPO of omphacite.

In sample B295, which is a coarse grained rutile eclogite collected from a depth of 586.10 m in the CCSD main borehole (Wang et al., 2009), the values $V_p(X)$-$V_p(Y)$, $V_p(Y)$-$V_p(Z)$ and particularly $V_p(X)$-$V_p(Z)$ decrease with increasing pressure from 0.1 to 300 MPa (Fig. 3.11b). The mode of variation suggest that Y-normal and particularly, Z-normal microcracks, control the P-wave velocity anisotropy in this sample.

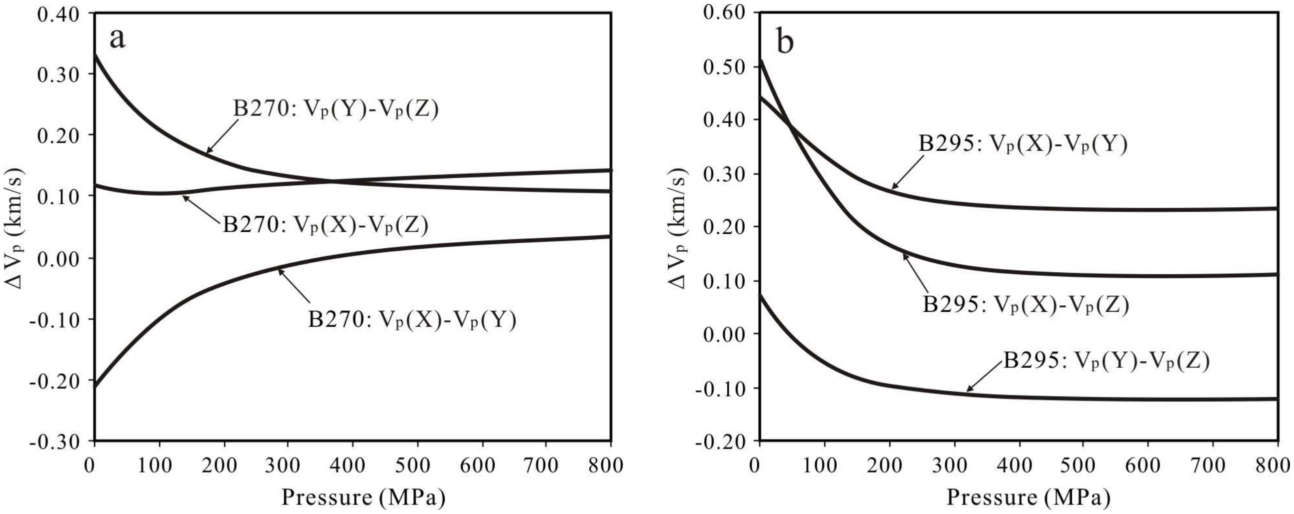

Figure 3.11 Differences in P-wave velocity (km/s) between different propagating directions as a function of pressure for samples B270 (a) and B295 (b).

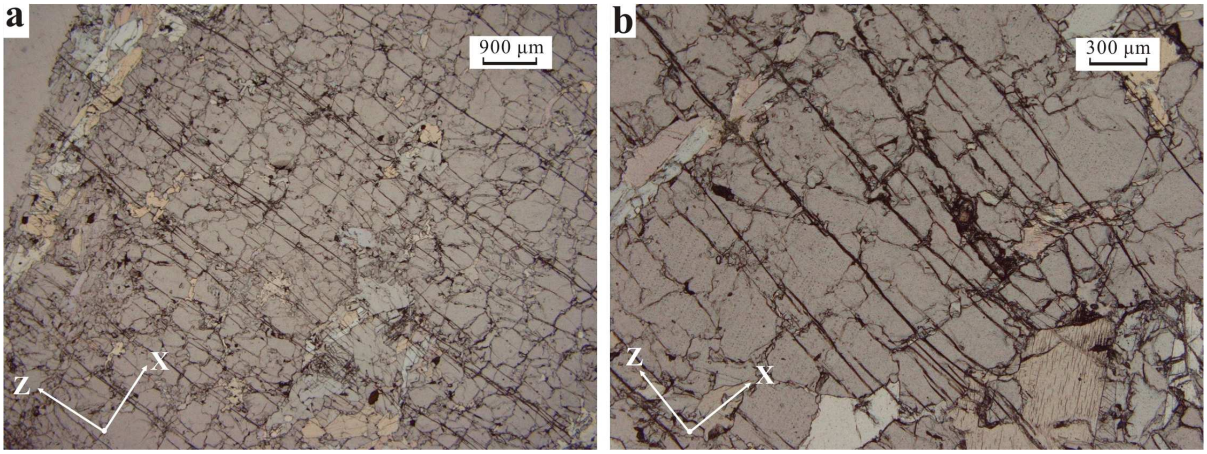

Figure 3.12 Optical micrographs (XZ plane) illustrating X-normal (Type 2) microcracks in samples collected from Sulu UHP terrane, China.

3.6.3 Shear wave splitting

The shear wave splitting versus pressure curves have been classified into 4 patterns (Fig. 3.10). For Pattern 1 (Fig. 3.10a), the quasi-constant splitting above the crack-closing pressure (200-300 MPa) should be related to intrinsic properties (i.e., LPO and compositional layering) whereas the splitting below the crack-closing pressure is caused by constructive interference of oriented microcracks and the LPOs of anisotropic minerals such as amphibole, mica, pyroxene and feldspar (Kern and Wenk, 1990; Ji and Salisbury, 1993; Kern et al., 2001). For example, $V_s(XY)-V_s(XZ)$ is positive for samples B534, B1536 and B1721. The rapid decrease in splitting in the low pressure regime is caused by a progressive increase in $V_s(XZ)$ due to the progressive closure of the foliation-parallel cracks (Type 1) which are common in these rocks while $V_s(XY)$ is not affected by the presence of these cracks.

Pattern 2 splitting (Fig. 3.10b) is caused by destructive interference of the effects of oriented microcracks and LPOs of anisotropic minerals. In other words, in the samples showing Pattern 2 splitting, microcracks are preferentially oriented in such a manner that the microcrack-induced splitting opposes the LPO-induced splitting. Microcracks in samples B592 and B1651 are principally perpendicular to the foliation (XY) and to the lineation (X). The presence of these microcracks (Type 2, Fig 3.12) causes a decrease in $V_s(ZX)$ but has little influence on $V_s(ZY)$. Accordingly, the progressive closure of these microcracks with increasing pressure increases the $V_s(ZX)-V_s(ZY)$ splitting in the low pressure regime. Almost no shear wave splitting can be observed in the Z-directions of samples B592 and B1651 below 20 MPa because the crack- and LPO-induced anisotropies entirely cancel each other (Fig. 3.10b). Interestingly, the shear wave splitting along the X-direction in sample B274 (eclogite) is induced almost entirely by the preferred orientation of microcracks (normal to the Y-direction, Type 3), as proposed by Crampin (1987), because it becomes zero at pressures above ~200 MPa (Fig. 3.10b).

For Pattern 3 (Fig. 3.10c), the reduction and then the increase in splitting at low and moderate pressures have the same origins as Patterns 1 and 2, respectively. In the samples displaying this pattern (e.g., samples B1694, B2078, and B2184), two sets of orthogonally aligned microcracks (Types 2 and 3) cause destructive and constructive interference with the LPO-induced splitting, respectively. The Z-minicore from sample B2078 (orthogneiss) is taken as an example to explain the complex interaction among the effects of the progressive closure of two sets of orthogonally oriented microcracks, LPO and confining pressure (Fig. 3.13). The Y-perpendicular microcracks (Type 3), which occur along grain boundaries and are commonly very flat with small ratios of aperture to length, are easily closed below ~60 MPa (Fig. 3.13c). In contrast, the X-perpendicular microcracks (Type 2, Fig. 3.12), which are generally intragranular cracks in hard minerals (Ji et al., 1997b, 2003) are more difficult to close and their full closure occurs only above ~300 MPa (Fig. 3.13b). The progressive closure of these types of microcracks with increasing pressure yields the complex shear wave splitting versus pressure curves shown in Figs. 3.10c and 3.13d.

Pattern 4 of shear wave splitting, which is quite special, which corresponds directly to the LPO-induced intrinsic properties of the samples in either the low or the high pressure regimes. In sample B274, the microcracks that are dominantly aligned normal to the Y-direction have little influence on the splitting of S-waves propagating in this direction. Hence the difference between $V_s(YX)$ and $V_s(YZ)$ remains almost constant with increasing pressure (Fig. 3.10d). In sample B1608, however, the closure of the microcracks of Types 2 and 3 with increasing pressure makes both $V_s(ZX)$ and $V_s(ZY)$ increase so simultaneously that the difference between $V_s(ZX)$ and $V_s(ZY)$ remains almost unchanged with increasing pressure (Fig. 3.10d). In other words, the effects of X- and Y-normal microcracks on the shear wave velocities propagating in the Z-direction are almost entirely cancelled by each other in the rock sample.

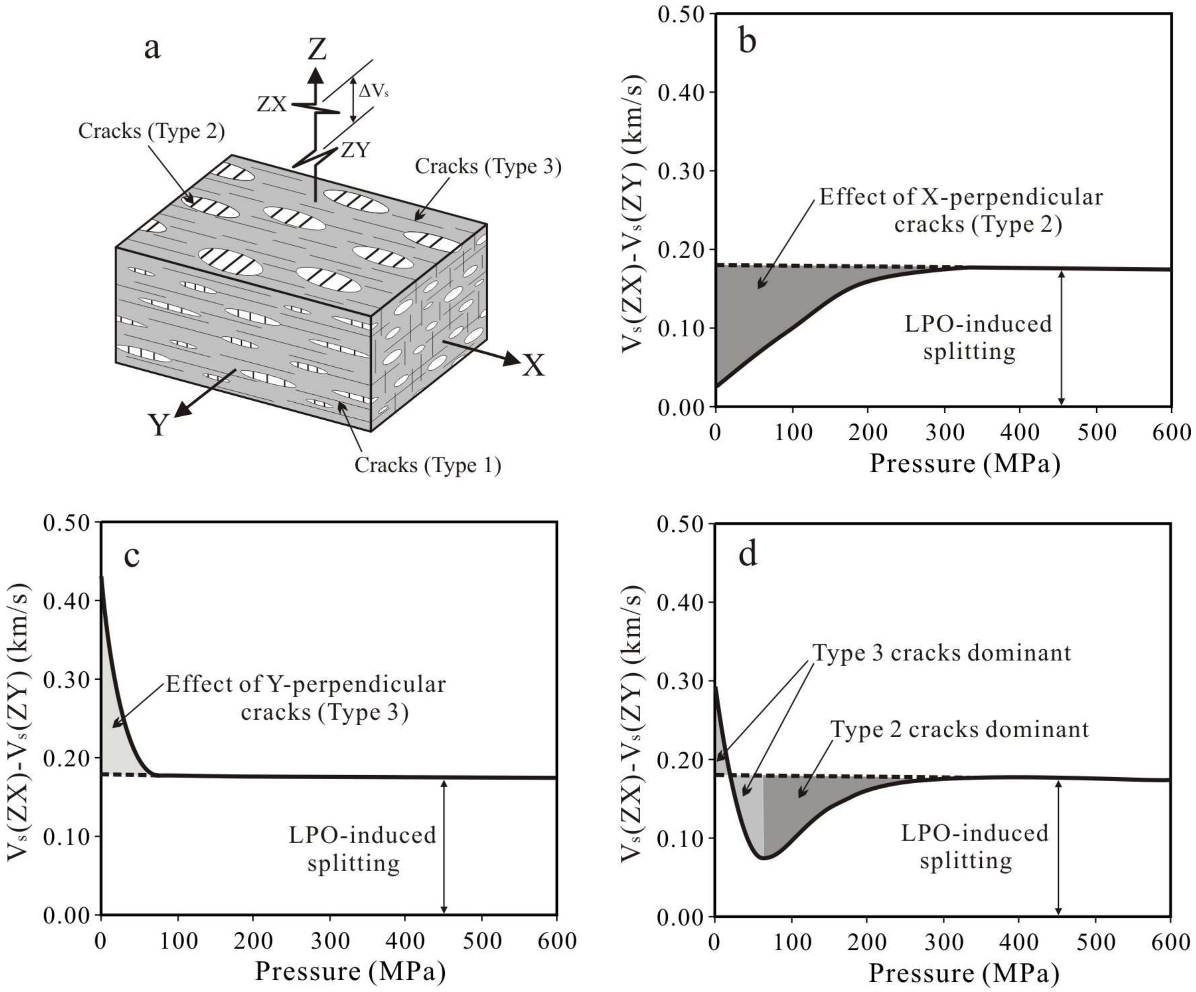

Figure 3.13 Interpretation for the summed contribution of oriented cracks and mineral LPO to shear wave splitting observed along the direction normal to foliation.

3.6.4 Comparison between surface-derived and CCSD core samples

Much of our knowledge of the seismic properties of rocks comes from the investigations of rocks samples collected from surface exposures (Christensen, 1989; Ji et al., 2002). The core material recovered from the CCSD borehole provided us an excellent opportunity to compare the V_p-P behaviors between the deep core samples and their surface equivalents.

Figure 3.14a illustrates the distributions of P_c values for the CCSD core and surface samples of 4 lithologies (i.e., felsic gneiss, eclogite, retrograde eclogite, and amphibolite). For each lithology, the mean P_c value for the CCSD core samples is significantly lower than that of their surface equivalents (Table 3.6). For example, the $\overline{P_c}$ values for the core and surface felsic gneisses are 179 and 269 MPa, respectively. Similarly, the $\overline{P_c}$ values for the core and surface eclogites are 138 and 342 MPa, respectively.

The average values of V_0, D, B_0, and k for the core and surface samples of the 4 lithologies are given in Table 3.6 (Kern et al., 1999; Wang et al., 2005a, b; Ji et al., 2007a). As shown in Figs. 3.14b-d, the CCSD core samples are characterized by significantly higher $\overline{B}_0$ (1.346 km/s) and $\overline{k}$ (2.274×10^{-2} MPa^{-1}), but lower $\overline{D}$ (2.287×10^{-4} km/s/MPa) values than their surface analogues ($\overline{B}_0$=0.828 km/s, $\overline{k}$=1.227×10^{-2} MPa^{-1}, $\overline{D}$=3.115×10^{-4} km/s/MPa), although the latter fall into the category of visibly fresh or slightly weathered rocks in the outcrops (the rock hammer rings and bounces back, Ehlen, 2002).

Generally speaking, the seismic velocities of the deep borehole core samples are significantly more and less sensitive to pressure in the nonlinear and linear regimes, respectively, than the surface-derived samples. Based on the theory of continuum elasticity, Walsh (1965) and Sneddon and Lowengrub (1969) show that the closure pressure for thin-disk-shaped cracks in a homogeneous, isotropic material is linearly proportional to their aspect ratio (α=W/L, where W and L are the aperture and length of the cracks, respectively). Thin-disk-shaped cracks with small α are more readily closed by the application of hydrostatic pressure than those with large α. The mean P_c value for the core samples is significantly lower than that for their surface equivalents (Table 3.6). The above fact can be explained by the optical observations that the microcracks in the core and surface samples are distinctly different: the cracks in the core samples, which formed mainly by drilling damage and stress relief fracturing, are fresh, clean, sharp-edged and typically straight, have smaller α values, and contain no secondary minerals (Figs. 3.15a-b). Furthermore, the opposing walls of each crack are probably well matched and can be perfectly closed by relatively lower pressures. The cracks in the surface samples (Figs. 3.15c-d), however, have sinuous and discontinuous edges with higher α values as they may have been partially dissolved or sealed with hydrated secondary minerals such as kaolinite, illite, chlorite, sericite, serpentine, calcite, quartz, gibbsite and goethite. The partially dissolved or filled cracks are hard to close completely under hydrostatic pressures due to crack surface mismatch (Morrow et al., 1994), which accounts for the characteristic reduction in the pressure sensitivity of P-wave velocities in the nonlinear regime.

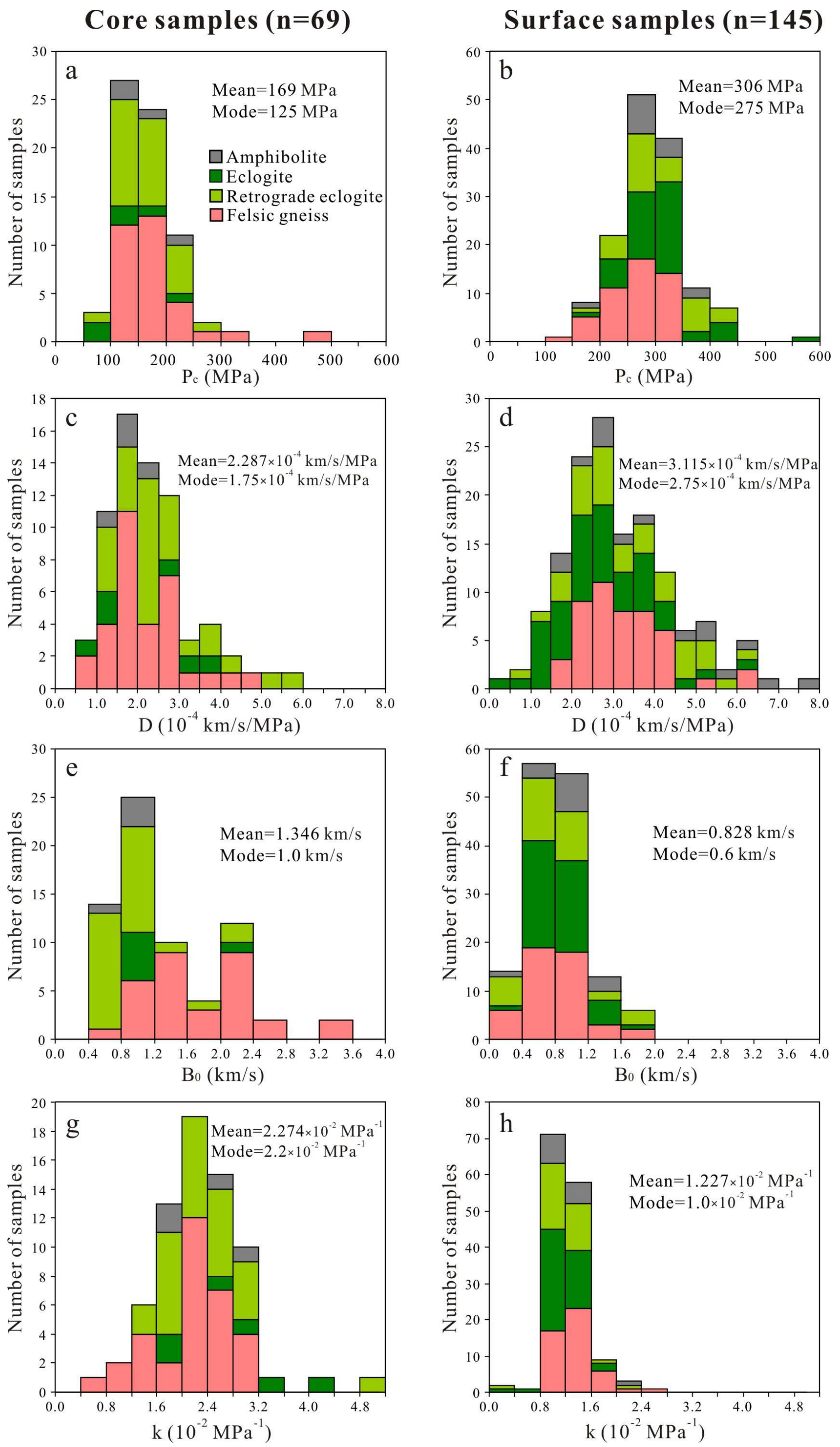

Figure 3.14 Histograms for the CCSD deep borehole core samples (left) and their surface equivalents (right). (a) P_c, the crack-closing pressure; (b) D, the intrinsic pressure derivative of velocity; (c) B_0, the maximum velocity increase due to crack closure; and (d) k, the decay constant controlling the shape of the nonlinear segment of the velocity-pressure curve.

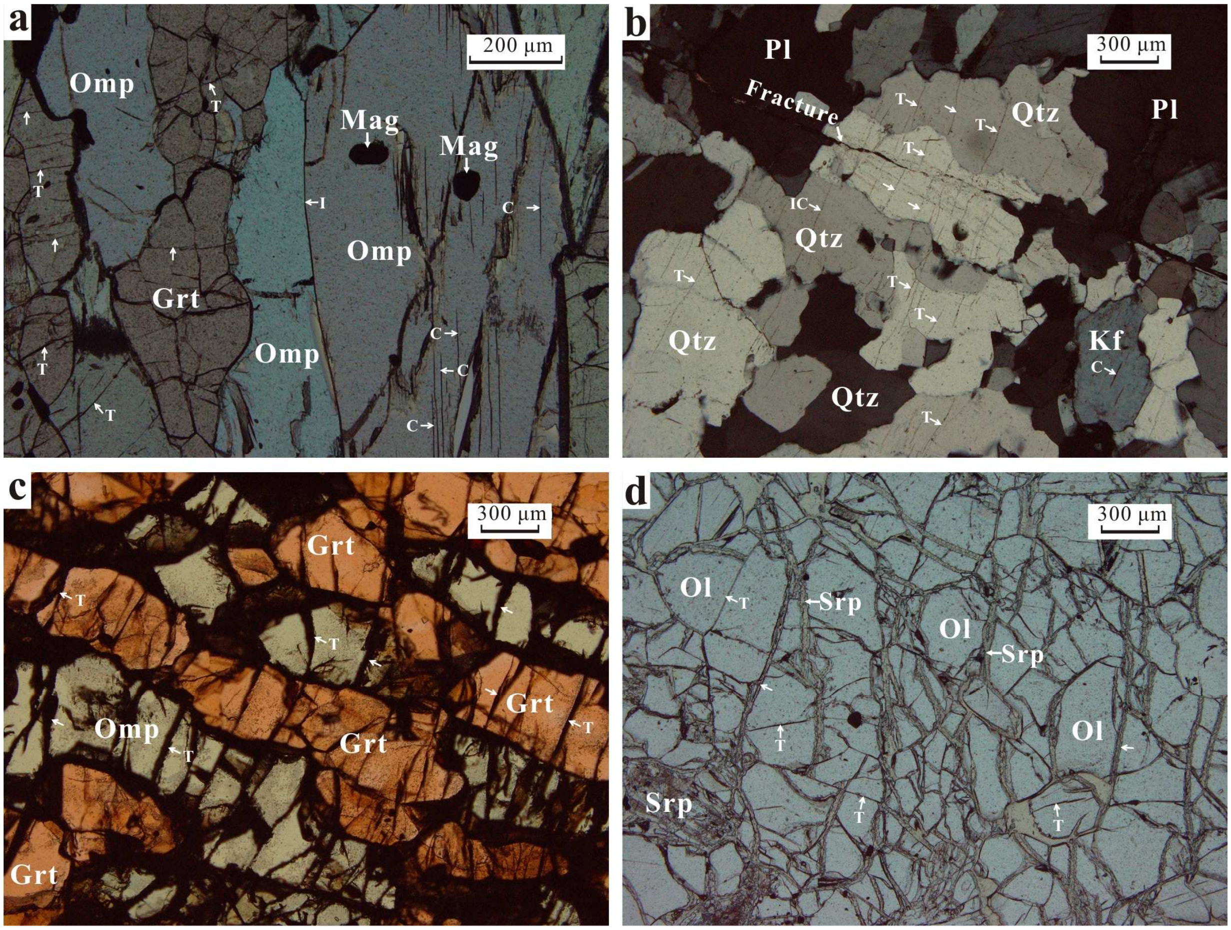

Figure 3.15 Optical micrographs (XZ plane) illustrating typical differences in the nature of intergranular (I), transgranular (T) and cleavage (C) cracks between the borehole core (a: eclogite from 552.0 m depth; b: granitic gneiss from 3926.7 m depth) and surface (c: eclogite; d: peridotite) samples. The microcracks in the surface samples are generally filled with weathering and low temperature alternation products, whereas those formed by drilling damage and stress-relief in the core samples are commonly clean without filling secondary minerals. Abbreviation: Grt, garnet; Kf, K-feldspar; Mag, magnetite; Ol, olivine; Omp, omphacite; Pl, plagioclase; Qtz, quartz; Srp, serpentine.

The increase in both B_0 and k for the core samples can be caused by extensive decompaction due to drilling, core retrieval and rapid pressure and temperature releases during retrieval of the core from great depths to the surface. The larger D values for the surface samples mainly reflect the presence of weathering and alteration products which fill or partially fill the cracks and pores and are distributed along grain boundaries of rocks that have been long exposed to the surface. These weathering and alteration materials, which are mechanically weak and ductile, can be compacted by applied hydrostatic pressure and tend to improve grain-to-grain contact conditions. Consequently the surface samples display relatively higher pressure sensitivity (*D*) in the linear regime.

Table 3.6 Parameters describing the V_p-P relationships for the CCSD borehole core samples and their analogues from surface exposures

Lithology	**Sampling Source**	**Number of Samples**	$\overline{P_c}$ **MPa**	$\overline{V_0}$ **km/s**	$\overline{D}$ **10^{-4} km/s/MPa**	$\overline{B_0}$ **km/s**	$\overline{k}$ **10^{-2} MPa^{-1}**
Amphibolite	Core	4	169±44	6.691±0.422	1.701±0.325	0.898±0.181	2.186±0.575
	Surface	15	301±50	6.330±0.528	4.160±1.826	0.881±0.297	1.206±0.267
Eclogite	Core	6	138±49	8.164±0.374	2.182±1.159	1.200±0.491	2.832±0.967
	Surface	48	342±173	7.652±0.210	2.984±1.251	0.834±0.349	1.154±0.315
Retrogade eclogite	Core	27	164±42	7.183±0.406	2.552±1.151	0.951±0.419	2.298±0.735
	Surface	34	328±156	6.817±0.466	3.333±1.409	0.771±0.453	1.182±0.323
Felsic gneiss	Core	32	179±73	6.236±0.179	2.157±0.883	1.762±0.676	2.160±0.553
	Surface	48	269±48	6.064±0.208	3.075±0.947	0.799±0.353	1.355±0.299

For each lithologic category, the mean V_0 value for the core samples is also systematically higher than that of surface samples (Fig. 3.6, Table 3.6). This indicates that the deep core material is much fresher than surface-derived analogues since the presence of chemical weathering and alteration products (e.g., kaolinite, illite, chlorite, sericite, serpentine, calcite, quartz, gibbsite, goethite, smectite and halloysite) along cracks and grain boundaries (Fig. 3.15c-d) can effectively decrease V_0. The above results suggest that high pressure data from core samples are more reliable than those from surface samples for extrapolation to deeper crust (Fig. 3.16). The crystalline rocks exposed at or near the Earth's surface where pressure and temperature conditions are far different from those of their formation, have unavoidably experienced weathering to adjust to the prevailing surficial conditions. The degree and nature of weathering vary widely and are controlled by many factors such as parent rock type, topography, climate, biological activity, and fluid composition (e.g., water, carbon dioxide, oxygen and organic acids released by decomposing plants). The composition and structures of weathered rocks are affected by various processes such as dissolution of primary minerals, formation of secondary phases, redox processes (particularly important for iron-bearing minerals), transport of materials, coprecipitation and ion exchange (e.g., White and Brantley, 1995; Islam et al., 2002). In the nonlinear regime, however, even the data from the borehole samples cannot be extrapolated precisely to the upper crust above the depth equivalent of the crack-closure pressure (Fig. 3.16) because most of the microcracks in core samples were probably not present in-situ and resulted from drilling and core-retrieval damage and stress-relief microfracturing.

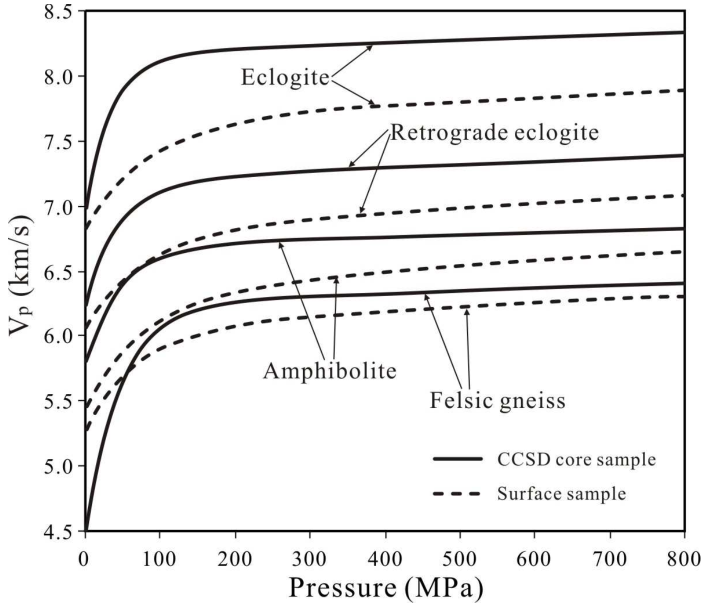

Figure 3.16 V_p-P curves computed from the parameters given in Table 3.6. Differences between the surface-derived and deep borehole core samples are clearly elucidated. An extrapolation of the surface sample data to deeper crustal levels will unavoidably lead to underestimates of V_p values. Note that for felsic gneiss, V_p of the core sample is lower and higher that of the surface sample, respectively, below and above ~60 MPa due to extensive microfracturing caused by drilling damage and stress-relief.

Petrographic observations suggest that Type 2 stress-relief microfractures (Fig. 3.12) are more abundant in quartz and garnet than in amphibole and other retrograde minerals. This may explain why the differences in B_0 between core and surface samples are much larger for felsic gneisses and eclogites than for amphibolites and retrograde eclogites (Table 3.6 and Fig. 3.14c). Thus, stress-relief and thermal-cracking damage are correlated with the contents of brittle minerals such as quartz (Morrow et al., 1994) and garnet (Ji et al., 1997b, 2003).

The comparison between the V_p-P behaviors for the core and surface samples implies also that the seismic velocities of brittle crust, particularly in fault zones, may not be constant over time because such rocks may experience cyclic crack-seal processes (Morrow et al., 1994). Mass transfer along with hydrothermal circulation causes such cracks to be repeatedly healed and sealed (Sibson et al., 1988), causing seismic velocity to fluctuate with time.

3.6.5 Comparison between calculated and measured seismic velocities

In this section, the seismic velocity (V_p or V_s) of each equivalent isotropic rock, which corresponds to the arithmetic mean of the values measured in three orthogonal directions for each sample (Christensen and Ramananantoandro, 1971; Ji et al., 2003), will be compared with the value computed from the volume fractions (Table 3.1) and elastic constants of constituent minerals (Table 3.7) at standard conditions (zero porosity, 0.1 MPa and 25 °C) using four different mixture rules [i.e., Voigt, Reuss, Voigt-Reuss-Hill (VRH) and geometric averages]. The relative error (R_e) between the theoretically calculated (V_c) and experimentally measured (V_e) velocity for each sample is defined as：

$$R_e = \frac{V_c - V_e}{V_e} \times 100\% \tag{3.6}$$

The smaller the R_e, the better the agreement between the calculated and measured velocities. Furthermore, a goodness-of-fit coefficient (R^2) is also used as a statistical measure of the comparison between the calculated and observed data.

$$R^2 = 1 - \frac{\sum_{i=1}^{M} (V_{ci} - V_{ei})^2}{\sum_{i=1}^{M} (V_{ei} - \overline{V_e})^2} \tag{3.7}$$

where V_{ci} and V_{ei} are the calculated and experimental values (either V_p or V_s) of *i*th sample, respectively; $\overline{V_e}$ is the mean experimental value of M samples. A perfect fit gives a value of $R^2=1$.

It has not been clear which mixture rule is the best to predict the average elastic properties of a given polymineralic rock. Crosson and Lin (1971) reported that the Voigt average from room pressure elastic constants offers a better prediction of V_p for the quasi-monomineralic Twin Sisters dunite (94.1% olivine, 4.9% orthopyroxene and 1% chromite and magnetite) than the other averages at pressures above 200 MPa. Seront et al. (1993) found that the Voigt average gives the closest approximation (within 0.1 km/s) to the high pressure (800 MPa) experimental V_p values of anorthosite (90% plagioclase and 10% olivine), while the Reuss and VRH values are significantly lower. The closest agreement between calculated and measured seismic velocities at 500-600 MPa has been reported for high-grade mylonites using the Voigt average (Siegesmund et al., 1989; Ji et al., 1993; Barruol and Kern, 1996). However, Christensen and Ramananantoandro (1971) and Babuska (1972) found that the VRH average from room pressure elastic constants provided the best prediction for the elastic wave velocities of dunite and bronzitite measured at 1.0 GPa. Hurich et al. (2001) claimed that the Voigt average resulted in the least error between measured and calculated P-wave velocities at 400 MPa for granitic rocks while the Reuss average produced the best fit for gabbroic rocks. Thus either the Voigt average (e.g., Mainprice and Casey, 1990; Ji et al., 1994; Kern et al., 1996a, 2001; Saruwatari et al., 2001) or the VRH values (e.g., Baker and Carter, 1972; Long and Christensen, 2000) have been used in the numerical modeling of rock seismic properties.

Table 3.7 Bulk (K) modulus, shear (μ) modulus (VRH average) and densities of monomineralic aggregates of rock-forming minerals used for calculations of seismic velocities

Minerals	**Density (g/cm^3)**	**K (GPa)**	**μ (GPa)**	**References**
Plagioclase (An9)	2.610	50.80	29.25	Hearmon, 1984
Plagioclase (An53)	2.680	70.68	33.56	Hearmon, 1984
K-feldspar	2.560	53.73	27.23	Hearmon, 1984
Quartz	2.648	37.84	44.29	Hearmon, 1984
Zircon	4.649	227.77	108.72	Hearmon, 1984
Hornblende	3.120	87.14	43.15	Hearmon, 1984
Magnetite	5.206	161.00	91.37	Hearmon, 1984
Rutile	4.260	212.95	111.63	Hearmon, 1984
Calcite	2.712	73.31	31.97	Hearmon, 1984
Albite	2.620	56.90	28.60	Hearmon, 1979
Garnet	4.131	176.83	95.89	Babuska et al., 1978
Epidote	3.400	106.15	61.20	Ryzhova et al., 1966
Orthopyroxene (En80)	3.354	103.46	74.72	Frisillo and Barsch, 1972
Zoisite	3.343	125.30	72.90	Mao et al., 2007
Omphacite	3.327	130.73	79.16	Bhagat et al., 1992
Diopside	3.289	112.93	67.09	Levien et al., 1979
Muscovite	2.844	58.18	35.36	Vaughan and Guggenheim, 1986
Talc	2.793	41.60	22.60	Bailey and Holloway, 2000
Serpentine	2.620	68.50	38.50	Bezacier et al., 2010

Figure 3.17 shows the histogramatic distributions of R_e for the Voigt, Reuss, VRH and geometric averages of V_0(P) (the projected zero pressure P-wave velocity) values and P-wave velocities at 200, 400 and 600 MPa for 22 CCSD core samples.

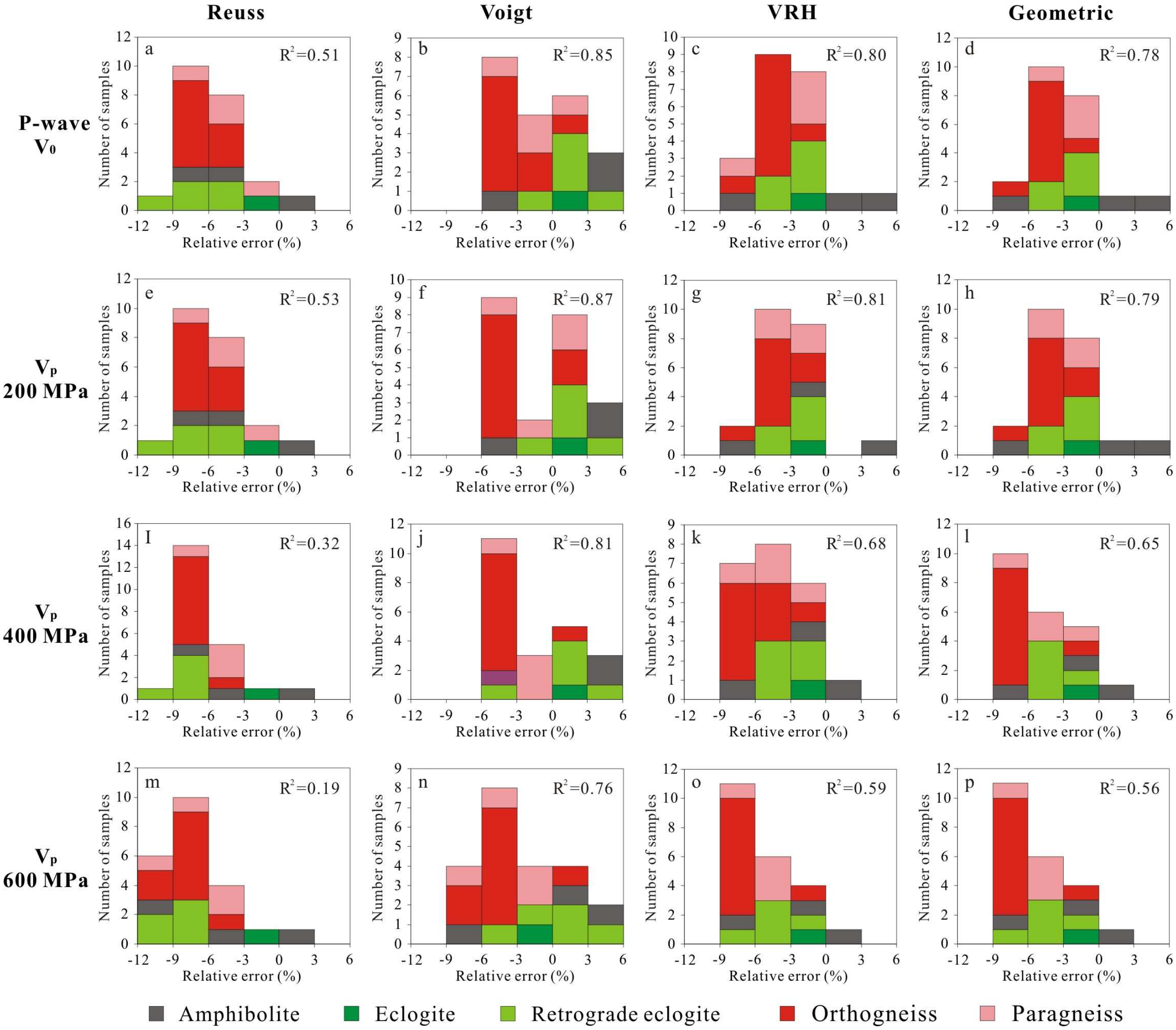

Figure 3.17 Relative errors of the Reuss, Voigt, VRH and Geometric averages for P-wave velocities (the reference value V_0 and the values at 200, 400 and 600 MPa) for CCSD borehole core samples. The relative error and R^2 are defined by Eq. (3.6) and Eq. (3.7), respectively.

It is interesting to note: (1) The Reuss average yields a systematic underestimation of the P-wave velocities for the samples. (2) The VRH average differs very little from the geometric mean but always yields slightly better results than the geometric mean although the latter is regarded as more rigorous in its physical implication (Mathies and Humber, 1993; Mainprice and

Humber, 1994). (3) The Voigt scheme gives the best estimate of P-wave velocities. This is consistent with previous observations of Crosson and Lin (1971), Ji et al. (1993), Seront et al. (1993) and Kern et al. (1996). The goodness-of-fit coefficient (R^2) decreases with increasing pressure from 200 to 600 MPa. The Voigt average calculated for the ideal, porosity-free aggregate from room pressure single crystal elastic constants exhibits a better match to velocities measured at 200 MPa than to V_0 values. The data do not confirm the previous observations that the closest agreement between calculated and measured P-wave velocities was observed for samples at 500-600 MPa (Siegesmund et al., 1989; Ji et al., 1993; Barruol and Kern, 1996).

The calculated S-wave velocities for this set of 22 samples according to the Voigt method at standard conditions display the best agreement with the measured data at 200-600 MPa (Fig. 3.18). The VRH scheme, which is better than the geometric mean, can also offer a remarkably good prediction for the S-wave velocities at pressures below 200 MPa. The Reuss scheme systematically underestimates the S-wave velocities for most of the samples, thus gives the worst agreement with the experimental values (Fig. 3.18).

The discrepancies between the calculated and measured seismic velocities (Figs. 3.17 and 3.18) are thought to be caused mainly by the following two sources of errors: (1) The constituent minerals (e.g., amphibole, pyroxene, plagioclase and garnet) in the measured rocks may not have exactly the same chemical compositions as the single crystals for which the published elastic constants were determined because the elastic constants have not been determined for a range of compositions. Also the elastic constants for biotite, phengite, sericite, chlorite, lizardite and chrysotile are unavailable. It is a common practice that the elastic constants of muscovite are used to represent those of biotite and phengite, and the elastic constants of serpentine for those of chlorite. (2) The modal composition of each sample is obtained using standard point counting or image analysis techniques on a single thin section, from a very small volume of each sample, as compared to the volume of the minicore sample in which velocities are measured. As long as compositional heterogeneity exists, the thin section may not be an accurate representation of the rock sample. As the uncertainties discussed above are difficult to avoid in the case of natural samples, comparisons between calculated and observed values in hot-pressed, porosity-free, isotropic multiphase composites with well controlled chemical compositions and volume fractions for each phase may be preferable for testing the mixing rules (Watt et al., 1976; Zhang et al., 1996; Ji and Wang, 1999). Much work remains to be done in this area to yield better constraints on the interpretation of seismic data.

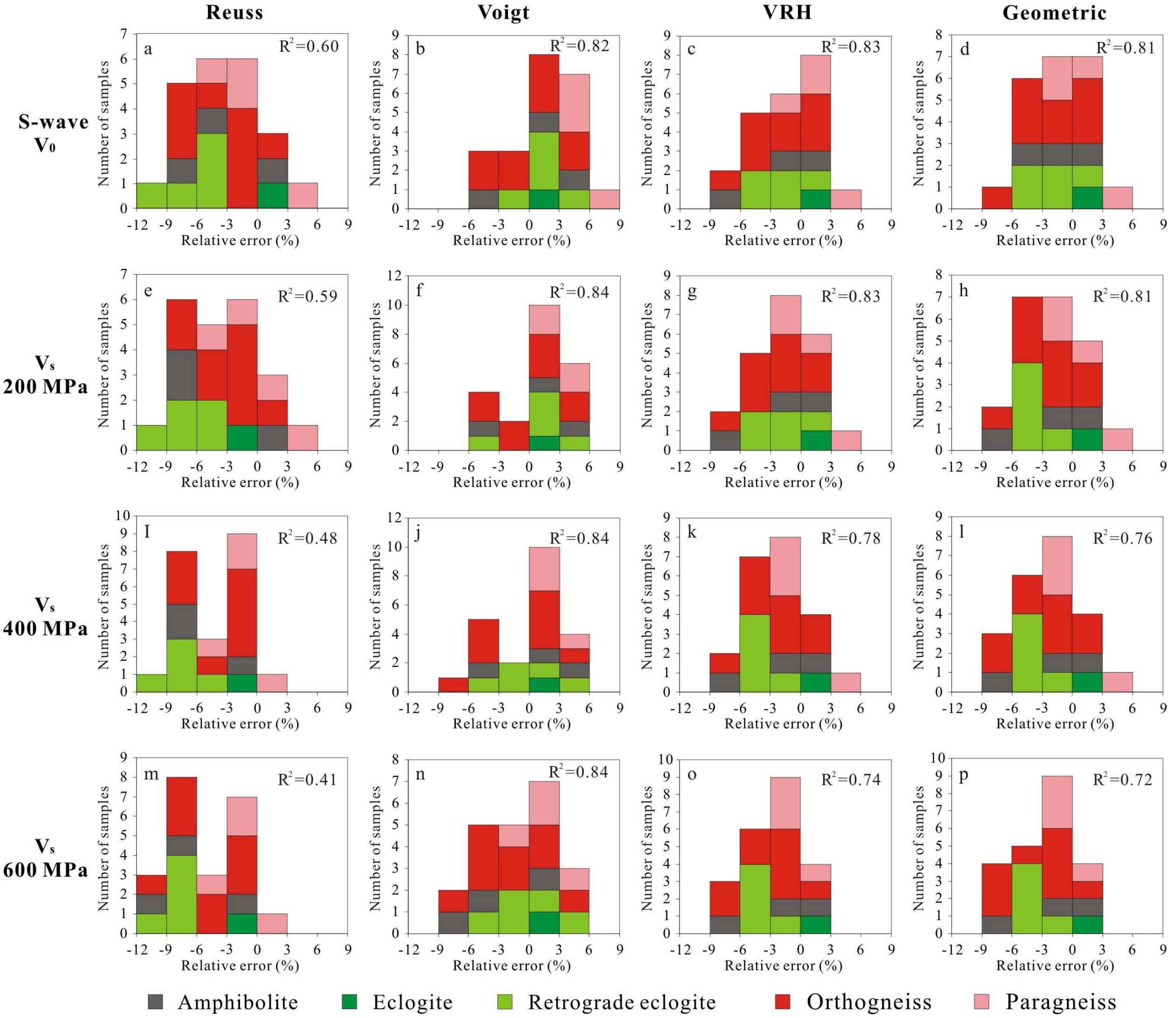

Figure 3.18 Relative errors of the Reuss, Voigt, VRH and Geometric averages for S-wave velocities (the reference value V_0 and the values at 200, 400 and 600 MPa) for CCSD borehole core samples. The relative error and R^2 are defined by Eq. (3.6) and Eq. (3.7), respectively.

3.6.6 Comparison with borehole logging data

The temperature increases from ~15 °C at the surface to 135 °C at a depth of 5000 m in the CCSD main hole, giving an average thermal gradient of 24 °C/km. Assuming that the seismic velocities of the rock samples have little temperature-dependence in this range of temperatures

(Kern et al., 2002), we calculated the P- and S-wave velocities of each dry sample at an in-situ lithostatic pressure (P_i) corresponding to its downhole depth,

$$P_i = (\sigma_V + \sigma_H^{Max} + \sigma_H^{Min}) / 3 \tag{3.8}$$

where σ_v is the vertical stress and equals ρgz [ρ is the average density (2.85 g/cm^3) of the overlying rocks from surface to depth z, and g is the acceleration of gravity], σ_H^{Max} is the maximum horizontal stress, and σ_H^{Min} the minimum horizontal stress). The σ_H^{Max} and σ_H^{Min} values (Fig. 3.19a), which were measured by Cui et al. (2009) using wellbore breakout techniques, display linear correlations with depth (m):

$$\sigma_H^{Max} = 0.0327z - 0.7738 \quad (R^2=0.99) \tag{3.9}$$

$$\sigma_H^{Min} = 0.0246z - 4.2543 \quad (R^2=0.96) \tag{3.10}$$

The calculated velocity results for the 22 samples are plotted on the V_p-depth and V_s-depth profiles constructed from borehole logging data (Fig. 3.19c). A good correlation (≤5%) between the laboratory-measured and borehole logging velocity data occurs at depths below about 3500 m where the rocks are dominated by felsic orthogneiss and paragneiss that are relatively dry and intact with few visible fractures. Above this depth, however, the rocks are fractured and saturated with water, and thus display an obvious discrepancy in either P- or S-wave velocity with the velocities of dry core samples measured under the laboratory conditions. The measured velocities at in-situ pressures do not match the logging observations mainly for the following reasons:

Seismic properties measured in the field sample much larger volumes than those measured in the laboratory (Jahns et al., 1994; Huenges et al., 1997). This is the so-called "scaling problem". For example, sample B274 from a depth of 552 m is a fresh rutile eclogite with V_p=7.90 km/s and V_s=4.64 km/s, while the rocks around this depth, which were measured by in-situ sonic logging experiments, are dominantly retrograde eclogites with average values V_p=7.1 km/s and V_s=4.0 km/s (Fig. 3.19c). In contrast, the use of highly retrograde eclogite to represent an interval of fresh or weakly retrograde eclogite will unavoidably lead to an underestimation of both V_p and V_s in the depth range between 950-3050 m. The degree of retrograde metamorphism is thus a critical factor controlling the seismic properties of eclogites. Furthermore, the rocks on meter scale are often fractured and the fractures are filled with water. This gives a reasonable explanation why the logging velocities above the depth of 3500 m are generally lower than the laboratory velocities measured at equivalent pressures.

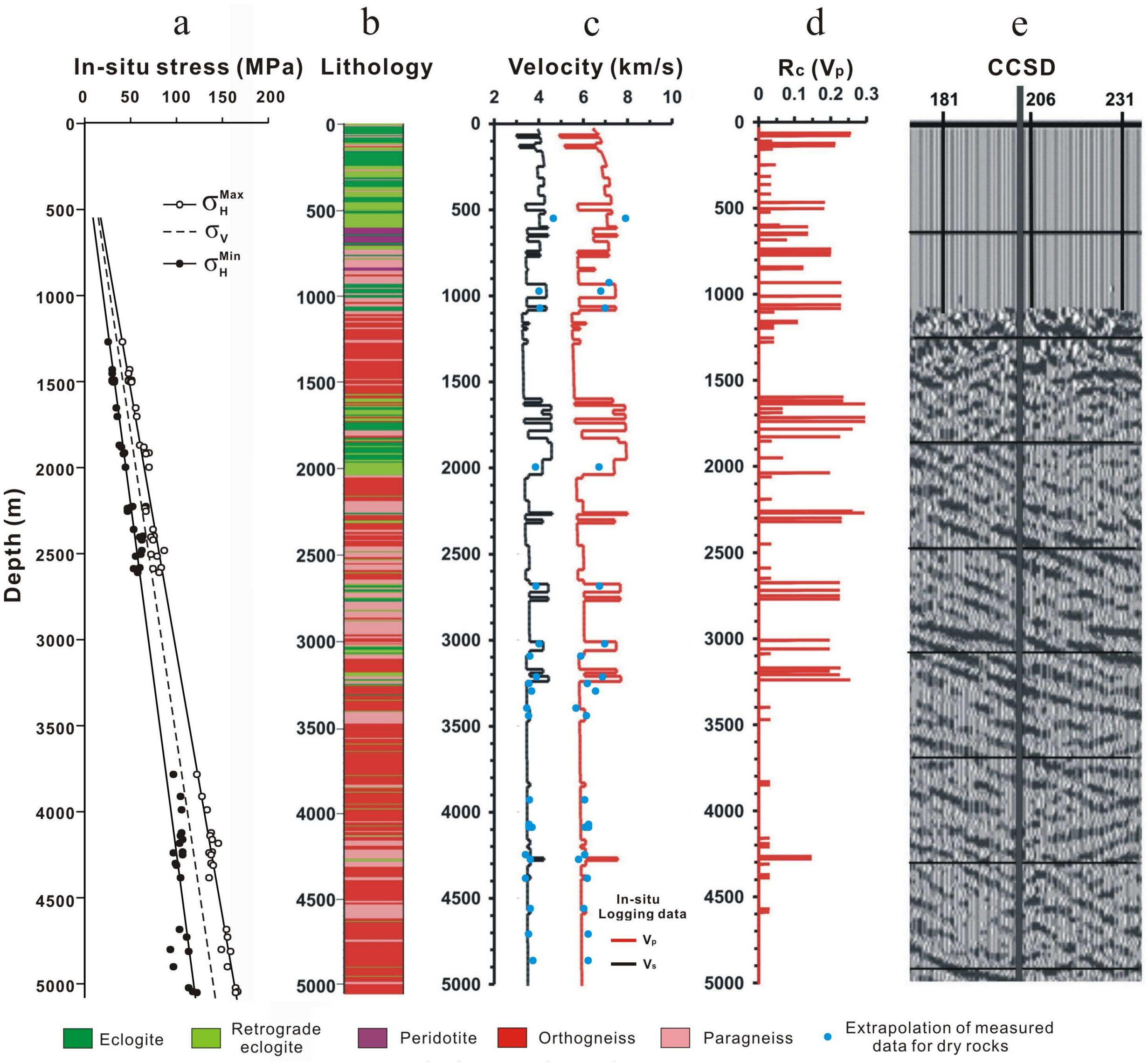

Figure 3.19 (a) Variations of the maximum (σ_H^{Max}) and minimum (σ_H^{Min}) horizontal stresses and the vertical stress (σ_V) as a function of depth in the CCSD main hole. (b) Lithological profile in the main bole. (c) Measured P- and S-wave velocities at in-situ lithostatic pressure (P_i) plotted on the velocity-depth profiles derived from borehole logging. (d) Reflection coefficients. (e) Seismic reflection profile.

Not all of the drilled rocks are satisfactory for laboratory high-pressure measurements and those selected are free of visible fractures and may thus not be representative of all of the drilled rocks.

The samples were measured under laboratory conditions that are different from the in-situ conditions before drilling and core recovery. For example, the upper crust is water-saturated but only dry samples were measured in the laboratory. Water saturation raises P-wave velocities, whereas S-wave velocities are only weakly affected (Nur and Simmons, 1969b; Mavko et al., 2009). In addition, the borehole logging-derived velocities may also have been affected by the in-situ stress field which is non-hydrostatic (Fig. 3.19a; Jahns et al., 1994).

Furthermore, as shown in Figures 3.3 and 3.4, the drilling-induced cracks and the microcacks generated during anelastic strain recovery following retrieval of the cores may not be fully closed at the laboratory pressures (0-137 MPa) corresponding to the depth of the hole (0-5158 m). However, these stress-relief cracks and microcracks do not exist in the in-situ rocks investigated by the sonic log.

The normal-incidence reflection coefficient (R_c) profile (Fig. 3.19d) constructed from the bulk densities and P-wave velocities of the rocks recovered from the lithologic column (Fig. 3.19b) explain the seismic reflection profile quite well (Fig. 3.19e). The strong seismic reflections consistently occur at the gently dipping contacts between eclogites (peridotites or retrograde eclogites) and their host rocks such as felsic gneisses. Comparison of the reflection image with the R_c profile suggests that the seismic reflections originate from mafic (eclogite and retrograde eclogite) or ultramafic packages within dominantly felsic rocks.

3.7 Conclusions

The Chinese Continental Scientific Drilling (CCSD) borehole represents the deepest penetration (5158 m) into an ultrahigh pressure (UHP) metamorphic terrane in any of the world's continents. Experimentally measured P- and S-wave velocity-pressure data for both the borehole core samples and their lithologic equivalents from surface exposures are very well described by a four-parameter exponential equation with clear physical significance: $V(P) = V_0 + DP - B_0 \exp(-kP)$, where V_0 is the extrapolated intrinsic reference velocity for the sample at zero pressure assuming pores/cracks are absent; D is the intrinsic pressure derivative of velocity in the linear elastic regime above the crack closure pressure (P_c); B_0 is the initial velocity drop caused by the presence of pores/cracks at zero pressure; and k is the decay constant of the velocity drop in the nonlinear poro-elastic regime. Compared with their surface analogues, the deep borehole core samples reveal significantly lower P_c and D but significantly higher V_0, B_0 and k values. The comparison suggests that the high pressure ($>P_c$) data from the deep core samples are much more reliable than data from surface analogues that have been subjected to long histories of weathering and alteration along intergranular and transgranular cracks, for extrapolation to deeper crust. The marked increases in B_0 and k and decrease in P_c indicate substantial decompaction of the core materials due to drilling and core-retrieval damage and stress-relief microfracturing.

Seismic hysteresis, whose variation with pressure is subject to exponential decay, is caused by irreversible changes in grain contacts, increases in microcrack aspect ratios and reductions of void space during the pressurization-depressurization cycle. The effect of compression on the V_p/V_s ratios is negligible for non-porous or crack-free compacted rocks. At high pressures (>200-300 MPa), anisotropy and shear wave splitting are controlled by the lattice-preferred orientations of minerals and compositional layering. However, at low pressures (<200-300 MPa), the anisotropy and shear wave splitting are mainly controlled by the summed effect of open microcracks aligned at different preferred orientations with respect to the structural framework (i.e., foliation and lineation). It is shown that the velocity-pressure data can successfully provide important hints about the preferred orientation of microcracks that causes P-wave velocity anisotropy and shear wave splitting in the low pressure regime.

The comparison between calculated and average measured P- and S-wave velocities of equivalent isotropic (fabric-free) crystalline rocks shows that the Voigt average yields the best agreement with the measured data; the Voigt-Reuss-Hill average, which is better than the geometric mean, can also offer remarkably good predictions for the seismic wave velocities, but the Reuss average systematically underestimates the velocities for most of the rocks and gives the poorest agreement with the experimental values.

The laboratory-measured velocities show a fairly good agreement with the velocities obtained from the sonic log in the depth range between 3500-5158 m where felsic orthogneiss and paragneiss are the dominant lithologies. The discrepancies between the laboratory and borehole logging velocities for eclogites and retrograde ecologites above a depth of 3100 m are mainly attributed to scaling problems, the presence of open fractures in the upper levels of the borehole, different degrees of retrograde metamorphism, differences in water saturation, and the presence of non-hydrostatic pressure conditions in the borehole wall. The comparison of the seismic reflection image at the borehole site with the calculated normal-incidence seismic reflection coefficient (R_c) profile indicates that the seismic reflections in the vicinity of the CCSD borehole originate from mafic (eclogite and retrograde eclogite) or ultramafic layers within dominantly felsic rocks.

CHAPTER 4 LAMÉ PARAMETERS OF COMMON ROCKS IN THE EARTH'S CRUST AND UPPER MANTLE

4.1 Abstract

Lamé parameter (λ) and shear modulus (μ) are the most important, intrinsic, elastic properties of rocks. λ, which relates stresses and strains in perpendicular directions, is closely related to the incompressibility and contains a high proportion of information about the resistance to a change in volume caused by a change in pressure. Recent studies have emphasized the role played by λ in the discrimination of gas sands from carbonates and shale in sedimentary basins and in the seismic reflection of crustal fault zones. Here we analyzed the equivalent isotropic elastic data of 475 natural rocks in order to characterize λ values for common types of crystalline rocks in the Earth's crust and upper mantle and their variations with pressure (P), temperature (T) and mineralogical composition. When no partial melting, metamorphic reaction, dehydration or phase transformation occurs, λ of a crystalline rock as a function of P and T can be described by $\lambda = a + (d\lambda/dP)P - c\exp(-kP) - (d\lambda/dT)T$, where a is the projected λ value at zero pressure if microcracks were fully closed; dλ/dP is the pressure derivative in the linear elastic regime; c is the initial λ drop caused by the presence of microcracks at zero pressure; k is a decay constant of the λ drop in the nonlinear poro-elastic regime; and dλ/dT is the temperature derivative. λ increases respectively nonlinearly and linearly with increasing pressure at low (<~300 MPa) and high (>~300 MPa) pressures. In the regime of high pressures, λ decreases quasi-linearly with increasing temperature with dλ/dT values in the range of $1\text{-}10\times10^{-3}$ GPa/ºC. Approaching the α-β quartz transition temperature, quartzite displays negative λ values. In the λ-ρ (density) and μ-λ plots, the main categories of lithology can be clearly distinguished. The ultramafic rocks display systematic decreases in both μ and λ with increasing degree of serpentinization. Eclogites, mafic rocks (gabbro, diabase, mafic granulite, and mafic gneiss) and felsic rocks (granite, diorite, felsic gneiss, intermediate gneiss and

metasediments) are characterized by high, moderate and low μ and λ values, respectively. For pyroxene and olivine, both λ and ρ increase but μ decreases with increasing Fe/Mg ratios. In the plagioclase series, both λ and μ increases with increasing anorthite content. Increases in the contents of garnets, sillimanite, rutile, zircon, ilmenite and spinel result systematically in an increase in rock's λ and μ values. The present results provide improved constraints on the discrimination of composition for crustal and upper mantle rocks in terms of λ and μ.

4.2 Introduction

The elastic properties of a homogeneous isotropic rock can be uniquely described using two independent moduli termed lambda (λ) and mu (μ). λ and μ, which are named the Lamé modulus and shear modulus, respectively, both vary as a function of measurement conditions (e.g., pressure and temperature). As pointed out by Goodway (2001) in a seminal paper, only λ and μ appear in the tensor form of Hooke's law, but not Young's modulus (E), bulk modulus (K), or Poisson's ratio (υ). It is thus clear that λ and μ are the most important intrinsic and invariant elastic moduli required to describe stress in terms of strain for materials or rocks. However, most scientists are familiar with the physical significance of μ, E, K, and υ, but not that of λ, probably because the physical significance of λ is less straightforward. Actually λ relates stresses and strains in perpendicular directions; in the case of uniaxial strain where $\varepsilon_1 \neq 0$, and $\varepsilon_2 = \varepsilon_3 = 0$ (i.e., where there is no displacement perpendicular to the x-axis), for example, $\lambda = \sigma_2/\varepsilon_1 = \sigma_3/\varepsilon_1$. λ is closely related to incompressibility (K) and contains information about the resistance to a change in volume caused by a change in pressure (Goodway, 2001).

The most common geophysical parameters measurable are compressional (P) and shear (S) wave velocities (V_p and V_s) and densities (ρ) of elastic media. The Lamé parameter λ and shear modulus μ for isotropic elasticity can be easily determined from the measured seismic data:

$$\lambda = \rho(V_p^2 - 2V_s^2) \tag{4.1}$$

$$\mu = \rho V_s^2 \tag{4.2}$$

$$\lambda/\mu = (V_p/V_s)^2 - 2 \tag{4.3}$$

$$\lambda\rho = Z_p^2 - 2Z_s^2 \tag{4.4}$$

$$\mu\rho = Z_s^2 \tag{4.5}$$

where Z is the acoustic impedance; P-wave impedance $Z_p=\rho V_p$, and S-wave impedance $Z_s=\rho V_s$. $\lambda = 0$ if $V_p/V_s = \sqrt{2}$ and $\lambda < 0$ if $V_p/V_s < \sqrt{2}$. $\lambda/\mu \geq 1$ if $V_p/V_s \geq \sqrt{3}$ (e.g., serpentine, calcite, feldspar, hornblende, fayalite, dolomite), and $0 \leq \lambda/\mu < 1$ if $\sqrt{2} \leq V_p/V_s < \sqrt{3}$ (e.g., quartz, staurolite, bronzite, diallage and enstatite). The information about the impedance or λρ and μρ data can be extracted from the inversion of P- and S-wave reflectivities (Estabrook and Kind, 1996; Goodway et al., 1997; Goodway, 2001; Gray, 2003). Chavez-Perez and Louie (1997, 1998) suggested that variations in λ control seismic reflections of crustal fault zones. Obviously, both λ and μ offer the most fundamental and orthogonal parameterization of elastic seismic waves to extract information about the composition and structure of rocks in the Earth's interior. In the literature, however, only E, K, μ and υ are usually reported although λ is an intrinsic and invariant property of elastic media under given conditions. So far, little systematic research work has been carried out on the characterization of λ values for crystalline rocks (Christensen, 1966; Kern, 1979).

In this chapter, I will investigate the pressure- and temperature-dependences of λ values for common categories of crystalline rocks from the Earth's crust and upper mantle, and explore the potential implications of λ as a discriminant of composition for common rock types in the Earth's crust and upper mantle. The emphasis of this study is placed on the properties of crystalline igneous and metamorphic rocks. For the λ values of common sedimentary rocks (i.e., sandstone, shale, limestone and dolomite) and their applications in the exploration of oil or gas reservoirs, the reader is referred to the papers of Goodway et al. (1997), Goodway (2001), Gray and Andersen (2000), Dufour et al. (2002), Gray (2003), and Li et al. (2003).

4.3 Data for analysis

The high-quality data used for the analysis were taken from a database of 475 samples on which P-wave velocities have been well measured for the X, Y and Z directions and S-wave velocities for six pairs of propagation-vibration directions at high hydrostatic pressures (≥ 500 MPa) using the same laboratory equipment and the same methods (i.e., the pulse transmission technique, Birch, 1960; Christensen, 1974; Kern, 1982). The uncertainty of measurements is estimated to be <0.5% for V_p, <1% for V_s, and ±0.005 g/cm^3 for density. For each sample, λ and μ as a function of pressure or temperature were calculated from arithmetic mean V_p, V_s values and density using Eq. (4.1) and (4.2), respectively. In this database, 87 samples were measured by our group: 57 from the Dabie-Sulu ultrahigh pressure metamorphic terrane and 20 from the Yunkai Mountains of China (Wang et al., 2005a, b; Ji et al., 2007a; Wang and Ji, 2009), and 10 from the Tantato high grade metamorphic domain in northern Saskatchewan, Canada (Ji and Salisbury, 1993; Ji et al., 1993). The literature data were taken from the Handbook of Seismic Properties of Minerals, Rocks and Ores (Ji et al., 2002 and the references cited therein).

4.4 Results

4.4.1 Pressure dependence

In using λ to place constraints on lithology in the crust and upper mantle, it is primary to understand how λ varies with pressure and temperature. Figure 4.1 shows typical λ-P data for common lithologies such as ultramafic rocks (peridotite, serpentinite, and partially serpentinized peridotite, Fig. 4.1a), mafic rocks (eclogite, mafic gneiss, mafic granulite, and amphibolite, Fig. 4.1b), felsic rocks (granite, diorite, felsic gneiss and metasediments, Fig. 4.1c), marble and sedimentary rocks (limestone and sandstone, Fig. 4.1d) up to 1.0 GPa, a pressure equivalent to depths of approximately 35 km. These rocks display systematically an initial non-linear increase in λ at low pressures followed by a more gradual linear increase at high pressures. This phenomenon indicates that λ is strongly affected by the presence of microcracks within the rock. The rapid, non-linear rise in λ below a critical pressure can be attributed to the progressive closure of microcracks with varying aspect-ratio spectra with increasing pressure. The linear increase in λ above the critical pressure where all microcracks have been fully closed in the rock marks an elastic volume contraction of crack-free material under hydrostatic compression.

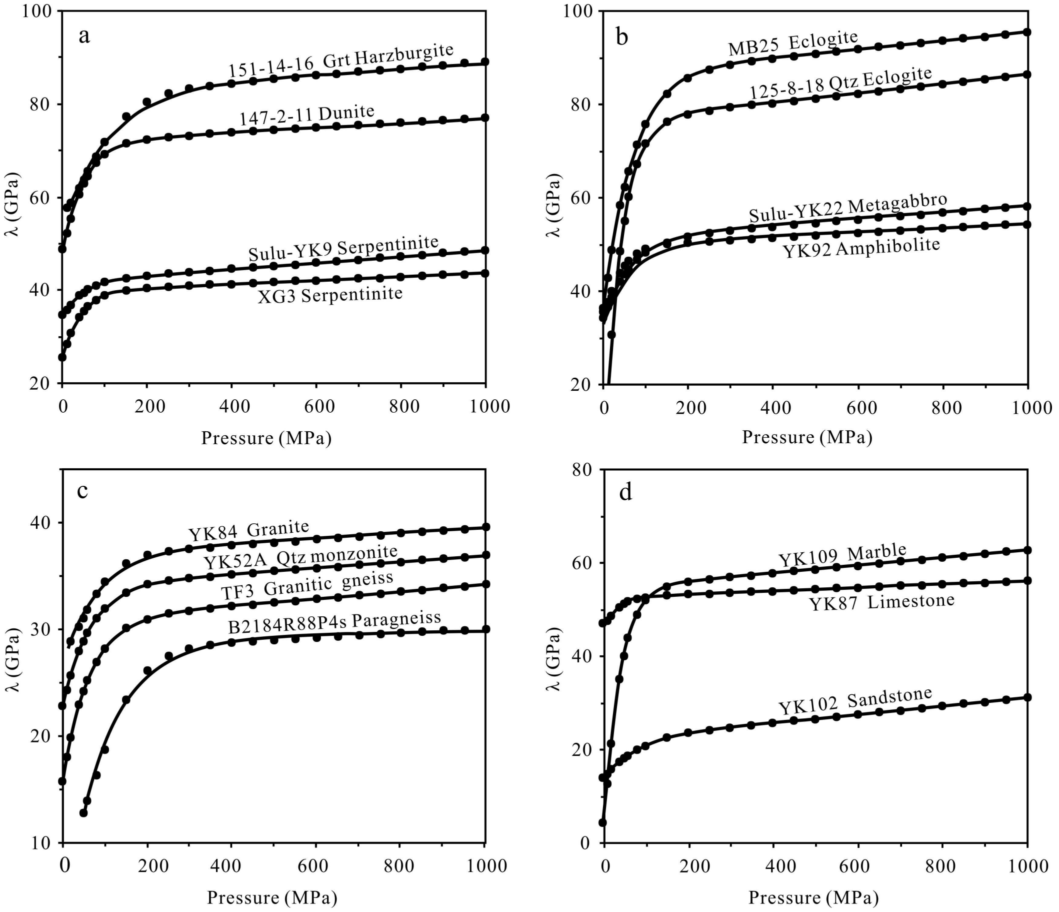

Figure 4.1 Lamé parameter (λ) as a function of pressure for selected lithologies from the Sulu ultrahigh pressure metamorphic terrain and the Yunkai Mountains, China. Dots: experimental data; Line: the best-fitting according to Eq. (4.6) using a least squares method. Grt: garnet; Qtz: quartz.

λ as a function of confining pressure can be described by the following equation:

$$\lambda = a + (d\lambda/dP)P - c\exp(-kP) \tag{4.6}$$

where *a* is the projected λ value of a non-porous or crack-free compacted rock at zero pressure, which is determined from extrapolation of the linear λ-P relationship obtained at high pressures to zero pressure; dλ/dP is the pressure derivative in the linear elastic regime; *c*, which is the ambient λ drop caused by the presence of pores/microcracks at zero pressure, determines the maximum magnitude of the λ increase due to the closure of pores and microcracks; *k*, which is a decay constant of the λ drop, controls the shape of the nonlinear segment of the λ-P curve. The *k* value is a parameter to characterize the facility of the successive closure of cracks of varying aspect-ratio spectra with increasing pressure. Flatter cracks yield a larger *k* value than more spherical pores. The zero-pressure λ value of the rock containing microcracks is the same as (*a*-*c*).

In Eq. (4.6), *a* and dλ/dP are two parameters which describe the λ value of the microcrack- or pore-free solid matrix, while *c* and *k* are two parameters related to the porosity and geometrical shape of pores (e.g., aspect ratio, spatial arrangement, orientation and size distribution), and in turn on the formation and deformation processes of the rocks. The same type of mathematical expression as Eq. (4.6) has been used by previous workers to describe the pressure dependence of seismic velocities (Stierman et al., 1979; Zimmerman et al., 1986; Eberhart-Phillips et al., 1989; Shapiro, 2003; Wang et al., 2005a, b; Ji et al., 2007a; Wang and Ji, 2009). The equation can be derived based on an assumption that the difference between the property (e.g., seismic velocities or elastic moduli) of a nonporous material and its porous counterpart at a given confining pressure has a maximum value (*c*) at P=0 and then decays progressively with increasing P at a rate proportional to the value of the property at the applied confining pressure (Ji et al., 2007a). The last term of Eq. (4.6) possesses the same form of the expression that is commonly used to describe natural phenomena such as radioactivity decay, cooling, and vibration attenuation.

Equation (4.6) was used to curve-fit λ-P data for samples collected from the Dabie-Sulu ultrahigh pressure (UHP) metamorphic belt using a least squares method and gave excellent results with well-constrained *a*, dλ/dP, *c* and *k* parameters. Table 4.1 lists such parameters, together with the data of density and modal composition, for 57 UHP samples collected from the boreholes of the Chinese Continental Scientific Drilling project (Ji and Xu, 2009) and surface quarries. The information about the locality and recovery depth for these samples were presented in Wang et al. (2005a, b), Ji et al., (2007a), and Wang and Ji (2009). Based on the values reported in Table 4.1, extrapolation and interpolation can be easily performed using Eq. (4.6).

4.4.2 Effect of temperature

Laboratory data on the effect of temperature on seismic wave velocities and density of rocks are rather limited and were mainly from H. Kern's laboratory. Figure 4.2 presents the λ values as a function of temperature at a confining pressure of 600 MPa for some common rocks from the upper mantle and the continental crust. The λ values were calculated using the mean V_p and V_s data reported by Barruol (1993), Kern et al. (1999, 2002), and Kern and Tubia (1993). When no partial melting (Spetzler and Anderson, 1968), metamorphic reaction, dehydration or phase transformation (Kern, 1982) occurs, most solid rocks such as garnet peridotite, harzburgite and pyroxenite (Fig. 4.2a), eclogites (Fig. 4.2b), amphibolites (Fig. 4.2c), gabbro, granite and granitic gneiss (Fig. 4.2d) display that λ decreases linearly with increasing temperature due to thermal effects (e.g., thermal dilatation of mineral lattices, microcracking and grain boundary widening induced by differential thermal expansion). The gradual decrease in λ occurs over the range from room temperature to 600 ºC, which can be easily understood from Eq. (4.1) because dV_p/dT is significantly larger than dV_s/dT for most rocks (Kern and Tubia, 1993; Kern et al., 1996b, 1999, 2002; Ji et al., 2002). For basalt, however, the temperature dependence is negligible in the range from room temperature up to 600 ºC (Fig. 4.2d and Table 4.2) probably because the elastic velocities in basaltic glass at a hydrostatic pressure of 600 MPa increase with temperature due to reduction of porosity (Kern, 1982).

Table 4.1 Densities, modal compositions and four coefficients to describe the Lamé parameters (λ) for 57 samples from Dabie-Sulu UHP metamorphic belt (China).

Sample No.	**Lithology**	**Density**	**Modal composition**[a]	**Lamé parameters**[b]			
		(g/cm^3)	**(vol. %)**	**a (GPa)**	**dλ/dP**	**c (GPa)**	**k (GPa^{-1})**
203-5-15	Amphibolite	3.07	Pl 35.0, Amp 41.0, Bt 15.0, Qtz 8.0, Chl 1.0	32.22	3.32	22.69	13.07
B1608	Grt-Bt-Pl amphibolite	2.98	Pl 42.0, Amp 40.0, Grt 4.0, Bt 8.0, Qtz 4.0, Chl 2.0	56.18	2.76	18.47	9.28
B1651	Amphibolite	3.00	Amp 48.0, Chl 13.0, Grt 3.0, Cpx 15.0, Pl 12.0, Qtz 5.0, Ep 2.0, Opq 2.0	49.44	3.81	6.98	14.51
B2068	Bt-Pl amphibolite	2.85	Pl 39.0, Amp 39.0, Bt 12.0, Qtz 7.0, Chl 3.0	39.55	1.84	15.59	26.84
QL4	Amphibolite	2.96	Amp 50.0, Chl 12.0, Grt 3.0, Cpx 15.0, Pl 10.0, Qtz 5.0, Ep 2.0, Rt 2.0, Opq 1.0	42.81	10.52	14.77	4.95
YM4	Amphibolite	3.09	Amp 80.0, Qtz 8.0, Pl 5.0, Opx 5.0, Opq 2.0	56.31	2.88	11.82	13.32
86351	Coarse-grained eclogite	3.49	Grt 63.0, Cpx 35.0, Rt 1.5, Qtz 0.5	90.37	0.00	19.02	7.26
98401	Eclogite	3.48	Grt 30.0, Cpx 45.0, Amp 15.0, Rt 2.0, Qtz 1.0, Opq 1.0, Symp 6.0	72.55	0.00	16.16	13.69
98501	Eclogite	3.47	Grt 25.0, Cpx 20.0, Amp 37.0, Bt 2.0, Phn 2.0, Opq 2.0, Rt 1.0, Qtz 1.0, Symp 20.0	66.30	0.00	13.61	7.27
125-15-18	Qtz eclogite	3.48	Grt 45.0, Cpx 31.0, Amp 6.5, Qtz 12.0, Phn 5.0, Rt 0.5	82.76	10.95	44.12	14.99
125-8-18	Qtz eclogite	3.38	Grt 40.0, Cpx 35.0, Amp 4.0, Symp 12.0, Qtz 7.0, Phn 1.5, Rt 0.5	76.63	9.66	75.09	24.63
315-1-11	Phn eclogite	3.43	Grt 36.0, Cpx 40.0, Amp 5.0, Phn 17.0, Qtz 1.0, Rt 1.0	80.26	0.00	45.19	12.70
315-4-11	Fine-grained Phn eclogite	3.53	Grt 44.0, Cpx 46.0, Phn 5.0, Qtz 2.0, Rt 2.0, Opq. 1.0	80.47	0.00	16.54	15.96
C397 PC 2a	Eclogite	3.39	Grt 40.0, Cpx 30.0, Symp 15.0, Amp 3.5, Qtz 5.0, Phn 5.0, Rt 1.5	84.96	4.80	1.18	40.31
C398 PC 5b	Qtz eclogite	3.39	Grt 41.0, Cpx 39.0, Symp 8.0, Amp. 5.0, Phn 2.0, Qtz 5.0	79.85	6.28	4.04	6.93
C399 PC c1	Retrogressed Qtz eclogite	3.24	Grt 35.0, Symp 34.0, Amp 8.0, Qtz 20.0, Bt 2.0, Rt 1.0	80.57	6.36	30.07	13.78
DG1	Fine-grained eclogite	3.46	Grt 45.0, Cpx 50.0, Symp 2.5, Amp 1.0, Rt 1.0, Qtz 0.5	77.90	0.00	22.57	14.02
JZ1	Fine-grained eclogite	3.49	Grt 25.0, Cpx 63.0, Amp 5.0, Rt 2.0, Qtz 2.0, Phn 1.0, Symp 2.0	72.24	4.40	42.77	4.71
MB22	Coarse-grained eclogite	3.50	Grt 63.0, Cpx 35.0, Rt 1.5, Qtz 0.5	74.79	5.25	12.91	10.65
MB23	Coarse-grained eclogite	3.48	Grt 70.0, Cpx 26.0, Phn 2.0, Rt 1.0, Qtz 1.0	93.33	4.68	40.25	10.25
MB25	Coarse-grained eclogite	3.59	Grt 65.0, Cpx 33.0, Rt 1.5, Qtz 0.5	86.67	8.84	50.94	14.54
MB26	Coarse-grained eclogite	3.56	Grt 70.0, Cpx 29.0, Rt 0.8, Qtz 0.2	90.46	7.75	20.79	8.36
MB27B	Coarse-grained eclogite	3.58	Grt 68.0, Cpx 31.0, Rt 1.0	87.03	3.09	19.30	8.71
MB2B	Coarse-grained garnetite	3.61	Grt 88.0, Cpx 10.0, Phn 1.5, Rt 0.5	84.68	0.00	27.39	16.67
MB30	Coarse-grained eclogite	3.60	Grt 70.0, Cpx 29.0, Rt 0.5, Qtz 0.5	84.72	1.26	22.44	9.73
MB34	Coarse-grained garnetite	3.64	Grt 75.0, Cpx 23.0, Rt 1.0, Qtz 1.0	91.36	1.50	29.32	8.28
MB-OU-14	Garnetite	3.56	Grt 82.0, Cpx 8.0, Phn 7.0, Rt 1.0, Qtz 2.0	91.73	10.73	34.33	1.63
SB1	Fine-grained eclogite	3.37	Grt 33.0, Cpx 60.0, Amp 2.0, Rt 2.0, Qtz 1.0, Symp 2.0	81.05	1.05	20.08	6.15
26-10-17	Granitic Gneiss	2.64	Pl 32.0, Kfs 31.0, Qtz 33.0, Bt 3.0, Opq 1.0	31.82	5.28	12.87	21.33
178-6-6	Bt dioritic gneiss	2.74	Pl 49.0, Qtz 37.0, Bt 12.0, Opq 2.0	34.27	4.32	18.93	11.19
19-13-13	Granitic Gneiss	2.64	Pl 31.0, Kfs 30.0, Qtz 34.0, Bt 4.0, Opq 1.0	31.81	2.51	29.28	16.80
210-15-21	Granitic gneiss	2.63	Pl 30.0, Kfs 35.0, Qtz 31.0, Bt 3.0, Opq 1.0	33.10	2.69	9.51	12.21
219-1-2	Granitic gneiss	2.63	Pl 32.0, Kfs 31.0, Qtz 30.0, Amp 3.0, Bt 3.0, Opq 1.0	40.60	4.54	36.68	17.61
703-29	Grt-Bt-Hbl dioritic gneiss	2.93	Pl 44.0, Qtz 38.0, Amp 5.0, Grt 7.0, Bt 6.0,	46.07	3.88	36.88	14.05
B1578	Bt-Ms-Pl-Kfs orthogneiss	2.65	Pl 40.0, Kfs 25.0, Qtz 25.0, Ms 4.0, Bt 3.0, Grt 1.0, Opq 2.0	29.71	3.04	35.45	20.63
B1628	Hbl-Mag felsic orthogneiss	2.65	Pl 38.0, Kfs 15.0, Qtz 35, Amp 7.0, Grt 1.5, Opq 2.0	36.89	2.99	12.11	12.10
B1694	Felsic orthogneiss	2.63	Pl 30.0, Kfs 42.0, Qtz 21.0, Cpx 4.0, Amp1.5, Opq 1.0, Rt 0.5	39.31	0.00	24.42	3.81
B2078	Felsic orthogneiss	2.63	Pl 31.0, Kfs 35.0, Qtz 25.0, Bt 4.0, Amp 4.0, Opq 1.0	31.38	1.41	65.20	36.74
TF1	Granitic gneiss	2.66	Qtz 35.0, Pl 40.0, Kfs 15.0, Opx 7.0, Grt 1.5, Opq 1.0, Rt 0.5	20.30	3.94	12.30	9.99
TF3	Granitic gneiss	2.66	Qtz 20.0, Pl 30.0, Kfs 42.0, Opx 4.0, Opq 1.5, Rt 0.5	30.87	3.27	15.20	16.12
B1536	Hbl-Phn eclogite	3.11	Grt 26.0, Symp 47.0, Amp 9.0, Qtz 12.0, Phn 5.0, Rt. 1.0	54.30	4.30	43.64	28.84
Sulu-YK1	Metagabbro	3.08	Pl 62.0, Cpx 5.0, Grt 15.0, Qtz 5.0, Ms 9.0, Chl 4.0	55.44	4.11	9.89	31.12
Sulu-YK22	Metagabbro	2.96	Pl 45.0, Cpx 14.0, Grt 9.0, Qtz 10.0, Ms 5.0, Chl 11.0, Zo 5.0, Opq. 1.0	51.07	7.18	16.96	15.40
Sulu-YK2A	Metagabbro	3.07	Pl 64.0, Cpx 5.0, Grt 12.0, Qtz 5.0, Ms 10.0, Chl 4.0	53.59	3.78	19.77	64.43
Sulu-YK3B	Metagabbro	3.00	Pl 72.0, Cpx 4.0, Grt 8.0, Qtz 4.0, Ms 9.0, Chl 3.0	50.13	3.61	16.21	21.99
YM1	Marble	2.86	Dol 87.0, Cal 7.0, Qtz 4.0, Grt 1.0, Cpx 1.0	41.15	1.62	21.35	24.74
B2168	Bt-Hbl-Pl-Kfs paragneiss	2.65	Pl 39.0, Kfs 20.0, Qtz 30.0, Amp 6.0, Bt 4.0, Opq 1.0	38.70	1.13	35.47	22.18
B2184	Bt-Hbl-Pl-Kfs paragneiss	2.66	Pl. 40.0, Kfs 15.0, Qtz 40.0, Bt 4.0, Opq 1.0	29.03	0.80	26.57	9.93
B2242	Hbl-Bt-Pl-Kfs paragneiss	2.66	Pl 38, Kfs 18.0, Qtz 35.0, Amp 7.5, Opq 1.5	39.52	2.81	12.36	28.81
B2339	Hbl-Pl-Kfs paragneiss	2.65	Pl 42.0, Kfs 21.0, Qtz 25.0, Amp 8.0, Grt. 3.0, Opq 1.0	32.99	1.84	14.05	7.45
147-2-11	Dunite	3.16	Ol 88.0, Srp11.0, Opq 1.0	71.89	5.11	24.07	19.41
150-3-20	Lherzolite	3.12	Ol 70.0, Opx 8.0, Cpx 11.0, Srp 10.0, Opq 1.0	64.92	1.28	41.98	10.17
151-14-16	Grt-Harzburgite	3.21	Ol 68.0, Opx 14.0, Cpx 8.0, Grt 5.0, Srp 4.0, Phl 1.0	83.41	5.31	29.64	8.88
160-12-11	Grt-Harzburgite	3.17	Ol 67.0, Opx 10.0, Cpx 13.0, Grt 4.0, Srp 4.0, Phl 2.0	67.09	5.83	74.65	28.92
166-42-43	Phl dunite	3.25	Ol 86.0, Opx 2.0, Phl 4.0, Srp 5.0, Opq 3.0	63.20	4.72	24.35	16.00
Sulu-YK9	Serpentinite	2.60	Srp 85.0, Tlc 10.0, Opq 5.0	41.99	6.73	7.67	21.43
XG3	Serpentinite	2.66	Srp 80.0, Ol 15.0, Opq 5.0	40.03	3.66	14.48	23.07

[a] Abbreviations: Amp: amphibole; Bt: biotite; Chl: chlorite; Cpx: clinopyroxene; Ep: epidote; Grt: garnet; Hbl: hornblende; Kfs: K-feldspar; Mag: magnetite; Ms: muscovite; Ol: olivine; Opq: opaques; Opx: orthopyroxene; Phl: phlogopite; Phn: phengite; Pl: plagioclase; Qtz: quartz; Rt: rutile; Srp: serpentine; Symp: symplectite; Tlc: talc; Zo: zoisite.

[b] The goodness of fit coefficients R^2>0.98 for all the sample.

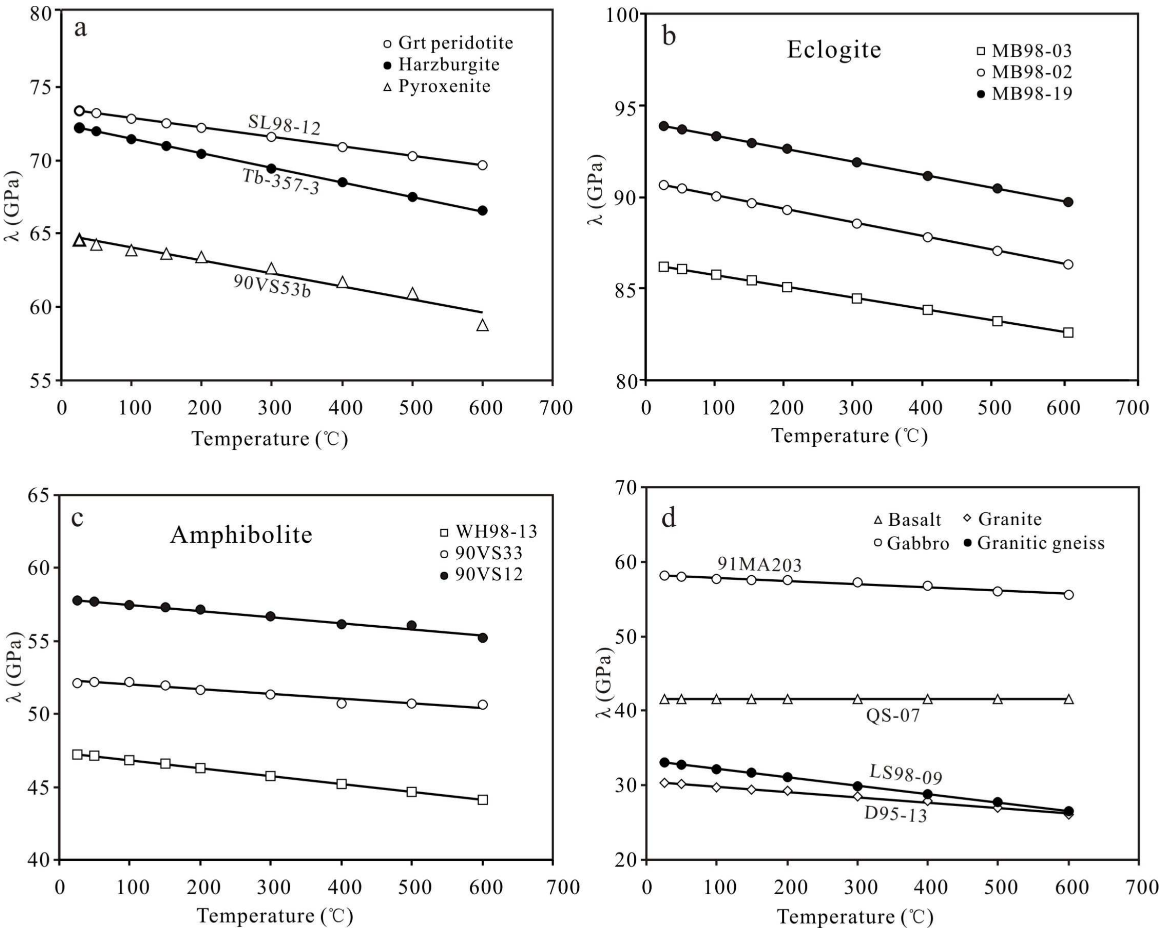

Figure 4.2 The effect of temperature on Lamé parameter for harzburgite, garnet (Grt) peridotite and pyroxenite (a), eclogites (b), amphibolites (c), and basalt, granite, granitic gneiss and gabbro (d) at a hydrostatic pressure of 600 MPa. The original wave velocities and density data are from Barruol (1993), Kern et al. (1999, 2002), and Kern and Tubia (1993).

Thus, the λ-T relationship for crystalline rocks can be described by a linear equation:

$$\lambda = \lambda_0 - (d\lambda/dT)T \tag{4.7}$$

where λ_0 is the projected the λ value when T=0 ºC, and dλ/dT is the temperature derivative. The values λ_0 and dλ/dT as well as the modal composition for each sample illustrated in Fig. 4.2 are given in Table 4.2. For these samples, dλ/dT varies generally from 3×10^{-3} to 10×10^{-3} GPa/ºC. It is important to point out that the presence of partial melting (Spetzler and Anderson, 1968), metamorphic reaction, dehydration or phase transformation (Kern, 1982) may cause a significant deviation from the above linear relationship between the elastic moduli and temperature.

Examples are illustrated in Fig. 4.3 using two UHP rocks from the Dabie region: sample D95-27 is a serpentinized lherzolite consisting of 43% serpentine, 19% olivine, 13% clinopyroxene, 22% garnet, and 3% opaque oxides, and sample D95-35 is retrograde eclogite composed of 45% amphibole, 24% chlorite, 13% plagioclase, 13% opaque oxides, 4% apatite and 1% epidote. Dehydration of water-bearing minerals such as serpentine, chlorite and probably some amphibole, which occurs at ~400 ºC, results in an abrupt drop in the Lamé modulus for the samples.

Table 4.2 Densities, modal compositions and two parameters (λ_0 and $d\lambda/dT$) to describe the effect of temperature for 13 samples shown in Fig. 4.2.

Sample No.	**Lithology**	**Density**	**Modal composition**[a]	**λ_0**	**$d\lambda/dT$**	**R^2**	**Ref.**[b]
		g/cm^3		**(GPa)**	**GPa/°C**		
90VS12	Amphibolite	3.14	Hbl 59.0, Pl 35.0, Qtz 4.0, Opq 1.0	57.92	0.0042	0.98	1
90VS33	Amphibolite	3.07	Hbl 54.2, Pl 35.8, Pyx 8.0, Opq 2.0	52.32	0.0032	0.94	1
QS-07	Basalt	2.74	Matrix 70.0, Pyx 19.0, Pl phenocryst 6.0, Idd 5.0	41.65	0.000005	0.81	3
MB98-02	Eclogite	3.57	Grt 57.0, Omp 42.0, Rt 0.6, Mus 0.2	90.81	0.0075	0.99	3
MB98-03	Eclogite	3.45	Grt 46.0, Omp 53.0, Mus 0.6	86.36	0.0062	0.99	3
MB98-19	Eclogite	3.61	Grt 80.0, Omp 15.0, Phl 3.5, Qtz 1.0, Opq 0.5	94.05	0.0072	0.99	3
91MA203	Gabbro	2.90	Pl 75.0, Opx 22.0, Hbl 2.0, Bt 1.0	58.23	0.0042	0.98	1
D95-13	Granite	2.65	Pl 54.0, Kfs 23.0, Qtz 20.0, Bt 3.0	30.57	0.0071	0.99	2
LS98-09	Granitic gneiss	2.64	Kfs 53.0, Qtz 29.0, Mus 6.0, Pl 8.0, Ep 4.0, Sp 0.2, Bt 0.1	33.33	0.0112	1.00	3
WH98-13	Grt amphibolit	3.24	Hbl 65.0, Qtz 18.0, Grt 15.0, Mag 2.0, Pl 0.4	47.39	0.0054	0.99	3
SL98-12	Grt peridotite	3.39	Ol 73.0, Mag 14.0, Grt 12.0, Pyx 1.0	73.5	0.0065	1.00	3
Tb-357-3	Harzburgite	3.30	Ol 74.0, Opx 21.5, Cpx 2.5, Spl 1.6, Serp 0.4	72.42	0.0098	1.00	4
90VS53b	Pyroxenite	3.24	Pyx 68.5, Pl 25.4, Spl 4.5, Opq 1.6	64.97	0.0089	0.96	1

[a] Abbreviations: Bt: biotite; Cpx: clinopyroxene; Ep: epidote; Grt: garnet; Hbl: hornblende; Idd: iddingsite; Kfs: K-feldspar; Mag: magnetite; Mus: muscovite; Ol: olivine; Omp: omphacite; Opq: opaque; Opx: orthopyroxene; Phl: phlogopite; Pl: plagioclase; Pyx: proxene; Qtz: quartz; Rt: rutile; Srp: serpentine; Sp: sphalerite; Spl: spinel.

[b] 1: Barruol (1993); 2: Kern et al. (1999); 3: Kern et al. (2002); 4: Kern and Tubia (1993).

Therefore, the laboratory experimental results can be extrapolated into the Earth's interior using the following equation if there is no partial melting, metamorphic reaction, dehydration or phase transformation.

$$\lambda(P,T) = a + (d\lambda/dP)P - c\exp(-kP) - (d\lambda/dT)T \qquad (4.10)$$

The results computed from Eq. (4.10) have the potential of providing valuable constraints on the interpretation of the lithological and mineralogical composition of the Earth's crust and upper mantle.

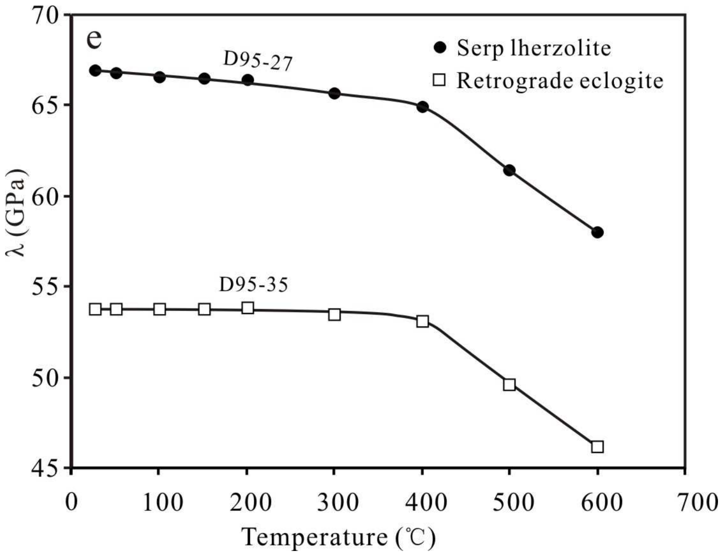

Figure 4.3 Lamé modulus λ as a function of temperature at 600 MPa for a serpentinized lherzolite sample and a retrograde eclogite sample from the Dabie-Sulu UHP metamorphic terrane. The elastic moduli wave calculated from the velocities and density data measured by Kern et al. (1999).

4.4.3 Effect of α-β quartz transition

A quartzite is taken as an example to illustrate the effect of phase transition on λ. Figure 4.4a presents the mean V_p and V_s data as a function of temperature at a confining pressure of 600 MPa for an ultramylonitic quartzite (89SB114a) consisting of 100% quartz. This sample was collected from a ductile shear zone in the Saint Barthelemy Massif (Northern Pyrenees, France), and its P- and S-wave velocities and densities were measured in three propagation directions (X, Y, Z) and six propagation-polarization directions (XY, XZ, YX, YZ, ZX and ZY), respectively (Barruol, 1993; Barruol et al., 1992). The P-wave velocity falls pronouncedly when approaching the α-β quartz transition temperature (~650 °C at 600 MPa), and jumps abruptly after the transition while little change occurs in the S-wave velocity across the transition. A similar phenomenon was observed in other quasi-isotropic quartzites (Kern, 1979). The λ values (Fig. 4.4b) computed from the mean V_p, V_s and density values for the quartzite become negative in the temperature range from 450 °C to 650 °C. An abrupt increase in λ occurs above 650 °C at 600 MPa, reflecting a pronounced increase in V_p/V_s ratio in the beta quartz. Previous experiments (e.g., Shen et al., 1993) showed that the α-β quartz transition temperature increases linearly with increasing the confining pressure. In the quartz-rich continental crust with an anomalously high geothermal gradient (dT/dz>25 °C), one may expect to detect low, very low and high λ values for the upper crust (<450 °C), middle crust (450-650 °C) and lower crust (>650 °C), respectively. In other words, as the α-β quartz transition is expected to occur in the quartz-bearing rocks (i.e., granite, diorite, and felsic gneiss) across the boundary between the middle and the lower crusts, a significant decrease in λ or υ may mark this boundary.

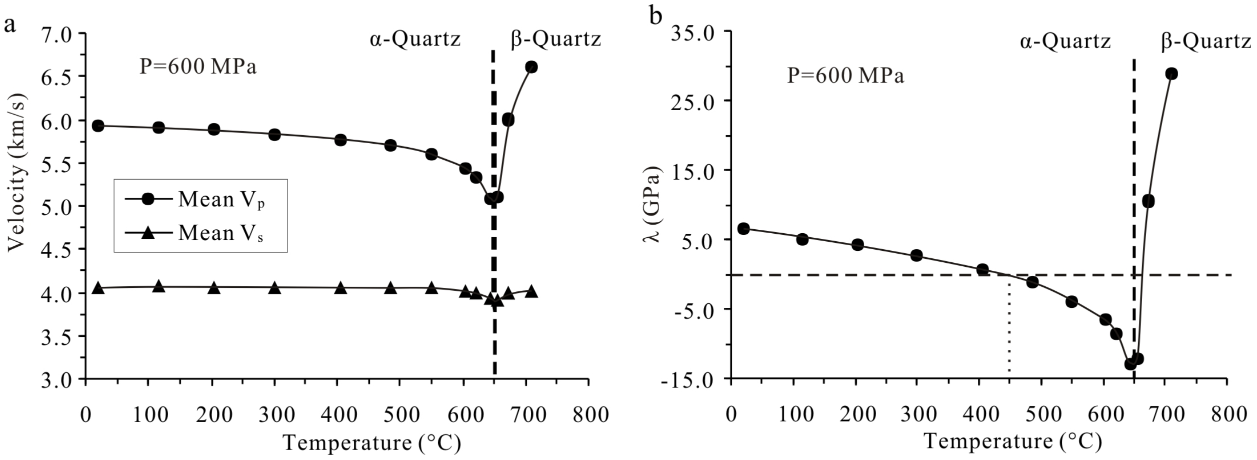

Figure 4.4 Mean P- and S-wave velocities (a) and Lamé parameter (b) as a function of temperature for a quartzite at a confining pressure of 600 MPa. The wave velocity data from Barruol (1993). The α-β quartz transition occurs at ~650 °C.

4.4.4 λ-ρ correlation

Figure 4.5 shows fields of different types of rocks within the λ-ρ plots at a hydrostatic confining pressure of 600 MPa under which the effect of microcracks is eliminated. The field boundary contours were drawn by eye according to the distribution of experimental data. For peridotites, both λ and ρ values decrease progressively with increasing the content of serpentine (chrysotile, antigorite and lizardite, Watanabe et al., 2007; Fig. 4.5a). This trend is consistent with the preliminary results of Christensen (1966) for ultramafic rocks. The field of peridotites is relatively large due to varying contents of garnet, spinel and magnetite, which have high values in both λ and ρ. For mafic rocks, eclogite displays significantly higher values of both λ and ρ than gabbro, diabase, mafic gneiss, mafic granulite and amphibolite. The large variations in both λ and ρ for eclogites are attributable to varying volume fractions of garnet, rutile and magnetite. Acid and intermediate rocks (i.e., granite, diorite, felsic gneiss, intermediate gneiss and metasediments) have lower λ and ρ values than the mafic crystalline rocks (Fig. 4.5b). The fields for limestone/marble, anorthosite and basalt are also identified in Fig. 4.5c.

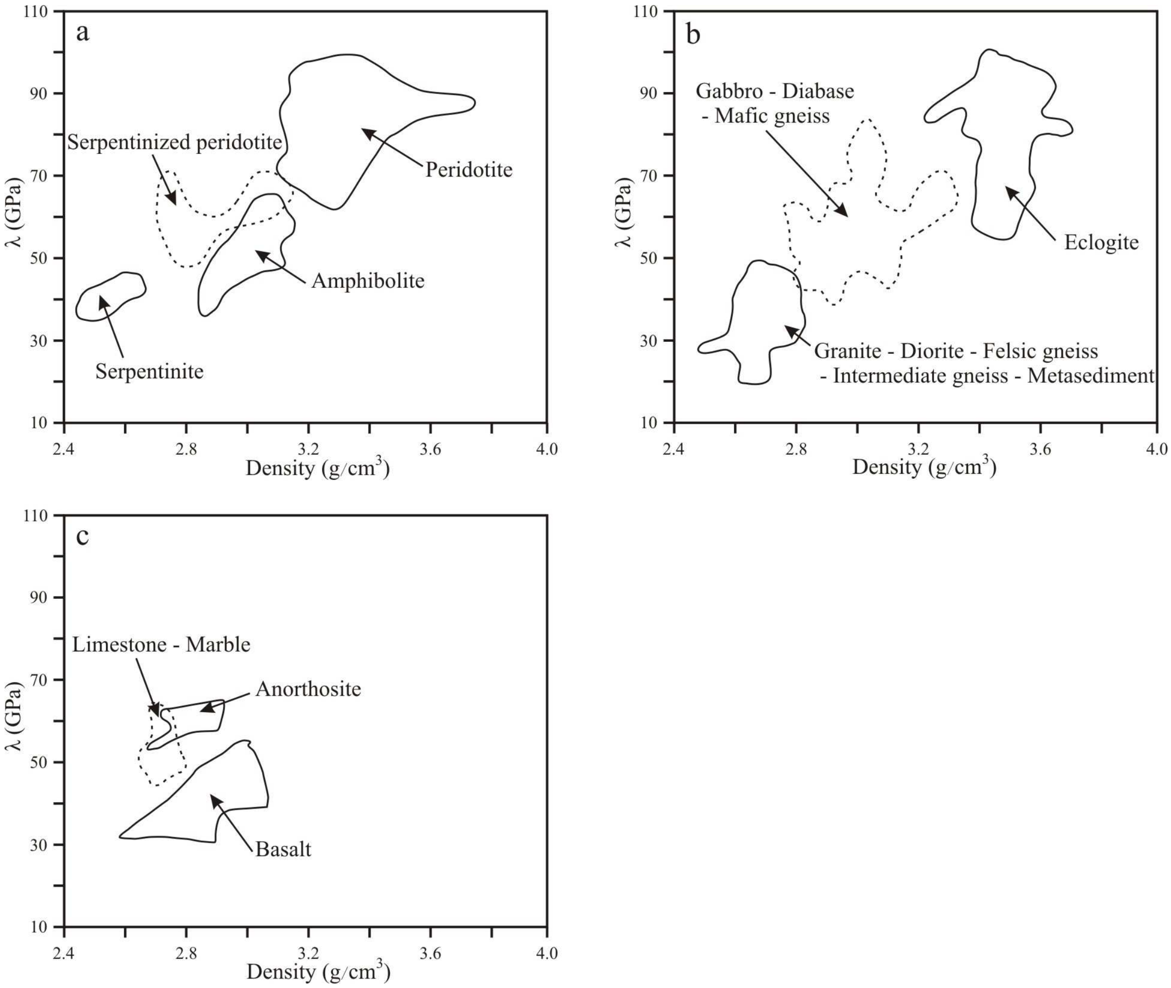

Figure 4.5 λ-ρ plots for 31 amphibolites, 38 peridotites, 12 serpentinites and 15 partially serpentinized peridotites (a), 54 eclogites, 118 mafic rocks (gabbro, diabase, mafic gneiss and mafic granulite) and 145 felsic rocks (granite, diorite, felsic gneiss, intermediate gneiss, and metasediments) (b), and 8 anorthosites, 21 basalts and 29 limestones/marbles (c) at a hydrostatic pressure of 600 MPa.

As shown in Fig. 4.6a, λ illustrates a clear trend of linear increase with density. The best-fitting of the data for 401 samples gives: $\lambda=57.814\rho-118.51$ ($R^2=0.79$), λ is in GPa, and ρ is in g/cm^3. In the statistical analysis, porous (basalt and sandstone) and hydrated (serpentinite) rocks are not included. There is considerable scatter in the distribution of the λ-ρ data for peridotites and eclogites due to mineralogical complexities (mainly the content of garnet). This will be analyzed in more detail in the Section 4.5.

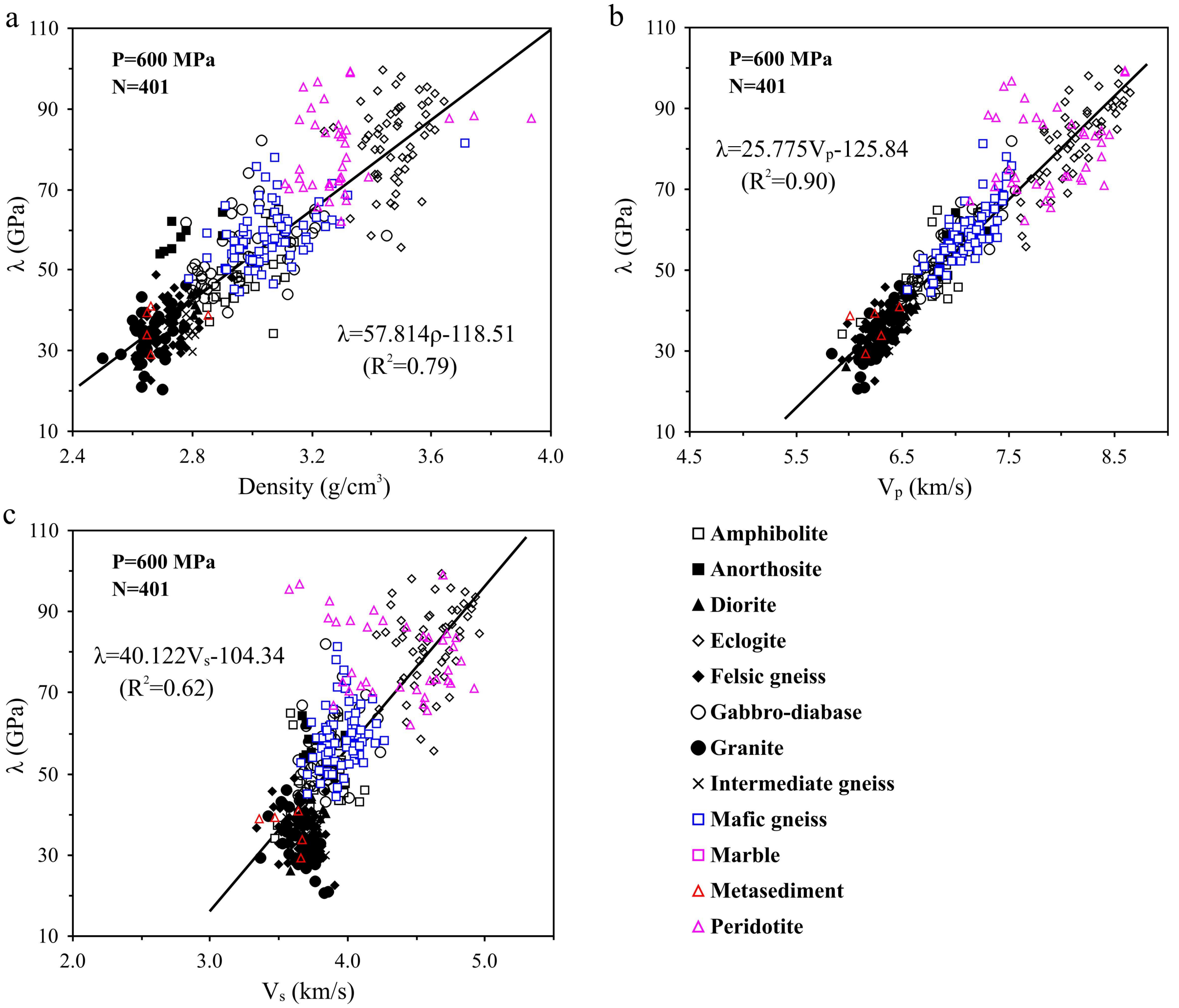

Figure 4.6 Variations in Lamé parameter (λ) with density (a), V_p (b), and V_s (c) for various types of rocks at a hydrostatic pressure of 600 MPa. 401 samples. Serpentinite and porous rocks such as basalt and limestone are not included.

4.4.5 λ-V_p correlation

Figure 4.7 provides λ-V_p plots for different categories of rocks at a confining pressure of 600 MPa. The trend of λ variation with V_p for peridotites with various degrees of serpentinization reflects essentially progressive decreases in both λ and V_p with increasing content of serpentine (Fig. 4.7a). It is noted that the presence of garnet, spinel or chromite may cause a significant increase in λ for peridotites. Eclogite displays higher values of both λ and V_p than the other mafic rocks such as gabbro, diabase, mafic gneiss, mafic granulite and amphibolite. Acid and intermediate rocks such as granite, diorite, felsic gneiss, intermediate gneiss and metasediments have lower λ and V_p values (Fig. 4.7b). Limestones/marbles show intermediate λ and V_p values between anorthosite and sandstone (Fig. 4.7c). The best-fitting of data for 401 samples (except of basalt, sandstone and serpentinite) gives: $\lambda=25.775V_p-125.84$ ($R^2=0.90$), where λ is in GPa, and V_p is in km/s (Fig. 4.6b).

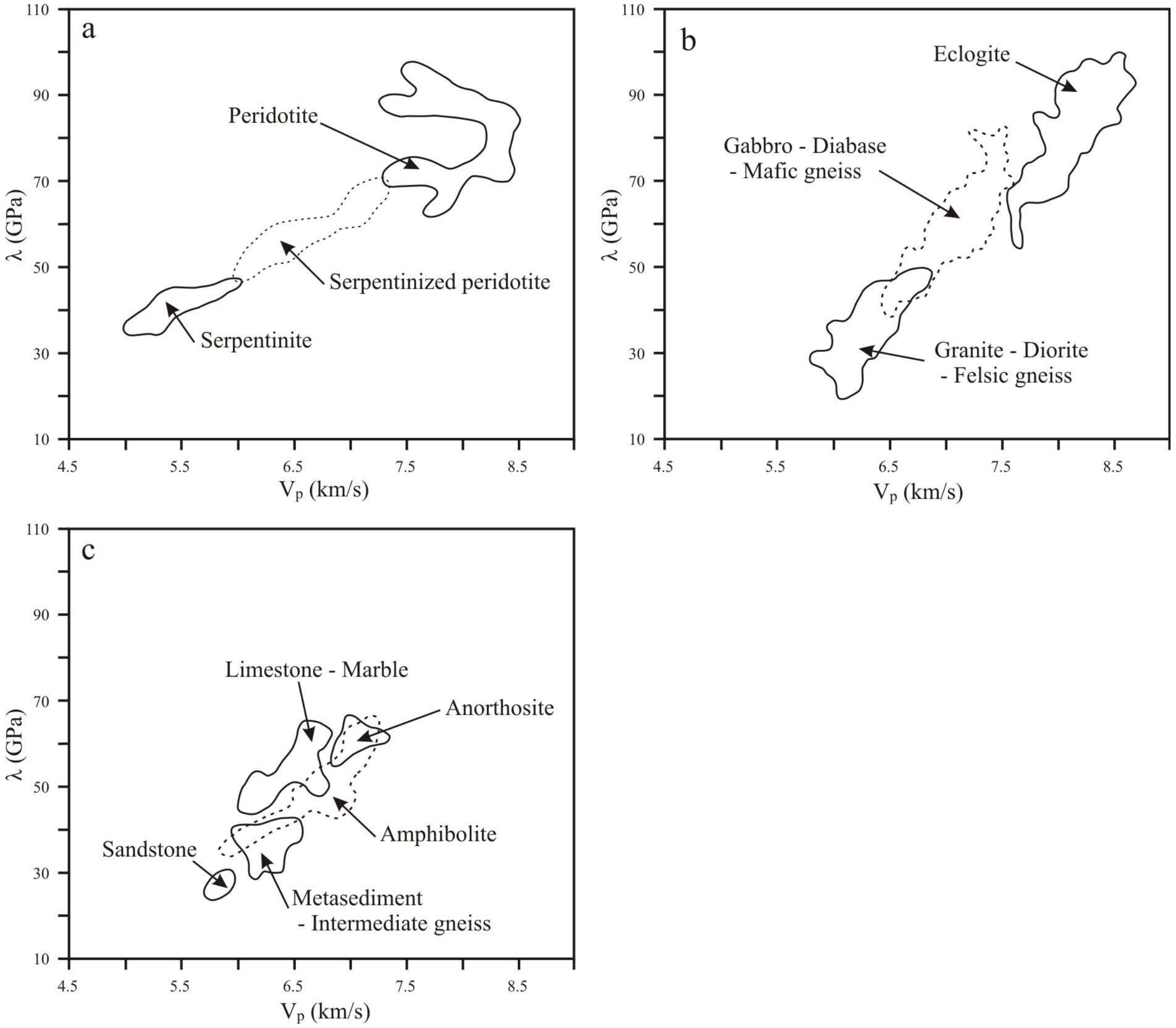

Figure 4.7 λ-V_p plots for 38 peridotites, 12 serpentinites and 15 partially serpentinized peridotites (a), 54 eclogites, 118 mafic rocks (gabbro, diabase, mafic gneiss and mafic granulite) and 145 felsic rocks (granite, diorite, felsic gneiss, intermediate gneiss, and metasediments) (b), and 31 amphibolites, 8 anorthosites, 21 basalts, and 29 limestones/marbles (c) at a hydrostatic pressure of 600 MPa.

4.4.6 λ-V_s correlation

Variations of λ values as a function of V_s are shown in Fig. 4.8 for different groups of rocks at a hydrostatic confining pressure of 600 MPa. Fresh peridotites can be clearly distinguished from serpentinite and partially serpentinized peridotites in the λ-V_s diagram (Fig. 4.8a). Eclogite can be easily separated from the other mafic rocks such as gabbro, diabase, mafic gneiss and mafic granulite according to their λ-V_s plots. Felsic rocks including granite, diorite, felsic gneiss, intermediate gneiss and metasediments are characterized by relatively lower λ values (Fig. 4.8b). Important differences between Fig. 4.7b and Fig. 4.8b originate from the high V_s value of quartz, which affects the relative positions of quartz-rich rocks (e.g., granite, granodiorite, diorite, and felsic gneiss). Porous volcanic basalts show significantly lower values in both λ and V_s than calcite-rich limestone-marble and plagioclase-rich anorthosite (Fig. 4.8c). The best-fitting of the data from 401 samples (excluding basalt, sandstone, and serpentinite) yields: $\lambda=40.122V_s-104.34$ ($R^2=0.62$), where λ is in GPa, and V_s in km/s (Fig. 4.6c). Obviously, the correlation of λ with V_p (Fig. 4.6b) is remarkably better than that with V_s (Fig. 4.6c).

4.4.7 μ-λ correlation

It is interesting to plot μ as a function of λ because these two invariants form the basic elements within all the elastic properties. If different types of rocks tend to separate from each other in the μ-λ diagram, these two parameters may be used as a discriminant of lithological compositions. As shown in Fig. 4.9, fresh peridotites, serpentinites and partially serpentinized peridotites can be distinguished from each other in the μ-λ plot. The ultramafic rocks display systematic decreases in both μ and λ with increasing degree of serpentinization. λ is always larger than μ with the mean μ/λ ratios equal to 0.810, 0.641 and 0.460 for the peridotite (38 samples), serpentinized peridotite (15 samples) and serpentinite (12 samples), respectively. The ratios correspond to the mean Poisson's ratios of 0.275, 0.305 and 0.343 for the peridotite, serpentinized peridotite and serpentinite, respectively. In Fig. 4.9a, amphibolites (31 samples) deviate clearly from the trend of the ultramafic rocks. According to the μ-λ plot, eclogite can be separated from other mafic rocks (e.g., gabbro, diabase, amphibolite, mafic gneiss and mafic granulite) as well as felsic rocks (e.g., granite, diorite, felsic gneiss, intermediate gneiss, and metasediments). The mean μ/λ ratios are 0.818, 0.915 and 1.057, corresponding to the mean

Poisson’s ratios of 0.275, 0.261 and 0.243, for the mafic rocks (118 samples), eclogites (54 samples) and felsic rocks (145 samples), respectively. Eclogite exhibits remarkably higher values of both μ and λ than the other common mafic rocks such as gabbro, diabase, mafic gneiss, mafic granulite and amphibolite. Data of acid and intermediate rocks (e.g., granite, diorite, felsic gneiss, intermediate gneiss and metasediments) cluster in a small area with lower μ and λ values. Limestone/marble (29 samples), basalt (21 samples) and anorthosite (8 samples) can also be separated from each other in the μ-λ plots (Fig. 4.9c).

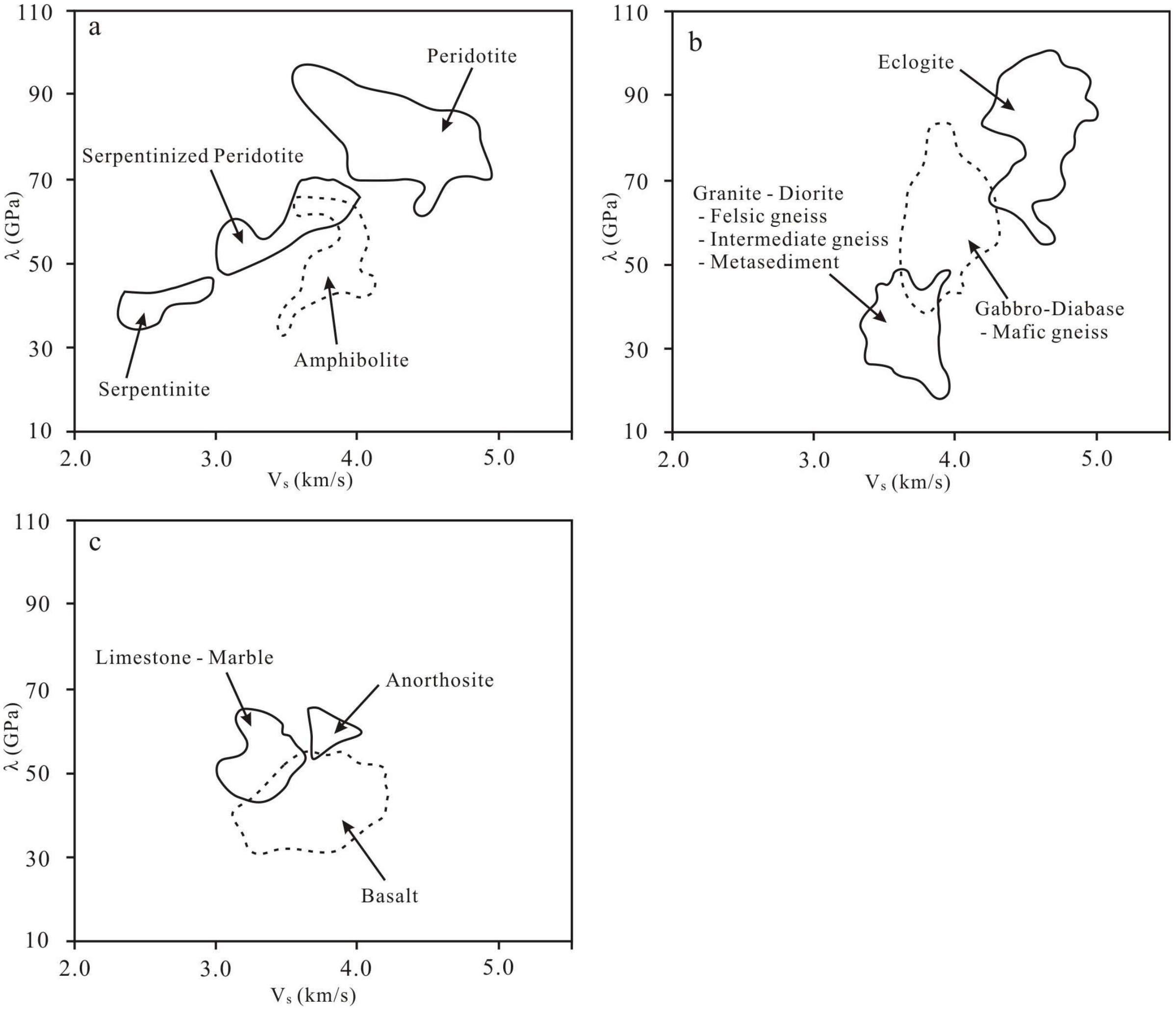

Figure 4.8 λ-V_s plots for 31 amphibolites, 38 peridotites, 12 serpentinites and 15 partially serpentinized peridotites (a), 54 eclogites, 118 mafic rocks (gabbro, diabase, mafic gneiss and mafic granulite) and 145 felsic rocks (granite, diorite, felsic gneiss, intermediate gneiss, and metasediments) (b), and 8 anorthosites, 21 basalts, and 29 limestones/marbles (c) at a hydrostatic pressure of 600 MPa.

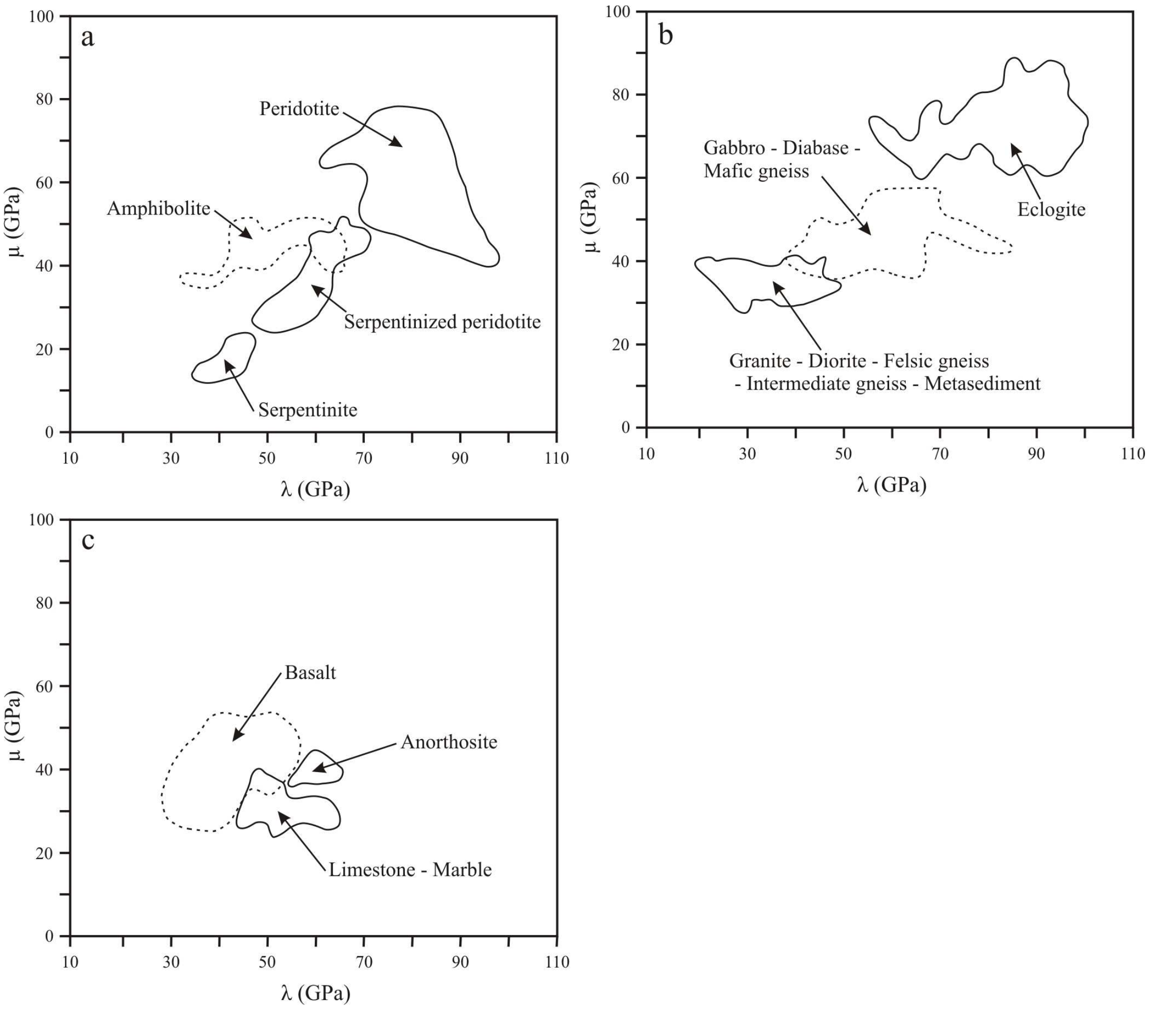

Figure 4.9 μ-λ plots for 31 amphibolites, 38 peridotites, 12 serpentinites and 15 partially serpentinized peridotites (a), 54 eclogites, 118 mafic rocks (gabbro, diabase, mafic gneiss and mafic granulite) and 145 felsic rocks (granite, diorite, felsic gneiss, intermediate gneiss, and metasediments) (b), and 8 anorthosites, 21 basalts and 29 limestones/marbles (c) at a hydrostatic pressure of 600 MPa.

4.5 Discussion

In this section, the relationship between λ and mineral composition of crystalline rocks is analyzed (Figs. 4.4-4.8). Figures 4.10a and b, plotting λ versus ρ, and μ versus λ, respectively, provide some interesting perspectives on λ characteristics of pure monomineralic aggregates of common rock-forming minerals. The λ value of a polymineralic composite rock depends presumably on the volume fractions and the λ values of its constituent minerals. The contribution of each constituent mineral to the bulk λ value of a composite rock can be analyzed for the moment only in a qualitative manner because a relevant mixture rule for λ is not available (Lubarda, 1998; Nadeau, 1999; Berryman, 1995; Ji and Xia, 2002; Ji, 2004; Marko et al., 2009). The utilization of the λ-ρ and μ-λ plots for lithological discrimination is also discussed.

Quartz is characterized by extremely low values in both λ (~8.1 GPa) and ρ (2.65 g/cm^3) but moderate value in μ (44.4 GPa; Bass, 1995). Hence, it lies obviously below and above the general trends in the λ-ρ (Fig. 4.9a) and μ-λ (Fig. 4.9b) diagrams, respectively. Moreover, quartz-rich sandstones should have significantly lower λ or $\lambda\rho$ values than calcite-rich or dolomite-dominant carbonates. This feature can be used for quick determination of reservoir lithology and in turn is economically important for oil- or gas-field exploration in sedimentary basins (Goodway et al., 1997; Goodway, 2001; Gray and Andersen, 2000; Gray, 2003; Dufour et al., 2002). In the seismological investigation of carbonate reservoir in the Western Canadian sedimentary basin (Goodway et al., 1997; Li et al., 2003), for example, $\lambda\rho$ and μ/λ were used as a good indicator for distinguishing tight limestone ($\lambda\rho$=~90.0 GPa·g/cm^3 and μ/λ=~0.81), wet dolomite ($\lambda\rho$=~75.0 GPa·g/cm^3, μ/λ =~1.24) and gas dolomite ($\lambda\rho$=~37.5 GPa·g/cm^3, μ/λ=~2.08). The gas effect is apparent on reducing the $\lambda\rho$ and increasing μ/λ values because the presence of gas in porous, grain-supported rocks causes a significant decrease in its incompressibility (K) but does not affect its rigidity (μ). As a result, λ is significantly reduced by the presence of gas. In petroleum industry, therefore, layers of low λ or $\lambda\rho$ values derived from the inversion of AVO (amplitude versus offset) stacks often suggest the presence of gas in a sandstone or dolomite reservoir (Goodway and Tessman, 2000; Gray and Andersen, 2000). In addition, coals have low rigidity and thus low shear modulus, and have low incompressibility and hence low λ values.

Feldspars, which are the most abundant minerals in the Earth's crust, form a ternary system of three end-members: $KAlSi_3O_8$ (orthoclase), $NaAlSi_3O_8$ (albite) and $CaAl_2Si_2O_8$ (anorthite). For the plagioclase series, λ, μ and ρ all increase nearly linearly with increasing the amount of anorthite component (Fig. 4.10). There is a nearly linear relationship between λ and ρ or between μ and λ for plagioclase feldspars. The alkali feldspars have lower λ and μ values than plagioclase feldspars. Nepheline (Ne) and serpentine (Srp) lie at almost the same position as orthoclase (Or) in the λ-ρ diagram, although these three minerals are separated in the μ-λ diagram with $\mu_{Ne}>\mu_{Or}>\mu_{Srp}$. In either the λ-ρ or μ-λ diagram (Fig. 4.10), both alkali and plagioclase feldspars can be clearly separated from quartz. Thus, the λ-ρ and μ-λ plots may be used to discriminate quartz- from feldspar-dominant layers or domains in the continental crust. Furthermore, Fig. 4.10 illustrates the reason why acid and intermediate rocks (e.g., granite, diorite, felsic gneiss, intermediate gneiss and metasediments), which consist of alkali feldspar, plagioclase, quartz, and mica, are low in both λ and ρ or μ and λ values.

Accessory minerals such as zircon, rutile, ilmenite, sillimanite and spinel show generally very high λ and μ values with respect to the main rock-forming silicate minerals (Fig. 4.10). Increasing the content of these minerals will result in an increase of λ and μ for the bulk rock.

In the μ-λ diagram (Fig. 4.10b), pyroxenes (ferrosilite, augite, diallage, bronzite, enstatite, diopside, hedenbergite and aegirine) form a lozenge-shaped domain while high pressure pyroxenes, omphacite and jadeite, lie far outside this domain. Compared with jadeite and omphacite, diallage, enstatite, bronzite and augite have relatively lower λ values. Ferrosilite has a much higher density than diopside, but both minerals show similar λ values. The role of Fe-Mg substitution in orthopyroxenes can be seen by the comparison between enstatite ($MgSiO_3$) and ferrosilite ($FeSiO_3$): ρ=3.198 g/cm^3, μ=75.7 GPa, λ=57.3 GPa, and μ/λ=1.32 for enstatite whereas ρ=4.002 g/cm^3, μ=52.0 GPa, λ=66.3 GPa, and μ/λ=0.78 for ferrosilite. Hornblende shows similar λ and ρ values to enstatite. In the μ-λ diagram, however, hornblende lies close to anorthite. Obviously, mafic rocks (e.g., gabbro, diabase, mafic gneiss and mafic granulite) in which pyroxene and labradorite-rich plagioclase (50% to 70% anorthite) are principal constituents have moderate μ, λ and ρ values between the end-members.

In the olivine group [$(Fe, Mg)_2SiO_4$], both λ and ρ values increase with increasing content of Fe_2SiO_4 (fayalite) whereas the μ value increases with increasing content of Mg_2SiO_4 (forsterite). In other words, λ shows a positive correlation with ρ, but a negative correlation with μ for olivine. The role of Fe-Mg substitution in olivines is particularly significant: ρ=3.222 g/cm^3, μ=81.7 GPa, λ=74.2 GPa, and μ/λ=1.1 for forsterite whereas ρ=4.377 g/cm^3, μ=50.8 GPa, λ=102.7 GPa, and μ/λ=0.49 for fayalite. Figure 4.10 also indicates the position of olivine with forsterite content Fo100 to Fo90, which represents the typical composition of common olivine in the upper mantle. In both the λ-ρ and μ-λ diagrams, the upper mantle olivine is located close to omphacite. A peridotite which is a mixture of olivine, orthopyroxene and clinopyroxene should lie somewhere among these three end-members, and the exact position depends on the volume fraction of each constituent and also on the amount of accessory minerals such as spinel, garnet, magnetite and ilmenite. The μ, λ and ρ of peridotites decrease with increasing degree of serpentinization because serpentine, as their hydrated product has extremely low values in λ (32.3 GPa), μ (15.67 GPa) and ρ (2.516 g/cm^3). Thus, the λ or λρ data may allow the prediction of the serpentine content in the oceanic lithosphere from the inversion of surface seismic data through AVO methods.

In the λ-ρ or μ-λ diagram (Fig. 4.10), silicate garnets can be classified into two groups: pyralspite (pyrope-almandine-spessartine) and ugrandite (uvarovite-grossular-andradite) groups. From pyrope to almandine or spessartine, λ remains almost unchanged, but ρ increases considerably. The μ and λ values for pyrope, almandine and spessartine are very similar (Fig. 4.10b). Therefore differences in the relative proportions of these components have little influence on the μ and λ values of pyralspite. Uvarovite displays higher λ values than andradite although they have similar densities. From grossular to andradite, λ increases slightly but ρ increases and μ decreases significantly (Fig. 4.10).

Eclogites, which consist of garnet and omphacite with rutile and magnetite as accessory minerals, are certainly very high in μ, λ and ρ values (Figs. 4.5 and 4.10). The mafic granulite-eclogite transformation occurs near the base of thickened continental crust that is forced into the upper mantle during a collisional orogeny. Such a huge mass of eclogite may delaminate from the crust and sink into the mantle. As indicated by Fig. 4.5b and Fig. 4.9b, the transition from mafic granulite or gabbro to eclogite should result in a significant increase in λ, μ and ρ. Such striking contrasts make distinction between eclogite and mafic granulite possible. Eclogite has seismic velocities similar to surrounding mantle peridotite (Figs. 4.6b-c). However, the distinction of eclogite from peridotite is likely in the λ-ρ diagram (Fig. 4.6a).

Muscovite shows a relatively lower λ value with respect to its density (Fig. 4.10). If the similar situation is true for other phyllitic minerals (e.g., biotite, phengite, phlogopite and chlorite) whose elastic constants are not available due to experimental restrictions, one would expect that the mica-rich rocks, which often occur in retrograde shear zones within the continental crust, are characterized by low λ values.

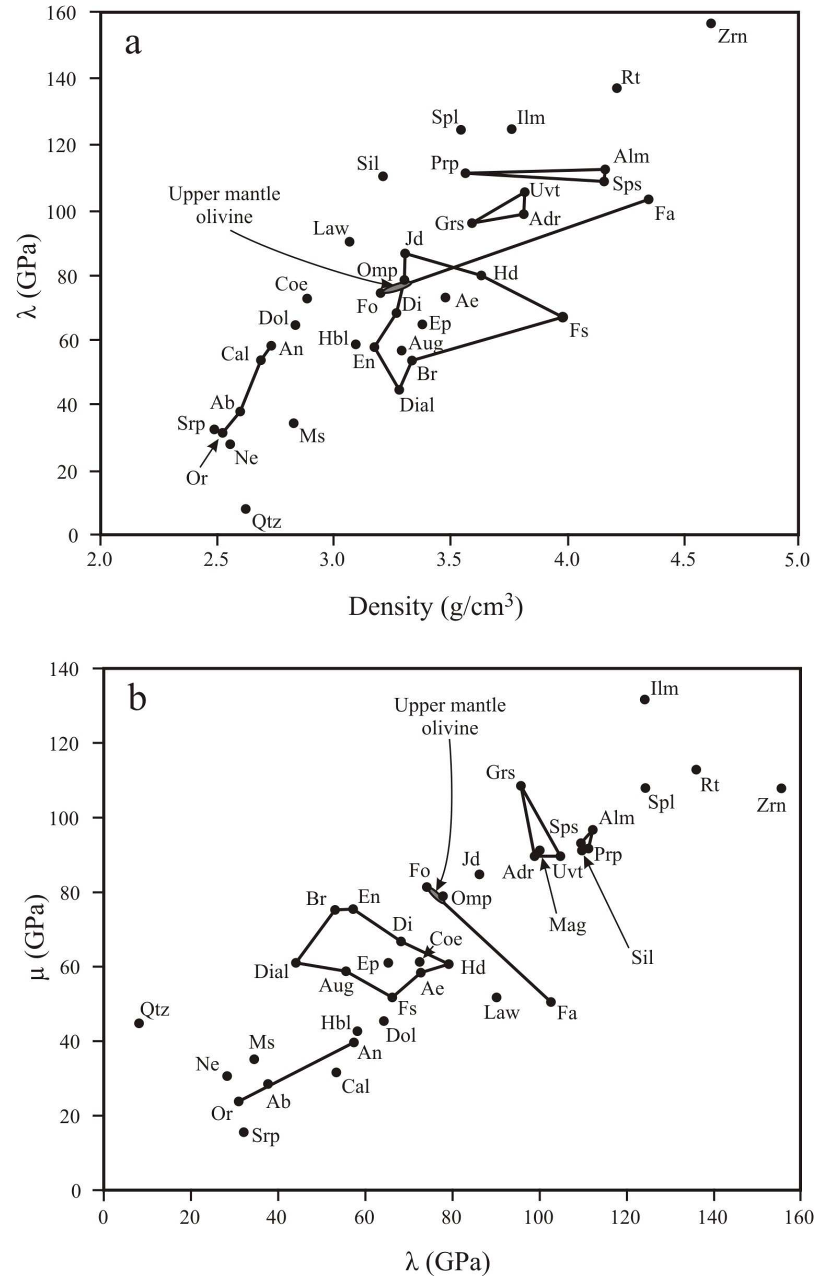

Figure 4.10 λ-ρ (a) and μ-λ (b) plots for main rock-forming minerals. Ab: albite; Adr: andradite; Ae: aegirine; Alm: almandine; An: anorthite; Aug: augite; Br: bronzite; Cal: calcite; Coe: coesite; Cpx: clinopyroxene; Di: diopside; Dial: diallage; Dol: dolomite; En: enstatite; Ep: epidote; Fa: fayalite; Fo: forsterite; Fs: ferrosilite; Grs: grossular; Hbl: hornblende; Hd: hedenbergite; Ilm: ilmenite; Jd: jadeite; Law: lawsonite; Mag: magnetite; Mus: muscovite; Ne: nepheline; Omp: omphacite; Or: orthoclase; Prp: pyrope; Qtz: quartz; Rt: rutile; Sil: sillimanite; Spl: spinel; Sps: spessartine; Srp: serpentine; Uvt: uvarovite; Zrn: zircon. The values of λ and μ for each mineral were calculated from the elastic constants compiled in Bass (1995).

As illustrated in Fig. 4.9, the variation range in either μ or λ is much larger for mafic rocks than high-silica rocks. These differences reflect the fact that there is considerable variation in plagioclase, clinopyroxene, orthopyroxene, hornblende, and garnet in mafic rocks of various origins (magmatic crystallization for gabbro and diabase, and metamorphism for mafic granulite and mafic gneiss). Both the μ and λ values of these minerals are very disparate and hence a change in their relative proportion has a significant effect on these elastic parameters. In the felsic rocks, however, the dominant minerals are potassium feldspar and sodic plagioclase, both having similar μ and λ values. Thus variations in μ and λ correspond mainly to the difference in the relative proportion of quartz in the felsic rocks. Similarly, the large range of variations in μ and λ values for eclogites result principally from the difference in the relative proportion of garnet.

Metamorphism is also an important factor to influence the λ value of a rock. For example, pelitic rocks at greenschist facies grades contain chlorite, muscovite, quartz and albite. At the upper amphibolite or granulite facies grades, however, the rocks with the same chemical composition contain garnet, sillimanite, oligoclase or andesine, quartz and hornblende or pyroxene (Burlini and Fountain, 1993). Increases in the contents of garnet, sillimanite, hornblende and pyroxene and in anorthite content of plagioclase during progressive metamorphism should systematically result in an increase in rock's λ value.

Finally, the presence of fluids in porous materials such as sedimentary rocks affects significantly λ but not μ (Goodway*,* 2001). μ and λ are sensitive to the rock matrix and pore fluids, respectively. For example, it is impossible to distinguish shale (V_p=2.898 km/s) from gas sandstone (V_p=2.857 km/s) according their P-wave velocities. However, it is easy to discriminate these rocks according to their λ values: 12.3 GPa for shale and 5.9 GPa for gas sandstone. The reason is simple. As $V_p = \sqrt{(\lambda + 2\mu)/\rho}$, the λ decrease of sandstone due to the gas porosity is nearly completely offset by an increase in 2μ resulting from the predominance of quartz in sandstone over shale.

4.6 Conclusions

Lamé parameter (λ), which is closely related to the incompressibility and contains a high proportion of information about the resistance to a change in volume caused by a change in pressure, is an important, intrinsic, elastic property of rocks. Only λ and shear modulus (μ) appear in Hooke's law but not Young's modulus (E), the bulk modulus (K) or Poisson's ratio (υ). Unfortunately, so far little has been known about the characteristic λ value for each common type of crystalline rocks that constitute the Earth's crust and upper mantle and its variation with pressure (P), temperature (T) and mineralogical composition. Here such a gap is filled by analyzing in details the λ values of 475 natural rocks on which mean P- and S-wave velocities have been measured at high hydrostatic pressures ($\geq 400\,\mathrm{MPa}$) using the same laboratory equipment and the same method. The λ value of an equivalent isotropic crystalline rock as a function of confining pressure (P) and temperature (T) can be described by $\lambda = a + (d\lambda/dP)P - c\exp(-kP) - (d\lambda/dT)T$, where *a* is the projected λ value at zero pressure if microcracks were fully closed; dλ/dP is the pressure derivative in the linear elastic regime; *c* is the initial λ drop caused by the presence of microcracks at zero pressure; *k* is a decay constant of the λ drop in the nonlinear poro-elastic regime; and dλ/dT is the temperature derivative. The laboratory experimental data may be extrapolated to the Earth's interior using the above equation if no partial melting, metamorphic reaction, dehydration or phase transformation occurs. In the λ-ρ and μ-ρ plots, the main categories of lithology can be clearly discriminated. The ultramafic rocks display systematic decreases in both μ and λ with increasing degree of serpentinization. Eclogites, mafic rocks (gabbro, diabase, mafic granulite, and mafic gneiss) and felsic rocks (granite, diorite, felsic gneiss, intermediate gneiss and metasediments) are characterized by high, moderate and low μ and λ values, respectively. For pyroxenes and olivines, both λ and ρ increase but μ decreases with increasing Fe/Mg ratios. In the plagioclase series, both λ and μ increases with increasing anorthite content. Increases in the contents of garnets, sillimanite, rutile, zircon, ilmenite and spinel result systematically in an increase in rock's λ and μ values. The results suggest that the λ-ρ and μ-ρ plots can be used as a discriminant of composition for rocks in the Earth's crust and upper mantle. This is particularly important because the connection between composition and seismic P- or S-wave velocity is not unique due to similar velocities of many common rock types.

CHAPTER 5 ON THE FORMATION OF SEISMIC ANISOTROPY AND SHEAR WAVE SPLITTING IN OCEANIC SUBDUCTION ZONES

5.1 Abstract

Subduction zones are critically important regions where significant geological processes (e.g., phase transition, dehydration, partial melting, volcanism, and seismic activity) take place. Seismic anisotropy originated from different parts of subduction system (i.e., overriding plate, mantle wedge, subducting slab, and subslab mantle) can be distinguished by analyzing seismic wave raypaths. This chapter presents a state-of-art overview on shear wave splitting patterns measured from global oceanic subduction zones, and on mechanism models [e.g., 2D corner flow, 3D trench-parallel flow induced by trench migration, olivine lattice preferred orientations (LPO) and serpentinization]. Olivine LPOs formed by (010)[100], (010)[001], (100)[001], {0kl}[100], (001)[100] and {110}[001] slip systems are classified as A, B, C, D, E and F-type fabrics, respectively. The A, D, and E-type fabrics cause fast polarization directions (ϕ) parallel to the mantle flow while ϕ formed by B-type fabric is perpendicular to the mantle flow. Olivine C-type LPO also results in a ϕ parallel to the mantle flow, but the resultant delay time (δt) is much smaller than A-type. F-type fabric results in almost no splitting in the direction normal to the mantle flow plane. In mantle wedge and subducting lithosphere mantle, the most important hydrous mineral is antigorite, which is characterized by low flow strength, low seismic velocities, and extremely high elastic anisotropy. Accordingly, the extensively serpentinized mantle wedge rocks usually have relative high seismic anisotropy and shear wave splitting. If more than ~10-20% serpentinization occurs, serpentine LPO would control the seismic anisotropy of deformed mantle rocks. As shear wave splitting in the mantle wedge depends on both the degree of serpentinization and the slab dip, highly serpentinized and steeply dipping subduction systems are more likely to produce a trench-parallel ϕ.

5.2 Introduction

When a shear wave (S wave) propagates in an anisotropic medium, it splits into two orthogonally polarized fast (V_{s1}) and slow (V_{s2}) components. As the two components propagate through the anisotropy region at different velocities, they accumulate a time delay. The delay (splitting) time (δt) provides information about the thickness of the anisotropic layer and the strength of its seismic anisotropy. The fast polarization direction (ϕ), which reflects the polarization azimuth of fast wave within the plane perpendicular to the propagation direction, oriented with respect to the principal axes (X, Y, Z) and planes (e.g., foliation S, shear plane C) of finite strain ellipsoid. The shear wave splitting parameters, ϕ and δt, are the two most significant parameters to measure the seismic anisotropy of the Earth's crust and upper mantle.

Subduction zones are critical regions where significant geological processes (e.g., phase transition, dehydration, partial melting, volcanism, and seismic activity) take place. Thus shear wave splitting has become a powerful geophysical tool to characterize the seismic anisotropy and structure of subduction zones, especially oceanic subduction zones. Seismic anisotropy formed by different parts of a subduction system (i.e., overriding plate, mantle wedge, subducting slab, and subslab mantle) can be distinguished by analyzing seismic wave raypaths (Fig. 5.1).

(1) Direct S waves (blue rays in Fig. 5.1) which are generated from subducting slab earthquakes and then recorded at seismic stations on the overriding plate, mainly reflect anisotropy of the mantle wedge (e.g., Fischer and Wiens, 1996; Fischer et al., 2000; Levin et al., 2004; Long and van der Hilst, 2006; Pozgay et al., 2007; Abt et al., 2009), because the contribution by the overriding crust is almost negligible (Ji and Salisbury, 1993; McNamara et al., 1994; Herquel et al., 1995; Sherrington et al., 2004; Frederiksen et al., 2003; Ozacar and Zandt, 2004). For instance, samples of Haast schists and mylonites collected from surface outcrops in the Alpine fault of New Zealand display strong P- and S-wave anisotropy (up to 17%), but reflection seismic experiments using crustal SmS phases show only weak splitting ($\delta t \leq 0.1$ s)

(Okaya et al., 1995; Godfrey et al., 2000). This discrepancy may be attributed to differently oriented and complicated structures formed by multiple phases of deformation in the scale of shear wave window, which produce destructive interference and obscure or cancel any splitting that existed in the sample or outcrop scale (Ji and Salisbury, 1993; Ji et al., 1994; Pulford et al., 2003).

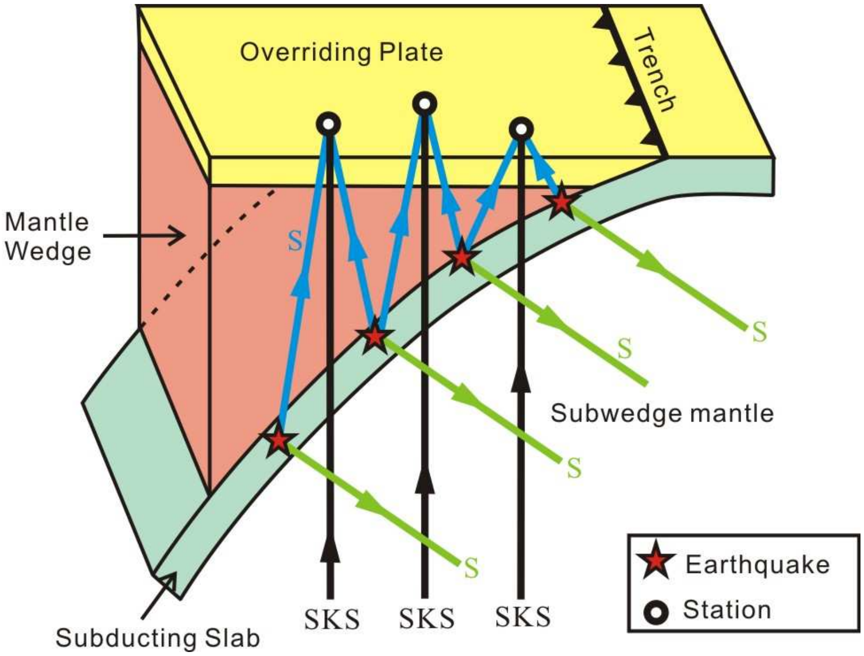

Figure 5.1 Illustration of various raypaths of S and SKS waves that detect seismic anisotropy originated from different parts of subduction system (i.e., overriding plate, mantle wedge, subducting slab, and subwedge mantle).

(2) Teleseismic S waves (green rays in Fig. 5.1) which are generated from slab earthquakes and recorded at distant stations, if removed anisotropy beneath the receiver, mainly reflect the anisotropy beneath the mantle wedge (e.g., Russo and Silver, 1994; Russo, 2009).

(3) Teleseismic SKS (SKKS) waves (black rays in Fig. 5.1) recorded at stations on the overriding plate, contains information of all anisotropy layers along the raypaths. The subwedge anisotropy can be estimated from a correction for anisotropy in the mantle wedge from the teleseismic measurements (e.g., Abt et al., 2010).

5.3 Splitting in oceanic subduction zones

In the 80s of the 20th century, Ando et al. (1983), Fukao (1984), and Bowman and Ando (1987) firstly reported shear wave splitting data in Japan and Tonga subduction zones. Since then, a large number of splitting studies in subduction zone regions have been performed. Long and Siver (2008, 2009) compiled shear wave splitting behavior observed in global oceanic subduction zones (Fig. 5.2). Blue and red arrows in Fig. 5.2 indicate average ϕ_{MW} (the fast polarization direction of the mantle wedge) and ϕ_{SW} (the fast polarization direction of the subwedge), respectively.

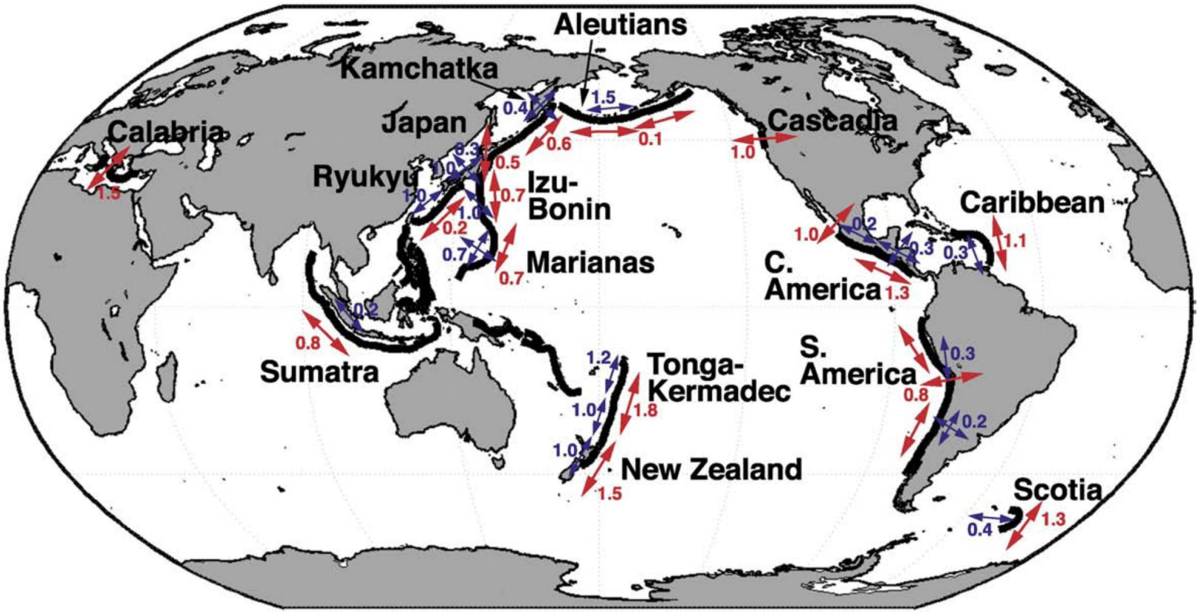

Figure 5.2 Shear wave splitting patterns of mantle wedge (blue) and subwedge mantle (red). Arrows indicate average fast polarization directions (ϕ), and numbers show the associated average delay times (δt, in sec). After Long and Becker (2010).

The characteristics of shear wave splitting in the subwedge are evident: ϕ_{SW} are overwhelmingly trench-parallel, such as the Aleutians (Long and Silver, 2008), Kamchatka-Kuril (Peyton et al., 2001; Levin et al., 2004), Ryukyu arc (Long and van der Hilst, 2005, 2006), Izu-Bonin-Mariana (Wirth and Long, 2010; Wookey et al., 2005), Tonga-Kermadec-New

Zealand (Long and Silver, 2008; Audoine et al. 2004), Middle America, South America (Abt et al., 2009; Polet et al.,2000; Russo and Silver, 1994) and Sumatra (Long and Silver, 2009). In a few subduction zones, ϕ_{SW} are mainly oblique to the trench (e.g, Honshu; Long and Silver, 2009) or even trench-perpendicular (e.g., Cascadia, Currie et al., 2004; central South America, Polet et al., 2000). The subwedge delay time (δt_{SW}) varies in a wide range, for example, the subwedge beneath Ryukyu arc is almost isotropic ($\delta t_{SW} < \sim 0.2$ s) while the average δt_{SW} values beneath Tonga-Kermadec ranges from ~1.0 s up to ~2.4 s (Long and Silver, 2009).

The splitting patterns in the mantle wedge are usually complex. Some subduction zones exhibit trench-parallel ϕ_{MW}, such as the Aleutians, Japan Sea and the western Honshu (Fouch and Fischer, 1996), the Hikurangi subduction zone in New Zealand (Marson-Pidgen et al., 1999), the Sumatra subduction zone (Hammond et al., 2010); ϕ_{MW} are oblique or perpendicular to the trench in some other subduction zones, such as Izu-Bonin-Mariana (Fouch and Fischer, 1996) and the northwestern part of Chile (Polet et al., 2000). A few subduction zones exhibit a transition in ϕ_{MW} from trench-parallel close to the trench to trench-perpendicular in backarc regions (e.g., the northeastern Japan, Nakajima and Hasegawa, 2004; Huang et al., 2011), but the opposite transition is also reported (e.g., Kamchatka, Levin et al. 2004). Shear wave splitting data in some mantle wedges are too complex to characterize, taking Japan as an example, where ϕ_{MW} are parallel, perpendicular, and highly oblique to the trench from Kyushu in the south to Hokkaido in the north (Salah et al., 2008; Wirth and Long, 2010). The global δt_{MW} (delay time in the mantle wedge) also varies in a wide range, for example, the mantle wedges of the western South America (Russo and Silver, 1994) and Colombia in Middle America (Shih et al., 1991) are nearly isotropic ($\delta t_{MW} = 0.1\text{-}0.4$ s); but the observed δt_{MW} are up to 1.5 s in the Hikurangi subduction zone (Marson-Pidgen et al., 1999).

A variety of mechanism models have been proposed to explain the complex and diverse shear wave splitting patterns in the oceanic subduction zones. Here some typical models will be presented and discussed, although at present none of them has perfectly interpreted the splitting data observed from global subduction zones.

5.4 Corner flow in the mantle wedge

Seismic anisotropy can have a variety of causes, including (1) Composite different elastic layers, each layer is isotropic or anisotropic (Backus, 1965; Ji et al., 2004). Seismic velocities propogating parallel to the layer planes are much higher than perpendicular to them. (2) Preferentially-aligned cracks whatever dry or fluid/melt-filled (Crampin and Booth, 1985; Kendall, 1994; Wang and Ji, 2009). Seimic velocities propagating across aligned cracks are much lower than parallel to them. (3) Lattice preferred orientations (LPO) of anisotropic minerals. It is widely accepted that seismic anisotropy in the upper mantle is controlled by the fabrics of olivine and orthopyroxene, which are the two most important constitutive minerals in the upper mantle (Hess, 1964; Nicolas and Christensen, 1987; Ji et al., 1994; Mainprice, 2007).

Olivine is volumetrically the most important mineral in the upper mantle (Fig. 5.3). It has a P-wave anisotropy of up to 22.9%, with the maximum (10.0 km/s), intermediate (8.4 km/s) and minimum velocity (7.7 km/s) along the direction of [100], [001] and [010], respectively (Ji et al., 2002). The maximum shear wave splitting (1.0 km/s) occurs in the [101] direction, while little or no splitting occurs in the [100] direction. Seismic anisotropy and shear wave splitting data in the upper mantle are interpreted mostly in terms of current or frozen LPO of olivine, which is generally thought to be formed by dislocation creep in the lithospheric mantle (Ji et al., 1994; Silver, 1996; Savage, 1999) or the asthenosphere (Vinnik et al., 1992), because diffusion creep- or grain boundary slip-dominated superplastic deformation cannot produce LPO (Karato and Wu, 1993). When an aggregate of olivine is deformed in the dislocation creep regime, the strength of LPO will increase with increasing strain. However, the increase of LPO strength is not unlimited, it will saturate when the strain exceeds a certain critical value (say, γ=4-5).

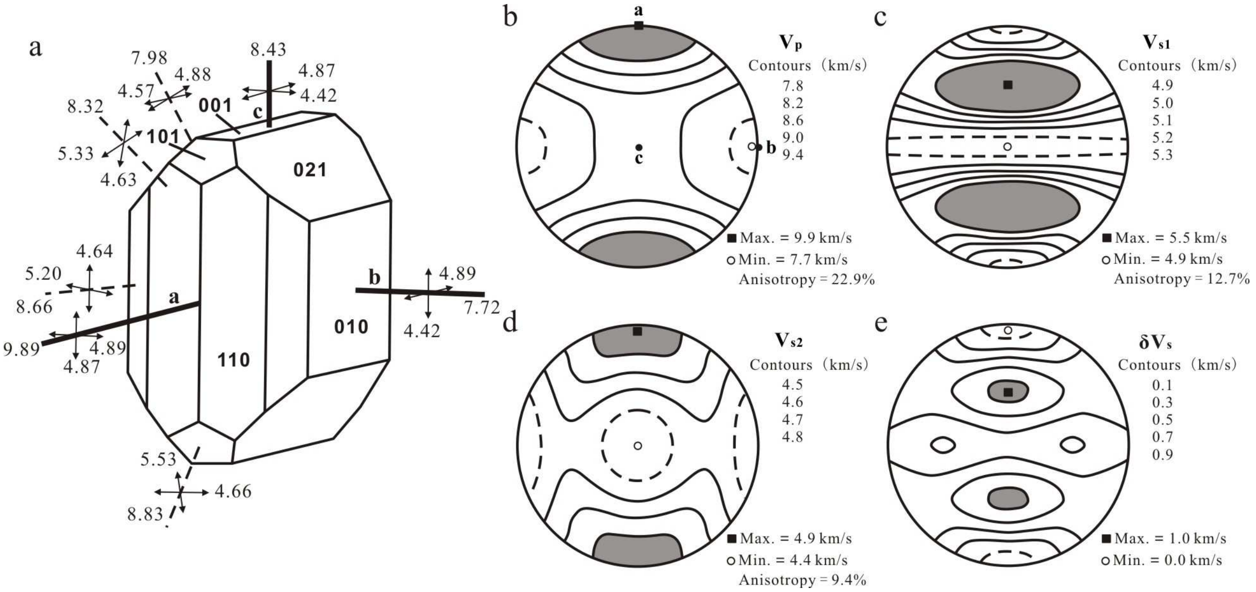

Figure 5.3 Seismic velocities of olivine single crystal. (a) V_p, V_{s1} and V_{s2} values in main crystallographic directions (in km/s, $V_p>V_{s1}>V_{s2}$). (b-e) V_p, V_{s1}, V_{s2} and δV_s ($V_{s1}-V_{s2}$) are shown in equal area stereographic projection with respect to the olivine crystallographic axes of a, b, and c.

The most common olivine LPO found in natural and experimentally deformed samples is characterized by the (010) plane parallel to the shear plane (C-plane), [100] axis parallel to the shear direction (Ji et al., 1994; Saruwatari et al., 2001). The angle between the shear plane and the maximum compression plane (i.e., foliation or XY plane of the finite strain ellipsoid), as well as the angle between the shear direction and the maximum stretching direction (i.e., X axis of the finite strain ellipsoid), tends to decrease with increasing shear strain. In the mantle wedge, the rheological coupling between the subducting slab and the wedge usually forms two-dimensional (2D) corner flow (Fig. 5.4), which will induce strong olivine LPO with (010) plane parallel to the flow plane and the [100] direction parallel to the flow direction. This classical model predicts ϕ_{MW} parallel to absolute subducting slab motion (i.e., perpendicular or highly oblique to the trench) and δt_{MW} depending on the convergence velocity and the slab dip angle. The slabs with fast subducting velocities are more likely to cause a larger-scale corner flow, which would result in higher strain and stronger LPO. In certain subduction zones where slab dip is nearly constant,

δt_{MW} values are predicted to be uniform (McKenzie, 1979; Ribe, 1989; Fischer et al., 2000), which is consistent with splitting data observed in some backarc regions, for example, the western Tonga-Kermadec subduction zone (Fischer and Wiens, 1996) and the backarc regions of Izu-Bonin (Fouch and Fischer, 1996). Theoretically speaking, mantle flow is more or less stagnant or even trench-parallel in the wedge corner (Fig. 5.4), consequently produces relatively weak or complicated LPO patterns, and thus scattered ϕ_{MW} and δt_{MW} values.

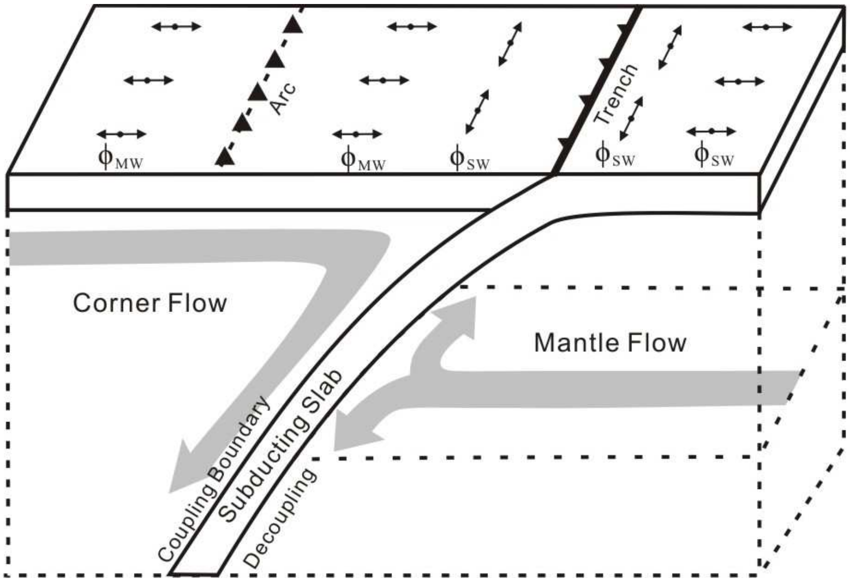

Figure 5.4 Shear wave splitting patterns produced by 2D corner flow in the mantle wedge and 3D trench-parallel flow in the subslab mantle when olivine develops A-type fabrics.

Physical modeling of corner flow indicates that the strength of mineral LPO in the wedge has strong dependence on slab dip (Buttles and Olson1998). Fischer et al. (2000) demonstrated that the wedge splitting patterns of the Tonga subduction zone could be numerically modeled using the LPO of olivine and orthopyroxene induced by 2D corner flow. However, 2D corner flow model could not interpret the trench-parallel ϕ_{MW} measured in some subduction zones; even the interpretation of trench-normal ϕ_{MW} needs being refined. Besides, corner flow model predicts an increasing δt_{MW} with increasing convergence velocity, but no such correlation has been observed (Long and Silver, 2008).

5.5 Trench migration

Russo and Silver (1994) originally attributed the trench-parallel seismic anisotropy beneath the Nazca Plate to trench-parallel flow induced by slab rollback and trench migration (Fig. 5.4 and 5.5). Buttles and Olson (1998) physically modeled the effect of slab rollback on producing trench-parallel splitting in the subslab mantle, and predicted the amount of rollback to be the most important parameter in the development of trench-parallel splitting patterns. After that, many studies have explored the significance of trench-parallel mantle flow, including laboratory experiments (Kincaid and Griffiths, 2003; Funiciello et al., 2006) and numerical modeling (Piromallo et al., 2006; Stegman et al., 2006; Schellart et al., 2007; Becker and Faccenna, 2009). As the slab dip angle increases (Fig 5.5a), the subslab mantle is forced to flow parallel to the trench, resulting in strong olivine LPO and trench-parallel ϕ_{SW}. The increase of dip angle may be a common geological phenomenon (Hsui et al., 1990; Houseman and Gubbins, 1997). During subduction, oceanic crust (basalt and gabbro) firstly converts to denser eclogite, then eclogite transforms to denser garnetite (Ringwood, 1991; Ji and Zhao, 1994); olivine transforms to denser spinel (γ-phase) in the transition zone. On account of the gravitation effect, slabs are speculated to rotate towards steeper dip angles. Trench migration is another possible mechanism to induce trench-parallel mantle flow. A retreating slab compels the subslab mantle (Fig. 5.5b), resulting in trench-parallel ϕ_{SW} (Fig. 5.4). Conversely, an advancing slab compels the mantle wedge (Fig. 5.5c), producing trench-parallel $\phi_{MW.}$

Long and Silver (2008, 2009) compared average δt_{SW} observed from 15 subduction zones with several tectonic parameters, such as trench migration velocity, convergence velocity, age of subducting slab, slab dip angle, maximum depth of seismicity. They concluded that subwedge delay time gave a linear correlation (R=0.72) with the trench migration velocity in a Pacific hot spot reference frame (Heurt and Lallemand, 2005). For subduction systems with nearly stationary trenches, such as the Aleutians, δt_{SW} values are usually very small, indicating nearly isotropic subwedge. In contrast, the trench of Tonga-Kermadec subduction system which is migrating at up to 5 cm/yr, gives a large average δt_{SW} value of 1.8 s, with the maximum up to 2.4 s (Fig 5.6a). It is widely accepted that the delay time is proportional to the anisotropy of propagation medium and the effective raypath length. Subduction systems with fast-moving trenches are more likely to induce a larger-scale trench-parallel flow and produce a larger region of coherent LPO in the upper mantle, and thus a larger delay time to be measured. However, Long and Silver (2008, 2009) did not take into account the possible influence of migration direction. Global trench motion is near equally partitioned between advance (53%) and retreat (47%) in Pacific hot spot reference frame (Gripp and Gordon, 2002; Funiciello et al., 2008). Retreating trenches (e.g., the west coast of South America and Middle America, Ryukyu arc) primarily effect on the mantle beneath the subducting slab, producing trench parallel ϕ_{SW}. On the contrary, subducting slabs with advancing trenches compel the mantle wedge, thus significantly influence ϕ_{MW} and δt_{MW}, rather than ϕ_{SW} and δt_{SW}. As Long and Silver (2008, 2009) did not take into consideration the trench motion direction in the plot (Fig. 5.6a), the geological implication of their results is still in debate.

2D corner flow and 3D trench-parallel flow may coexist in the mantle wedge of advancing subduction systems (Fig. 5.4), and work together to influence the anisotropy pattern (Long and Silver, 2008, 2009). Trench migration velocity (Vt) and convergence velocity (Vc), respectively, control the strength of 3D trench-parallel flow and 2D corner flow, thus Vt/Vc ratio can be used as a measure of the relative contribution of each of these two flow modes. For mantle wedges dominated by 2D corner flow (Vt/Vc<~0.2), ϕ_{MW} is normal to the trench, δt_{MW} decreases with increasing Vt/Vc (Fig. 5.6b). For mantle wedges dominated by 3D trench-parallel flow (Vt/Vc>~0.6), ϕ_{MW} is parallel to the trench, δt_{MW} tends to increase with increasing Vt/Vc ratio (Fig. 5.6b). For mantle wedges in the intermediate regime, mantle flow does not form coherent and strong LPO or according large δt_{MW} values (Fig. 5.6b). Although Long and Silver (2008, 2009) gave a relatively reasonable interpretation for global δt_{MW} values, their ϕ_{MW} predictions are not consistent with the observed values. For example, the mantle wedge of the Izu-Bonin subduction zone (Vt = ~5 cm/yr, Vt/Vc = ~1) is placed in the 3D trench-parallel flow dominated regime (Long and Silver 2008, 2009), argues for a trench-parallel ϕ_{MW}. However, the measured ϕ_{MW} beneath Izu-Bonin is perpendicular to the strike of trench. Because of the nearly stationary trench, Aleutian subduction zone is predicted to be dominated by 2D corner flow (Long and Silver, 2008, 2009), however, the measured ϕ_{MW} is trench-parallel (Fig. 5.2). In addition, most of the global subduction systems have a much higher convergence velocity than the trench migration velocity (Vt/Vc<<1), whether 3D trench-parallel flow can dominate the mantle wedge or not is still unclear.

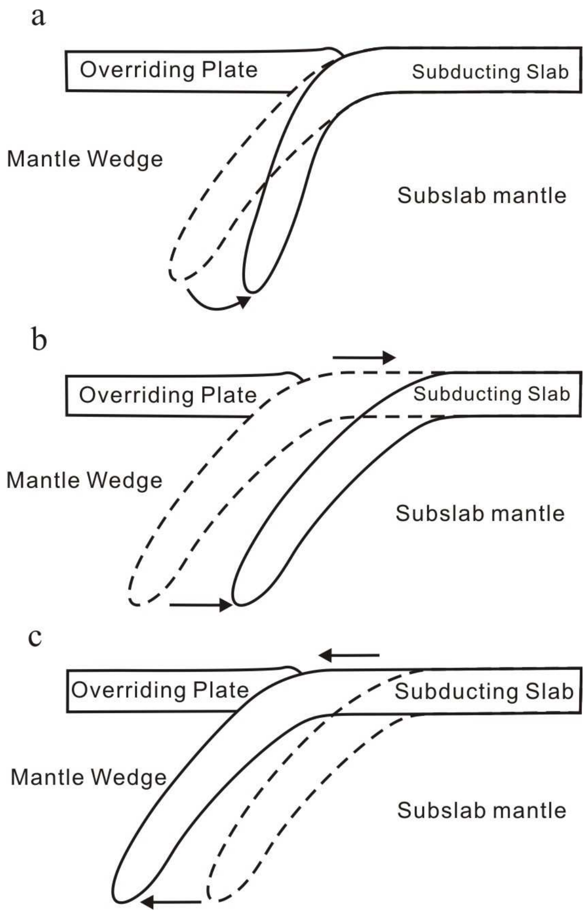

Figure 5.5 Schematic diagrams of rotating (a), retreating (b) and advancing (c) slabs. Dashed and solid lines indicate slab locations before and after the change, respectively. Arrows indicate the motions of the trench and the subducting slab.

The model of Long and Silver (2008, 2009) requires three main properties to ensure the trench-parallel flow beneath the slab without producing significant slab-entrained flow. First, in order to suppress slab-entrained downgoing flow, the subducting slabs are rheologically decoupled from the mantle material beneath it. Morgan et al. (2007) hypothesized a thin layer (~10-30 km) of hot, buoyant asthenosphere entrained beneath the subducting slab, this low-strength layer may act as a decoupling layer between the slab and the subslab mantle. Second, their model requires a barrier to flow at the 410-km or 660-km discontinuities (i.e., the boundary between upper and lower mantle), which is permeable to the cold strong subducting slabs but does not permit the flow of hot weak surrounding material (e.g., garnetite zone, Ringwood, 1991; Ji and Zhao, 1994). This barrier forces the surrounding mantle to flow horizontally by the motion of trench rather than underneath the slab. At present, seismic tomography has demonstrated that some slabs may penetrate the transition zone and the 660-km discontinuities, and ultimately reach the core-mantle boundary (e.g., van de Hilst et al., 1997; Li et al., 2008). However, the scale of mantle flow across the transition zone and the degree of mixing between the upper and lower mantle remain hotly debated (Tackley, 2008). Third, a distant barrier is required to force the mantle material to flow parallel to the trench, otherwise, a moving trench would simply force mantle to flow along with it in the trench migration direction (Buttles and Olsen, 1998; Kincaid and Griffiths, 2003). The upwelling flows from mid-ocean ridges or mantle plumes are possible mechanisms. Hot, low-viscosity subslab materials from mid-ocean ridges originally move towards the trench, then are forced to flow parallel to the trench as long as encountering the cold, relatively stiff subducting slab at the subduction zones. It is thought that subduction zones closer to mid-ocean ridge should have larger δt_{SW} due to larger-scale mantle flow. In fact, the west coast of South America is much closer to mid-ocean ridge than Tonga-Kermadec, but has a smaller δt_{SW} than that observed in the Tonga-Kermadec subduction zone.

5.6 Olivine B-type LPO

Early laboratory studies showed that, under experimental strain-rate conditions, olivine dominant slip system changes from (100)[001] to {110}[001], then to {0kl}[100], and finally to (010)[100] with increasing temperature, and the transition temperature deceases with increasing confining pressure (Carter and Ave Lallemant, 1970, Fig. 5.7a). The most prevailing slip system is (010)[100] in the upper mantle, which has been demonstrated by a large number of measurements of olivine fabrics in mantle xenoliths from kimberlites and basalts (Nicolas and Christensen, 1987; Mainprice and Silver, 1993; Ji et al., 1994, 1996; Saruwatari et al., 2001). After conducting a series of deformation experiments using a solid-medium Griggs apparatus, Carter and Ave Lallemant (1970) reported a map for active slip systems in olivine as a function of temperature and pressure. However, it is still uncertain if their slip system map can be reliably extrapolated to in-situ upper mantle for the following reasons: (1) The measured stress values had large uncertainties using the solid-medium Griggs apparatus; (2) The temperature distribution might not be uniform within the samples; and (3) The water content in their samples was not investigated.

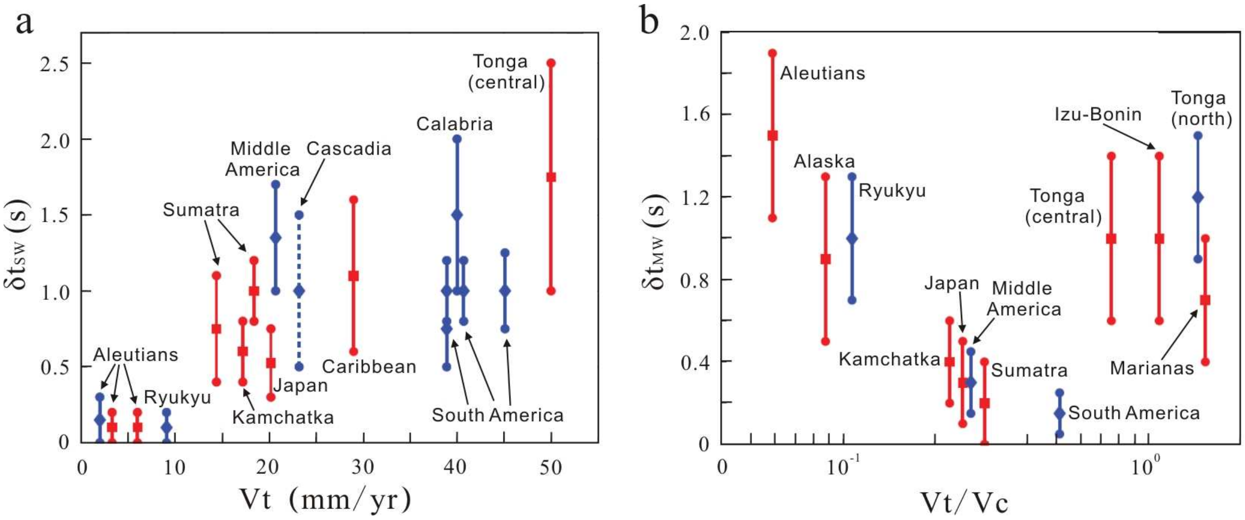

Figure 5.6 (a) Average subwedge delay time (δt_{SW}) versus trench migration velocity (Vt). (b) Average mantle wedge delay time (δt_{MW}) versus Vt/Vc. Vt/Vc represents trench migration velocity normalized by total convergence velocity. Retreating and advancing trenches are represented by blue diamonds and red squares, respectively (After Long and Silver, 2008).

In recent years, Karato and coworkers at Yale University have conducted a series of experiments on the effect of water content on olivine fabrics (e.g., Jung and Karato, 2001; Karato, 2002; Katayama et al., 2004; Skemer et al., 2006; Jung et al.,2006). According to their studies, olivine dominant slip system changes from (010)[100] to (001)[100] to (100)[001] with water content increasing at low stresses (<350-400 MPa); at high stresses (>350-400 MPa), {0kl}[100] dominates at low water content, and (010)[001] dominates at moderate-high water content (Fig. 5.7b). Olivine fabrics formed by (010)[100], (010)[001], (100)[001], {0kl}[100], (001)[100] and {110}[001] slip systems are identified as A-, B-, C-, D-, E-, and F-type (Fig. 5.7c).

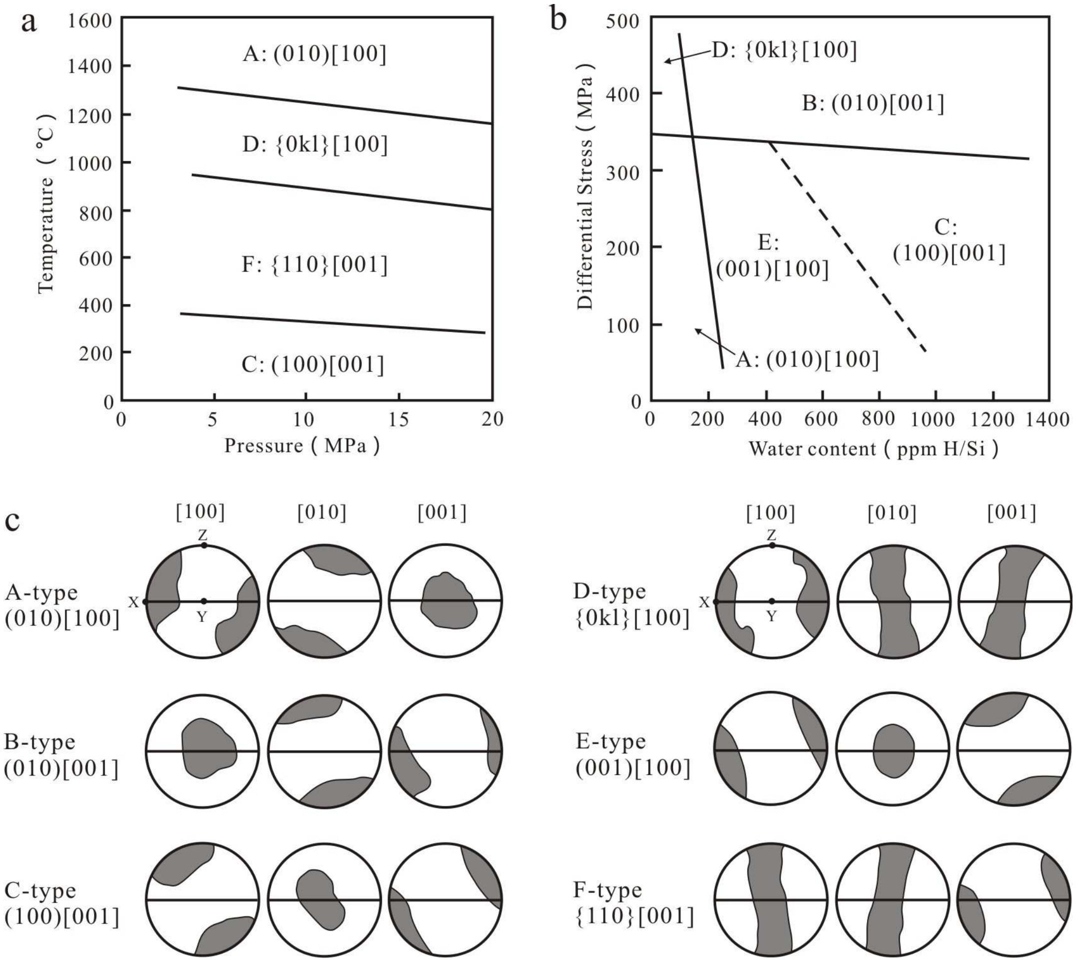

Figure 5.7 (a) Deformation fabrics of olivine at stain rate ~7.8×10^{-5} s^{-1} as a function of temperature and pressure (Data from Carter and Ave Lallemant, 1970). (b) Deformation fabrics of olivine at 1200-1300 °C and a stain rate of ~5.6×10^{-6}-9.5×10^{-4} s^{-1} as a function of differential stress and water content (Data from Jung and Karato, 2001 and Jung et al., 2006). (c) Typical pole figures of A, B, C, D, E and F-type LPOs in (a) and (b). Pole figures are presented in equal area stereographic projection with respect to three principal axes (X, Y, and Z) of the finite strain ellipsoid.

The conclusions of Karato and coworkers are in hot debate, because so far their experimental results have not been reproduced in other laboratories (Li et al., 2003; Li et al., 2003; Couvy et al., 2004; Li et al., 2004; Raterron et al., 2004, 2007; Ji et al., 2007b). The researchers in Mineral Physics Institute at Stony Brook (USA) and Laboratoire de Structure et Propriétés de l'Etat Solide at Lille (France) have emphasized the effects of confining pressure on olivine fabric transition. Couvy et al. (2004) performed simple shear experiments on olivine aggregates at 11 GPa and 1400 °C, conditions equivalent to those at depths of 330 km. Under these conditions, olivine deforms by dislocation creep with {hk0}[001] as the dominant slip system, forming F-type fabric. Raterron et al. (2007) reported a dominant slip-system transition in olivine from (010)[100] (A-type fabric) to (010)[001] (B-type fabric) with increasing pressure (ranging from 2.1 to 7.5 GPa), in the 1373-1677 K temperature range and in dry conditions. If the results of Raterron et al. (2007) can be extrapolated to the in-situ upper mantle, the most prevailing olive fabric would be B-type rather than A-type in the depth between 200 and 400 km. Recently, Jung et al. (2009) conducted low-stress (150-390 MPa), high-strain (γ=3-6) simple shear experiments on harzburgite at high pressures (3.1-3.6 GPa) and temperatures (1270-1300 °C), showing a pressure-induced fabric transition from A- to B-type in olivine. According to their results, the formation of B-type fabric may not depend only on high water content, and B-type LPO would be stable under dry conditions at depths greater than 80-90 km. It is noted that the fabric transition in olivine can be induced by at least four parameters: temperature, differential stress, water content and confining pressure. Hence, more experiments will be necessary to constrain the boundary conditions between the six olivine fabrics shown in Fig. 5.7c.

A-, D- and E-type fabrics are characterized by dislocation slip in the [100] direction, which is the fast velocity direction in olivine (Fig. 5.3), thus all these three LPOs would produce a fast polarization direction parallel to the mantle flow direction. If dislocation slip occurs on the {110} plane in the [001] direction (F-type fabric), [001] axes (intermediate velocity) would concentrate parallel to the stretching lineation (X direction), [100] axes (maximum velocity) and [010] axes (minimum velocity) would form circle girdles normal to the stretching lineation, in this case, little or no shear wave splitting occurs along the direction normal to mantle flow pane (XY). If (100)[001] slip system dominates in the mantle flow, C-type fabric forms with [001] axes (intermediate velocity) parallel to the stretching lineation, [100] axes (maximum velocity) normal to foliation (Z direction), and [010] axes (minimum velocity) parallel to foliation and normal to lineation (Y direction). When shear waves propagate normal to the mantle flow plane, C-type fabric produces a fast direction parallel to the flow direction as well as A-type fabric does, although the delay time is smaller than that produced by A-type fabric.

Olivine B-type fabric (Fig. 5.7) forms a seismic anisotropy pattern evidently different from those produced by the other five fabrics. The B-type fabric which results from dislocation slip on (010)[001], is characterized by [001] axes (intermediate velocity), [010] axes (minimum velocity), [100] axes (maximum velocity) parallel to X, Z and Y direction, respectively. For the case of horizontal flow in the upper mantle, the minimum velocity direction of olivine would be vertical, and the maximum direction would be horizontal and normal to the flow direction. Consequently, the fast polarization direction would be normal to the flow direction if shear waves propagate perpendicular to the flow plane.

The critical transition conditions between A- and B-type LPO are still being investigated. Laboratory experiments have suggested that B-type fabric is restricted to regions of upper mantle with significantly high water content (>200 ppm H/Si) and high differential stress (>320 MPa, Jung and Karato, 2001; Jung et al., 2006; Karato et al., 2008). As the partition coefficient of water between melt and olivine is estimated to be 10^4:1 (Grant et al., 2007), water tends to migrate from olivine into the melt (Karato, 1986; Hirth and Kohlstdt, 1996; Ji et al., 2008) during partial melting of mantle rocks. Therefore, high degree of partial melting would produce drier refractory residual material (such as olivine), B-type fabric is less likely to prevail under these conditions. Oceanic lithosphere is inferred to be composed of residual phases (primarily harzburgite and dunite) of partial melting occurred at mid-ocean ridges. Consequently, B-type fabric may not widely exist in the oceanic lithosphere due to the low water content of olivine. Beneath the volcanic arc, partial melting occurs widely in the mantle wedge. Since water preferentially enters basaltic melt and then intrudes into the crust or extrudes onto the Earth's surface, olivine in magma source regions would be too dry to form B-type fabric. B-type olivine is most likely to exist in the forearc mantle wedge (Katayama and Karato, 2006; Kneller et al., 2005, 2007, 2008), where large volumes of water are released from dehydration reactions in the subducting slab. However, the water in the forearc wedge may also react with peridotite to form serpentinite, which has much lower flow strength than olivine (Fig. 5.8, Brodie and Rutter, 1987; Escartin et al., 2001; Hilairet et al., 2007; Chenak and Hirth, 2010). In this case, differential stress in serpentinized peridotite is supposed to be low, and high stress-induced B-type fabric probably does not exist in serpentinized forearc mantle wedge.

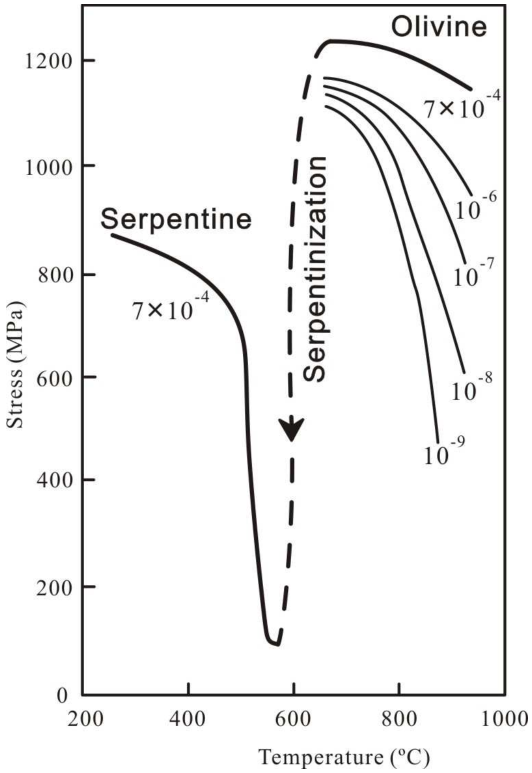

Figure 5.8 Comparison of flow strengths between olivine and serpentine. Strain rate (in s^{-1}) is indicated for each curve. Dashed curve shows the effect of serpentinization. (Experimental data from Brodie and Rutter, 1987).

If B-type LPO does dominate in the forearc mantle wedge (Kneller et al., 2005, 2007, 2008;

Mizukami et al., 2004; Skemer et al., 2006; Michibayashi et al., 2007; Tasaka et al., 2008), 2D corner flow induced ϕ_{MW} would be normal to the flow direction, i.e., trench-parallel. Therefore, forearc mantle wedge is characterized by B-type LPO and trench-parallel ϕ_{MW}; backarc mantle wedge is characterized by A-type LPO and trench-normal ϕ_{MW} (Fig. 5.9). This is consistent with splitting patterns observed in Hokkaido and Honshu of Japan (Nakajima and Hasegawa, 2004; Huang et al., 2011). The Ryukyu and Tonga subduction systems both show trench-parallel ϕ_{MW} in the forearc, however, trench-parallel ϕ_{MW} are observed in large regions of Ryukyu backarc (Long and van der Hilst, 2006), ϕ_{MW} in the Lau backarc (Tonga) are neither trench-normal nor trench-parallel, mostly oblique to the trench (Smith et al., 2001). In addtion, trench-parallel ϕ_{MW} are also found in the backarc of Mariana (Pozgay et al., 2007) and Costa Rica-Nicaragua (Abt et al., 2009; Hoernle et al., 2008). Furthermore, the splitting patterns from the Kamchatka (Levin et al., 2004) and Central Alaska subduction systems (Christensen et al., 2010) are opposite to the pattern shown in Fig. 5.9, they exhibit trench-normal ϕ_{MW} in the forearc and trench-parallel ϕ_{MW} in the backarc. Those splitting patterns mentioned above are still too complex to interpret by olivine A- and B- type fabric transition.

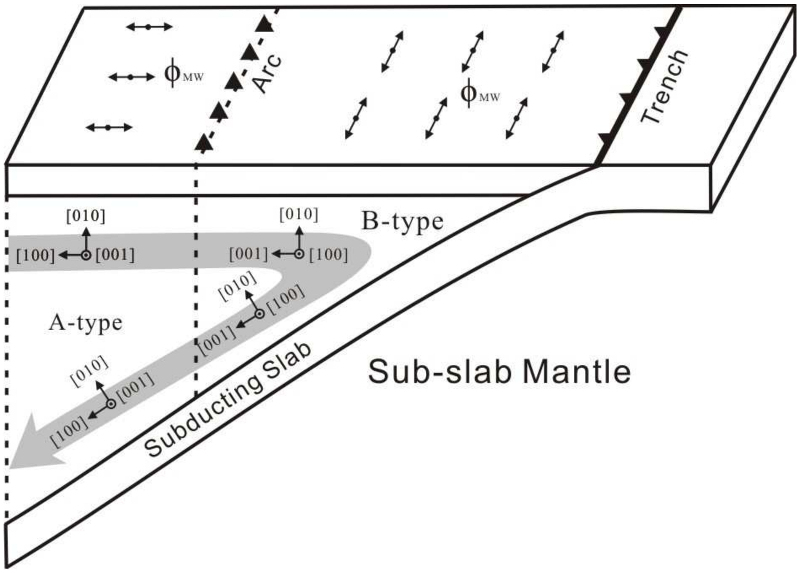

Figure 5.9 Shear wave splitting patterns resulted from olivine B-type fabrics beneath the forearc and A-type fabrics beneath the backarc.

5.7 Serpentinization

Serpentines are phyllosilicates formed from hydration of ultramafic rocks and are composed of three polymorphs: lizardite [$Mg_3Si_2O_5(OH)_4$], chrysotile [$Mg_3Si_2O_5(OH)_4$)] and antigorite [$Mg_{48}Si_{34}O_{85}(OH)_{62}$]. Being hydrous minerals, the stability of serpentines is mainly temperature-dependent rather than pressure-dependent (Fig. 5.10). Antigorite is the only serpentine mineral to be stable at temperatures >350 °C. The transition temperature from antigorite to olivine + orthopyroxene + water decreases with increasing confining pressure: 720 °C, 690 °C and 620 °C at 2.0 GPa, 3.0 GPa and 5.0 GPa, respectively (Ulmer and Trommsdorff, 1995). It should be emphasized that high Al-, Cr- and water content would lead the reaction curve to migrate toward higher temperature (Padron-Navarta et al., 2010). Antigorite is thought to be the dominant serpentine mineral in subducting lithosphere mantle, and it could be stable at temperature up to 800-850 °C in the wet mantle wedge.

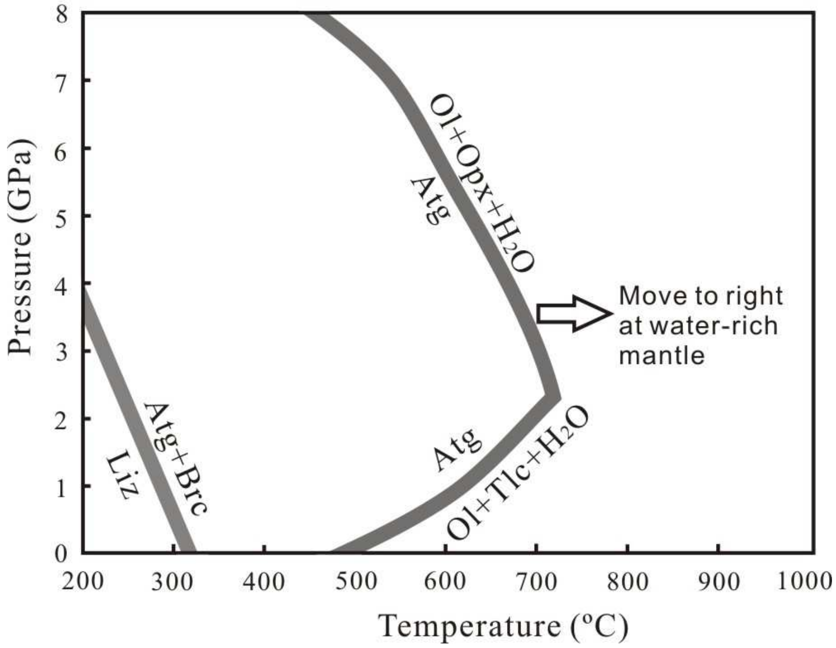

Figure 5.10 Diagram showing the stability fields of lizardite and antigorite. Mineral abbreviations: Atg, antigorite; Liz, lizardite; Ol, olivine; Brc, brucite; Tlc, talc; Opx, orthopyroxene. Reaction boundaries are given by Ulmer and Trommsdorff (1995) and Evans (2004).

Hydration reactions of olivine [$(Fe, Mg)_2SiO_4$], forsterite (Mg_2SiO_4), enstatite ($MgSiO_3$) and talc [$Mg_3Si_4O_{10}(OH)_2$] are as following:

1. Forsterite + Enstatite + Water →Antigorite

   $14Mg_2SiO_4 + 20MgSiO_3 + 31H_2O \rightarrow Mg_{48}Si_{34}O_{85}(OH)_{62}$

2. Forsterite + Talc + Water→Serpentine

   $6Mg_2SiO_4 + Mg_3Si_4O_{10}(OH)_2 + 9H_2O \rightarrow 5Mg_3Si_2O_5(OH)_4$

   or $18Mg_2SiO_4 + 4Mg_3Si_4O_{10}(OH)_2 + 27H_2O \rightarrow Mg_{48}Si_{34}O_{85}(OH)_{62}$

3. Forsterite + Silica + Water →Lizardite/Chrysotile

   $3Mg_2SiO_4 + SiO_2 + 4H_2O \rightarrow 2Mg_3Si_2O_5(OH)_4$

4. Forsterite + Water →Serpentine + Brucite

   $2Mg_2SiO_4 + 3H_2O \rightarrow Mg_3Si_2O_5(OH)_4 + Mg(OH)_2$

   or $34Mg_2SiO_4 + 51H_2O \rightarrow Mg_{48}Si_{34}O_{85}(OH)_{62} + 20Mg(OH)_2$

5. Enstatite + Water→Antigorite + Talc

   $90MgSiO_3 + 45H_2O \rightarrow Mg_{48}Si_{34}O_{85}(OH)_{62} + 14Mg_3Si_4O_{10}(OH)_2$

6. Olivine + Water + Carbonic acid →Lizardite/Chrysotile + Magnetite + Methane

   $(Fe, Mg)_2SiO_4 + H_2O + CO_2 \rightarrow Mg_3Si_2O_5(OH)_4 + Fe_3O_4 + CH_4$

7. Olivine + Water + Carbonic acid → Lizardite/Chrysotile + Magnetite + Magnesite +Silica

   $(Fe, Mg)_2SiO_4 + H_2O + CO_2 \rightarrow Mg_3Si_2O_5(OH)_4 + Fe_3O_4 + MgCO_3 + SiO_2$

8. Forsterite + Water + Carbonic acid →Talc + Magnesite

   $4Mg_2SiO_4 + H_2O + 5CO_2 \rightarrow Mg_3Si_4O_{10}(OH)_2 + 5MgCO_3$

9. Talc + Water →Lizardite/Chrysotile + Silica

   $Mg_3Si_4O_{10}(OH)_2 + H_2O \rightarrow Mg_3Si_2O_5(OH)_4 + 2SiO_2$

10. Talc + Magnesite + Water →Lizardite/Chrysotile + Carbonic acid

    $Mg_3Si_4O_{10}(OH)_2 + 3MgCO_3 + 3H_2O \rightarrow 2Mg_3Si_2O_5(OH)_4 + 3CO_2$

The reactions to form antigorite from low-temperature serpentine (lizardite and chrysotile) are as following:

11. Lizardite/Chrysotile →Antigorite + Brucite

$17Mg_3Si_2O_5(OH)_4 \rightarrow Mg_{48}Si_{34}O_{85}(OH)_{62} + 3Mg(OH)_2$

12. Lizardite/Chrysotile + Silica →Antigorite + Water

    $16Mg_3Si_2O_5(OH)_4 + 2SiO_2 \rightarrow Mg_{48}Si_{34}O_{85}(OH)_{62} + H_2O$

13. Lizardite/Chrysotile →Antigorite + Forsterite + Water

    $20Mg_3Si_2O_5(OH)_4 \rightarrow Mg_{48}Si_{34}O_{85}(OH)_{62} + 6Mg_2SiO_4 + 9H_2O$

The P-T fields of reactions (1-2) and (11) are indicated in Fig. 5.10, whereas the fields of the other reactions are still poorly understood. Dehydration of serpentine could be the reverse of hydration reactions (1-10).

The strong influence of serpentine on subduction zone dynamics has received increasing attention recent years, because: (1) Serpentines have distinct physical properties, such as very low P- and S-wave velocities (Fig. 5.11), extremely high seismic anisotropy, high shear wave splitting (Fig 5.12, Table 5.1), and high V_p/V_s and Poisson's ratio (Ji et al., 2002, 2009; Dewandel et al., 2003; Watanabe et al., 2007). Based on these properties, one can explore new geophysical methods to investigate subduction zones (Bostock et al., 2002; Faccenda et al., 2008; Boudier et al., 2009; Katayama et al., 2009); (2) Since serpentines are major water carriers within subduction zones (~13 wt.%, Schmidt and Poli, 1998; Ulmer and Trommsdorff, 1995), they may release huge volumes of free water by dehydration reactions at greater depth, and such quantity of water may trigger partial melting of mantle wedge and produce forearc volcanism (Hyndman and Peacock, 2003; Wada et al., 2008); and (3) Serpentines have considerably low flow strength (Fig. 5.8, Brodie and Rutter, 1987; Escartin et al., 2001; Hilairet et al., 2007; Chenak and Hirth, 2010) and low friction coefficient (Moore et al., 1996; Moore and Lockner, 2007). Consequently, serpentinization can have a major effect on the thermal structure of a subduction zone, on the rheological coupling between the subducting slab and the mantle wedge, and on the distribution of seismicity. The widely serpentinized regions can be deformed primarily by dislocation creep, thus appear to be aseismic and generate low heat flux (Hirauchi and Yamaguchi, 2007).

Hydration of the wedge can produce serpentine minerals, in which antigorite is the only stable serpentine mineral at greater depth. The shallow regions of forearc are usually low-temperature, thus lizardite and chrysotile could exist (Evans, 1977, 2004). A wide range of geological data (e.g., serpentine mud volcanoes of the Izu-Bonin-Mariana subduction zone) and geophysical data (e.g., reduced seismic velocities and high V_p/V_s ratio) indicate that extensive serpentinization in the forearc mantle is a global phenomenon, for example, extensive forearc mantle serpentinization are suggested in Cascadia (Bostock et al., 2002; Brocher et al., 2003), in the southwestern Japan (Kamiya and Kobayashi, 2000; Seno et al., 2001), in the central Andes (Graeber and Asch, 1999) and in Costa Rica (DeShon and Schwartz, 2004).

The P- and S-wave anisotropy of antigorite single crystal are, respectively, up to 46% and 66% (Bezacier et al., 2010), much higher than those of olivine single crystal (~23% and ~20%, respectively; Fig. 5.3, Kumazawa and Anderson, 1969; Ji et al., 2002). Due to the low flow strength (Fig. 5.8), antigorite is easily ductilely deformed and forms strong LPO with (001) plane parallel to the shear plane and [100] axis parallel to the shear direction (Katayama et al., 2009; Hirauchi et al., 2010; Kern et al., 1997). In strongly deformed shear zones (e.g., the shear zone between the subducting plate and the overlying mantle wedge), the shear plane (e.g., the boundary of the subducting plate) is parallel to the foliation, and the shear direction (e.g., the subduction direction) is parallel to the lineation. The A-type olivine LPO-induced seismic anisotropy of deformed mantle rocks is only about 3-5%, and has orthogonal symmetry: the maximum, intermediate and minimum P-wave velocity are aligned parallel to three principal axes of the finite strain ellipsoid, i.e., X (parallel to the stretching lineation), Y (perpendicular to lineation and parallel to foliation) and Z (normal to foliation), respectively. Serpentine LPO usually produces high (>10%) and axial symmetric seismic anisotropy in deformed rocks: the minimum velocity direction is oriented parallel to Z direction, and velocity in the XY plane is almost isotropic. It is inferred that the velocity difference (anisotropy) between XY plane and Z direction of serpentinized peridotite increases with increasing serpentine content. The seismic anisotropy of deformed serpentinized peridotite would be controlled by serpentine LPO if the serpentine content is more than ~20%, in this case, X and Y directions in foliation plane could be hardly distinguished in terms of seismic velocity.

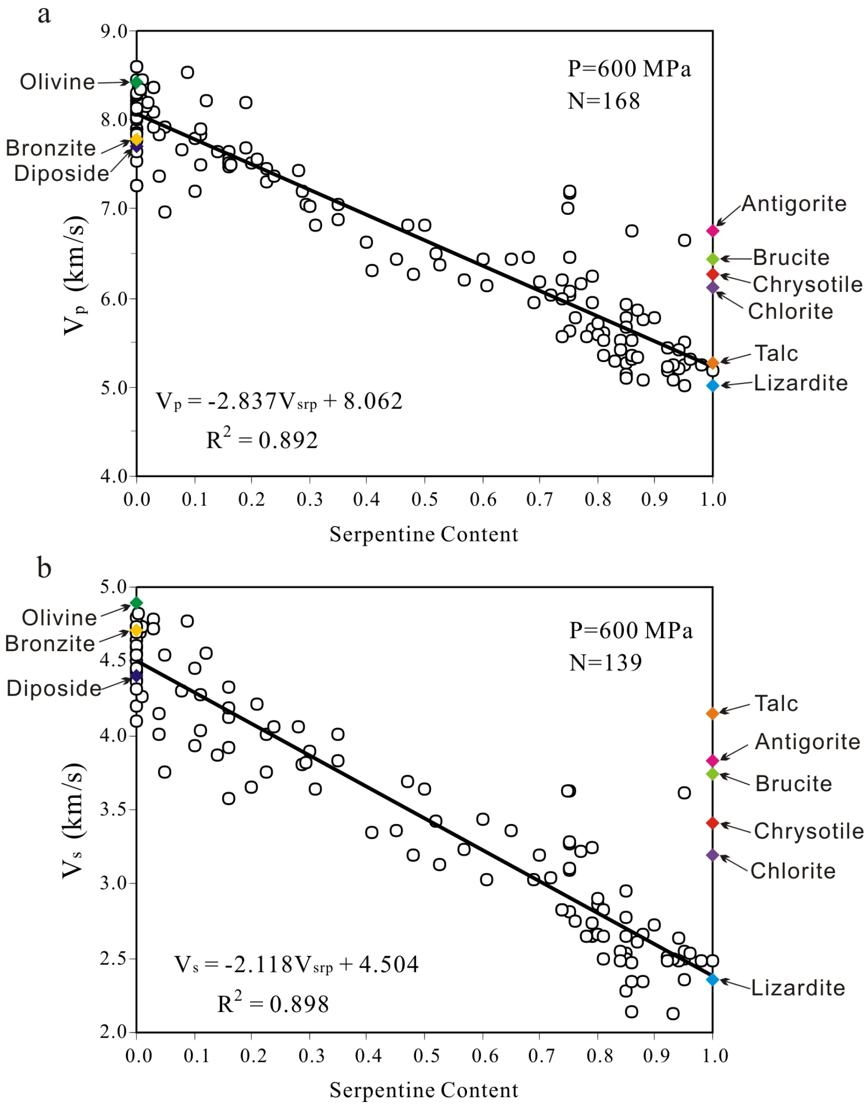

Figure 5.11 V_p (a) and V_s (b) as a function of serpentine content for mantle rocks. Seismic velocities were measured at 600 MPa, N indicate sample numbers. Velocities of main rock-forming minerals (olivine, bronzite, and diopside) and hydrous minerals (antigorite, lizardite, chrysotile, talc, brucite, and chlorite) are also indicated for comparison.

Katayama et al. (2009) simple-sheared antigorite aggregates at a pressure of 1.0 GPa and temperature of 300-400 °C. The shear wave anisotropy (A_s) is up to ~32% at stain of $\gamma \approx 2.0$, such a high anisotropy is consistent with the value measured in natural deformed samples (Kern et al., 1997; Ji et al., 2002; Christensen, 2004; Wang et al., 2005b; Watanabe et al., 2007). Hence serpentinization would strongly influence the seismic anisotropy geometry and the strength of subducting slab and mantle wedge. Unfortunately, previous models of seismic anisotropy in subduction zones usually ignored the contribution of serpentinization.

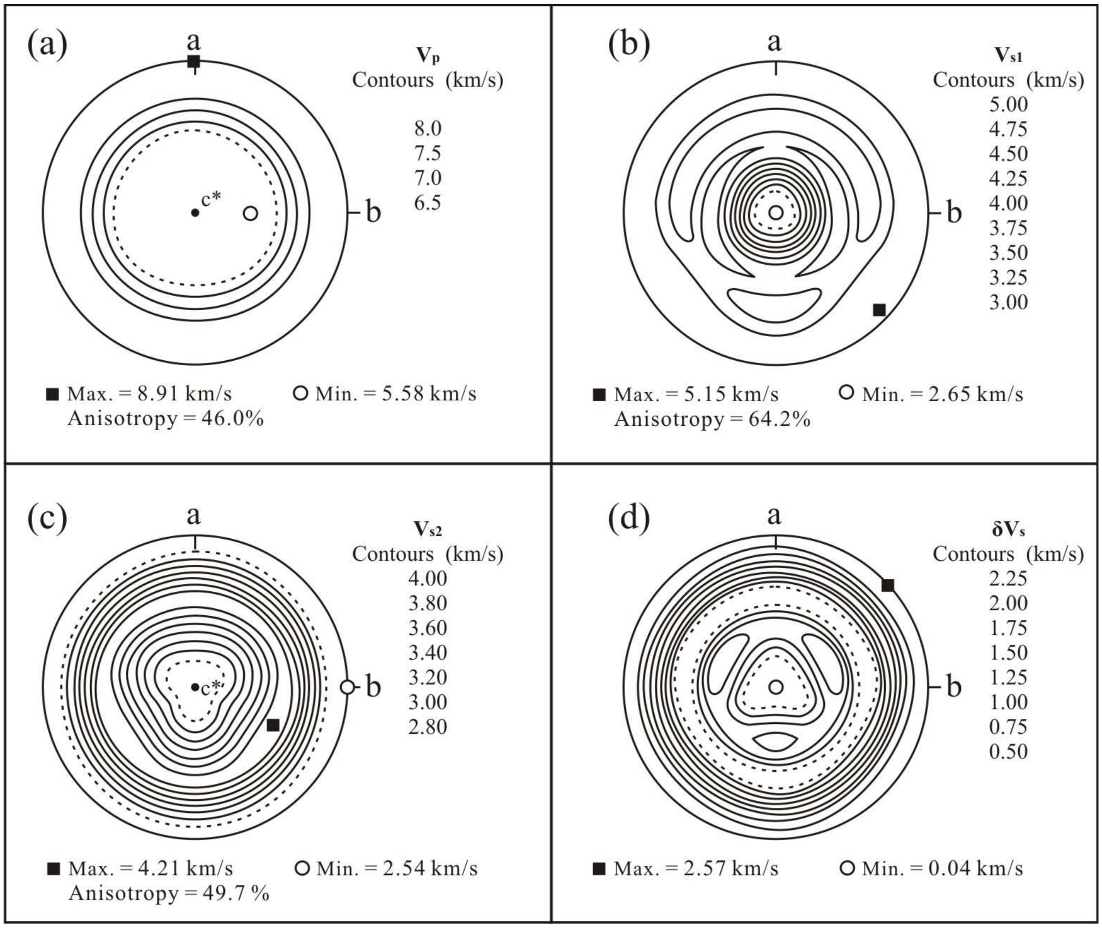

Figure 5.12 Seismic velocities of antigorite single crystal. V_p, V_{s1}, V_{s2} and δV_s (V_{s1}-V_{s2}) are shown in equal area stereographic projection with respect to the crystallographic orientations of a, b, and c*, where c* is perpendicular to (001) plane. Elasticity data of antigorite are from Bezacier et al. (2010)

It is impossible to explain the delay time beneath Ryukyu (1-2 s) in terms of olivine LPO because the inferred anisotropic layer would be 100-200 km, even thicker than the entire mantle wedge. However, only 10-20 km thick serpentinite layer is needed if the splitting pattern is induced by serpentine LPO (Katayama et al., 2009). Generally, the extensively serpentinized mantle wedge would produce higher seismic anisotropy and stronger shear wave splitting.

The degree of mantle wedge serpentinization perhaps depends on the ages of subducting slab (Wada et al., 2008; Katayama et al., 2009). A very young and warm slab has high thermal gradient, and can release most of water in the forearc region, leading to a high degree of mantle wedge serpentinization. Ryukyu is such a warm subduction zone, in which dehydration reactions occur at ~40 km depth, causing extensive serpentinization of mantle wedge and large delay times (1-2 s). In contrast, a very old and cold slab has low thermal gradient, and should retain most of water until farther depth is reached, leading to a lower degree of mantle wedge serpentinization. Beneath the northeastern Japan, most dehydration reactions are limited to >100 km depth, resulting little serpentinization and short delay times (0.1-0.2 s).

Table 5.1 Elastic constants (GPa) and properties of antigorite single-crystal at ambient conditions (Data from Bezacier et al., 2010).

C_{11}	**C_{22}**	**C_{33}**	**C_{44}**	**C_{55}**	**C_{66}**	**C_{12}**	**C_{13}**	**C_{23}**	**C_{15}**	**C_{25}**	**C_{35}**	**C_{46}**	**Ks**	**G**	**Density**	**V_p**	**V_s**
						(GPa)							**(GPa)**	**(GPa)**	**(g/cm^3)**	**(km/s)**	**(km/s)**
208.4	201.6	96.7	17.4	18.3	65.0	66.2	15.9	5.0	2.4	-4.4	2.5	-13.1	68.5	38.5	2.6	6.76	3.83

The most extensively serpentinized regions may occur in the shear zone between the subducting slab and the overlying mantle wedge (Fig. 5.13a). Shear deformation is concentrated in this thin serpentinite layer because its flow strength is much lower than that of the surrounding peridotite. Strong antigorite LPO develops with (001) plane parallel to the plane between the mantle wedge and the subducting slab, [100] axis parallel to the subduction direction. Therefore, the maximum velocity is parallel to the foliation and the minimum velocity is normal to the foliation. Shear wave splitting technique only measures the fast polarization direction in the horizontal plane, thus either ϕ_{MW} or δt_{MW} would be influenced by the subduction angle. In a steeply dipping subduction zone (e.g., Mariana, Tonga-Kermadec, and Scotia), the serpentinite-layer-induced fast and slow directions are trench-parallel and trench-normal, respectively. In contrast, in low-angle subduction zones, such as South America, the serpentinite layer between wedge and slab is oriented subhorizontally, thus contributes little to the splitting measured by the seismic stations on the plate.

Trench-parallel splitting patterns may also be attributed to serpentinization of oriented faults in subducting oceanic plates (Fig. 5.13b, Feccenda et al., 2008), if the serpentinized faults have not suffered latter shear deformation, reorientation, or tectonic replacement. Tensile faults in the upper boundary of subducting slab are usually subvertical below the forearc (Feccenda et al., 2008; Jiao et al., 2000; Ranero et al., 2005). Hydration of ultramafic rocks along the fault planes leads to the formation of sheet silicates such as serpentines, talc and brucite.

Boudier et al. (2009) investigated orientation relationships between antigorite (atg) and olivine (ol) in Moses Rock from the Utah-Farallon subduction zone. TEM imaging and electron back scattering diffraction (EBSD) patterns reveal two topotactic relationships: (1) $(100)_{ol} \parallel (001)_{atg}$, $[001]_{ol} \parallel [010]_{atg}$, $[010]_{ol} \parallel [100]_{atg}$; (2) $(010)_{ol} \parallel (001)_{atg}$, $[001]_{ol} \parallel [010]_{atg}$, $[001]_{ol} \parallel [100]_{atg}$. Type (1) contact is more frequent in subducting plates where olivine developed A-type fabric: The preferred orientation of olivine [100] axis is parallel to the stretching lineation and the (001) plane of antigorite is parallel to the lineation-normal faults plane, thus antigorite (001) plane is perpendicular to olivine [100] axis. The fast polarization directions in olivine and antigorite are, respectively, parallel to $[100]_{ol}$ and $(001)_{atg}$, in other words, the anisotropy produced by olivine is perpendicular to that by antigorite. As a result, the splitting pattern in serpentinized peridotite with type (1) contact is controlled together by the LPO strength of olivine and serpentine, and the degree of serpentinization. Seismic anisotropy produced by olivine LPO in subducting oceanic plates is trench-normal, in contrast, seismic anisotropy produced by serpentine LPO in the vertical faults is trench-parallel. As discussed above, shear wave splitting will be dominated by serpentine LPO if serpentinization is more than 20%, thus the slab-originated ϕ would be trench-parallel only if more than 20% serpentinization occurs in the subducting slab. .

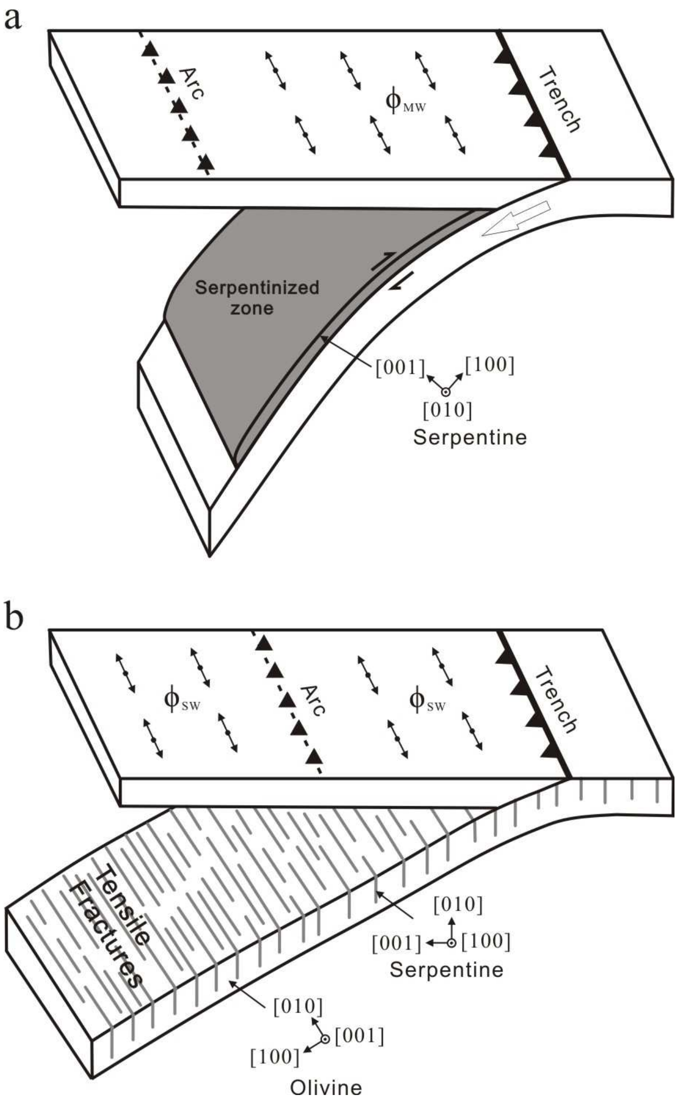

Figure 5.13 (a) Shear wave splitting patterns produced by a serpentinized shear zone between the subducting slab and the mantle wedge. Serpentine in the shear zone is characterized by (001) plane parallel to shear plane, and [100] axis parallel to shear direction. (b) Shear wave splitting patterns induced by serpentinized fractures in subducting oceanic plates. Serpentine has a maximum concentration of (001) plane parallel to fault plane. Olivine in the subducting plate developed A-type LPO with (010) plane parallel to subducting plates and [100] axis parallel to subducting direction.

Seismic anisotropy of mantle wedge could be the result of competition between antigorite fabric and olivine A-type fabric. 2D corner flow in the mantle wedge produces olivine A-type

LPO, with ϕ_{MW} parallel to the strike of trench. Serpentinization would change this splitting pattern: 10-20% serpentinization can almost cancel the anisotropy induced by olivine LPO. If more than 20% serpentinization occurs in the mantle wedge, and olivine and serpentine have type (1) contact, splitting parameters (ϕ_{MW} and t_{MW}) would primarily depend on the LPO of serpentine. As the (001) plane of serpentine is normal to the trench, the measured ϕ_{MW} is trench-parallel. If the above interpretation is correct, ϕ_{MW} and t_{MW} could be measures of the degree and the distribution of serpentinization in the mantle wedge.

CHAPTER 6 CONCLUSIONS AND FUTURE WORK

6.1 Main conclusions

The 12 May 2008 Wenchuan earthquake occurred in Longmen Shan complex is the largest active tectonic event reported to date in Sichuan (China). The calculated geothermal and rheological profiles indicate that the depth of the mainshock hypocenter (~19 km) corresponds to the base of the schizosphere, below which the Longmen Shan complex switches from the brittle to ductile behaviour. Both P- and S-wave velocities (V_p and V_s) of 12 representative samples from the Longmen Shan complex have been measured at hydrostatic confining pressure up to 800 MPa. The comparison of the experimental data with in-situ seismic data reveals that the crust of the Longmen Shan range consists of 4 layers from the surface to the Moho: Layer 1: V_p<4.88 km/s (0-3 km thick, sedimentary rocks such as limestone, sandstone, conglomerate, and mudstone); Layer 2: V_p=5.95-6.25 km/s (25-28 km thick, felsic rocks equivalent to the Longmen Shan complex); Layer 3: V_p=6.55 km/s (10 km thick, 67.5% felsic and 32.5% mafic rocks); and Layer 4: V_p=6.90 km/s (8 km thick, 20.0% felsic and 80.0% mafic rocks). The average V_p/V_s ratio of 1.71 or Poisson's ratio of 0.24 calculated for the whole crust is consistent with the results measured using teleseismic receiver function techniques. Considering the crustal structure, surface heat flow (59.7 mW/m^2), and thickness of the schizosphere, the highest temperature in the crust above the Moho at 46 km is less than ~500 °C which is significantly lower than the melting point of dry or wet felsic rocks. Therefore, the channel flow, which requires partial melting and an extremely low viscosity of the rocks, is unlikely to occur beneath the Longmen Shan range. Furthermore, the present study, which yields a moment magnitude of 7.9-8.0 given the variation in the dip of the coseismic ruptures and the uncertainty in the depth to which the coseismic rupture may propagate downwards below the focal depth of the mainshock, presents the first accurate quantification of the 2008 Wenchuan earthquake's size.

Much of our knowledge of the seismic properties of rocks comes from the investigations of rocks samples collected from surface exposures. The Chinese Continental Scientific Drilling (CCSD) borehole, which represents the deepest penetration (5158 m) into an ultrahigh pressure (UHP) metamorphic terrane in any of the world's continents, provided an excellent opportunity to compare the seismic velocity-pressure behaviors between the deep core samples and their surface equivalents. Experimentally measured P- and S-wave velocity-pressure data for both the borehole core samples and their lithologic equivalents from surface exposures are very well described by a four-parameter exponential equation with clear physical significance: $V(P) = V_0 + DP - B_0 \exp(-kP)$, where V_0 is the extrapolated intrinsic reference velocity for the sample at zero pressure assuming microcracks are absent; D is the intrinsic pressure derivative of velocity in the linear elastic regime above the crack closure pressure (P_c); B_0 is the initial velocity drop caused by the presence of pores/cracks at zero pressure; and k is the decay constant of the velocity drop in the nonlinear poro-elastic regime. The CCSD core samples are characterized by significantly higher V_0, B_0 and k values and lower D and P_c values than their surface analogues. In other words, the seismic velocities of the deep core samples are generally more and less sensitive to pressure in the nonlinear and linear regimes, respectively, than the surface-derived samples. The comparison suggests that the high pressure ($>P_c$) data from the deep core samples are much more reliable than data from surface analogues that have been subjected to long histories of weathering and alteration along intergranular and transgranular cracks, for extrapolation to middle-lower crustal depths. The marked increases in B_0 and k and decrease in P_c indicate substantial decompaction of the core materials due to drilling and core-retrieval damage and stress-relief microfracturing.

At high pressures (>200-300 MPa), seismic anisotropy and shear wave splitting are controlled by the lattice preferred orientations of anisotropic minerals (e.g., amphibole, mica, pyroxene and feldspar) and compositional layering. However, at low pressures (<200-300 MPa), the anisotropy and shear wave splitting are mainly controlled by constructive or destructive interference of oriented open microcracks and the LPOs of anisotropic minerals. It is well known that velocities of P-waves propagating or S-waves polarizing across aligned cracks are much lower than parallel to them. With increasing pressure, microcracks with smaller aspect-ratios will close first and subsequently those with larger aspect-ratios. The variations in velocities and their directional dependence with increasing pressure thus can successfully provide important hints about the preferred orientation of microcracks that causes P-wave velocity anisotropy and shear wave splitting in the low pressure regime.

At pressures below P_c, the progressive closure of Z-normal (foliation-parallel) microcracks cause gradual increases in $V_p(Z)$ but little influence on $V_p(X)$ or $V_p(Y)$. Accordingly, the closing of Z-normal microcracks with increasing pressure would cause a rapid decrease in $V_p(X)$-$V_p(Z)$ and $V_p(Y)$-$V_p(Z)$, while the influence on $V_p(X)$-$V_p(Y)$ is almost negligible. The Y-normal microcracks occur along grain boundaries and commonly very flat with small ratios of aperture to length, are easily closed below ~100 MPa. The closing of Y-normal microcracks would result in a rapid decrease in $V_p(X)$-$V_p(Y)$, a rapid increase in $V_p(Y)$-$V_p(Z)$, and almost no change in $V_p(X)$-$V_p(Z)$. The X-normal microcracks are generally intragranular cracks. Compared with Z-normal and Y-normal microcracks, the X-normal cracks are more difficult to be closed. With increasing pressure, the closing of X-normal microcracks would produce a rapid increase in $V_p(X)$-$V_p(Y)$ and $V_p(X)$-$V_p(Z)$ and a negligible effect on $V_p(Y)$-$V_p(Z)$. The role of microcrack preferred orientations on shear wave splitting is as following: with increasing pressure, the closing of Z-normal microcracks would cause a decrease in $V_s(YX)$-$V_s(YZ)$ and $V_s(XY)$-$V_s(XZ)$, while the influence on $V_p(ZX)$-$V_p(ZY)$ is almost negligible; the closing of Y-normal microcracks would result in a rapid decrease in $V_p(ZX)$-$V_p(ZY)$, a rapid increase in $V_p(XY)$-$V_p(XZ)$, and almost no change in $V_p(YX)$-$V_p(YZ)$; the closing of X-normal microcracks would produce a rapid increase in $V_p(ZX)$-$V_p(ZY)$ and $V_p(YX)$-$V_p(YZ)$ and a negligible effect on $V_p(XY)$-$V_p(XZ)$.

Seismic hysteresis, whose variation with pressure is subject to exponential decay, is caused by irreversible changes in grain contacts, increases in microcrack aspect ratios and reductions of void space during the pressurization-depressurization cycle. The effect of compression on the V_p/V_s ratios is negligible for non-porous or crack-free compacted rocks. The comparison between calculated and average measured P- and S-wave velocities of equivalent isotropic (fabric-free) crystalline rocks shows that the Voigt average yields the best agreement with the measured data; the Voigt-Reuss-Hill average, which is better than the geometric mean, can also offer remarkably good predictions for the seismic wave velocities, but the Reuss average systematically underestimates the velocities for most of the rocks and gives the poorest agreement with the experimental values.

The laboratory-measured velocities show a fairly good agreement with the velocities obtained from the sonic log in the depth range between 3500-5158 m where felsic orthogneiss and paragneiss are the dominant lithologies. The discrepancies between the laboratory and borehole logging velocities for eclogites and retrograde eclogites above a depth of 3100 m are mainly attributed to scaling problems, the presence of open fractures in the upper levels of the borehole, different degrees of retrograde metamorphism, differences in water saturation, and the presence of non-hydrostatic pressure conditions in the borehole wall. The comparison of the seismic reflection image at the borehole site with the calculated normal-incidence seismic reflection coefficient (R_c) profile indicates that the seismic reflections in the vicinity of the CCSD borehole originate from mafic (eclogite and retrograde eclogite) or ultramafic layers within dominantly felsic rocks.

Lamé parameter (λ), which is closely related to the incompressibility and contains a high proportion of information about the resistance to a change in volume caused by a change in pressure, is an important, intrinsic, elastic property of rocks. Based on a detailed analysis on the λ values of 475 natural rocks on which mean seismic velocities have been measured at high hydrostatic pressures (≥ 400 MPa) using the same laboratory equipment and the same method, it is found that the λ value of an equivalent isotropic crystalline rock as a function of confining pressure (P) and temperature (T) can be described by $\lambda=a+(d\lambda/dP)P-c\exp(-kP)-(d\lambda/dT)T$, where a

is the projected λ value at zero pressure if microcracks were fully closed; $d\lambda/dP$ is the pressure derivative in the linear elastic regime; c is the initial λ drop caused by the presence of microcracks at zero pressure; k is a decay constant of the λ drop in the nonlinear poro-elastic regime; and $d\lambda/dT$ is the temperature derivative. The laboratory experimental data may be extrapolated to the Earth's interior using the above equation if no partial melting, metamorphic reaction, dehydration or phase transformation occurs.

In the λ-ρ and μ-ρ plots, the main categories of lithology can be clearly discriminated. The ultramafic rocks display systematic decreases in both μ and λ with increasing the degree of serpentinization. Eclogites, mafic rocks (gabbro, diabase, mafic granulite, and mafic gneiss) and felsic rocks (granite, diorite, felsic gneiss, intermediate gneiss and metasediments) are characterized by high, moderate and low μ and λ values, respectively. For pyroxene and olivine, both λ and ρ increase but μ decreases with increasing the Fe/Mg ratios. In the plagioclase series, both λ and μ increases with increasing the anorthite content. Increases in the contents of garnets, sillimanite, rutile, zircon, ilmenite and spinel result systematically in an increase in rock's λ and μ values. The results suggest that the λ-ρ and μ-ρ plots can be used as a discriminant of composition for rocks in the Earth's crust and upper mantle. This is particularly important because the connection between composition and seismic P- or S-wave velocity is not unique due to similar velocities of many common rock types.

Subduction zones are critically important regions where significant geological processes (e.g., phase transition, dehydration, partial melting, volcanism, and seismic activity) take place. Seismic anisotropy originated from different parts of subduction system (i.e., the overriding plate, the mantle wedge, the subducting slab, and the subslab mantle) can be distinguished by analyzing seismic wave raypaths. The shear wave splitting patterns measured from global oceanic subduction zones reveal that the fast polarization directions in the subwedge (ϕ_{SW}) are overwhelmingly trench-parallel, whereas those in the mantle wedge (ϕ_{MW}) are usually complex. Both the delay times in the subwedge and in the mantle wedge vary in a wide range. A variety of mechanism models have been proposed to explain the complex and diverse shear wave spitting observations in global oceanic subduction zones, however, none of them could offer a perfectly interpretation at present.

Olivine LPOs formed by (010)[100], (010)[001], (100)[001], {0kl}[100], (001)[100] and {110}[001] slip systems are identified as A, B, C, D, E and F-type fabrics, respectively. The A, D, and E-type fabrics cause fast polarization directions (ϕ) parallel to the mantle flow while ϕ formed by B-type fabric is perpendicular to the mantle flow. Olivine C-type LPO also results in a ϕ parallel to the mantle flow, but the resultant delay time (δt) is much smaller than A-type. F-type fabric results in almost no splitting in the direction normal to the mantle flow plane. In mantle wedge and subducting lithosphere mantle, the most important hydrous mineral is antigorite, which is characterized by extremely low flow strength, low seismic velocities, and high elastic anisotropy. Accordingly, the extensively serpentinized mantle wedge rocks usually have relative high seismic anisotropy and shear wave splitting. If more than ~10-20 vol.% serpentinization occurs, serpentine LPO would control the seismic anisotropy of the deformed mantle rocks. As the shear wave splitting in mantle wedge depends on both the degree of serpentinization and the slab dip, those highly serpentinized and steeply dipped subduction systems are more likely to produce a trench-parallel ϕ.

6.2 Future work

During my study period in École Polytechnique de Montréal, I also completed laboratory measurements of both P- and S-wave velocities at confining pressures up to 800 MPa for 12 rock samples collected from the Tibet plateau. Among the twelve samples, five are retrograde eclogites and amphibolites collected from a MORB-type eclogite belt in the Songduo region of the Lhasa block, seven are serpentinized harzburgites collected from the Luobusha region of the Indus-Yalung Tsangbo suture zone (Fig. 6.1). This suture zone, which is characterized by a distribution of dismembered ophiolite suite and tectonic mélange, forms a tectonic boundary between the Gangdese continental margin of the Lhasa terrane and the Himalayan main collision orogenic zone. The modal and chemical compositions of the samples used for measurements of seismic velocities are given in Table 6.1 and 6.2, respectively. Parameters V_0, D, B_0 and k determined for the P- and S-wave velocities of each minicore sample during depressurization, using a least square regression method, are given in Tables 6.3. The goodness-of-fit coefficients (R^2) are consistently higher than 0.95.

Table 6.1 Description of the studied samples from the Tibet plateau, China

Sample	Lithology	Density (g/cm^3)	Modal composition[a] (vol. %)
06Y-345	Retrograde eclogite	3.41	Grt 37.0, Amp 32.0, Omp 15.0, Ep 10.0, Zo 4.0, Qtz 1.5, Rt 0.5
06Y-524	Amphibolite	3.08	Amp 50.0, Ep 30.0, Qtz 10., Kfs 3.0, Phn 3.0, Zo 1.0, Ilm 1.0, Mag 1.0, Rt 0.5, Ap 0.5
06Y-526	Amphibolite	2.97	Amp 28.0, Ep 23.0, Phn 20.0, Tlc 13.0, Qtz 5.0, Kfs 4.0, Zo 4.0, Grt 2.0, Ilm 1.0
06Y-550	Retrograde eclogite	3.47	Hbl 31.0, Grt 30.0, Ep 20.0, Omp 10.0, Phn 5.0, Zo 3.0, Ilm 0.5, Rt 0.5
06Y-604	Retrograde eclogite	3.29	Hbl 30., Grt 30.0, Ep 14.0, Omp 14.0, Zo 6.0, Qtz 5.0, Ilm 0.5, Rt 0.5
L5	Srp harzburgite	3.03	Ol 57.0, Opx 15.0, Cpx 2.0, Srp 24.0, Ilm 1.0, Mag 1.0
L8a	Srp harzburgite	2.80	Ol 25.0, Opx 17.0, Cpx 2.0, Srp 50.0, Ilm 6.0
L8b	Srp harzburgite	3.09	Ol 64.0, Opx 15.0, Cpx 1.0, Srp 16.0, Ilm 2.0, Mag 2.0
L8c	Srp harzburgite	3.11	Ol 56.0, Opx 16.0, Cpx 4.0, Srp 21.0, Mag 3.0
L24	Srp harzburgite	3.18	Ol 67.0, Opx 15.0, Cpx 3.6, Srp 11.0, Mag 3.4
L25	Srp harzburgite	3.22	Ol 70.0, Opx 19.0, Cpx 1.0, Srp 8.0, Mag 2.0
L26	Srp dunite	3.17	Ol 77.5, Opx 8.5, Cpx 2.0, Srp 10.0, Mag 2.0

[a] Abbreviations: Amp: amphibole; Ap: Apatite; Cpx: clinopyroxene; Ep: epidote; Grt: garnet; Hbl: hornblende; Ilm: ilmenite; Kfs: K-feldspar; Mag: magnetite; Ol: olivine; Omp:omphacite; Opx: orthopyroxene; Phn: phengite; Qtz: quartz; Rt: rutile; Srp: serpentine; Tlc: talc; Zo: zoisite

Table 6.2 Chemical composition (wt.%) of the studied samples from the Tibet plateau, China

Sample	SiO_2	Al_2O_3	Fe_2O_3	CaO	MgO	Na_2O	K_2O	Cr_2O_3	TiO_2	MnO	P_2O_5	LOI	Total
06Y-345	46.02	14.70	13.46	13.17	8.16	1.88	0.05	0.04	1.66	0.23	0.12	0.61	100.10
06Y-524	48.37	14.40	13.97	8.93	6.65	2.46	0.56	0.03	1.98	0.32	0.15	2.15	99.97
06Y-526	50.90	15.29	8.77	8.45	8.78	3.50	0.71	0.05	1.08	0.15	0.14	2.20	100.02
06Y-550	43.58	15.66	14.33	13.37	9.05	1.11	0.02	0.05	1.89	0.23	0.15	0.47	99.91
06Y-604	45.59	15.42	11.88	13.79	9.44	1.18	0.08	0.07	1.17	0.19	0.08	1.14	100.03
L5	42.29	1.00	8.33	1.05	40.42			0.41		0.13	0.01	5.14	98.78
L8a	39.34	0.70	7.74	0.82	38.42			0.39		0.12	0.01	10.70	98.24
L8b	43.10	1.13	8.89	0.77	42.14			0.23		0.13	0.01	3.40	99.80
L8c	43.17	1.46	8.31	1.71	39.78			0.41		0.13	0.01	3.31	98.29
L24	42.99	1.77	8.61	1.92	40.68			0.37		0.13	0.01	3.53	100.01
L25	43.92	0.52	8.88	0.67	42.90			0.39		0.13	0.01	1.05	98.47
L26	41.82	0.25	9.12	0.27	44.71			0.41		0.13	0.01	1.73	98.45

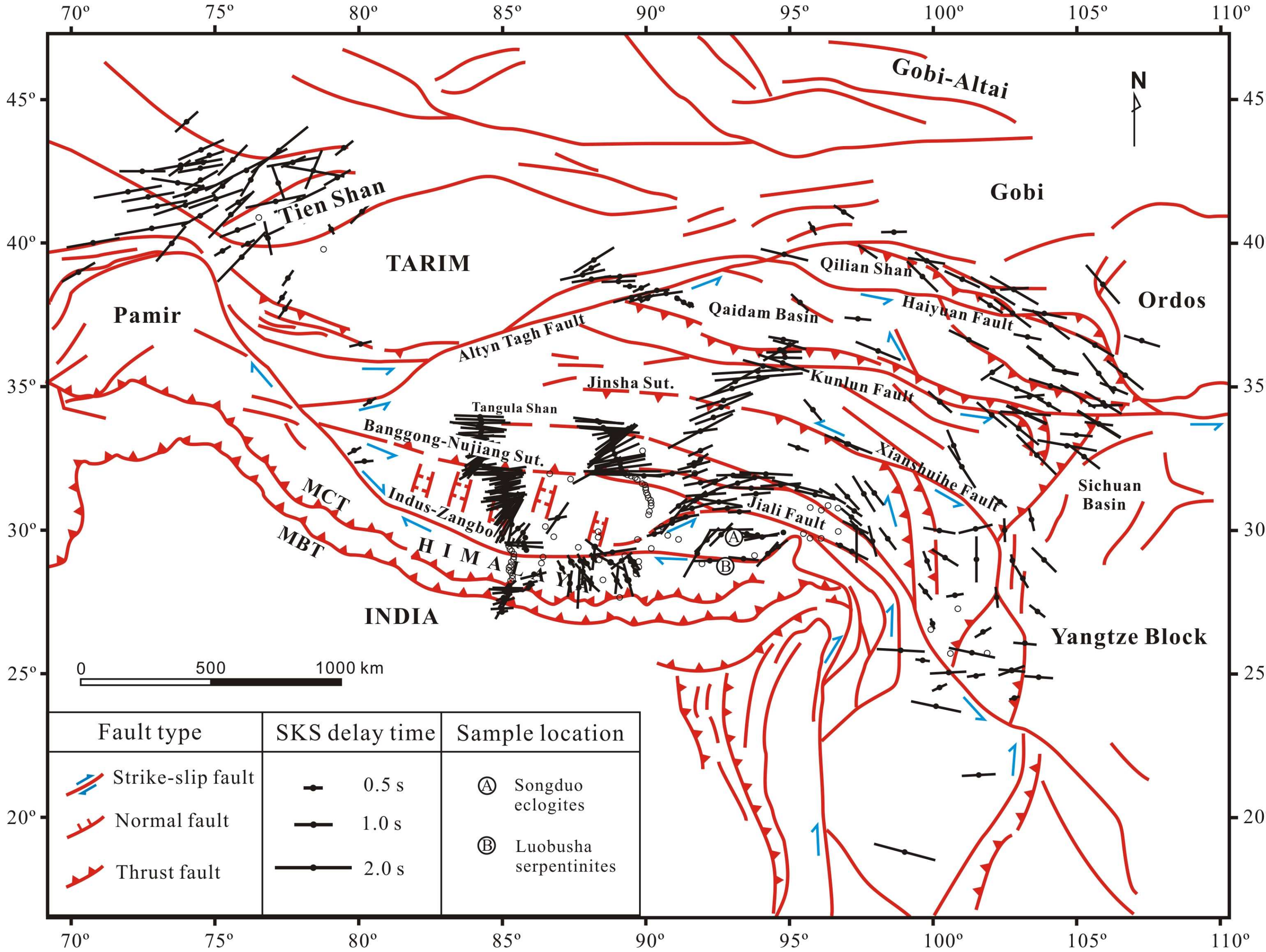

Figure 6.1 A map showing tectonic framework of the Tibet Plateau with data of SKS delay times and the locations of studied samples. A: Songduo; B: Luobusha.

Table 6.3 Parameters of V_p-pressure and V_S-pressure curves measured during depressurization for samples from the Tibet plateau, China.

Sample	**Lithology**	**Density**	**V_p [a]**					**V_s [a]**				
		(g/cm^3)	**Λ**	**V_0**	**D**	**B_0**	**k**	**Λ**	**V_0**	**D**	**B_0**	**k**
06Y-345	Retrograde eclogite	3.41	A	7.793	3.211	1.584	2.398	A	4.422	1.569	0.237	1.680
			B	7.689	2.694	1.142	2.931	B	4.442	0.980	0.146	1.615
06Y-524	Amphibolite	3.08	X	7.402	2.849	1.793	2.218	XY	4.212	1.682	0.170	1.784
								XZ	3.711	1.049	0.305	1.730
			Z	6.385	3.839	1.249	2.446	ZX	3.635	1.893	0.242	1.959
								ZY	3.582	1.695	0.326	2.128
06Y-526	Amphibolite	2.97	Y	6.822	5.130	1.401	2.016	YX	4.028	1.011	0.304	1.866
								YZ	3.595	1.585	0.288	1.709
			Z	6.267	9.152	1.261	1.706	ZX	3.710	0.669	0.349	1.509
								ZY	3.627	1.481	0.456	2.038
06Y-550	Retrograde eclogite	3.47	A	7.545	2.704	1.274	1.755	A	4.398	2.323	0.159	1.717
06Y-604	Retrograde eclogite	3.29	X	7.728	1.447	1.782	1.864	XY	4.378	1.284	0.682	2.277
								XZ	4.210	2.596	0.280	1.248
			Y	7.715	0.863	1.683	1.526	YX	4.269	1.489	0.368	1.182
								YZ	4.165	3.216	0.297	1.610
			Z	7.362	3.292	2.422	2.478	ZX	4.187	1.928	1.445	2.270
								ZY	4.278	2.143	0.600	2.123
L5	Srp harzburgite	3.03	A	7.453	1.644	1.520	3.339	A	4.109	1.531	0.718	2.564
			B	7.228	1.159	0.362	2.259	B	3.960	0.496	0.580	2.337
			C	7.214	0.706	1.032	2.603	C	3.922	0.946	0.813	2.004
L8a	Srp harzburgite	2.80	A	6.782	1.006	0.652	2.294	A	3.673	0.381	0.177	2.519
			B	6.713	1.068	0.832	2.404	B	3.561	0.391	0.185	2.816
L8b	Srp harzburgite	3.09	A	7.396	1.192	0.573	2.859	A	4.268	0.680	0.290	3.686
			B	7.522	0.642	0.598	3.162	B	4.303	0.660	0.079	2.045
L8c	Srp harzburgite	3.11	A	7.552	1.227	0.714	3.108	A	4.229	0.269	0.325	4.064
			B	7.399	1.776	1.564	3.115	B	4.163	0.482	0.201	2.508
			C	7.515	0.963	0.704	4.109	C	4.165	0.821	0.281	6.397
L24	Srp harzburgite	3.18	X	7.769	0.946	1.566	3.695	XY	4.260	0.878	0.180	3.859
								XZ	4.178	0.385	0.173	3.891
			Y	7.702	1.716	0.640	2.794	YX	4.192	0.329	0.094	2.123
								YZ	4.190	0.266	0.089	1.783
			Z	7.755	1.952	0.266	1.797	ZX	4.286	0.538	0.096	1.951
								ZY	4.358	0.192	0.167	2.323
L25	Srp harzburgite	3.22	A	7.294	4.108	1.241	2.490	A	4.300	0.528	1.219	1.571
			B	7.336	3.947	0.960	2.015	B	4.200	1.152	0.520	2.481
			C	7.767	1.968	1.674	3.775	C	4.255	0.836	0.184	1.955
L26	Srp dunite	3.17	A	7.672	2.114	1.449	2.514	A	4.350	1.730	1.188	2.633

[a] Λ is the direction of wave propataion and polarization, V_0 in km/s, D in 10^{-4} km/s/MPa, B_0 in km/s, k in 10^{-2} MPa^{-1}

After my Ph.D. thesis defense, I will analyze these experimental data and the proposed work will focus on:

(1) Correlations between seismic velocities, bulk density, mineralogy and chemical compositions.

(2) Roles of the geometry and state of microcracks, lattice preferred orientations of anisotropic minerals (e.g., serpentine, amphibole, olivine and pyroxene using EBSD techniques) and finite strain axes (i.e., foliation and lineation) on seismic anisotropy and shear wave splitting.

(3) Comparison between laboratory-measured seismic data (e.g., velocities, anisotropy) and the values theoretically calculated from LPOs, elastic constants, and volume fractions of the constituent minerals.

(4) Application of the experimental data to explain the in-situ seismic data (e.g., shear wave splitting and received function data) in the Tibet plateau in terms of lithology and structure.

(5) Correlations between seismic anisotropy and deformation mechanisms (i.e., dislocation creep, diffusion creep or superplasticity).

(6) Validation of the various conflicting models for the formation of Tibet plateau. Special attention will be given to the role of serpentinization in the successive growth of Tibet plateau.

REFERENCES

Aagaard, B. (2006). Finite-element simulations of ground motions in the San Francisco bay area from large earthquakes on the San Andreas Fault. *Seismol. Res. Lett.*, *77*, 275.

Abt, D. L., Fischer, K. M., Abers, G. A., Protti, M., González, V., & Strauch, W. (2010). Constraints on upper mantle anisotropy surrounding the Cocos slab from SK(K)S splitting. *J Geophys Res*, *115*, B06316, doi:10.1029/2009JB006710.

Abt, D. L., Fischer, K. M., Abers, G. A., Strauch, W., Protti, M., & González, V. (2009). Shear wave anisotropy beneath Nicaragua and Costa Rica: implications for flow in the mantle wedge. *Geochem Geophys Geosyst*, *Q05S15*, doi:10.1029/2009GC002375.

Anderson, D. & Dziewonski, A. (1982). Upper mantle anisotropy: evidence from free oscillations. *Geophys. J. R. astr. Soc.*, *69*, 383-404.

Anderson, D. L. (1961). Elastic wave propagation in layered anisotropic media. *J. Geophys. Res.*, *66*, 2953-2963.

Ando, M., Ishikawa, Y., & Yamazaki, F. (1983). Shear wave polarization anisotropy in the upper mantle beneath Honshu, Japan. *J. Geophys. Res.*, *88(B7)*, 5850-5864.

Angerer, E., Crampin, S., Li, X. Y., & Davis, T. L. (2002). Processing, modelling, and predicting time-lapse effects of overpressured fluidinjection in a fractured reservoir. *Geophys. J. Int.*, *149*, 267-280.

Audoine, E., Savage, M. K., & Gledhill, K. (2004). Anisotropic structure under a back arc spreading region, the Taupo Volcanic Zone, New Zealand. *J Geophys Res*, 109, B11305, doi:10.1029/2003JB002932.

Babuska, V. (1972). Elasticity and anisotropy of dunite and bronzitite. *J. Geophys. Res.*, *77(35)*, 6955-6965.

Babuska, V., Fiala, J., Kumazawa, M., Ohno, I., & Sumino, Y. (1978). Elastic properties of garnet solid solution series. *Phys. Earth Planet. Inter.*, *16*(2), 157-176.

Backus, G. E. (1965). Possible forms of seismic anisotropy of the uppermost mantle under oceans. *J. Geophys. Res.*, *70*, 3429.

Bailey, E., & Holloway, J. R. (2000). Experimental determination of elastic properties of talc to 800 ºC, 0.5 GPa: Calculations of the effect on hydrated peridotite, and implications for cold subduction zones. *Earth Planet. Sci. Lett.*, *183*, 487-498.

Baker, D. W. & Carter, N. L. (1972). Seismic velocity anisotropy calculated for ultramafic minerals and aggregates. In H. Heard, I. Borg, N. L. Carter, & B. Raleigh (eds.), *Flow and Fracture of Rocks* (pp. 157-166). Geophys. Monogr., AGU, Washington, DC.

Barazangi, M., & Ni, J. (1982). Velocities and propagation characteristics of Pn and Sn waves beneath the Himalayan Arc and Tibetan Plateau: Possible evidence for underthrusting of Indian continental lithosphere beneath Tibet. *Geology*, *10*, 179-185.

Barruol, G. (1993). *Pétrophysique de la croûte inférieure—Rôle de l'anisotropie sismique sur la réflectivité et le déphasage des ondes S*. Ph.D. Thesis. Université de Montpellier II, France.

Barruol, G., & Kern, H. (1996). Seismic anisotropy and shear-wave splitting in lower-crustal and upper-mantle rocks from the Ivrea Zone—Experimental and calculated data. *Phys. Earth Planet. Inter.*, *95*, 175-194.

Barruol, G., & Mainprice, D. (1993). 3D seismic velocities calculated from LPOs and reflectivity of a lower crustal section - Example of the Val Sesia (Ivrea Zone, Northern Italy). *Geophys. J. Int.*, *115*, 1169-1188.

Barruol, G., Mainprice D., Kern, H., Saint Blanquat, M., & Compte, P. (1992). 3D seismic study of a ductile shear zone from laboratory and petrofabric data (Saint Barthélémy Massif, Northern Pyrénées, France). *Terra Nova*, 4, 63-76.

Bass, J. D. (1995). Elasticity of minerals, glasses, and melts. In T. J. Ahrens (ed.), *Mineral Physics and Crystallography: A Handbook of Physical Constants* (pp. 45-63). AGU Ref. Shelf, vol. 2, AGU, Washington, D. C., USA.

Becker, T. W., & Faccenna, C. (2009). A review of the role of subduction dynamics for regional and global plate motions. In S. Lallemand, & F. Funiciello (eds.), *Subduction Zone Geodynamics* (pp. 3-34). Berlin: Springer.

Ben-Ismail, W., Barruol, G. & Mainprice, D. (2001). The Kaapvaal craton seismic anisotropy: petrophysical analyses of upper mantle kimberlite nodules. *Geophys. Res. Lett.*, *28*, 2497-2500.

Berckhemer, H., Rauen, A., Winter, H., Kern, H., Kontny, A., Lienert, M., (…) Soffel, H. C. (1997). Petrophysical properties of the 9-km-deep crustal section at KTB. *J. Geophys. Res.*, *102(B8)*, 18,337-18,361, doi:10.1029/96JB03396.

Berryman, J. G. (1995). Mixture theories for rock properties. In T. J. Ahrens (ed.), R*ock Physics and Phase Relations: A Handbook of Physics Constants* (pp. 205-228). AGU, Washington, D.C., USA.

Berryman, J. G. (1995). Mixture theories for rock properties. In T. J. Ahrens (ed.), *American Geophysical Union Handbook of Physical Constants* (pp. 205-228). New York: AGU.

Bezacier, L., Reynard, B., Bass, J. D., Sanchez-Valle, C., & Van de Moortèle, B. (2010). Elasticity of antigorite, seismic detection of serpentinites, and anisotropy in subduction zones. *Earth Planet. Sci Lett*, *289*, 198-208.

Bhagat, S., J. D. Bass, & J. Smyth (1992), Single-crystal elastic properties of omphacite-C2/c by Brillouin spectroscopy. *J. Geophys. Res.*, *97(5)*, 6843-6848.

Bianco, F., Scarfi, L., Del Pezzo, E., & Patane, D. (2006). Shear wave splitting time variation by stress-induced magma uprising at Mt. Etna volcano. *Geophys. J. Int.*, *167*, 959-967.

Birch, F. (1960). The velocity of compressional waves in rocks to 10 kilobar, Part 1. *J. Geophys. Res.*, *65*, 1083-1102.

Birch, F. (1961). The velocity of compressional waves in rocks to 10 kilobars, Part 2. *J. Geophys. Res.*, *66*, 2199-2224.

Bostock, B. C., Hyndman, R. D., Rondenay, S., & Peacock, S. M. (2002). An inverted continental Moho and the serpentinization of the forearc mantle. *Nature*, *417*, 536-538.

Boudier, F., Baronnet, A., & Mainprice, D. (2009). Serpentine mineral replacements of natural olivine and their seismic implications: Oceanic lizardite versus subduction-related antigorite. *J. Petrol.*, 51, 495-512.

Bowman, J. R., & Ando, M. (1987). Shear-wave splitting in the upper-mantle wedge above the Tonga subduction zone. *Geophys. J. R. Astron. Soc.*, *88*, 25-41.

Boyd, F. R. a& Gurney, J. J. (1986). Diamonds and the african lithosphere. *Science*, *232*, 472-477.

Boyd, F. R., & Nixon, P. H. (1973). Structure of the upper mantle beneath Lesotho. In: *Carnegie Institution Year Book* (pp. 431-445). Washington, D.C.

Brocher, T. M. (2005a). Empirical relations between elastic wavespeeds and density in the Earth's crust. *Bull. Seism. Soc. Am.*, *95(6)*, 2081-2092.

Brocher, T. M. (2005b). Compressional and shear wave velocity versus depth in the San Francisco Bay Area, California: Rules for USGS Bay Area velocity model 05.0.0. U.S. Geological Survey Open-File Report 2005-1317, 58 pp. http://pubs.usgs.gov/of/2005/1317/

Brocher, T. M. (2008). Key elements of regional seismic velocity models for long period ground motion simulations. *J. Seism.*, *12(2)*, 217-221.

Brocher, T. M., Parsons, T., Trehu, A. M., Snelson, C. M., & Fisher, M. A. (2003). Seismic evidence for widespread serpentinized forearc upper mantle along the Cascadia margin. *Geology*, *31*, 267-270.

Brodie, K. H., & Rutter, E. H. (1987). The role of transiently fine-grained reaction products in syntectonic metamorphism: Natural and experimental examples. *Can. J. Earth. Sci.*, *24*, 556-564.

Burchfiel, B.C., Royden, L.H., van der Hilst, R.D., Hager, B.H., Chen, Z., King, R.W., (…) Kirby, E. (2008). A geological and geophysical context for the Wenchuan earthquake of 12 May 2008, Sichuan, China. *GSA Today*, *18 (7)*, 4-11.

Burke, M. M., & Fountain, D. F. (1990). Seismic properties of rocks from an exposure of extended continental crust-new laboratory measurements from the Ivrea Zone. *Tectonophysics*, *182*, 119-146.

Burlini, L., & Fountain, D. M. (1993). Seismic anisotropy of metapelites from the Ivrea-Verbano zone and Serie dei Laghi (northern Italy). *Phys. Earth. Planet. Inter.*, *78*, 301-317.

Burlini, L., & Kunze, K. (2000). Fabric and seismic properties of Carrara marble mylonite, *Phys. Chem. Earth (A)*, *25*, 133-139.

Buttles, J., & Olson, P. (1998). A laboratory model of subduction zone anisotropy. *Earth. Planet. Sci. Lett.*, *164*, 245-262.

Byerlee, J. D. (1978). Friction of rocks. *Pure and Applied Geophysics*, *116*, 615-626.

Campbell, A. J. & Heinz, D. L. (1992). A high pressure test of Birch's law. *Science*, *257*, 66-68.

Carter, N. L., & Ave Lallemant, H. G. (1970). High temperature flow of dunite and peridotite. *Geol. Soc. Amer. Bull.*, *81*, 2181-2202.

Castagna, J. P., Batzle, M. L., & Eastwood, R. L. (1985). Relationship between compressional and shear wave velocities in clastic silicate rocks. *Geophysics*, *50*, 571-581.

Castagna, J. P., Batzle, M. L., & Kan, T. K. (1993). Rock physics-the link between rock properties and AVO response. In J. P. Castagna, & M. M. Backus (Eds.), Offset-Dependent Reflectivity—Theory and Practice of AVO Analysis (pp. 124-157). Society of Exploration Geophysicists.

Chai, M., Brown, J. M. & Slutsky L. J. (1997). The elastic constants of an aluminous orthopyroxene to 12.5 GPa. *J. Geophys. Res.*, *102*, 14,779-14,785.

Chavez-Perez, S., & Louie, J. N. (1997). Isotropic scattering and seismic imaging of crust fault zones using earthquakes. *Society of Exploration Geophysicists Annual Convention 1997*, Special Session 2.2., Expanded abstracts, 1949-1952.

Chavez-Perez, S., & Louie, J. N. (1998). Crustal imaging in southern California using earthquake sequences. *Tectonphysics, 286*, 223-236.

Chen, J. H., Liu, Q. Y., Li, S., Guo, B., Li, Y., Wang, J., & Qi, S. (2009). Seismotectonic study by relocation of the Wenchuan Ms 8.0 earthquake sequence. *Chinese J. Geophys.*, *52*, 390-397 (in Chinese with English abstract).

Chen, S. F., & Wilson, C. J. L. (1995). Emplacement of the Longmen Shan thrust-nappe belt along the eastern margin of the Tibetan Plateau. *J. Struct. Geol.*, *18*, 413-430.

Chenak, L. J., & Hirth, G. (2010). Deformation of antigorite serpentinite at high temperature and pressure. *Earth. Planet. Sci. Lett.*, *296*, 23-33.

China Earthquake Networks Center (CENC, 2008). Rupture Process of the 2008 M_s 8.0 Wenchuan Earthquake. http://www.cenc.ac.cn

Cholach, P. Y., Molyneux, J. B., & Schmit, D. R. (2005). Flin Flon Belt seismic anisotropy: elastic symmetry, heterogeneity, and shear-wave splitting. *Can. J. Earth Sci.*, *42*, 533-554.

Christensen, D. H., & Abers, G. A. (2010). Seismic anisotropy under central Alaska from SKS splitting observations. *J Geophys Res*, *115*, B04315, doi:10.1029/2009JB006712.

Christensen, N. I. (1965). Compressional wave velocities in metamorphic rocks at pressures to 10 kilobars. *J. Geophys. Res.*, *70*, 6147-6164.

Christensen, N. I. (1966). Elasticity of ultrabasic rocks. *J. Geophys. Res.*, *71*, 5921-5931.

Christensen, N. I. (1971). Shear wave propagation in rocks. *Nature*, *229*, 549-550.

Christensen, N. I. (1974). Compressional wave velocities in possible mantle rocks to pressures of 30 kilobars. *J. Geophys. Res.*, 79, 407-412.

Christensen, N. I. (1985).. Measurements of dynamic properties of rocks at elevated temperatures and pressures. In H. J. Pincus, & E. R. Hoskins (eds.), *Measurements of Rock Properties at Elevated Pressures and Temperatures* (pp. 93-107). ASTM STP, Am. Soc. for Test. and Mater., West Conshohocken, Pa.

Christensen, N. I. (1989), Seismic velocities. In R. S. Carmichael (ed.), *Practical Handbook of Physical Properties of Rocks and Minerals* (pp. 429-546). Florida: CRC Press.

Christensen, N. I. (2004). Serpentinites, Peridotites, and Seismology. *International Geology Review*, *46*, 795-816.

Christensen, N. I., & Ramananantoandro, R. (1971). Elastic moduli and anisotropy of dunite to 10 kilobars. *J. Geophys. Res.*, 76, 4003-4010.

Christensen, N. I., & Szymanski, D. L. (1988). Origin of reflections from the Brevard fault zone. *J. Geophys. Res.*, *93*, 1087-1102.

Christensen, U. (1995). Effects of phase transitions on mantle convection. *Annu. Rev. Earth Planet. Sci.*, *23*, 65-87.

Clark, M.K., & Royden, L. H. (2000). Topographic ooze: Building the eastern margin of Tibet by lower crustal flow. *Geology*, *28*, 703-706.

Clowes, R. M., Cook, F. A., Green, A. G., Keen, C. E., Ludden, J.N., Percival, J. A., (…) West, G. F. (1992). Lithoprobe: New perspectives on crustal evolution. *Can. J. Earth Sci.*, *29*, 1813-1864.

Collins, M. D., & Brown J. M. (1998). Elasticity of an upper mantle clinopyroxene. *Phys. Chem. Miner., 26*, 7-13.

Couvy, H., Frost, D. J., Heidelbach, F., Nyilas, K., Ungar, T., Mackwell, S., Cordier, P. (2004). Shear deformation experiments of forsterite at 11 GPa-1400 °C in the multianvil apparatus. *Eur J Mineral*, *16*, 877-889.

Crampin S., Volti, T., & Stefansson, R. (1999). A successfully stress-forecast earthquake. *Geophys. J. Int.*, *138*, F1-F5.

Crampin, S. (1970). The dispersion of surface waves in multilayered anisotropic media. *Geophys. J. Roy. Astron. Soc.*, *21*, 387-402.

Crampin, S. (1981). A review of the wave motion in anisotropic and cracked elastic-media. *Wave motion*, *3*, 343-391.

Crampin, S. (1987). Geological and industrial implications of extensive-dilatancy anisotropy. *Nature*, *328*, 491-496.

Crampin, S., & Booth, D. C. (1985). Shear-wave polarizations near the North Anatolian fault, II, Interpretation in terms of crackinduced anisotropy. *Geophys. J. R. Astron. Soc.*, *83*, 75-92.

Crampin, S., & Peacock, S. (2005). A review of shear-wave splitting in the compliant crack-critical anisotropic Earth. *Wave Motion*, *41*, 59-77.

Crampin, S., & Peacock, S. (2008). A review of our current understanding of shear-wave splitting and common fallacies in interpretation. *Wave Motion*, *45*, 675-722.

Crampin, S., Evans, R., & Atkinson, B. (1984). Earthquake prediction: a new physical basis. *Geophys. J. R. Astron. Soc.*, *76*, 147-156.

Crosson, R. S., & Lin, J. W. (1971). Voigt and Reuss prediction of anisotropic elasticity of dunite. *J. Geophys. Res.*, *76*, 570-578.

Cui, J. W., Wang, L. J., Li, P. W., Tang, Z. M., & Sun, D. S. (2009). Wellbore breakouts of the main borehole of Chinese Continental Scientific Drilling (CCSD) and determination of the present tectonic stress state. *Tectonophysics*, *475*(2), 218-223.

Currie, C. A., Cassidy, J. F., Hyndman, R., & Bostock, M. G. (2004). Shear wave anisotropy beneath the Cascadia subduction zone and western North American craton. *Geophys J Int*, *157*, 341-353.

Das, S. (1982). Appropriate boundary conditions for modelling very large earthquakes and physical consequences. *Bull. Seism. Soc. Am.*, 72, 1911-1926.

de Sigoyer, J., Carrier, A., Wu, X., Billerot, A., Robert, A., & Pubellier, M. (2008). Long-term petrological evolution of the Wenchuan and Beichuan fault zones (Longmen Shan, Sichuan). *American Geophysical Union*, *89 (53)*, T33A-2037.

DeShon, H. R., & Schwartz, S. Y. (2004). Evidence for serpentinization of the forearc mantle wedge along the Nicoya Peninsula, Costa Rica. *Geophys Res Lett*, 31, doi:10.1029/2004GL021179.

Dewandel, B., Boudier, F., Kern, H., Warsic, W., & Mainprice, D. (2003). Seismic wave velocity and anisotropy of serpentinized peridotite in the Oman ophiolite. *Tectonophysics*, *370*, 77-94.

Dick, H. J. B. (1987). Petrologic variability of the oceanic upper mantle. In J. S. Noller, S. H. Kirby, & J. E. Nielson-Pike (eds.), *Geophysics and Petrology of the Deep Crust and Upper Mantle*, USGS Circular *956*, 17-20.

Dong, S.W., Zhang, Y.Q., Wu, Z.H., Yang, N., Ma, Y.S., Shi, W., Chen Z.L., (…) An, M.J. (2008). Surface ruptures and co-seismic displacement produced by the M_s 8.0 Wenchuan earthquake on the 12th May, 2008, Sichuan, China: eastward growth of Qinghai-Tibet Plateau. *Acta Geologica Sinica*, *82(5)*, 938-948.

Duffy, T. S., & Anderson, D. L. (1989). Seismic velocities in mantle minerals and the mineralogy of the upper mantle. *J. Geophys. Res.*, *94*, 1895-1912.

Duffy, T.S., & Anderson, D. L. (1989). Seismic velocities in mantle minerals and the mineralogy of the upper mantle. *J. Geophys. Res.*, *94*, 1895-1912.

Dufour, J., Squires, J., Goodway, W. N., Edmunds, A., & Shook I. (2002). Integrated geological and geophysical interpretation case study, and Lamé rock parameter extractions using AVO analysis on the Blackfoot 3C-3D seismic data, southern Alberta, Canada. *Geophysics*, *67*, 27-37.

Dziewonski, A. M., & Anderson, D. L. (1981). Preliminary reference Earth model. *Phys. Earth. Planet. Inter.*, *25(4)*, 297-356.

Eberhart-Phillips, D., Han, D. H., & Zoback, M. D. (1989). Empirical relationships among seismic velocity, effective pressure, porosity, and clay content in sandstone. *Geophysics*, *54*, 82-89.

Ehlen, J. (2002). Some effects of weathering on joints in granitic rocks. *Catena*, *49*, 91-109.

Emmermann, R., & Lauterjung, J. (1997). The German Continental Deep Drilling Program KTB: Overview and major results. *J. Geophys. Res.*, *102(B8)*, 18,179-18,201.

Escartin, J., Hirth, G., & Evans, B. W. (2001). Strength of slightly serpentinized peridotites: implications for the tectonics of oceanic lithosphere. *Geology*, *29(11)*, 1023-1026.

Estabrook, C. H., & Kind, R. (1996). The nature of the 660-kilometer upper-mantle seismic discontinuity from precursors to the PP phase. *Science*, *274*, 1179-1182.

Evans, B. W. (1977). Metamorphism of alpine peridotites and serpentinites. *Annu. Rev. Earth Planet. Sci.*, *5*, 397-448.

Evans, B. W. (2004). The serpentinite multisystem revisited: chrysotile is metastable. *Int Geol Rev*, *46*, 479-506.

Faccenda, M., Burlini, L, Gerya T V, & Mainprice, D. (2008). Fault-induced seismic anisotropy by hydration in subducting oceanic plates. *Nature*, *455*, 1097-1101.

Fischer, K. M., & Wiens, D. A. (1996). The depth distribution of mantle anisotropy beneath the Tonga subduction zone. *Earth Planet. Sci. Lett.*, *142*, 253-260.

Fischer, K. M., Parmentier, E. M., Stine, A. R., & Wolf, E. R. (2000). Modeling anisotropy and plate-driven flow in the Tonga subduction zone back arc. *J. Geophys. Res.*, *105*, 16181-16191.

Fouch, M. J., & Fischer, K. M. (1996). Mantle anisotropy beneath northwest Pacific subduction zones. *J. Geophys. Res.*, *101*, 15987-16002.

Fountain, D. M. (1987). Geological and geophysical nature of the lower continental crust as revealed by exposed cross sections of the continental crust. In J. S. Noller, S. H. Kirby, & J. E. Nielson-Pike (eds.), *Geophysics and Petrology of the deep Crust and Upper Mantle* (956, pp.25-26). United States Geological Survey Circular.

Frederiksen, A. W., Folsom, H., & Zandt, G. (2003). Neighbourhood inversion of teleseismic Ps conversions for anisotropy and layer dip. *Geophys. J. Int.*, *155*, 200-212.

Frisillo, A. L., & Barsch, G. R. (1972). Measurement of singlecrystal elastic constants of bronzite as a function of pressure and temperature. *J. Geophys. Res.*, *77*, 6360-6384.

Fukao, Y. (1984). Evidence from core-reflected shear waves for anisotropy in the earth’s mantle. *Nature*, *309*, 695-698.

Funiciello, F., Faccenna, C., Heuret A, Lallemand, S., Di Giuseppe, E., & Becker T. W. (2008). Trench migration, net rotation and slab-mantle coupling. *Earth Planet. Sci. Lett.*, *271*, 233-240.

Funiciello, F., Moroni, M., Piromallo, C., Faccenna, C., Cenedese, A., & Bui, H. A. (2006). Mapping mantle flow during retreating subduction: laboratory models analyzed by feature tracking. *J Geophys Res*, *111*, B03402, doi:10.1029/2005JB003792.

Gao, Y., & Crampin, S. (2004). Observations of stress relaxation before earthquakes. *Geophys. J. Int.*, *157*, 578-582.

Gardner, G. H. F., Wyllie, M. R. J., & Droschak, D. H. (1965). Hysterisis in the velocity-pressure characteristics of rocks. *Geophysics*, *30*, 111-134.

Gebrande, H. (1982). Elastic wave velocities and constants of elasticity of rocks and rock-forming minerals. In Hellwege, K. H. (ed.), *Physical Properties of Rocks, Landolt-Börnstein Numerical Data and Functional Relationships in Science and Technology V1b* (pp. 1-99). Berlin: Springer.

Gercek, H. (2007). Poisson’s ratio values for rocks. *International Journal of Rock Mechanics and Mining Sciences*, *44*, 1-13.

Gerst, A., & Savage, M. (2004). Seismic anisotropy beneath Ruapehu volcano: a possible eruption forecasting tool. *Science*, *306*, 1543-1547.

Godfrey, N. J., Christensen, N. I., & Okaya, D. A. (2000). Anisotropy of schists: Contributions of crustal anisotropy to active source seismic experiments and shear wave splitting observations. *J. Geophys. Res.*, *105(B12)*, 27991-28007.

Goodway, B. (2001). AVO and Lamé constants for rock parameterization and fluid detection. *CSEG Recorder*, June, 39-60.

Goodway, B., & Tessman, J. (2000). Comparative reservoir imaging using new seismic-acquisition technology. *World Oil*, *221*, 49-54.

Goodway, B., Chen, T., & Downton, J. (1997). Improved AVO fluid detection and lithology discrimination using Lamé petrophysical parameters, λρ, μρ, and λ/μ fluid stack, from P and S inversions, 67th Ann. *Internat. Mtg., Soc. Expl. Geophys.*, Expanded Abstracts, 183-186.

Graeber, F. M., & Asch, G. (1999). Three dimensional models of P-wave velocity and P-to-S velocity ratio in the southern central Andes by simultaneous inversion of local earthquake data. *J. Geophys. Res.*, *104*, 20237-20256.

Grant, K. J., Kohn, S. C., & Brooker, R. A. (2007). The partitioning of water between olivine, orthopyroxene and melt synthesised in the system albite-forsterite-H_2O. *Earth Planet. Sci. Lett.*, *260*, 227-241.

Gray, D. (2003). A better way to extract fundamental rock properties with much less noise. *World Oil*, *224*, 49-53.

Gray, D., & Andensen, E. (2000). The application of AVO and inversion to formation properties. *World Oil*, *221*, 85-90.

Greenfield, R. J., & Graham, E. K. (1996). Application of the simple relation for describing wave velocity as a function of pressure in rocks containing microcracks. *J. Geophys. Res.*, *101*, 5643-5652.

Gripp, A. E., & Gordon, R. G. (2002). Young tracks of hot spot and current plate velocities. *Geophys. J. Int.*, *150*, 321-361.

Guyer, R. A, & Johnson, P. A. (1999). Nonlinear mesoscopic elasticity: evidence for a new class of materials. *Physics Today*, April, 30-36.

Hammond, J. O. S., Wookey, J., Kaneshima, S., Inoue, H., Yamashina, T., & Harjadi, P. (2010). Systematic variation in anisotropy beneath the mantle wedge in the Java-Sumatra subduction system from shear-wave splitting. *Phys. Earth Planet. Inter.*, *178*, 189-201.

Hansen, F. D., & Carter, N. L. (1982). Creep of selected crustal rocks at 1000 MPa. *Trans. Amer. Geophys. Union*, *63*, 437.

Harvard University, 2008. Global CMT Catalog, 200805120628A Eastern Sichuan, China. http://www.globalcmt.org/CMTsearch.html.

Hashin, Z., & Shtrikman, S. (1963). A variation approach to the theory of the elastic behavior of multiphase materials. *Journal of the Mechanics and Physics of Solids*, *11*, 127-140.

Hearmon, R. F. S. (1979). The elastic constants of crystals and other anisotropic materials. In K. H. Hellwege & A. M. Hellwege (eds.), *Landolt-Bornstein Tables* (III/11, pp. 1-244). Berlin: Springer-Verlag.

Hearmon, R. F. S. (1984), The elastic constants of crystals and other anisotropic materials, In K. H. Hellwege & A. M. Hellwege (eds.), *Landolt-Bornstein Tables*, (III/18, pp. 1-154). Berlin: Springer-Verlag.

Herquel, G., Wittlinger, G., & Guilbert, J. (1995). Anisotropy and crustal thickness of northern-Tibet: New constraints for tectonic modelling. *Geophys Res Lett*, *22(14)*, 1925-1928.

Hess, H. (1964). Seismic anisotropy of the uppermost mantle under oceans. *Nature*, *203*, 629-631.

Heuret, A., & Lallemand, S. (2005). Plate motions, slab dynamics and back-arc deformation. *Phys. Earth Planet. Inter.*, *149*, 31-51.

Hilairet, N., Reynard, B., Wang, Y., Daniel, I., Merkel, S., Nishiyama, N., & Petitgirard, S. (2007). High-pressure creep of serpentine, interseismic deformation, and initiation of subduction. *Science*, *318*, 1910-1913.

Hill, R. (1952). The elastic behavior of a crystalline aggregate. *Physical Society – Proceedings*, *65*, 349-354.

Hill, R. (1965). A self consistent mechanics of composite materials. *J. Mech. Phys. Solids.*, *13*, 213-222.

Hirauchi, K. I., & Yamaguchi, H. (2007). Unique deformation processes involving the recrystallization of chrysotile within serpentinite: implications for aseismic slip events within subduction zones. *Terra Nova*, *19(6)*, 454-461.

Hirauchi, K. I., Katayama, I., Uehara, S., Miyahara, M., & Takai, Y. (2010). Inhibition of subduction thrust earthquakes by low-temperature plastic flow in serpentine. *Earth Planet. Sci. Lett.*, *295*, 349-57.

Hirth, G., & Kohlstedt, D. L. (1996). Water in the oceanic upper mantle-implications for rheology, melt extraction and the evolution of the lithosphere. *Earth Planet. Sci. Lett.*, *144*, 93-108.

Hoernle, K., Abt, D. L., Fischer, K. M., Nichols, H., Hauff, F., Abers, G. P., (…) Strauch, W. (2008). Geochemical and geophysical evidence for arc-parallel flow in the mantle wedge beneath Costa Rica and Nicaragua. *Nature*, *451*, 1094-1098.

Holcomb, D. J. (1981). Memory, relaxation, and microfracturing in dilatant rock. *J. Geophys. Res.*, *86*, 6235-6248.

Houseman, G. A., & Gubbins, D. (1997). Deformation of subducted oceanic lithosphere. *Geophys. J. Int.*, *131*, 535-551.

Hsui, A. T., Tang, X. M., & Toksoz, M. N. (1990). On the dip angle of subducting plates. *Tectonophpsics*, *179*, 163-175.

Hu, S.B., He L.J., & Wang, J.Y. (2001). Compilation of heat flow data in the China continental area (3rd edition). *Chinese J. Geophys.*, *44 (5)*, 611-626 (in Chinese with English abstract).

Huang, Z., Zhao, D., & Wang, L. (2011). Shear wave anisotropy in the crust, mantle wedge, and subducting Pacific slab under northeast Japan. *Geochem. Geophys. Geosyst.*, *12*, Q01002, doi:10.1029/2010GC003343.

Hubbard, J., & Shaw, J. (2009). Uplift of the Longmen Shan and Tibetan plateau, and the 2008 Wenchuan (M=7.9) earthquake. *Nature*, *458*, 194-197.

Huenges, E., Erzinger, J., Kück, J., Engeser, B., & Kessels, W. (1997). The permeable crust: geohydraulic properties down to 9101 m depth. *J. Geophys. Res.*, *102(B8)*, 18255-18265.

Hurich, C. A., Deemer, S. J., & Indares, A. (2001). Compositional and metamorphic controls on velocity and reflectivity in the continental crust: An example from the Grenville Province of eastern Québec. *J. Geophys. Res.*, *106*, 665-682.

Hyndman, R. D., & Peacock, S. M. (2003). Serpentinization of the forearc mantle. *Earth Planet. Sci Lett*, *212*, 417-432.

Islam, M. R., Stuart, R., Risto, A. & Vesa P. (2002). Mineralogical changes during intense chemical weathering of sedimentary rocks in Bangladesh, *J. Asian Earth Sci.*, *20*, 889-901.

Issak, D. G. (1992). High-temperature elasticity of iron-bearing olivine. *J. Geophys. Res.*, *97*, 1871-1885.

Ivankina T. I., Kern, H., & Nikitin, A. N. (2005). Directional dependence of P- and S-wave propagation and polarization in foliated rocks from the Kola superdeep well: evidence from laboratory measurements and calculations based on TOF neutron diffraction. *Tectonophysics*, *407*, 25-42.

Jaeger, J. C. (1969). *Elasticity, Fracture and Flow, with Engineering and Geological Application*s. London: Methuen & Co.

Jahns, E., Siegesmund, S., & Chlupác, T. (1994). In situ seismic velocities versus laboratory measurements: an example from the KTB. *Scientific Drilling*, *5*, 215-226.

Ji, C. (2008). Preliminary Result of the May 12, 2008 M_w 7.97 SiChuan Earthquake. http://www.geol.ucsb.edu/faculty/ji/big_earthquakes/2008/05/12/ShiChuan.html

Ji, S. C. & Wang, Z. C. (1999). Elastic properties of forsterite–enstatite composites up to 3.0 GPa. *J. Geodyn.*, *28*, 147-174.

Ji, S. C. (2004). A generalized mixture rule for estimating the viscosity of solid-liquid suspensions and mechanical properties of polyphase rocks and composite materials. *J. Geophys. Res.*, *109*, B10207.

Ji, S. C. (2008). *Deformation Mechanisms, Rheology and Seismic Properties of Rocks*. Beijing: Geological Publishing House.

Ji, S. C., & Mainprice, D. (1988). Natural deformation fabrics of plagioclase: Implications for slip systems and seismic anisotropy. *Tectonophysics*, *147*, 145-163.

Ji, S. C., & Salisbury, M. H. (1993). Shear-wave velocities, anisotropy and splitting in high-grade mylonites. *Tectonophysics*, *221*, 453-473.

Ji, S. C., & Xia, B. (2002). *Rheology of Polyphase Earth Materials*. Montreal: Polytechnic International Press.

Ji, S. C., & Xu, Z. Q. (eds.) (2009). The Chinese Continental Scientific Drilling (CCSD). *Tectonophysics*, *475*, 201-403.

Ji, S. C., & Zhao, P. (1994). Layered rheological structure of subducting oceanic lithosphere. *Earth Planet. Sci. Lett.*, *124,* 75-94.

Ji, S. C., 2009. Seismicity of Chinese continent. Beijing: Science Presss. (in Chinese)

Ji, S. C., Long, C. X., Martignole, J., & Salisbury, M. H. (1997a). Seismic reflectivity of a finely layered, granulite-facies ductile shear zone in the southern Grenville province (Quebec). *Tectonophysics*, *279*, 113-133.

Ji, S. C., Rondenay, S., Mareschal, M., & Senechal, G. (1996). Obliquity between seismic and electrical anisotropies as an indicator of movement sense for ductile mantle shear zones. *Geology*, 24, 1033-1036.

Ji, S. C., Rybacki, E., Wirth, R., Jiang, Z. T., & Xia B. (2005). Mechanical and microstructural characterization of calcium aluminosilicate (CAS) and SiO_2/CAS composites deformed at high-temperature and high-pressure. *Journal of the European Ceramic Society*, *25*, 301-311.

Ji, S. C., Salisbury, M. H., & Hanmer, S. (1993). Petrofabric, P-wave anisotropy and seismic reflectivity of high-grade tectonites, *Tectonophysics*, *222*, 195-226.

Ji, S. C., Saruwatari, K., Mainprice, D., Wirth, R., Xu, Z.Q., & Xia, B. (2003). Microstructures, petrofabrics and seismic properties of ultrahigh-pressure eclogites from Sulu region, China: Implications for rheology of subducted continental crust and origin of mantle reflections. *Tectonophysics*, *370*, 49-76.

Ji, S.C., Sun, S., Wang, Q., Marcotte, D., 2010. Lamé parameters of common rocks in the Earth's crust and upper mantle. *Journal of Geophysical Research*, 115, B06314, doi:10.1029/2009JB007134.

Ji, S. C., Wang, Q., & Salisbury, M. H. (2009). Composition and tectonic evolution of the Chinese continental crust constrained by Poisson's ratio. *Tectonophysics*, *463*, 15-30.

Ji, S. C., Wang, Q., & Xia, B. (2002). *Handbook of Seismic Properties of Minerals, Rocks and Ores*. Montreal: Polytechnic International Press.

Ji, S. C., Wang, Q., & Xu, Z. Q. (2007b). Reply to the comment of S. Karato on "Petrofabrics and seismic properties of garnet peridotites from the USP Sulu Terrane (China)" by Xu et al. [Tectonophysics 421 (2006) 111–127]. *Tectonophysics*, *429*, 291-296.

Ji, S. C., Wang, Q., & Xu, Z. Q. (2008). Break-Up of the North China Craton through Lithospheric Thinning. *Acta Geologica Sinia, 82(2)*, 174-193 (in Chinese with Engish abstract).

Ji, S. C., Wang, Q., Marcotte, D., Salisbury, M. H., & Xu, Z. Q. (2007a). P-wave velocities, anisotropy and hysteresis in ultrahigh-pressure metamorphic rocks as a function of confining pressure. *J. Geophys. Res., 112*, B09204, doi: 10.1029/2006JB004867.

Ji, S. C., Wang, Q., Xia, B., & Marcotte, D. (2004). Mechanical properties of multiphase materials and rocks: a simple phenomenological approach using generalized means. *Journal of Structural Geology*, *24*, 1377-1390.

Ji, S. C., Xu, Z. Q., Wang, Q., Sun, S., Li, H. (2008). Continental Extrusion and Seismicity in China. *Acta Geologica Sinica*, *82(12)*, 1644-1667 (in Chinese with English abstract).

Ji, S. C., Zhao, P. & Saruwatari, K. (1997b). Fracturing of garnet crystals in anisotropic metamorphic rocks during uplift. *J. Struct. Geol.*, *19*, 603-620.

Ji, S. C., Zhao, X., & Francis, D. (1994). Calibration of shear-wave splitting in the subcontinental upper mantle beneath active orogenic belts using ultramafic xenoliths from the Canadian Cordillera and Alaska. *Tectonophysics*, *239*, 1-27.

Jia, D., Li, Y., Lin, A., Wang, M., Chen, W., Wu, X., (…) Luo, L. (2010). Structural model of 2008 M_w 7.9 Wenchuan earthquake in the rejuvenated Longmen Shan thrust belt, China. *Tectonophysics*, *491*, 174-184.

Jia, D., Wei, G., Chen, Z., Li, B., Zeng, Q., & Yang, G. (2006). Longmen Shan fold-thrust belt and its relation to the western Sichuan Basin in central China: new insights from hydrocarbon exploration. *AAPG Bulletin*, *90*, 1435-1447.

Jiao, W., Silver, P. G., Fei, Y., & Prewitt, C. T. (2000). Do intermediate- and deep-focus earthquakes occur on preexisting weak zones? An examination of Tonga subduction zone. *J. Geophys. Res.*, *105*, 28,125-28,138.

Jones, L. A., & Wang, H. F. (1981). Ultrasonic velocities in Cretaceous shales from the Williston basin. *Geophysics*, *46*, 288-297.

Jung, H., & Karato, S. (2001). Water-induced fabric transitions in olivine. *Science*, *293*, 1460-1463.

Jung, H., Katayama I, Jiang Z, Hiraga, T., & Karato, S. (2006). Effect of water and stress on the lattice-preferred orientaion of olivine. *Tectonophysics*, *421*, 1-22.

Jung, H., Mo, W., & Green, H. W. (2009). Upper mantle seismic anisotropy resulting from pressure-induced slip transition in olivine. *Nat. Geosci.*, *2*, 73-77.

Kamiya, S., & Kobayashi, Y. (2000). Seismological evidence for the existence of serpentinized wedge mantle. *Geophys Res Lett*, *27*, 819-822.

Kaneshima, S. (1990). Origin of crustal anisotropy: shear wave splitting studies in Japan. *J. Geophys. Res.*, *95*, 121-133.

Kaneshima, S., & Ando, M. (1988). Crustal anisotropy inferred from shear-wave splitting. The Third International Workshop on Seismic Anisotropy, Berkeley, USA.

Kaneshima, S., Ando, M. & Kimura, S. (1988). Evidence from shear-wave splitting for the restriction of seismic anisotropy to the upper crust. *Nature*, *335*, 627-629.

Karato, S, Jung, H., Katayama, I., & Skemer, P.. (2008). Geodynamic significance of seismic anisotropy of the upper mantle: new insights from laboratory studies. *Annu. Rev. Earth Planet. Sci.*, *36*, 59-95.

Karato, S. (1986). Does partial melting reduce the creep strength of the upper mantle? *Nature*, *319*, 309-310.

Karato, S. (2002). *The Dynamics Structure of the Deep Earth: an Interdisciplinary Approach*. New Jersey: Princeton and Oxford.

Karato, S. I., & Karki, B. B. (2001). Origin of lateral variation of seismic wave velocities and density in the deep mantle. *J. Geophys. Res.*, *106(B10)*, 21,771-21,783.

Karato, S., & Wu, P. (1993). Rheology of the upper mantle: a synthesis. *Science*, *260*, 771-778.

Katayama, I., & Karato, S. (2006). Effects of temperature on the B- to C-type fabric transition in olivine. *Phys. Earth Planet. Int.*, *157*, 33-45.

Katayama, I., Hirauchi, K. I., Michibayashi K, & Ando, J. I. (2009). Trench-parallel anisotorpy produced by serpentine deformation in the hydrated mantle wedge. *Nature*, *461*, 1114-1118.

Katayama, I., Jung, H., & Karato, S. (2004). New type of olivine fabric from deformation experiments at modest water content and low stress. *Geology*, *32*, 1045-1048.

Kendall, J. M. (1994). Teleseismic arrivals at a mid-ocean ridge: Effects of mantle melt and anisotropy. *Geophys. Res. Lett.*, *21*, 301- 304.

Kennett, B. L., Widiyantoro, N., S., & van der Hilst, R. D. (1998). Joint seismic tomography for bulk sound and shear wave speed in the Earth's mantle. *J. Geophys. Res.*, *103(B6)*, 12,469-12,493.

Kern, H. & Tubia, J. M. (1993). Pressure and temperature dependence of P- and S-wave velocities, seismic anisotropy and density of sheared rocks from Sierra Alpujata massif (Ronda peridotites, southern Spain). *Earth Planet. Sci. Lett.*, *119*, 191-205.

Kern, H. (1979). Effect of high-low quartz transition on compressional and shear wave velocities in rocks under high pressure. *Physics and Chemistry of Minerals*, *4*, 161-171.

Kern, H. (1982). P- and S-wave velocities in crustal and mantle rocks under the simultaneous action of high confining pressure and high temperature and the effect of the rock microstructure. In W. Schreyer (ed.), *High-Pressure Research in Geosciences* (pp. 15-45). Stuttgart: E. Schweizerbart'sche Verlagsbuchhandlung.

Kern, H. (1990). Laboratory seismic measurements: an aid in the interpretation of seismic field data. *Terra Nova*, 2(6), 617-628.

Kern, H., & Wenk, H. R. (1990). Fabric-related velocity anisotropy and shear wave splitting in rocks from Santa Rosa mylonite zone, California. *J. Geophys. Res.*, *95*, 11,213-11,223.

Kern, H., Burlini, L., & Ashchepkov, I. V. (1996a). Fabric-related seismic anisotropy in upper-mantle xenoliths: evidence from measurements and calculations. *Phys. Earth Planet. Inter.*, *95*, 195-209.

Kern, H., Gao, S., & Liu, Q. S. (1996b). Seismic properties and densities of middle and lower crustal rocks exposed along the North China Geoscience Transect. *Earth Planet. Sci. Lett.*, *139*, 439-455.

Kern, H., Gao, S., Jin, Z. M., Popp, T., & Jin, S. Y. (1999). Petrophysical studies on rocks from the Dabie ultrahigh-pressure (UHP) metamorphic belt, central China: implications for the composition and delamination of the lower crust. *Tectonophysics*, *301*, 191-215.

Kern, H., Jin, Z. M., Gao, S., Popp, T., & Xu, Z. Q. (2002). Physical properties of ultrahigh-pressure metamorphic rocks from the Sulu terrain, eastern central China: implications for the seismic structure at the Donghai (CCSD) drilling site. *Tectonophysics*, *354*, 315-330.

Kern, H., Popp, T., Gorbatsevich, F., Zharikov, A., Lobanov, KV., & Smirnov, Y. P. (2001). Pressure and temperature dependence of V_p and V_s in rocks from the superdeep well and from surface analogues at Kola and the nature of velocity anisotropy. *Tectonophysics*, *338*, 113-134.

Kern. H., Liu, B., & Popp, T. (1997). Relation between anisotropy of P and S wave velocities and anisotropy of attenuation in serpentinite and amphibolite. *J. Geophys. Res.*, *102*, 3051-3065.

Kincaid, C., & Griffiths, R. W. (2003). Laboratory models of the thermal evolution of the mantle during rollback subduction. *Nature*, *425*, 58-62.

Kitamura, K. (2006). Constraint of lattice-preferred orientation (LPO) on V_p anisotropy of amphibole-rich rocks. *Geophys. J. Int.*, *165*, 1058-1065.

Kneller, E. A., Long, M. D., & van Keken, P. E. (2008). Olivine fabric transitions and shear-wave anisotropy in the Ryukyu subduction system. *Earth Planet. Sci. Lett.*, *268*, 268-282.

Kneller, E. A., van Keken, P. E., Karato, S., & Park, J. (2005). B-type fabric in the mantle wedge: insights from high-resolution non-Newtonian subduction zone models. *Earth Planet. Sci. Lett.*, *237*, 781-797.

Kneller, E. A., van Keken, P. E., Katayama, I., & Karato, S. (2007). Stress, strain, and B-type olivine fabric in the fore-arc mantle: sensitivity tests using high-resolution steady-state subduction zone models. *J. Geophys. Res.*, *112*, doi:10.1029/2006JB004544.

Koketsu, K., Hatayama, K., Furumura, T., Ikegami, Y., & Akiyama, S. (2005). Damaging long-period ground motions from the 2003 M_w 8.3 Tokachi-oki, Japan earthquake. *Seismol. Res. Lett.*, *76*, 67-73.

Koketsu, K., Yokota, Y., Ghasemi, H., Hikima, K., Miyake, H., & Wang, Z. (2009). Source process and ground motions of the 2008 Wenchuan earthquake. Investigation report of the 2008 Wenchuan Earthquake, China, Grantin-Aid for Special Purposes of 2008, MEXT. http://shake.iis.u-tokyo.ac.jp/wenchuan/

Kozlovsky, Y. A. (ed.) (1987). The Superdeep Well of the Kola Peninsula. Berlin: Springer.

Kumazawa, M., & Anderson, O. L. (1969). Elastic moduli, pressure derivatives, and temperature derivatives of single-crystal olivine and single-crystal forsterite. *J. Geophys. Res.*, 74, 5961-5972.

Lakes, R. S. (1987). Foam structures with a negative Poisson's ratio. *Science*, *235*, 1038-1040.

Levien, L., Weidner, D. J. & Prewitt, C. T. (1979). Elasticity of diopside. *Phys. Chem. Miner.*, *4*, 105-113.

Levin, V., Droznin, D., Park, J., & Gordeev, E. (2004). Detailed mapping of seismic anisotropy with local shear waves in southeastern Kamchatka. *Geophys. J. Int.*, *158*, 1009-1023.

Li, C. Y., Wei, Z. Y., Ye, J. Q., Han, Y. B., & Zheng, W. J. (2010). Amounts and styles of coseismic deformation along the northern segment of surface rupture, of the 2008 Wenchuan Mw 7.9 earthquake, China. *Tectonophysics*, *491*, 35-58.

Li, C., van der Hilst, R. D., Engdahl, E. R., & Burdick, S. (2008). A new global model for P wave speed variations in Earth's mantle. *Geochem. Geophys. Geosyst.*, *9*, Q05018, doi:10.1029/2007GC001806.

Li, H. B., Fu, X., van der woerd, J., Si, J. L., Wang, Z. X., Hou, L. W., (…) Tapponnier, P. (2008). Co-seisimic surface rupture and dextral-slip oblique thrusting of the M_s 8.0 Wenchuan earthquake. *Acta Geologica Sinica*, *82(12)*, 1623-1643 (in Chinese with English abstract).

Li, L., Raterron, P., Weidner D, & Chen, J. (2003). Olivine flow mechanisms at 8 GPa. *Phys. Earth Planet. Inter.*, *138*, 113-129.

Li, L., Weidner, D., Raterron, P., Chen, J., & Vaughan, M. (2004). Stress measurements of deforming olivine at high pressure. *Phys. Earth Planet. Inter.*, *143*, 357-367.

Li, T. F., Yang, J. S., & Zhang, R. Y. (2003). Peridotite from the pre-pilot hole (PP1) of Chinese continental scientific drilling project and its bearing on depleted and metasomatic upper mantle. *Acta Geologica Sinica*, *77*, 492-509.

Li, Y. Y., Downton, J., & Goodway, B. (2003). Recent applications of AVO to carbonate reservoirs in the western Canadian sedimentary basin. *The Leading Edge*, *22*, 670-674.

Liang, C., & Song, X. (2006). A low velocity belt beneath northern and eastern Tibetan Plateau from Pn tomography. *Geophys. Res. Lett.*, *33*, L22306, doi:10.1029/2006GL027926.

Liebermann, R., & Ringwood, A. (1973). Birch's Law and Polymorphic Phase Transformations. *J. Geophys. Res.*, *78*(29), 6926-6932.

Lin, A., Ren, Z., & Jia, D. (2010). Co-seismic ground-shortening structures produced by the 2008 M_w 7.9 Wenchuan earthquake, China. *Tectonophysics*, *491*, 21-34.

Lin, A., Ren, Z., Jia, D., & Wu, X. (2009). Co-seismic thrusting rupture and slip distribution produced by the 2008 M 7.9 Wenchuan earthquake, China. *Tectonophysics*, *471*, 203-215.

Liou, J. G. & Zhang, R. Y. (1996). Occurrence of intragranular coesite in ultrahigh-P rocks from the Sulu region, eastern China: implications for lack of fluid during exhumation. *American Mineralogist*, *81*, 1217-1221.

Liou, J. G., Hacker, B. R., & Zhang, R. Y. (2000). Into the forbidden zone. *Science*, *287*, 1,215-1,216.

Liou, J. G., Zhang, R. Y., Ernst, W. G., Rumble, D., & Maruyama, S. (1998). High-pressure minerals from deeply subducted metamorphic rocks. *Rev. Miner. Geochem.*, *37*, 33-96.

Liu, F. L., Xu, Z. Q., Liou, J. G., & Song, B. (2004). SHRIMP U-Pb ages of ultrahigh-pressure and retrograde metamorphism of gneisses, South-western Sulu terrain, Eastern China. *J. Metamorp. Geol.*, *22*, 315-326.

Liu, F. L., Xu, Z. Q., Liou, J. G., Dong, H. L., & Xue, H. M. (2007). Ultrahigh-pressure Mineral Assemblages in Zircons from the Surface to 5158 m Depth in Cores of the Main Drill Hole, Chinese Continental Scientific Drilling Project, SW Sulu Belt, China. *Inter. Geol. Rev.*, *49*, 454-478.

Liu-Zeng, J., Zhang, Z., Wen, L., Tapponnier, P., Sun, J., Xing, X., (…) van der Woerd, J. (2009). Co-seismic ruptures of the 12 May 2008, M_S 8.0 Wenchuan earthquake, Sichuan: East–west crustal shortening on oblique, parallel thrusts along the eastern edge of Tibet. *Earth Planet. Sci. Lett.*, *286*, 355–370.

Lloyd, G. E., & Kendall, J. M. (2005). Petrofabric Derived Seismic Properties of a Mylonitic Quartz Simple Shear Zone: Implications for Seismic Reflection Profiling. In P. K. Harvey, T. Brewer, P. A. Pezard, & V. A. Petrov (eds.), *Petrophysical Properties of Crystalline Rocks* (240, pp. 75-94). London: Gelogocal Society Special Publication.

Long, C. & Christensen, N. I. (2000). Seismic anisotropy of South African upper mantle xenoliths. *Earth Planet. Sci. Lett.*, *179*, 551-565.

Long, M. D., & Becker, T. W. (2010). Mantle dynamics and seismic anisotropy. *Earth Planet. Sci. Lett.*, *297*, 341-354.

Long, M. D., & Silver, P. G. (2008). The subduction zone flow field from seismic anisotropy: a global view. *Science*, *319*, 315-318.

Long, M. D., & Silver, P. G. (2009). Mantle flow in subduction systems: the subslab flow field and implications for mantle dynamics. *J. Geophys. Res.*, *114*, B10312, doi:10.1029/2008JB006200.

Long, M. D., & van der Hilst, R. D. (2005). Upper mantle anisotropy beneath Japan from shear wave splitting. *Phys. Earth Planet. Inter.*, *151*, 206-222.

Long, M. D., & van der Hilst, R. D. (2006). Shear wave splitting from local events beneath the Ryukyu arc: trench-parallel anisotropy in the mantle wedge. *Phys. Earth Planet. Inter.*, *155*, 300-312.

Lu, M., Li, X. J., An, X. W., & Zhao J. X. (2010). A preliminary study on the near-source strong-motion characteristics of the great 2008 Wenchuan earthquake in China. *Bull. Seismol. Soc. Am.*, *100 (5B)*, 2491-2507.

Lu, Z. Q. (2005). Role of hysteresis in propagating acoustic waves in soils. *Geophys. Res. Lett.*, *32*, L14302, doi:10.1029/2005GL022980.

Lubarda, V. A. (1998). A note on the effective Lamé constants of polycrystalline aggregates of cubic crystals. *J. Appl. Mech.*, *65*, 769-770.

Maaloe, S., & Aoki, K. (1977). The major element composition of upper mantle estimated from the composition of lherzolites. *Contrib. Mineral Petrol.*, *63*, 161-173.

Mainprice, D. (2007). Seismic anisotropy of the deep Earth from a mineral and rock physics perspective. In G. Schubert (ed.), *Treatise on Geophysics*, *2*, 437-492.

Mainprice, D. , Barruol, G. , & Ismaïl, W. (2000). The seismic anisotropy of the Earth's mantle: from single crystal to polycrystal. In S. Karato, A. Forte, R. Liebermann, G. Masters, & L. Stixrude (eds.), *Earth's Deep interior: Mineral physics and Tomography from the atomic to the global scale*, *117*, 237-264.

Mainprice, D., & Casey, M. (1990). The calculated seismic properties of quartz mylonites with typical fabrics: relationship to kinematics and temperature. *Geophys. J. Int.*, *103(3)*, 599-608.

Mainprice, D., & Humbert, M. (1994). Methods of calculating petrophysical properties from lattice preferred orientation data. *Surveys in Geophysics*, *15*, 575-592.

Mainprice, D., & Silver, P. (1993). Interpretation of SKS-waves using samples from the sub-continental lithosphere. *Phys. Earth Planet. Inter.*, 78, 257-280.

Makeyeva, L. I., Vinnik, L. P., & Roecker, S. W. (1992). Shear-wave splitting and small-scale convection in the continental upper mantle. *Nature*, *358*, 144-146.

Mao, Z., Jiang, F., & Duffy, T. S. (2007). Single-crystal elasticity of zoisite $Ca_2Al_3Si_3O_{12}$ (OH) by Brillouin scattering. *Am. Mineral.*, *92*, 570-576.

Marson-Pidgeon, K. M., Savage, K., Gledhill, K., & Stuart, G. (1999). Seismic anisotropy beneath the lower half of the North Island, New Zealand. *J. Geophys. Res.*, *104*, 20,277-20,286.

Matthies, S., & Humbert, M. (1993). The Realization of the Concept of a Geometric Mean for Calculating Physical Constants of Polycrystalline Materials. *Physica Status Solidi (b)*, *177*, K47-K50.

Mavko, G., Mukerji, T., & Dvorkin, J. (2009). *The Rock Physics Handbook: Tools for Seismic Analysis in Porous Media*. Cambridge: Cambridge Univ. Press.

McKenzie, D. (1979). Finite deformation during fluid flow. *J. Geophys.*, *58,* 689-715.

McNamara, D. E., Owens, T. J., Silver, P. G., & Wu, F. (1994). Shear wave anisotropy beneath the Tibetan Plateau. *J. Geophys. Res.*, *99(B7)*, 13,655-13,665.

McSkimin, H. J., & Andreatch, P. (1962). Analysis of the pulse superposition method for measured ultrasonic wave velocities as a function of temperature and pressure. *J. Acoust. Soc. Am.*, *34*, 609-637.

Meglis, I. L, Engelder, T., & Graham, E. K. (1991). The effect of stress-relief on ambient microcrack porosity in core samples from the Kent Cliffs (New York) and Moodus (Connecticut) scientific research boreholes. *Tectonophysics*, *186*, 163-173.

Meissner, R., Rabbel, W., & Kern, H. (2006). Seismic lamination and anisotropy of the lower continental crust. *Tectonophysics*, *416*, 81-99.

Michibayashi, K., Tasaka, M., Ohara, Y., Ishii, T., Okamoto, A., & Fryer, P. (2007). Variable microstructure of peridotite samples from the southern Mariana Trench: evidence of a complex tectonic evolution. *Tectonophysics*, *444*, 111-118.

Middlemost, E. A. (1994). Naming materials in the magma/igneous rock system. *Earth Sci. Rev.*, *37*, 215-224.

Miller, V., & Savage, M. (2001). Changes in seismic anisotropy after volcanic eruptions: evidence from Mount Ruapehu. *Science*, *293*, 2231-2235.

Mizukami, T., Wallis, S. R., & Yamamoto, J. (2004). Natural example of olivine lattice preferred orientation patterns with a flow-nomal a-axis maximum. *Nature*, *427*, 29-32.

Montagner, J. P. & Tanimoto, T. (1991). Global upper mantle tomography of seismic velocities and anisotropies. *Geophys. J. Res.*, *96*, 20,337-20,351.

Moore, D. E., & Lockner, D. A. (2007). Comparative deformation behavior of minerals in serpentinized ultramafic rock: Application to the slab-mantle interface in subduction zones. *Int. Geol. Rev.*, *49*, 401-415.

Moore, D. E., Lockner, D. A., Summers, R., Ma, S. & Byerlee, J. D. (1996). Strength of chrysotile-serpentinite gouge under hydrothermal conditions: can it explain a weak San Andreas fault? *Geology*, *24*, 1041-1044

Morgan, P. J., Hasenclever, J., Hort, M., Rüpke, L., & Parmentier, E. M. (2007). On subducting slab entrainment of buoyant asthenosphere. *Terra Nova*, *19*, 167-173.

Morrow, C. A., Lockner, D., Hickman, S., Rusanov, M., & Rockel, T. (1994). Effects of lithology and depth on the permeability of core samples from the Kola and KTB drill holes. *J. Geophys. Res.*, *99*, 7263-7274.

Nadeau, J. C. (1999). A note on the effective Lamé constants of polycrystalline aggregates of cubic crystals. *J. Appl. Mech.*, *66*, 577.

Nakajima, J., & Hasegawa, A. (2004). Shear-wave polarization anisotropy and subduction-induced flow in the mantle wedge of northern Japan. *Earth Planet. Sci. Lett.*, *225*, 365-377.

Nakamura, T., Tsuboi, S., Kaneda, Y., & Yamanaka, Y. (2010). Rupture process of the 2008 Wenchuan, China earthquake inferred from teleseismic waveform inversion and forward modeling of broadband seismic waves. *Tectonophysics*, *491*, 72–84

Nicolas, A., & Christensen, N. I. (1987). Formation of anisotropy in upper mantle peridotites-a review. In K. Fuchs & C. Froideoaux (eds.), *Composition, Structure and Dynamics of the Lithosphere-Asthenosphere System* (pp. 111-123). Washington D C: AGU.

Nur, A., & Simmons, G. (1969a). Stress induced anisotropy in rocks: an experimental study. *J. Geophys. Res.*, *74*, 6667-6674.

Nur, A., & Simmons, G. (1969b). The effect of saturation on velocity in low porosity rocks. *Earth Planet. Sci. Lett.*, *7*, 183-193.

Nye, J. F. (1957). *Physical Properties of Crystals: Their Representation by Tensors and Matrices*. London: Oxford University Press, Amen House.

Okaya, D., Christensen, N. I., Stanley, D., & Stern, T. (1995). Crustal anisotropy in the vicinity of the Alpine Fault zone, South Island, New Zealand. *J. Geol. Geophys.*, *38*, 579-583.

Ozacar, A. A., & Zandt, G. (2004). Crustal seismic anisotropy in central Tibet: Implications for deformational style and flow in the crust. *Geophys. Res. Lett.*, *31*, doi:10.1029/2004GL021096.

Padron-Navarta, J. A., Hermann, J., Garrido, C. J., Sánchez-Vizcaíno V. L. & Gómez-Pugnaire, M. T. (2010). An experimental investigation of antigorite dehydration in natural silica-enriched serpentinite. *Contrib. Mineral Petrol.*, *159*, 25-42.

Park, J. & Yu, Y. (1993). Seismic determination of elastic anisotropy and mantle flow. *Science*, *261*, 1159-1162.

Peacock, S., Crampin, S., Booth, D. C. & Fletcher, J. B. (1988). Shear-wave splitting in the Anza seismic gap, Southern California: temporal variations as possible precursors. *J. geophys. Res.*, *93*, 3339-3356

Pei, S., Su, J., Zhang, H., Sun, Y., Toksöz, M. N., Wang, Z., (...) He, J. (2010). Three-dimensional seismic velocity structure across the 2008 Wenchuan M_s 8.0 earthquake, Sichuan, China. *Tectonophysics*, *491*, 211-217.

Peselnick, L., & Wilson, W. H. (1968). Wave velocities and hysteresis in Solenhofen limestone for pressures up to 12 kbar. *J. Geophys. Res.*, *73*, 3271-3286.

Peslier, A. (1999). *Petrologie et Geochimie Isotopique de Xenolithes Mantelliques de la Cordillere Canadienne*. Ph.D. thesis. Université de Montréal, Qc., Canada.

Peyton, V. V., Levin, J., Park, M., Brandon, M., Lees, J., Gordeev, E., & Ozerov, A. (2001). Mantle flow at a slab edge: Seismic anisotropy in the Kamchatka region. *Geophys. Re.s Lett.*, *28*, 379-382.

Pickett, G. R. (1963). Acoustic character logs and their application in formation evaluation. *Journal of Petroleum Technology*, *15*, 650-667.

Piromallo, C., Becker, T. W., Funiciello F, & Faccenna, C. (2006). Three-dimensional instantaneous mantle flow induced by subduction. *Geophys. Res. Lett.*, *33*, doi:10.1029/2005GL025390, Polet, J., Silver, P. G., & Beck, S. (2000). Shear wave anisotropy beneath the Andes from the BANJO, SEDA, and PISCO experiments. *J. Geophys. Res.*, *105*, 6287-6304.

Postma, G. W. (1955). Wave propagation in a stratified medium. *Geophysiques*, *20*, 780-806.

Pozgay, S. H., Wiens, D. A., Conder, J. A., Shiobara, H., & Sugioka, H. (2007). Complex mantle flow in the Mariana subduction system: evidence from shear wave splitting. *Geophys. J. Int.*, *170*, 371-386.

Prasad, M., Manghnani, M. H., & Siegesmund, S. (1994). Velocity and attenuation characteristics of selected KTB core samples. *Scientific Drilling*, *4*, 221-231.

Pulford, A., Savage, M., & Stern, T. (2003). Absent anisotropy: The paradox of the Southern Alps orogen. *Geophys. Res. Lett.*, *30(20)*, 2051, doi:10.1029/2003GL017758.

Ranero, C. R., Villasenor, A,, Morgan, P. J., & Weinrebe, W. (2005). Relationship between bend-faulting at trenches and intermediate-depth seismicity. *Geochem. Geophys. Geosyst.*, *6*, Q12002, doi:10.1029/2005GC000997.

Raterron, P., Chen, J., Li, L., Weidner, D. & Cordier, P. (2007). Pressure-induced slip-system transition in forsterite: Single-crystal rheological properties at mantle pressure and temperature. *Am. Mineral.*, *92*, 1436-1445.

Raterron, P., Wu, Y., Weidner, D. J., & Chen, J. (2004). Low-temperature olivine rheology at high pressure. *Phys. Earth Planet. Inter.*, *145*, 149-159.

Reuss, A. (1929). Berechnung der Fliessgrenze von Mischkristallen (Calculation of flow limits of mixed crystals on basis of plasticity of monocrystals). *Zeitschrift fuer Angewandte Mathematik und Mechanik*, *9(1)*, 49-58.

Ribe, N. M. (1989). Seismic anisotropy and mantle flow. *J. Geophys. Res.*, *94*, 4123-4223.

Ringwood, A. (1975). *Composition and Petrology of the Earth's Upper Mantle*. London: McGraw-Hill.

Ringwood, A. (1991). Phase transformations and their bearings on the constitution and dynamics of the mantle. *Geochem Cosmochem Acta*, *55*, 2083-2110.

Riznichenko, Y. V. (1949). Seismic quasi-anisotropy. *Isw. Akad Nauk SSSR*, *13*, 518-544.

Robert, A., Pubellier, M., de Sigoye, J., Vergne, J., Lahfid, A., Cattin, R., (...) Zhu, J. (2010). Structural and thermal characters of the Longmen Shan (Sichuan, China). *Tectonophysics*, *491*, 165-173.

Royden, L. H., Burchfiel, B. C., King, R. W., Wang, E., Chen, Z., Shen, F., Liu, Y. (1997). Surface deformation and low crustal flow in eastern Tibet. *Science, 276*, 788-790.

Russo, R. M. (2009). Subducted oceanic asthenosphere and upper mantle flow beneath the Juan de Fuca slab. *Lithosphere*, *1*, 195-205.

Russo, R. M., & Silver, P. G. (1994). Trench-parallel flow beneath the Nazca plate from seismic anisotropy. *Science*, *263*, 1105-1111.

Ryzhova, T. V., Aleksandrov, K. S., & Korobkova, V. M. (1966). The elastic properties of rock-forming minerals, V. Additional data on silicates. *Phys. Solid Earth*, *2*, 63-65.

Salah, M. K., Seno, T., & Iidaka, T. (2008). Upper mantle anisotropy beneath central and southwest Japan: an insight into subduction-induced mantle flow. *J. Geodyn.*, *46*, 21-37.

Saruwatari, K., Ji, S., Long, C., & Salisbury, M. H. (2001). Seismic anisotropy of mantle xenoliths and constraints on upper mantle structure beneath the southern Canadian Cordillera. *Tectonophysics*, *339*, 403-426.

Savage, M. K. (1999). Seismic anisotropy and mantle deformation: what have we learned from shear wave splitting? *Rev. Geophys.*, *37*, 65-106.

Savage, M. K., & Silver, P. (1993). Mantle deformation and tectonics: constraints from seismic anisotropy in the western United States. *Phys. Earth Planet. Int.*, *78*, 207-227.

Savage, M. K., Peppin, W. A., & Vetter, U. R. (1990). Shear wave anisotropy and stress direction in and near Long Valley Caldera, California, 1979-1988. *J. Geophys. Res.*, *95*, 11,165-11,177.

Schellart, W. P., Freeman, J., Stegman, D. R., Moresi, L. & May, D. (2007). Evolution and diversity of subduction zones controlled by slab width. *Nature*, *446*, 308-311

Schmidt, M. W., & Poli, S. (1998). Experimentally based water budgets for dehydrating slabs and consequences for arc magma generation. *Earth Planet. Sci. Lett.*, *163*, 361-379.

Scholz, C. H. (1990). The mechanics of earthquakes and faulting. Cambridge: Cambridge University Press.

Schon, J. H. (1996). *Physical Properties of Rocks*. Pergamon.

Seno, T., Zhao, D., Kobayashi, Y., & Nakamura, M. (2001). Dehydration of serpentinized slab mantle: Seismic evidence from southwest Japan. *Earth Planets Space*, *53*, 861-871.

Seront, B., Mainprice, D. & Christensen, N. I. (1993). A determination of the three-dimensional seismic properties of anorthosite: comparison between values calculated from the petrofabric and direct laboratory measurements. *J. Geophys. Res.*, *98(B2)*, 2209-2221.

Shapiro, S. A. (2003). Elastic piezosensitivity of porous and fractured rocks. *Geophysics*, *68*, 482-486.

Shearer, P. M., & Orcutt, J. A. (1986). Compressional and shear wave anisotropy in the oceanic lithosphere—The Ngendei seismic refraction experiment. *Geophys. J. R. Astron. Soc.*, *87*, 967-1003.

Shen, A. H., Bassett, W. A., & Chou, I. M. (1993). The α-β quartz transition at high temperatures and pressures in a diamond-anvil cell by laser interferometry. *Am. Mineral.*, *78*, 694-698.

Sherrington, H. F., Zandt, G., & Frederiksen, A. (2004). Crustal fabric in the Tibetan Plateau based on waveform inversions for seismic anisotropy parameters. *J. Geophys. Res.*, *109*, B02312, doi:10.1029/2002JB002345.

Shih, X. R., & Meyer, R. P. (1990). Observation of shear wave splitting from natural events: South Moat of Long Valley Caldera, California, June 29, to August 12, 1982. *J. Geophys. Res.*, *95*, 11,179-11,195.

Shih, X. R., Schneider, J. F., & Meyer, R. P. (1991). Polarities of P and S waves, and shear wave splitting observed from the Bucaramanga nest, Colombia. *J. Geophys. Res.*, *96 (B7)*, 12,069-12,082.

Sibson, R. H., Robert, F., & Poulsen, K. H. (1988). High-angle reverse faults, fluid-pressure cycling, and mesothermal gold-quartz deposits. *Geology*, *16*, 551-555.

Siegesmund, S., Takeshita, T., & Kern H. (1989). Anisotropy of V_p and V_s in an amphibolite of the deeper crust and its relationship to the mineralogical, microstructural and textural characteristics of the rock. *Tectonophysics*, *157*, 25-38.

Siegesmund, S., Vollbrecht, A., Chlupac, T., Nover, G., Dürrast, H., Müller, J., & Weber K. (1993). Fabric-controlled anisotropy of petrophysical properties observed in KTB core samples. *Scientific Drilling*, *4*, 31-54.

Silver, P. G. (1996). Seismic anisotropy beneath the continents: Probing the depths of Geology. *Annu. Rev. Earth Planet. Sci.*, *24*, 385-432.

Silver, P. G., & Chan, W. W. (1988). Implications for continental structure and evolution from seismic anisotropy. *Nature*, *335*, 34-39.

Silver, P. G., & Chan, W. W. (1991). Shear wave splitting and subcontinental mantle deformation. *J. Geophys. Res.*, *96*, 16,429-16,454.

Silver, P. G., & Kaneshima, S. (1993). Constraints on mantle anisotropy beneath Precambrian North America from a transportable teleseismic experiment. *Geophys. Res. Lett.*, *20*, 1127-1130.

Skemer, P., Katayama, I., & Karato, S. (2006). Deformation fabrics of the Cima di Gagnone Peridotite Massif, Central Alpes, Swizerland: evidence of deformation under water-rich conditions at low temperatures. *Contrib. Mineral. Petrol.*, *152*, 43-51.

Smith, G. P., Wiens, D. A., Fischer, K. M., Leroy M. D., Webb, S. C., & Hildebrand, J. A. (2001). A complex pattern of mantle flow in the Lau back-arc. *Science*, *292*, 713-716.

Smith, M. L. & Dahlen, F. A. (1973). The azimuthal dependence of Love and Rayleigh wave propagation in a slightly anisotropic medium. *J. Geophys. Res.*, *78*, 3321-3333.

Sneddon, I.N., & Lowengrub, M. (1969). Crack Problems in the Classical Theory of Elasticity. New York: Wiley.

Sol, S., Meltzer, A., Bürgmann, R., van der Hilst, R. D., King, R., (…) Zurek, B. (2007). Geodynamics of the southeastern Tibetan Plateau from seismic anisotropy and geodesy. *Geology*, *35(6)*, 563-566.

Spetzler, H. A., & Anderson, D. L. (1968). The effect of temperature and partial melting on velocity and attenuation in a simple binary mixture. *J. Geophys. Res.*, *73*, 6051-6060.

Stegman, D. R., Freeman, J., Schellart, W. P., Moresi, L., & May, D. (2006). Influence of trench width on subduction hinge retreat rates in 3-D models of slab rollback. *Geochem. Geophys. Geosyst.*, *7*, Q03012, doi:10.1029/2005GC001056

Stierman, D. J., Healy, J. H., & Kovach, R. L. (1979). Pressure-induced velocity gradient: An alternative to a Pg refractor in the Gabilan range, central California. *Bull. Seism. Soc. Am.*, *69*, 397-415.

Sun, S., Ji, S.C., Wang, Q., Xu, Z.Q., Salisbury, M., 2011. Seismic velocities and anisotropy of core samples from the Chinese Continental Scientific Drilling (CCSD) borehole in the Sulu UHP terrane, eastern China. *Journal of Geophysical Research*, in press.

Sun, S., Ji, S.C., Wang, Q., Salisbury, M. Xu, Z.Q., 2011. Seismic wave velocity differences between surface-derived and deep borehole core samples from the Sulu UHP metamorphic terrane. *Geology*, submitted

Sun, S., Ji, S.C., Wang, Q., Wang, H.C., Long, C.X., Salisbury, M., 2011. Seismic properties of the Longmen Shan complex: Implications for the moment magnitude of the great 2008 Wenchuan earthquake in China. *Tectonophysics*, submitted.

Sun, S., Ji, S.C., 2011. On the formation of seismic anisotropy and shear wave splitting in oceanic subduction zones. *Geotectonica et Metallogenia*, 35, 627-646. (in Chinese with English abstract)

Svetlov, I. L., Epishin, A. I., Krivko, A. I., Samoilov, A. I., Odintsev, I. N., & Andreev, A. P. (1988). Anisotropy of Poisson's ratio of single crystals of nickl alloy. *Soviet Physics Doklady*, *33*, 771.

Tackley, P. J. (2008). Geodynamics: Layer cake or plum pudding? *Nat. Geosci.*, *1*, 157- 158.

Takanashi, M., Nishizawa, O., Kanagawa, K., &Yasunaga, K. (2001). Laboratory measurements of elastic anisotropy parameters for the exposed crustal rocks from the Hidaka Metamorphic Belt, Central Hokkaido, Japan. *Geophys. J. Int.*, *145*, 33-47.

Tanimoto, T. & Anderson, D. L. (1985). Lateral heterogeneity and azimuthal anisotropy of the Upper Mantle: Love and Rayleigh waves 100-205s. *J. geophys. Res.*, *90*, 1842-1858.

Tanimoto, T., & Anderson, D. L. (1984). Mapping mantle convection. *Geophys. Res. Lett.*, *11*, 287-290.

Tapponnier, P., Xu, Z., Roger, F., Meyer, B., Arnaud, N., Wittlinger, G., & Yang, J. (2001). Oblique stepwise rise and growth of the Tibet Plateau. *Science*, *294*, 1671-1677.

Tasaka, M., Michibayashi, K., & Mainprice, D. (2008). B-type olivine fabrics developed in the fore-arc side of the mantle wedge along a subducting slab. *Earth Planet. Sci. Lett.*, *272*, 747-757.

Tatham, D. J., Lloyd, G. E., Butler, R. W. H., & Casey, M. (2008). Amphibole and lower crustal seismic properties. *Earth Planet. Sci. Lett.*, *267*, 118-128.

Teanby, N., Kendall, J.-M., Jones, R. H., & Barkved, O. (2004). Stress-induced temporal variations in seismic anisotropy observed in microseismic data. *Geophys. J. Int.*, *156*, 459-466.

Tse, S.T., & Rice, J.R. (1986). Crustal earthquake instability in relation to the depth variation of frictional slip properties. *J. Geophys. Res.*, *91*, 9452-9472.

Tullis, J., 1990. Experimental studies of deformation mechanisms and microstructures in quartzo-feldspathic rocks. In D. J. Barber & P. G. Meredith (eds.), *Deformation Processes in Minerals, Ceramics and Rocks* (pp. 190-227). London: Uniwin Hyman.

Ulmer, P., & Trommsdorff, V. (1995). Serpentine stability to mantle depths and subduction-related magmatism. *Science*, *268*, 858-861.

United States Geological Survey (USGS, 2008). Magnitude 7.9 Eastern Sichuan, China. http://earthquake.usgs.gov/eqcenter/eqinthenews/2008/us2008ryan/

van der Hilst, R. D., Widiyantoro, S., & Engdahl, E. R. (1997). Evidence for deep mantle circulation from global tomography. *Nature*, *386*, 578-584.

Vaughan, M. T., & Guggenheim S. (1986). Elasticity of muscovite and its relationship to crystal structure. *J. Geophys. Res.*, *91(5)*, 4657-4664.

Vinnik, L. P., Kosarev, G. L., & Makeyeva, L. I. (1984). Anisotropy in the lithosphere from the observations of SKS and SKKS. Dokl. Acad. *Nauk USSR*, *278*, 1335-1339. (in Russian).

Vinnik, L. P., Krishna, V. G., Kind, R., Bormann, P., & Stammler, K. (1994). Shear wave splitting in the records of the German Regional Seismic Network. *Geophys. Res. Let.*, *21*, 457-460.

Vinnik, L. P., Makeyeva, L. I., & Milev, A. (1992). Global patterns of azimuthal anisotropy and deformations in the continental mantle. *Geophys J Int*, *111*, 433-447.

Voigt, W. (1928). *Lehrbuch der Kristallphysik*. Berlin-Leipzig: Teubner Verlag.

Vollbrecht, A., Stipp, M., Olesen, N. Ø. (1999). Crystallographic orientation of microcracks in quartz and inferred deformation processes: A study on gneisses from the German Continental Deep Drilling Project (KTB). *Tectonophysics*, *303*, 279-297.

Wada I, Wang K, He J, & Hyndman, R. D. (2008). Weakening of the subduction interface and its effects on surface heat flow, slab dehydration, and mantle wedge serpentinization, *J Geophys Res*, *113*, B04402, doi:10.1029/2007JB005190.

Walsh, J. P. (1965). The effects of cracks on the compressibility of rocks. *J. Geophys. Res.*, *70*, 381-389.

Wang, C. Y., Chan, W. W., & Mooney, W. D. (2003). Three-dimensional velocity structure of crust and upper mantle in southwestern China and its tectonic implications. *J. Geophys. Res.*, *108(B9)*, 2442, doi:10.1029/2002JB001973.

Wang, C. Y., Han, W. B., Wu, J. P., Lou, H., & Chan, W. W. (2007). Crustal structure beneath the eastern margin of the Tibetan Plateau and its tectonic implications. *J. Geophys. Res.*, *112*, B07307. doi:10.1029/2005JB003873.

Wang, C. Y., Zhu, L., Lou, H., Huang, B. S., Yao, Z., & Luo, X. (2010). Crustal thicknesses and Poisson's ratios in the eastern Tibetan Plateau and their tectonic implications. *J. Geophys. Res.*, *115*, B11301. doi:10.1029/2010JB007527.

Wang, E. Q., Meng, Q. R., & Chen Z. L. (2001). Early Mesozoic left-lateral movement along the Longmen Shan fault belt and its tectonic implications. *Earth Science Frontiers*, *8*, 375-384.

Wang, H., Liu, M., Shen, X., & Liu, J. (2010). Balance of seismicmoment in the Songpan-Ganze region, eastern Tibet: Implications for the 2008 Great Wenchuan earthquake. *Tectonophysics*, *491*, 154-164.

Wang, Q. (2009). *Seismic Velocities, Anisotropy, Hysterisis and Poisson's ratio of Ultrahigh Pressure (UHP) Metamorphic Rocks*. Ph.D., Université de Montréal, Qc., Canada.

Wang, Q., & Ji, S. C. (2009). Poisson's ratios of crystalline rocks as a function of hydrostatic confining pressure. *J. Geophys. Res.*, *114*, B09202, doi:10.1029/2008JB006167.

Wang, Q., Burlini, L., Mainprice, D., & Xu, Z. (2009). Geochemistry, petrofabrics and seismic properties of eclogites from the Chinese Continental Scientific Drilling boreholes in the Sulu UHP terrane, eastern China. *Tectonophysics*, *475*, 251-266.

Wang, Q., Ji, S. C., Salisbury, M. H., Pan, M. B., Xia, B., & Xu, Z. Q. (2005a). Pressure dependence and anisotropy of P-wave velocities in ultrahigh-pressure metamorphic rocks from the Dabie-Sulu orogenic belt (China): implications for seismic properties of subducted slabs and origin of mantle reflections. *Tectonophysics*, *398*, 67-99.

Wang, Q., Ji, S. C., Salisbury, M. H., Xia, B., Pan, M. B., & Xu, Z. Q. (2005b). Shear wave properties and Poisson's ratios of ultrahigh-pressure metamorphic rocks from the Dabie-Sulu orogenic belt: Implications for crustal composition. *J. Geophys. Res.*, *110*, B08208.

Wang, W. M., Zhao, L. F., Li, J., & Yao, Z. X. (2008). Rupture process of the 2008 M_s 8.0 Wenchuan earthquake of Shichuan, China. *Chinese J. Geophys.*, *51(5)*, 1403-1410 (in Chinese with English abstract).

Watanabe, T., Kasami, H., & Ohshima, S. (2007). Compressional and shear wave velocities of serpentinized peridotites up to 200 MPa. *Earth Planets Space*, *59*, 233-244.

Watt, J. P., Davies, G. F., & O'Connell, R. J. (1976). The elastic properties of composite materials. *Rev. Geophys. Space Phys.*, *14*, 541-563.

Webb, S. L. (1989). The elasticity of the upper mantle orthosilicates olivine and garnet to 3 GPa. *Phys. Chem. Miner., 16*, 684-692.

Webb, S. L., & Jackson, I. (1993). The pressure dependence of the elastic moduli of single-crystal orthopyroxene $(Mg_{0.8}Fe_{0.2})SiO_3$. *European Journal of Mineralogy*, *5*, 1111-1119.

Wepfer, W. W., & Christensen, N. I. (1991). A seismic velocity—confining pressure relation, with applications. *Int. J. Rock. Mech. Min. Sci. & Geomech. Abstr.*, *28*, 451-456.

White, A.P., & Brantley, S. L. (1995), Chemical weathering rates of silicate minerals. *Reviews in Mineralogy*, *31*. Washington D C: Mineralogical Society of America.

Wirth, E., & Long, M. D. (2010). Frequency-dependent shear wave splitting beneath the Japan and Izu-Bonin subduction zones. *Phys. Earth Planet. Inter.*, *181*, 141-154.

Wookey, J., Kendall, J. M., & Rumpker, G. (2005). Lowermost mantle anisotropy beneath the north Pacific from differential S-ScS splitting. *Geophys. J. Int.*, *161*, 829- 838.

Xu, M., Zhu C. Q., Tian, Y. T., Rao, S., & Hu S. B. (2011). Borehole temperature logging and characteristics of subsurface temperature in Sichuan Basin. *Chinese J. Geophys.*, *54(4)*, 1052-1060 (in Chinese with English abstract).

Xu, X., Wen, X., Yu, G., Chen, G., Klinger, Y., Hubbard, J., & Shaw, J. (2009). Coseismic reverse- and oblique-slip surface faulting generated by the 2008 M_w 7.9 Wenchuan earthquake, China. *Geology*, *37*, 515-518.

Xu, Z. J., & Song, X. (2010). Joint inversion for crustal and Pn velocities and Moho depth in Eastern Margin of the Tibetan Plateau. *Tectonophysics*, *491*, 185-193.

Xu, Z. Q., Hou, L. W., Wang, Z. X., et al. (1992). *Orogenic processes of the Songpan-Garzi orogenic belt of China*. Beijing: Geological Publishing House. (in Chinese)

Xu, Z. Q., Ji, S. C., Li, H. B., Hou, L. W., Fu, X. F., & Cai, Z. H. (2008). Uplift of the Longmen Shan range and the Wenchuan earthquake. *Episodes*, *31(3)*, 291-301.

Xu, Z. Q., Wang, Q., Tang Z. M., & Chen, F. Y. (2009a). Fabric kinematics of ultrahigh-pressure metamorphic rocks from the main borehole of the Chinese Continental Scientific Drilling Project: implications for continental subduction and exhumation. *Tectonophysics*, *475*, 233-248

Xu, Z. Q., Yang, W. C., Ji, S. C., Zhang, Z. M., Yang, J. S., Wang, Q., & Tang, Z. M. (2009b). Deep root of a continent collision belt: Evidence from the Chinese Continental Scientific Drilling (CCSD) deep borehole in the Sulu ultrahigh-pressure (HP-UHP) metamorphic terrane, China. *Tectonophysics*, *475*, 204-219.

Yan, D. P., Zhou, M. F., Wei, G. Q., Gao, J. F., Liu, S. F., Xu, P., & Shi, X. Y. (2008). The Pengguan tectonic dome of Longmen Mountains, Sichuan Province: Mesozoic denudation of a Neoproterozoic magmatic arc-basin system. *Science in China Series D: Earth Sciences*, *51(11)*, 1545-1559.

Yang, Z., Yu, X., Zheng, Y., Chen, Y., Ni, X., & Chan, W. (2004). Earthquake relocation and 3-dimensional crustal structure of P-wave velocity in central-western China. *Acta Seismol. Sin.*, 17(1), 20–30.

Yu, Y. & Park, J. (1994). Hunting for azimuthal anisotropy beneath the Pacific Ocean region. *J. Geophys. Res.*, *99*, 15,399-15,421.

Zhang, M., Ebrom, D. A., McDonald, J. A. & Tatham, R. H. (1996). Comparison of experimental velocity measurements with theoretical results in a solid-solid composite materials. *Geophysics*, *61*, 1429-1435.

Zhang, P., Zhou, Z., Xu, C., & Zhang, Q. (2008). Geochemistry of Pengguan complex in the Longmenshan region, western Sichuan province, SW China: petrogenesis and tectonic implications. *Geotectonica et Metallogenia*, *32(1)*, 105-116 (in Chinese with English abstract).

Zhang, R. Y. & Liou, J. G. (1996). Coesite inclusions in dolomite from eclogite in the southern Dabie Mountains, China: the significance of carbonate minerals in UHPM rocks. *American Mineralogist*, *81*, 181-186.

Zhang, Y., Feng, W. P., Xu, L. S., Zhou, C. H., & Chen, Y. T. (2009). Spatio-temporal rupture process of the 2008 great Wenchuan earthquake. *Science in China, Series D: Earth Sciences*, *52(2)*, 145-154.

Zhao, Y., & Anderson, D. L. (1994). Mineral physics constraints on the chemical composition of the Earth's lower mantle. *Phys. Earth Planet. Inter.*, *85*, 273-292.

Zhao, Z., Fan, J., Zheng, S. H., et al. (1997). Crustal structure and accurate hypocenter determination along the Longmenshan fault zone. *Acta Seismol. Sin.*, *19(6)*, 615-622 (in Chinese).

Zhu, A., Xu, X., Diao, G., Su, J., Feng, X., Sun, Q., & Wang, Y. (2008). Relocation of the M_s 8.0 wenchuan earthquake sequence in part: preliminary seismotectonic analysis. *Seismology and Geology*, *30(3)*, 759-767 (in Chinese with English abstract).

Zimmerman, R. W., Somerton, W. H., & King, M. S. (1986). Compressibility of porous rocks. *J. Geophys. Res.*, *91*, 12,765-13,277.